Titre: Title:	A Depth-Averaged Numerical Model for Simulating Heat and Fluid Flows in Vegetated Channels
Auteur: Author:	Mohammad Moradi Larmaei
Date:	2012
Type:	Mémoire ou thèse / Dissertation or Thesis
Référence: Citation:	Moradi Larmaei, M. (2012). A Depth-Averaged Numerical Model for Simulating Heat and Fluid Flows in Vegetated Channels [Thèse de doctorat, École Polytechnique de Montréal]. PolyPublie. https://publications.polymtl.ca/932/

Document en libre accès dans PolyPublie
Open Access document in PolyPublie

URL de PolyPublie: PolyPublie URL:	https://publications.polymtl.ca/932/
Directeurs de recherche: Advisors:	Tew-Fik Mahdi
Programme: Program:	Génie civil

UNIVERSITÉ DE MONTRÉAL

A DEPTH-AVERAGED NUMERICAL MODEL FOR SIMULATING HEAT AND FLUID FLOWS IN VEGETATED CHANNELS

MOHAMMAD MORADI LARMAEI

DÉPARTEMENT DES GÉNIES CIVIL, GÉOLOGIQUE, ET DES MINES

ÉCOLE POLYTECHNIQUE DE MONTRÉAL

THÈSE PRÉSENTÉE EN VUE DE L'OBTENTION

DU DIPLÔME DE PHILOSOPHIAE DOCTOR

(GÉNIE CIVIL)

AVRIL 2012

UNIVERSITÉ DE MONTRÉAL

ÉCOLE POLYTECHNIQUE DE MONTRÉAL

Cette thèse intitulée:

A DEPTH-AVERAGED NUMERICAL MODEL FOR SIMULATING HEAT AND FLUID
FLOWS IN VEGETATED CHANNELS

présentée par : MORADI LARMAEI Mohammad

en vue de l'obtention du diplôme de : Philosophiae Doctor

a été dûment acceptée par le jury d'examen constitué de:

M. TINAWI René, Ph.D., président

M. MAHDI Tew-Fik, Ph.D., membre et directeur de recherche

M. CAMARERO Ricardo, Ph.D., membre

M. ROBERT Jean-Loup, Ph.D., membre

DEDICATION

To my mother

ACKNOWLEDGEMENTS

RÉSUMÉ

Un modèle numérique complexe moyenné sur la profondeur est développé pour simuler l'hydrodynamique et le transfert de chaleur dans les canaux végétalisés, avec une capacité de simuler les ruptures de barrage et les phénomènes d'inondation. Le modèle est capable de simuler les deux types d'écoulements, laminaires et turbulents, il peut prendre en compte les effets des écoulements secondaires. Il utilise les derniers développements de la science des milieux poreux, afin de simuler l'écoulement dans les zones végétalisées et il est possible d'effectuer des simulations dimensionnelles ou adimensionnelles. Ce modèle moyenné sur la profondeur est capable de commencer une nouvelle simulation ou de reprendre une autre. Il utilise de nombreuses techniques innovantes pour minimiser automatiquement le temps de calcul pour des problèmes ayant un grand nombre de mailles de calcul. Il utilise beaucoup de techniques novatrices pour augmenter la précision des solutions, il offre un choix varié de conditions aux limites, il peut effectuer une solution du 2nd ordre et il supporte plusieurs techniques pour contrôler les erreurs résiduelles.

Comme première étape, le code numérique à deux dimensions est développé pour simuler l'écoulement et le transfert de chaleur. Les équations de transport sont résolues avec une méthode de collocation par volumes finis non structurés. Des données numériques et expérimentales sont utiliseés pour valider le code pour différentes conditions d'écoulement. Une technique multi-bloc de triangulation locale (MBLT) est développée et appliquée à plusieurs simulations pour diminuer la magnitude absolue des oscillations du champ de pression. Dans cette technique, une solution pour réduire la magnitude absolue des oscillations de pression est recherchée à travers la grille, de façon innovante, au lieu des équations de transport de masse et de mouvement. La technique de MBLT peut être simplement appliquée à des géométries complexes. Cette propriété la qualifie pour être utilisée dans le génie logiciel.

Le code bidimensionnel validé est ensuite étendu à un code moyenné sur la profondeur, lui même validé par d'autres données expérimentales et numériques. Une équation de vorticité y est également ajoutée afin de prendre en compte l'effet des courants secondaires. Les équations de transport de profondeur moyenne sont écrites d'une manière innovante, et les termes sources dus au fond du canal sont également discrétisées par une méthode innovante. Lorsque la profondeur d'eau est très faible, l'application de ces techniques élimine les oscillations numériques du niveau

d'eau. Un choix approprié de la grille pour les simulations d'écoulements moyennés sur la profondeur est alors investigué en étudiant la solution des équations de transport moyennées sur la profondeur pour des grilles et des conditions d'écoulement variées. Une méthode innovante, valeur totale – linéairement interpolée (TV-LI), est également développée pour l'interpolation des variables sur les faces des mailles, à partir de leurs centres. Cette technique réduit le temps de calcul et le taux de réduction augmente avec le nombre de mailles.

Le code moyenné sur la profondeur est amélioré en incluant la simulation des rivières à frontières mobiles, où la position du front d'eau est fonction du temps et de l'espace. Une méthode innovante est proposée pour contrôler la profondeur d'eau dans les régions peu profondes afin d'éviter la formation de zones avec une profondeur d'eau faussement négative. Une méthode innovante, incorporée dans ce code, du 2e ordre est développée pour traiter les fronts couvrant-découvrant. Cette technique d'ordre supérieur élimine la formation de fausses couches d'eau minces qui se forment normalement et s'étendent en aval quand une technique d'ordre inférieur de couvrant-découvrant est utilisée. Comme avantage important de cette fonction, le solveur va résoudre les équations de transport uniquement dans les régions réellement mouillées. Celà gardera le temps de calcul minimal.

Comme dernière étape dans le développement du code moyenné sur la profondeur, le code est étendu à la simulation des canaux partiellement végétalisés. Toute zone végétalisée est supposée être un milieu poreux et à leur tour, les équations discrétisées sont modifiées en utilisant le concept de double décomposition. La porosité et la densité de végétation sont redéfinies afin que la densité de végétation ou sa porosité puissent être dérivées l'une de l'autre. Celà garantira la conservation de masse, de quantité de mouvement et les autres propriétés du fluide. Dans les équations de quantité de mouvement, la force moyenne secondaire microscopique (moyennée dans le temps) est modifiée pour des milieux poreux végétalisés et sa forme macroscopique est obtenue. Un terme source de dissipation est dérivé, de façon innovante, et est ajouté à l'équation de vorticité pour simuler l'amortissement de la vorticité transversale par la végétation. Ce terme source d'amortissement réduit efficacement la magnitude absolue de la vorticité transversale et, en contre partie, il prend en compte l'amortissement des courants secondaires, induit par la végétation. Il est trouvé, suite à de nombreuses simulations numériques, que la force secondaire, calculée en solvant une équation de vorticité, n'améliorera la précision du champ de vitesse simulé que si les hypothèses d'eau peu profonde sont

fortement observées. L'hypothèse de l'équilibre thermique local est appliquée au transport de la chaleur dans les zones végétalisées et un modèle d'une équation d'énergie est résolu. Pour l'équation de l'énergie, les fonctions murs sont modifiées en utilisant une technique innovante afin de tenir compte de la propriété thermique de la végétation. Cela permettra d'accroître la précision du flux de chaleur calculé à proximité de la paroi. Pour prendre en compte la diffusion thermique due au gradient de porosité, un terme supplémentaire est développé et ajouté au modèle de l'énergie à une équation. Ce terme peut causer d'importants flux de chaleur diffusifs quand la grille près de la frontière d'une zone végétalisée est très fine. L'effet de la dispersion thermique laminaire sur le champ de température calculé à bas nombres de Reynolds et de Péclet est aussi investigué. Les simulations pour les canaux partiellement végétalisés avec des écoulements turbulents à leurs entrées, révèlent que, l'effet de dispersion thermique laminaire sur le champ de température calculé n'est pas significatif. Indépendamment des conditions d'écoulement, il a été observé au cours des simulations qu'un modèle de turbulence à grand nombre de Reynolds peut être appliqué seulement dans des zones de faible densité de végétation.

Afin de simuler les rivières ayant une bathymétrie complexe, un outil est développé pour l'interpolation des données topographique, à partir de points de mesure, aux centres des mailles. Selon la stratégie utilisée pour la mesure des données, cet outil peut être utilisé pour interpoler les données avec trois méthodes différentes. Ce qui fournira une occasion pour la reconstruction optimale de la topographie du lit.

Les modèles, développés dans cette thèse, sont destinés à être utilisés pou des applications d'ingénieries telles que les ruptures de barrage et les inondations, les écoulements en rivières avec ou sans végétation et pollution thermique. Tous les modèles sont développés en se basant sur les concepts de sous-programmes, modules, ''subroutine'' et ''function'', et, en contre partie, il est possible de les étendre à de nouvelles applications. Ce modèle bidimensionnel est également modifiable en un modèle tridimensionnel.

ABSTRACT

In this thesis, a complex depth-averaged model is developed for simulating heat and fluid flows in vegetated channels, with a capability to simulate dam-break and flooding phenomena. The model is able to simulate both laminar and turbulent flows, it can take the secondary flow effects of any kind into account, it uses the latest developments in porous media science in order to simulate the flow in vegetated zones, and it is able to perform either a dimensional or a dimensionless solution. This depth-averaged model is able to start a solution from scratch or perform a hot start, it uses many innovative techniques to automatically minimize the computational cost for problems which include huge number of computational cells, it uses many innovative techniques for increasing the accuracy of solutions, it supports variety of boundary conditions, it can perform a high-order solution, and it supports several techniques for controlling the residual errors.

As the first step, a two-dimensional numerical code is developed for simulating heat and fluid flows. The transport equations are solved using a collocated unstructured finite-volume scheme. Both numerical and experimental data are extensively used in order to validate the code for various flow conditions. A Multi-Block Local Triangulation (MBLT) technique is developed and successfully applied to several simulations for reducing the absolute magnitude of the oscillations in pressure field. In this technique, a solution for reducing the absolute magnitude of pressure oscillation is innovatively looked for through grid rather than the transport equations for mass and momentum. The MBLT technique can be simply applied to complicated geometries. This property makes the MBLT technique desirable to be used in engineering software.

The validated two-dimensional code is then extended to a depth-averaged code where, the depth-averaged code itself is validated against additional experimental and numerical data. A vorticity equation is also added to the depth-averaged code in order to take the secondary flow effect into account. The depth-averaged transport equations are written in an innovative way, and the source terms due to the channel bed are also discretized with an innovative method. When the water depth is very small, application of these techniques eliminates the oscillations from the profile of water surface. An appropriate choice of grid for the depth-averaged simulations is then suggested through investigating the solution of depth-averaged transport equations on various grids and flow conditions. An innovative method, Total Value – Linearly Interpolated (TV-LI), is also

developed for interpolating variables from cells center into the cells faces. This technique reduces the computational cost and, the amount of reduction in computational cost increases when the number of cells increases.

The depth-averaged code is further extended to include the capability to simulate streams with moving boundaries where the position of water edge is a function of time and space. An innovative method is suggested for controlling the water depth in shallow regions in order to prevent formation of zones with spurious negative water depth. An innovative high-order technique is developed for treating the wetting-drying fronts, and is added to the depth-averaged code. This high-order technique eliminates formation of spurious thin layers of water which normally form and extend downstream when a low-order wetting-drying technique is used. As an important advantage of this feature, the solver will solve the transport equations only in actual wet regions. This will keep the computational cost minimized.

As the final step in developing the depth-averaged code, the code is extended to simulation of partially-vegetated open channel flows. Any vegetated zone is assumed to be a porous medium and, in turn, the discretized equations are modified using the double-decomposition concept. Vegetation porosity and density are redefined so that either the vegetation density or its porosity can be derived from the other one. This will guaranty conservation of mass, momentum, and the other fluid properties. The microscopic time-mean secondary force in momentum equations is modified for vegetated porous media and its macroscopic form is derived. An innovatively derived dissipation source term is added to the vorticity equation for simulating the damping of stream-wise vorticity by vegetation. This damping source term efficiently reduces the absolute magnitude of the stream-wise vorticity in vegetated zones and, in turn, it takes the vegetation-induced damping of the secondary flow into account. It is found by means of performing many numerical simulations that, the secondary force calculated through solving a vorticity equation will improve the accuracy of the computed velocity field only when the assumptions of shallow flow are strongly hold. The local thermal equilibrium hypothesis is applied to the transport of heat in vegetated zones and, in turn, a one-energy equation model is solved. For the energy equation, the wall functions are modified using an innovative technique in order to take account of the thermal property of vegetation material. This will increase the accuracy of the calculated near-wall heat flux. For taking the thermal diffusion due to the porosity gradient into account, an extra term is developed and added to the one-energy equation model. This term can cause

significant diffusive heat flux when the grid near the border of a vegetated zone is very fine. The effect of laminar thermal dispersion on computed temperature field at low Reynolds and Peclet numbers is also investigated. Computations for partially vegetated channels with turbulent input flow reveal that, the laminar thermal dispersion effect on computed temperature field is not significant. Independent of the flow condition, it is observed during simulations that, a high Reynolds number turbulence model can be applied only to vegetated zones with a low vegetation density.

In order to simulate streams with complicated bed topography, a tool is developed for interpolating geo-data from measurement points into the cells center. Depending upon the strategy used for measuring geo-data, this tool can be used for interpolating data with three different methods. This will provide an opportunity for optimum reconstruction of bed topography.

The models which are developed in this thesis are aimed to be used for engineering applications such as dam-break and flooding, channel flow, vegetation, and thermal pollution. All models are developed based on sub-program, module, subroutine, and function concepts and, in turn, it is easily possible to extend them to new applications. The two-dimensional model is also extendable to a three-dimensional model.

CONDENSÉ EN FRANÇAIS

Dans cette thèse, un modèle numérique moyenné sur la profondeur, Shallow Fluent, a été développé pour simuler le transfert de chaleur et l'hydrodynamique dans des canaux végétalisés. Shallow Fluent résout les équations de continuité et de quantité de mouvement pour des écoulements laminaires, le modèle standard k-ε quand le champ d'écoulement est turbulent, l'équation de vorticité quand les écoulements secondaires sont appréciables, et l'équation d'énergie quand il y a transfert de chaleur. Les derniers développements en science des milieux poreux ont été utilisés pour résoudre les équations de transport dans des zones avec végétation, et une technique innovatrice de couvrant-découvrant du second ordre a aussi été utilisée pour traiter la frontière eau-région séche.

L'algorithme SIMPLE a été utilisé afin d'obtenir un couplage entre les champs de pression et de vitesse. Dans cet algorithme, l'équation de continuité est convertie en équation de correction de pression. Tout d'abord, les équations de quantité de mouvement sont résolues pour un premier champ de pression et de vitesse. Ensuite, le champ de vitesse est utilisé dans l'équation de correction de pression et un champ de correction de pression est obtenu. Enfin, ce nouveau champ de correction de pression est alors utilisé pour corriger les champs de pression et de vitesse ainsi que d'autres grandeurs scalaires, si applicables. Cette méthode itérative est alors répétée jusqu'à ce que la convergence soit atteinte.

Les termes convectifs sont discrétisés avec la méthode ''upwind''. Le théorème de Green est utilisé pour le calcul du gradient au centre des cellules, et la méthode à deux points est utilisée pour le calcul du gradient aux extrémités de chaque cellule. Les méthodes du premier ordre et du second ordre sont disponibles pour calculer les flux convectifs et diffusifs. Les variables sont stockées selon une disposition co-locale de données et la méthode de Rhie et de Chew a été programmée pour corriger la vitesse interpolée aux extrémités des cellules. Cette correction de la vitesse interpolée est seulement appliquée quand le calcul du résidu de l'équation de continuité est effectué. Tous les termes source sont discrétisés avec la méthode ''point-wise''.

La première étape du développement de Shallow Fluent aura été de réduire un solutionneur tridimensionnel élémentaire à un solutionneur bidimensionnel (le solutionneur tridimensionnel étant capable de résoudre des écoulements laminaires et stationnaires). Dès que le code tridimensionnel a été réduit à un solutionneur bidimensionnel, certains aspects du code ont été

modifiés et améliorés. Ces modifications incluent l'extension du code bidimensionnel à un solutionneur général, la définition de nouveaux types de condition frontière, la définition de nouveaux critères de convergence, le réarrangement des conditions d'entrée de l'algorithme SIMPLE, le remplacement des techniques d'interpolation, et, pour finir, l'application des méthodes de Rhie et de Chew pour corriger la vitesse interpolée aux frontières des cellules. La version laminaire du solutionneur bidimensionnel est alors validée en comparant plusieurs solutions numériques avec des données expérimentales. Ces solutions numériques seront aussi comparées à celles proposées par Fluent 6.3.

Le modèle standard de turbulence $k - \varepsilon$ a été ajouté à la version laminaire du solutionneur bidimensionnel dans le but de tenir compte des effets de la turbulence. L'approche standard ''wall-fonction'' a été employée pour traiter les écoulements près de la paroi lorsque des termes sources sont appliqués sur des cellules situés près des parois. Le modèle a été validé par Fluent 6.3 et des données expérimentales. Lorsqu'une technique ''multibloc'' est employée, des zones graves de pression de damier apparaissent à l'interface des blocs de fluide. Ces mêmes zones de pression de damier sont observées sur des simulations faites avec Fluent6.3. Il a été montré que les triangles locaux (LTs) ont un effet significatif sur le lissage du champ de pression. Un LT est composé d'une cellule triangulaire et de ses cellules voisines les plus proches et celui-ci est considéré comme parfait si la cellule centrale et ses trois cellules voisines forment un triangle équilatéral, sinon il sera considéré comme tordu. Les simulations nous révèlent que les LTs parfaits augmentent de manière significative le lissage du champ de pression. Une technique locale ''multibloc'' (MBLT) de triangulation a ainsi été conçue afin d'établir des LTs parfaits sur le domaine. Les simulations nous montrent que, lorsqu'un maillage triangulaire structuré est appliqué aux régions près de la paroi et un maillage de type MBLT à l'intérieur, les oscillations de damier n'apparaissent pas sur le champ de pression.

Ce code bidimensionnel (capable de simuler les transferts de chaleur et les mouvements du fluide pour des écoulements turbulents) a été étendu à un code moyenné sur la profondeur. Ces équations moyennées sur la profondeur dérivent de l'intégration des équations tridimensionnelles sur la profondeur d'eau et, ainsi, de ce fait, Shallow Fluent résout des équations hydrostatiques plutôt que les équations de St Venant. La raison pour laquelle les équations hydrostatiques sont utilisées plutôt que les équations de St Venant se trouve l'avenir de la Shallow Fluent. Nous devons tenir compte des effets de diffusion dans le calcul de la charge sédimentaire. Ainsi, les

équations paraboliques doivent être résolues au lieu des équations hyperboliques. La prise en compte des effets diffusifs dans le développement de Shallow Fluent est considérée comme plus importante que la capture des discontinuités.

Dans cette thèse, chaque équation de transport moyennée sur la profondeur est multipliée par la profondeur d'eau élevée à une certaine puissance et, les termes sources dus au lit du canal ont été discrétisés en utilisant une technique semi-implicite. Ainsi, La raison pour laquelle ces techniques ont été employées est que les termes sources dus au lit du canal ne tendent pas vers l'infini lorsque la profondeur d'eau tend vers zéro. Ces techniques permettent de stabiliser le solutionneur et laissent la surface de l'eau exempte de toutes oscillations.

Plusieurs simulations numériques montrent que de forts faux courants apparaissent quand les équations de transport moyennées sur la profondeur sont résolues en utilisant un maillage triangulaire structuré. La raison derrière ces faux courants réside dans l'arrangement des cellules sur la grille triangulaire structurée. En effet, l'existence de faux canaux (FCs) dans les maillages triangulaires structurés permet l'apparition de ces faux courants. L'effet des FCs ne se limite pas aux maillages triangulaires structurés. Chaque grille interdit un degré de l'effet de FC. Il a été prouvé au moyen de plusieurs simulations numériques que le raffinement du maillage réduit l'effet de FC sur les maillages triangulaires non structurées. Puisque les grilles de type Delaunay permettent des FCs continus plus courts comparativement aux grilles de type Front-Avancé, elles sont préférés aux triangulations du type Front-Avancé.

Quand un arrangement co-localisé des données est utilisé, les valeurs des variables situées sur les frontières des cellules doivent être interpolées en utilisant les cellules voisines. La méthode d'interpolation peut être simplement une moyenne arithmétique ou une moyenne pondérée plus complexe. Une interpolation linéaire basée sur la distance sera plus précise si la variable interpolée se comporte linéairement sur la distance d'interpolation. Dans plusieurs écoulements basiques de canaux ouverts, le débit unitaire se comporte de façon linéaire comparativement à la vitesse. Quand une technique linéaire d'interpolation est employée, on s'attend à ce que le débit unitaire interpolé sur les frontières des cellules soit plus précis que la vitesse interpolée. Le débit unitaire résulte de l'intégration de la vitesse sur la profondeur d'eau. On peut le qualifier de valeur totale de vitesse. La même stratégie peut être employée pour calculer toutes les valeurs des autres variables. La valeur de chaque variable sur les frontières des cellules peut être calculée en

divisant sa valeur totale interpolée sur les frontières des cellules par la profondeur d'eau interpolée sur ces mêmes frontières. Les simulations numériques effectuées dans cette thèse indiquent que cette technique n'affecte pas l'exactitude des solutions numériques. Elles indiquent également que cette technique réduit fortement les efforts de calculs pour des maillages fins. Cette technique s'appelle Valeur Total - Interpolation Linéaire ou, TV-LI.

Lorsque les lignes de courant sont courbées, les écoulements secondaires sont forts. La courbure d'une ligne de courant peut se produire en raison d'un blocage local dans le canal ou en raison d'une courbure du canal. Une équation de vorticité a été ajoutée au code moyenné sur la profondeur afin de tenir compte des effets secondaires de l'écoulement. Pour le développement de l'équation de vorticité, on suppose que les profils de courant et des vitesses latérales sont une fonction du courant de vorticité. Puisqu'une équation de transport est résolue, cette méthode est plus précise en comparaison des méthodes utilisant un profil de vitesse présumé.

Quand la position du front d'eau est une fonction du temps et de l'espace, une technique sera exigée pour simuler son mouvement. En effet, pendant le mouvement du front d'eau, les mailles peuvent être alternativement sèches et humides, la technique permettant de capturer la position temporelle et spatiale du front d'eau s'appelle la technique du couvrant-découvrant. Une cellule est supposé sèche si la profondeur d'eau de cette cellule est inférieure à une profondeur seuil, autrement elle sera supposé humide. Lorsqu'une des deux cellules voisines est humide avec une profondeur d'eau plus grande que la profondeur seuil et que l'autre est sèche, la cellule sèche peut recevoir de l'eau de la cellule humide. Ce processus s'appelle le processus de mouillage. On remarque à travers plusieurs simulations numériques que, avec un processus de mouillage d'ordre 1 (où le gradient de la surface d'eau n'est pas pris en considération) beaucoup de cellules seront faussement mouillées. Ces cellules faussement humides peuvent former de minces couches d'eau et par la suite se déplacer en aval et causer un mouillage encore plus faux. Dans cette thèse, un processus de mouillage d'ordre élevé est suggéré afin d'empêcher la formation de cellules faussement humides. On montre que la technique d'ordre élevé développée peut complètement empêcher la formation de fausses minces couches d'eau.

Pendant le processus du couvrant-découvrant, quand l'eau à l'intérieur d'une cellule est très peu profonde, la profondeur d'eau calculée lors de l'itération suivante ou au prochain pas de temps peut être négative. Une technique alors est exigée dans le but d'empêcher la formation de cellules

à profondeur d'eau négative. Dans Shallow Fluent, ceci est fait, de façon innovante, en limitant les corrections aux vitesses et à la profondeur d'eau. Lors des itérations, quand l'équation de correction de pression est résolue, la profondeur d'eau de chaque cellule sera vérifiée avant que n'importe quelle correction puisse être faite. Si la profondeur d'eau corrigée est plus faible que la profondeur seuil, la correction de pression sera modifiée de sorte que la nouvelle profondeur d'eau soit égale à la profondeur seuil. Avant un nouveau pas de temps, n'importe quelle cellule avec une profondeur égale à la profondeur seuil sera considérée comme sèche.

Ce code moyenné sur la profondeur a été amélioré pour pouvoir simuler des écoulements dans des canaux ouverts partiellement végétalisé. La végétation se comporte comme une matrice poreuse et cause une variation spatiale des variables d'écoulement. Puisque la résolution de la grille ne permet habituellement pas de capturer la matrice poreuse, la double-décomposition est exigée afin de tenir compte de la variation spatiale des variables de l'écoulement. Comme conséquence du processus de double-décomposition, la porosité d'un milieu poreux apparaîtra dans tous les termes d'une équation de transport, excepté le terme où l'effet de la matrice poreuse est formulé. Ce terme est où la densité de végétation apparaîtra. Il est alors essentiel de pouvoir dériver la densité de végétation de sa porosité et vice versa. Sinon, les lois de conservation ne seront pas satisfaites. Dans cette thèse, on observe pleinement cet effet quand la porosité de végétation et sa densité sont définies.

Dans la littérature, aucune forme macroscopique de la force secondaire dans les équations de mouvement n'est formulée. Il est possible de dériver le modèle macroscopique de la force secondaire de l'expression microscopique moyennée sur le temps en appliquant le procédé de la moyenne spatiale. Il est ainsi pensé dans cette recherche que le modèle microscopique moyenné sur le temps présenté pour la force secondaire en littérature est l'expression actuelle.

Puisque la matrice de végétation résiste aux écoulements secondaires du canal principal, une expression pour simuler cet effet sera introduite dans l'équation de vorticité. Dans l'équation de vorticité telle que présentée dans la littérature, l'atténuation des écoulements secondaires par la matrice de végétation n'est pas prise en considération. Un terme source fut alors développé et ajouté à l'équation de vorticité pour prendre en considération l'atténuation des écoulements secondaires par la matrice de végétation. Les simulations indiquent que ce terme source réduit

efficacement l'importance absolue de la vorticité en ce qui concerne le courant dans des zones végétalisées.

Plusieurs simulations ont été effectuées afin d'étudier l'effet de la force secondaire calculée sur le champ de vitesse. Ces simulations sont faites pour des canaux ayant differentes courbures, profondeurs et longueurs. La comparaison des données calculées avec celles mesurées indique que la force secondaire calculée en résolvant l'équation de vorticité améliorera l'exactitude du champ de vitesse calculé seulement quand les hypothèses de l'écoulement peu profond sont fortement maintenues. Autrement, le champ de vitesse calculé peut être très érroné.

Quand la température ou le flux de chaleur sur la surface d'une matrice poreuse est connue, en résolvant deux équations d'énergie, une pour la phase liquide et une pour la matrice poreuse, on améliore l'exactitude du calcul. Dans ce cas, un coefficient de transmission de chaleur sera utilisé pour calculer le transfert de la chaleur entre la phase liquide et la matrice poreuse. Dans les milieux poreux végétalisés, le problème ne réside pas seulement dans la valeur inconnue du coefficient de transmission de flux de chaleur mais également dans la valeur inconnue du champ de température ou du flux de chaleur sur la surface de la matrice poreuse. Ainsi, cela ne nous laisse alors aucun choix que de résoudre une équation d'énergie qui se base sur l'existence d'un équilibre thermique local. Un modèle d'équation d'énergie est approprié pour les milieux poreux végétalisés si on garde à l'esprit les techniques qui ont été utilisées pour calculer le flux thermique de la surface d'eau libre.

Dans les milieux poreux végétaux, la matrice poreuse peut toucher le mur frontière. Si cela se produit, la matrice poreuse affecte le flux thermique proche du mur. Une technique est alors exigée pour tenir compte de la propriété thermique de la matrice poreuse. Puisque l'hypothèse locale d'équilibre thermique est appliquée au transfert de chaleur, la même hypothèse sera employée pour prendre en considération la propriété thermique de la matrice poreuse. Elle sera faite au moyen de ''wall fonctions'' modifiées.

Dans le modèle d'équation de l'énergie utilisé dans la littérature de mécanique des fluides, la diffusion thermique due au gradient de porosité est ignorée. La raison derrière cette hypothèse réside dans l'application du modèle d'équation de l'énergie aux problèmes à porosité uniforme. Or, dans un modèle de canal ouvert partiellement végétalisé où l'hypothèse de porosité uniforme ne peut pas être formulée, le flux thermique diffusif dû au gradient de porosité devient significatif

pour les maillages fins. Afin de tenir compte de cette diffusion thermique, un terme supplémentaire a été développé et ajouté à l'équation de l'énergie.

Quand les nombres de Reynolds et de Peclet sont très petits, les flux diffusifs peuvent être comparables aux flux convectifs. Ainsi, l'effet de la dispersion thermique laminaire peut être significatif. Des simulations de canaux ouverts partiellement végétalisés avec écoulement d'entrée turbulent ont été étudiées pour savoir si ou non l'effet thermique laminaire de dispersion sur le champ de température calculé dans une zone végétalisés doit être pris en considération.

La plupart des écoulements à canaux ouverts sont turbulents. Il est alors raisonnable d'utiliser un modèle de turbulence à grand nombre de Reynolds afin de prendre en considération les effets turbulents. Indépendante de la turbulence dans le canal principal, l'énergie cinématique turbulente dans une région à l'abri d'une zone végétalisée peut être très faible. Ce phénomène qui est observé par plusieurs simulations numériques peut limiter l'application d'un modèle de turbulence à nombre de Reynolds élevé aux zones végétalisées à faible densité de végétation.

Le lit du canal et ses bords ensemble avec sa plaine inondable forme une géométrie compliquée. Un outil a été développé pour interpoler les données géo-référencées des points de mesure au centre des cellules. Selon la stratégie utilisée pour mesurer ces données géo-référencées, l'outil développé dans cette thèse peut être utilisé pour interpoler ces données avec trois méthodes différentes. Ces méthodes se composent de deux techniques pour l'interpolation des données qui ont été mesurées avec une disposition structurée et, une technique pour l'interpolation des données qui ont été mesurées avec une disposition non structurée. Un exemple des données mesurées avec une disposition structurée est les données des sections transversales des rivières. De nos jours, la plupart des données sont mesurées de façon non structurée. Les modes soutenus par l'outil développé fourniront un moyen pour une reconstruction optimale de la topographie du lit du canal indépendamment de la disposition et de la densité des données.

Le solutionneur développé est un modèle complet permettant de simuler le problème couplé du flux de chaleur à des écoulements turbulents de fluide dans des canaux végétalisés. Un tel problème peut inclure le phénomène de rupture de barrage, d'inondation et la simulation d'écoulements secondaires au niveau des courbures de canaux. Le solutionneur est intensivement validé avec des essais de référence et la supériorité de ses nouvelles techniques et algorithmes a été vérifiée.

Ce solutionneur complexe peut résoudre une variété de problèmes dimensionnels ou non et, en conséquence, peut être utilisé pour de nombreux problèmes en temps réel d'ingénierie. L'application d'une programmation orientée objet rend l'extension future du code facile et, de cette manière, peut être étendue à d'autres problèmes d'ingénierie.

TABLE OF CONTENTS

LIST OF TABLES

LIST OF FIGURES

LIST OF SYMBOLS AND ABREVATIONS

Nomenclature

a_0, a_j	coefficients in the discretized equations
c_p	specific heat capacity
C_{s_j}	volumetric flux at the cell face s_j
C_f	the bed friction coefficient in Articles 1, 2, and 3
C_{fr}, C_d	bed friction coefficient and vegetation drag coefficient, respectively, in Articles 4 and 5
d_v	stem diameter
F_r	Froude number
g	gravitational acceleration
G	the rate of production of k
h, h_v	water depth and vegetation effective height, respectively
$h_{c_{0\_c_j}}$	the normal distance between two neighbor cells
H_v	spacing between vegetation stems
k	turbulence kinematic energy
$K, \boldsymbol{K}$	thermal conductivity and the thermal conductivity tensor
L	length scale
MBLT	Multi-Block Local Triangulation

n	the direction along $\boldsymbol{n}$ or, the number of levels in MBLT method in Article 1 or, Manning's number in Articles 2 to Article 5
$\boldsymbol{n}$	unit vector normal to the cell face when there is no subscript, any unit normal otherwise
$\hat{\boldsymbol{n}}$	unit vector normal to velocity vector $\boldsymbol{u}$
N_{bcell}	number of the boundary cells in initial grid
N_{bcell_MBLT}	number of the boundary cells in MBLT grid
N_{Cell}	number of the cells (in initial grid considering the MBLT grid)
N_{cell_MBLT}	number of the cells in MBLT grid
N_{node}	number of the nodes in initial grid
N_{node_MBLT}	number of the nodes in MBLT grid
P, P'	pressure and pressure correction, respectively
P_{e_d}	stem Peclet number, defined as $P_{e_d} = c_{p_f}^* \phi \left|\langle \overline{\boldsymbol{u}_v} \rangle^{i^*}\right| d_v^* / K_f^*$
P_{e_H}	cavity Peclet number, defined as $P_{e_H} = c_{p_f}^* \phi \left|\langle \overline{\boldsymbol{u}_v} \rangle^{i^*}\right| H_v^* / K_f^*$
P_r	Prandtl number, defined as $P_r = c_{p_f}^* \mu_f^* / K_f^*$
P_{r_t}	Turbulent Prandtl number, defined as $P_{r_t} = c_{p_f}^* \mu_{t_\phi}^* / K_t^* = 0.85$
r	streamline curvature radius
$\boldsymbol{r}_{c_{j\_s_j}}, \boldsymbol{r}_{c_{0\_s_j}}$	distance vectors between the cell's center and the face's center
R	residual at the domain

R_e — flow Reynolds number, defined as $R_e = \rho_f^* U_{ref} l_{ref} / \mu_f^*$

R_{e_D} — stem Reynolds number based on reference velocity, defined as $R_{e_D} = \rho_f^* U_{ref} d_v / \mu_f^*$

R_{e_d} — stem Reynolds number based on resultant velocity, defined as $R_{e_d} = \rho_f^* \langle \overline{\boldsymbol{u_v}} \rangle^{i^*} d_v^* / \mu_f^*$.

REV — Representative Elementary Volume

$s_j, \boldsymbol{s}_j, s$ — cell face area, the area vector, and the area of an arbitrary surface, respectively

$S, \boldsymbol{S}$ — scalar and vector form of the source terms, respectively

t — time

u, v — velocity components in x and y directions, respectively

U — velocity scale

$\boldsymbol{u}$ — velocity vector

$\hat{\boldsymbol{u}}$ — momentum velocity vector

x, y — x and y directions

$| \; |$ — for any vector $\boldsymbol{b}$, $|\boldsymbol{b}|$ refers to the argument of the vector

$[-]$ — in figures, it refers to a dimensionless solution

$|\varrho|$ — for any vector $\boldsymbol{\varrho}$, $|\boldsymbol{\varrho}|$ refers to the argument of the vector

$\langle \varrho \rangle^i$ — for any variable ϱ, $\langle \varrho \rangle^i$ refers to its average over the volume of the fluid phase in REV

$\langle \varrho \rangle^v$ — for any variable ϱ, $\langle \varrho \rangle^v$ refers to its average over the volume of REV

$\bar{\varrho}$ for any depth-averaged variable ϱ, $\bar{\varrho}$ refers to its time-mean depth-averaged form

Greek symbols

α general relaxation factor

ε dissipation rate of k

η a dimensionless constant of about 1.0

ϑ normalized continuity residual

ϑ° continuity residual

ϑ°_{in} volumetric influx at the inlet boundary

λ vegetation density

μ, μ_t, μ_{t_ϕ} Laminar, turbulent, and macroscopic turbulent dynamic viscosities, respectively

ξ water surface elevation

ρ fluid density

σ Prandtl/Schmidt number

ς porosity-induced flux equivalent

$\tau, \boldsymbol{\tau}$ scalar and vector stresses

φ general scalar quantity

ϕ porosity

χ Prandtl/Schmidt number in general discretized equation for φ

ϖ vorticity

ω, ω_{rc}	general relaxation factor and the relaxation factor in pressure correction term, respectively
ω_s	magnitude of streamwise vorticity vector
Ω	volume

Subscripts

b	refers to the river/channel bed
bo	refers to boundaries
d	refers to the domain
f	refers to fluid phase
fs	Refers to the interface between fluid and solid phase, directed from fluid toward solid
j	refers to the neighboring cell
k	refers to turbulence kinematic energy
p_φ	refers to the implicit part of the source term in discretized equation for φ
ref	refers to reference value
R	refers to residual at the domain
REV, REV_f	refer to REV and the fluid in REV, respectively
sf	refers to secondary force
s_j	refers to cell face s_j
ss	refers to secondary shear

t	refers to turbulence
th	refers to threshold
u_φ, u_u	refers to the explicit part of the source term in discretized equation for φ and u, respectively
u_P	refers to the source term due to pressure gradient in momentum equations
v	refers to vegetation
vd	refers to vegetation drag force
w	refers to wall
ε	refers to dissipation rate of k
τ	refers to shear
φ	refers to φ
0	refers to central cell

Superscripts

n	refers to the current time step
P	refers to pressure
T	refers to the transpose of a vector
u	refers to u
φ	refers to φ
$=$	refers to discretized form
$\sim$	refers to approximate value in Roe's Riemann solver

..   refers to an initial guess in Article 1

+   refers to an initial guess (can be from previous iteration)

∗   refers to the dimensional form of a quantity

LIST OF APPENDICES

INTRODUCTION

In this thesis, it is aimed to develop a depth-averaged solver for simulation of heat and fluid flows in vegetated channels. Transfer of heat and momentum in a partially vegetated channel, while valuable for the cases such as analysis of thermal pollution due to a power plant, is not still performed using porous media science. Vegetation stems act as a solid matrix and, in turn, the porous media concept is the most suitable approach for dealing with the problem of heat and fluid flows in vegetated channels. In order to perform this investigation, a solver is developed and the whole research is divided to five separate stages.

At the first stage, a solver is developed which is able to simulate the heat and fluid flows in two-dimensional spaces. This solver then is validated before extending it to the case of the depth-averaged shallow flows. This stage allowed the author to minimize the possible coding error and, investigate a new approach for dealing with the problem of checkerboard oscillations. Such oscillations will appear in finite volume methods when the data structure is collocated.

At the second stage, the depth-averaging process is performed. After this step, the solver was able to simulate depth-averaged flows, but not the effect of flooding phenomenon and vegetation. Several techniques have been developed in order to increase the accuracy of the solutions and reduce the computational cost. A research has been performed in order to find an appropriate type of grid for depth-averaged simulations. The transport equation for the stream-wise vorticity has been solved for taking account of the secondary flow effects.

At the third stage, the solver is extended to the case of moving water fronts. Thus, it was possible to simulate any complicated depth-averaged flows including the flooding phenomenon, but not the effect of vegetation. In this stage, new methods are devised for a more accurate prediction of water front, preventing the formation of cells with negative water depth, and appropriate choice of the threshold water depth.

At the fourth stage, porous media concept is applied to the flow equations, and the discretized equations in the solver are modified. The stream-wise vorticity equation and the depth-averaged secondary force are also modified for taking the vegetation damping effect on the secondary flow into account. A research has been performed in order to find the conditions under which the vorticity-based secondary force will actually increase the accuracy of the computed velocity field.

At the last stage of this research, the porous media concept is applied to the energy equation and, heat and fluid flows in a partially vegetated channel are investigated. The local thermal equilibrium hypothesis is used and, in turn, the one-energy equation is solved. New techniques are suggested for the near wall treatment in porous regions, the effect of laminar thermal dispersion and porosity gradient on temperature field are examined, and the limits for the application of a high Reynolds number turbulence model in partially vegetated channels are investigated.

The thesis is divided into eight chapters. The first two chapters consist of:

- Chapter 1 - Literature review: The chapter is started with a general review of literature and then it is continued with specific review of literature for the steps taken during development of the solver.

- Chapter 2 – Methodology: This chapter provides the detail of the methodological approaches which are followed in this thesis in order to develop a state of the art depth-averaged solver.

The process of developing the depth-averaged solver and following the research objective are presented in Chapter 3 to Chapter 7:

- Chapter 3 – First step: A two-dimensional solver is developed for simulating heat and fluid flows.

- Chapter 4 - Second step: The two-dimensional solver is extended to a depth-averaged solver.

- Chapter 5 - Third step: The depth-averaged code is further extended for simulating problems with moving boundaries where the position of water edge is a function of time and space.

- Chapter 6 - Fourth step: The solver is extended for simulating flow in partially vegetated channels.

- Chapter 7 – Fifth step: The code is extended to simulation of problems which include heat transfer in partially vegetated open channels.

Additional validation tests and solver's application examples which are not discussed in Chapters 3 to 7 are presented in Appendix 1. A tool is also developed for interpolating geo-data from measurement points into the cells center. The rest of this thesis consists of:

- Chapter 8 – General discussion: In this chapter a review of the work is presented.

- Conclusion and recommendations: In this section the whole work is concluded, and some recommendations for future extension of the solvers are presented.

Main objective:

The main objective of this thesis is, development of a depth-averaged solver for simulation of heat and fluid flows in vegetated channels.

Specific objectives:

For developing a depth-averaged CFD solver, the specific objectives are observed through development phases as:

- "Problem definition" phase where every equation which is supposed to be solved must be known, together with every innovative improvement to the existing models. When this phase is finished, later on, the cost of modifications can be very high. In this thesis, many existing models are innovatively improved and, in turn, the "maintenance and evolution" phase are postponed, and the "obsolescence" date is delayed. These innovative improvements to the existing models, and innovatively developed techniques are presented in Chapters 3 to 7 of this thesis.

- The idea of an Object Oriented Programming, is strongly observed during "object and algorithm design" and "coding" phases. With object oriented, the author means developing subprograms which act as objects. From programming viewpoint, no matter what the object does, every object take specific input and gives specific output. These objects are put together to make the code as a whole.

- The whole solver development process, was divided into several steps and, the validation of every step is performed right at the end of that step.

- Maintenance will fall on future programmers shoulder.

In general, the obsolescence date of a depth-averaged tool is a function of advance in computers processor speed, programmers' way of coding, and the total future evolution of the code.

Not entire techniques used for developing a CFD solver can be improved in context of a Ph.D. thesis, but rather some key techniques. A key technique is the one with significant effect on computed results, especially when the existing version is not satisfactory. Such key technique can be a model or an algorithm and, developing key techniques is another objective of this thesis.

- The model equations and algorithms developed during "problem definition" and "object and algorithm design" phases of this thesis are presented in Chapters 3 to 7. These are briefly explained earlier in this text, in "Introduction" section. The general for of the equations is presented in Chapter 7.

Originality justification:

Development of a numerical solver either commercial or research is original from this view point that, something new has been come into existence. The originality of a developed solver, however, will be most strongly meaningful when many new techniques and algorithms are innovated and added to the solver. In this thesis, the original techniques and algorithms which are innovated and added to the developed solver consist of:

1. MBLT technique.

2. TV-LI technique.

3. A new way of writing the transport equations and discretizing the source terms.

4. New high order wetting-drying technique.

5. New technique for preventing the formation of cells with negative water depth.

6. Application of porous media concept to heat and fluid flows in vegetated zones.

7. New definition for vegetation porosity and its density.

8. Development of a macroscopic secondary force model.

9. Development of a damping source term for taking account of vegetation effects on stream-wise vorticity.

10. Modification of wall functions for taking the thermal property of vegetation material into account.

11. Development of a term for taking the diffusive heat flux due to porosity gradient into account and investigating the effect of this term on computed temperature field.

Moreover this thesis investigates:

12. The effect of the secondary force on velocity field when the secondary force is derived from stream-wise vorticity.

13. The effect of laminar thermal dispersion on computed temperature field at low Reynolds and Peclet numbers.

14. The applicability of a high Reynolds number turbulence model for simulating flow in partially vegetated open channels.

CHAPTER 1   LITERATURE REVIEW

Numerical simulation of shallow flows covers a wide range of methods which can be applied to one-dimensional problems (Cao et al. 2004, Liu et al. 2005, Wu and Wang 2008, Wu and Wang 2007), two-dimensional problems (Bechteler and Farshi 2001, Chen and Duan 2008, Lu et al. 2005, Mohammadian et al. 2004) or, three-dimensional problems (Biron et al. 2004, Khosronejad et al. 2007, Wang et al. 2007). A one-dimensional cross sectional averaged solver is not appropriate for simulating a wide river or channel, it cannot be used for capturing turbulent structures and, it cannot be used for simulation of dead zones or circulating zones. One of most important drawbacks of one-dimensional solvers is their poor representation of bed topography. With poorly reconstructed bed topography, the physical domain in computational space can be very different from field condition. A one-dimensional model then provides incomplete information and accuracy for modern practical applications. With a three-dimensional simulation, on the other hand, detail of flow field can be studied. Three-dimensional models are successfully applied to many rivers' reach (Lu et al. 2004). However, they may not be computationally efficient for simulation of long reach of rivers.

For most engineering applications depth-averaged models are efficiently applicable to channel reach scales. In a depth-averaged model, the techniques used for simulation of vegetation effects, bank retreat phenomenon, and movement of wetting-drying fronts, together with the numerical scheme used for solving the transport equations will affect the accuracy of a simulation. In a depth-averaged simulation compared with a cross sectional averaged one-dimensional simulation, it is possible to reconstruct the bed topography.

Solution of transport equations in structured body-fitted grids, as performed in (Chen and Duan 2008, Duan and Julien 2005, Nagata et al. 2000), may hardly be applicable to complicated geometries. Unstructured grids, on the other hand, are applicable to any complicated geometry. As a result, a numerical model which can solve the transport equations in unstructured grids is applicable to a wider range of engineering problems.

For the inviscid shallow flows the finite volume Riemann solvers (Roe, HHL…) or the relaxation approximation technique are appropriate choices (Delis and Papoglou 2008, Murillo et al. 2008). These numerical techniques are, however, developed for mathematically hyperbolic system of equations and, in turn, they may not be applicable to mathematically parabolic equations. For

instance, in simulation of sediment or contaminant transport diffusive fluxes are important and the governing equations are parabolic. For such problems SIMPLE algorithm is one of the most appropriate algorithms, and is widely applied to hydrostatic shallow flow equations (Bennett et al. 2008, Minh Duc 1998, Wu et al. 2005).

Depth-averaged equations can be derived by direct integration of three-dimensional equations over the water depth (Lane, 1998). Toro (2001) also can be followed for the derivation of depth-averaged continuity equation in shallow flows with variable bed topography. Any source term in the right hand side of the depth-averaged continuity equation represents the volumetric exchange of water or sediment with erodible beds; see (Cao and Pender 2004, Chen and Duan 2008, Duan and Julien 2005, Wu and Wang 2008). Such source term can take account of the precipitations if a lake is concerned.

Transport equations can be written either in conservative or non-conservative form. The conservative form of the equations is more suitable when there is a discontinuity in computational domain. For instance, in shallow flows sediment concentration or fluid density may experience discontinuity in a dam-break phenomenon over a movable bed (Cao et al. 2004, Wu and Wang 2008, Wu and Wang 2007). It is confirmed in this thesis through numerical simulations that, if the dam-break happens over a wet channel bed, the water surface and velocity will also experience discontinuity.

At high Reynolds numbers, when grid resolution is not enough to resolve the turbulent structures, other model equations have to be solved, together with continuity and momentum equations. Variety of model equations, from simple algebraic equations to Reynolds Stress Model, has been derived in order to take account of turbulence. In algebraic equations generation and dissipation of turbulence are assumed in local equilibrium; i.e. turbulence is dissipated where it is generated. Such algebraic equations, for instance, are used for developing wall functions for near-wall treatments (Launder and Spalding 1974). Algebraic equation models can be divided into isotropic and anisotropic models. Among them, zero-equation shallow flow eddy viscosity models are based on the assumption of isotropic turbulence and, the Algebraic Stress Model relies on anisotropic turbulence hypotheses. In a more complicated model such as $k - \varepsilon$ turbulence model or Reynolds Stress Model, transport of turbulence by convection and diffusion is taken account of. The $k - \varepsilon$ turbulence model is an isotropic model where turbulence kinematic energy and

dissipation rate are used for defining an eddy viscosity. The Reynolds Stress Model, on the other hand, is an anisotropic model and solves extra equations for Reynolds stresses. More detail of this matter can be found in (Ferziger and Peric 1996, Sotiropoulos 2005, Versteeg and Malalasekera 1995). Since in depth-averaged models turbulent structures are limited to a two-dimensional space, solving the Reynolds Stress Model cannot be the best option. The $k - \varepsilon$ turbulence model, on the other hand, suffices to provide necessary information about turbulence in a depth-averaged computational domain (Sotiropoulos 2005).

Lane (1998) discussed two main approaches for taking account of secondary flows in depth-averaged simulations. The first approach consists of two sub-approaches: in the first sub-approach a dimensionless shape function will be used for defining the velocity profile in vertical direction (Hsieh and Yang 2005, Sun et al. 2001), in the second sub-approach the velocity profile in both stream-wise and transverse direction is assumed known (Chen and Duan 2008, Duan and Julien 2005, Duan and Nanda 2006, Huang et al. 2006, Wu et al. 2005, Wu and Wang 2004). When velocity profiles are assumed known, the stream-wise velocity profile is usually the logarithmic or power velocity profile and the transverse one can be Rozovskii's (1957) velocity profile. Many parameters such as the irregularity of the lateral boundaries, variable bed topography, and turbulent structures affect the velocity profile and, in turn, velocity profiles cannot be known a priori. The second approach is based on qualitative arguments concerning the interaction of the lateral curvature, bottom friction, and vertical non-uniformity, to develop a model that reproduces the depth averaged influence of the secondary flow. This method is derived by Bernard (1993), and applied for example by Rodriguez et al. (2004). The last method which is not discussed by Lane (1998) consists of solving moment equations. This technique for instance is used by Wu and Wang (2004).

The thermal system in shallow flows has significant effect on life of flora and fauna, sedimentation mechanism, pollution distribution, and chemical processes. Zhang and Nepf (2009) investigated the thermally driven exchange flow between open water and aquatic canopy. Voller (2010) developed a numerical heat transfer model of a three-dimensional sediment delta deposit over both land and ocean domains. Shin et al. (2010) numerically simulated the temperature profile of riverbank filtrate water in the Daesan plant using HydroGeoSphere, and observed the pumping rate as the primary factor in determining filtrate water temperature.

In depth-averaged numerical simulations the temporal movement of the interface between water and land has to be captured with wetting-drying treatments. Any treatment of wetting-drying fronts consists of four steps. First, a threshold water depth has to be assumed. Then, every cell with water depth more than the threshold water depth has to be marked as wet; otherwise it has to be marked as dry. After that, dry cells have to be excluded from computations if possible. Finally, wetting-drying technique has to be applied (i.e. wetting dry cells and drying wet cells where applicable) when hydrodynamic computations for current time level are done. Wetting-drying process may make a numerical solver instable. For instance, as discussed by Toro (2001), Roe's Riemann solver can't strictly handle situations involving dry bed state. In (Brufau et al. 2004, Brufau et al. 2002) a mass conserving technique is introduced for the treatment of wetting-drying fronts when Roe's Riemann solver is used. Bennett et al. (2008), Minh Duc (1998), Wu (2004), and Wu et al. (2005) applied the wall boundary condition to wetting-drying fronts, and transport equations were solved in both wet and dry cells.

In three-dimensional simulations maximum roughness height is limited by near-bed cells height and, as a result, the near-bed cells dimension limit the maximum shear velocity at the bed (Lane and Ferguson 2005). In depth-averaged simulations, vegetation resistance force can be simulated by increasing bed roughness; i.e. decreasing Chezy coefficient (Klopstra et al. 1997), or increasing Manning's roughness coefficient (Wu et al. 1999). Chezy coefficient can become extremely small in vegetated zones and, in turn, when simulating sediment transport, vegetated regions can become zones of slow currents with high sediment transport rates (Mosselman 2005). The same problem can be expected when Manning's roughness coefficient is used. Another method for taking account of vegetation resistance force is the insertion of a vegetation induced drag force into momentum equations. In this method, every plant is simulated with an equivalent stem, and the drag force due to the matrix of such stems is calculated. Lopez and Garcia (2001) argued that, from mathematical/physical viewpoint, the simple addition of a drag-induced body force into momentum equations is incorrect. This technique, however, will be most meaningful when matrix of stems is considered as a porous matrix and, flow through a porous medium is simulated. This method for simulation of vegetation resistance force can be applied to riparian vegetations (Bennett et al. 2008, Choi and Kang 2004, Cui and Neary 2008, Fischer-Antez et al. 2001, Toda et al. 2005, Wilson et al. 2006).

1.1   Two-dimensional solver

In finite volume methods, the velocity components stored at the cell face will conserve the mass when solution is converged and, in turn, the computed pressure field will be smooth. This is the main idea behind developing finite volume algorithms for staggered (Ketabdari et al. 2008, Nobari et al. 2009, Zhang et al. 2011) and lattice (Zhang et al. 2007) grids. A checkerboard pressure field can be expected when a finite volume scheme is used with a collocated data structure (Acharya et al. 2007, Date 2005, Ferziger and Peric 1996, Versteeg and Malalasekera 1995). The reason behind such checkerboard pressure are: the interpolated velocity at the cell face is not mass conserving (Date 2003, Ferziger and Peric 1996), and the pressure of the central cell will not appear in discretized equations when momentum equations are integrated over a control volume (Acharya et al. 2007, Ferziger and Peric 1996, Versteeg and Malalasekera 1995). The first reason is held in this thesis. But, it is shown for triangular grids that the second reason will only alter the isotropy of a checkerboard pressure field. It is also indicated that the effectiveness of the Rhie and Chow (1983) type pressure correction technique will be a function of isotropy of the pressure oscillations.

A mass conserving velocity at the cell face can be obtained through modification of the interpolated cell face velocity by the difference between the interpolated pressure gradient and the gradient calculated at the cell face (Rhie and Chow 1983). A technique then has to be devised for interpolation of pressure gradients from cells' center into the cells' faces, and for calculation of cell volume at the cell face. These techniques are only required when the earliest type of Rhie and Chow (1983) method is used. This earliest version works best for laminar flows. Davidson (1996) has linearly interpolated the pressure gradient into the cell face. Ferziger and Peric (1996) have argued that the cell center pressure gradients should be interpolated with a weight of 0.5, since this approximation does not see the grid non-uniformity. This also has been observed by Croft (1998) through numerical simulations. Fue-Sang (2000) and Davidson (1996) used a background quadrilateral cell with vertices at the cells' center and the faces' vertices in order to calculate the cell volume at the cell face. When a collocated data structure is used, the Rhie and Chow (1983) type pressure interpolation technique is one of the most popular technique in research and engineering applications (Dalal et al. 2008, Darwish et al. 2009, Gao and Liu 2009, Norris et al. 2011). Rahman et al. (1997) proposed a pressure correction method for a SIMPLE

type algorithm with a vertex based data structure. Kang and Kim (2002) developed a pressure based finite volume scheme for unstructured grids in order to simulate reacting flows. Rahman et al. (1997) and Kang and Kim (2002) applied the Rhie and Chow (1983) type pressure interpolation technique in order to obtain a smooth pressure field.

The total pressure correction can be considered as the sum of the smoothing and mass conserving pressure corrections (Date 1996). Date (2003) compared this method with traditional Rhie and Chow (1983) type momentum interpolation technique and perceived the main difference in the way the pressure gradients were interpolated into the cell face. In Rhie and Chow (1983) type method, the pressure gradients is one-dimensionally interpolated while in Date's (1996) method a multidimensional averaging is performed. Date's (1996) method is later extended to unstructured grids (Date 2005, Pimpalnerkar et al. 2005). As far as the author of this thesis is aware, Date (1996) technique has never been verified by visualizing counters of pressure field in a benchmark test such as backward facing step where a checkerboard pressure is expected. It then does not seem to the author that this technique has significant advantage over Rhie and Chow (1983) type methods.

Touazi et al. (2008) have developed a collocated finite volume scheme for incompressible flows on the so-called "admissible" unstructured meshes. Admissible meshes satisfy two conditions: the straight line joining the centers of two adjacent control volumes is perpendicular to the common face, and the neighbouring control volumes and the associated centers are arranged in the same order, with respect to the common face. One of the main difficulties in this method was writing an accurate diffusion approximation. Chenier et al. (2009) have developed a new scheme for diffusion terms on general non-conforming grids. Because of restrictions imposed on the grid, this method still has some practical limitations; for more details, see (Chenier et al. 2009).

In this thesis, the mass conserving velocity at the cell face is obtained through Rhie and Chow (1983) type pressure interpolation technique. Rhie and Chow (1983) type technique, however, performs best when checkerboard pressure oscillations are not very anisotropic. It is shown in this thesis that, equilateral triangular cells prevent formation of anisotropic oscillations in a pressure field. In a grid with equilateral triangular cells every central cell and its immediate neighboring cells form a bigger equilateral triangle which is called Local Triangle, LT. When the polygon formed by a triangular cell and its neighboring cells is not a triangle, it is called a

distorted LT. Distorted LTs allow formation of anisotropic pressure oscillations and, in turn, reduce the performance of Rhie and Chow (1983) type techniques. According to this finding, a Multi-Block Local Triangulation, MBLT, method is devised so that the customary unstructured triangular grid can be considered as a level zero MBLT. In a level n MBLT method, an initial triangular cell is divided into $(n + 1)$ levels of triangular cells from level 0 to n, respectively. These smaller cells have the same geometry and, in turn, are similar to the initial cell. A MBLT of any level but more than zero establishes some appropriate LTs into the grid and, as a result, a smoother pressure field can be expected. Compared to a grid with equilateral triangular cells, a MBLT grid of any level consists of two types of regions where concentration of distorted LTs is high. One region is where the faces of initial grid exist. Another region is where the vertices of the initial grid exist. Numerical simulations performed in this thesis indicate a higher possibility for checkerboard oscillations where the vertices of the initial grid exist. It has to be mentioned that MBLT is a technique the author devised for removing pressure oscillations, but LT is a concept explaining how anisotropy of the checkerboard oscillations can affect the performance of the Rhie and Chow (1983) type techniques.

Since momentum equations are under-relaxed by general relaxation factor, Date (2003) argued, in order to have a relaxation factor independent solution the Rhie and Chow (1983) pressure correction term has to be under-relaxed with general relaxation factor. Ferziger and Peric (1996) maintained that, the difference in two solutions obtained using different relaxation factors is much smaller than discretization error and, in turn, there is little reason for concern. Ferziger and Peric (1996), however, only regarded the effect of general relaxation factor on coefficient of central cell in momentum equations. Since in this thesis Rhie and Chow (1983) type pressure interpolation technique is used, a hypothesis is established about proper choice of the relaxation factor in Rhie and Chow (1983) pressure correction term. It is illustrated by means of several numerical simulations that, this relaxation factor cannot be the general relaxation factor. Investigation of the effect of mass conservation also revealed its significant effect on having a relaxation factor independent solution.

Checkerboard oscillation is a result of local imbalance in mass and momentum and, as a result, it is always studied in laminar flows. In turbulent flows, where other source terms are added to momentum equations, these equations can behave in different way compared with the ones of a laminar flow. A smooth pressure field in a turbulent flow then is not guaranteed if the pressure

field in its equivalent laminar flow is smooth. If at a cell the magnitude of checkerboard oscillation relative to the gage pressure or pressure gradient increases with Cell Reynolds number, a higher relative oscillation will be expected in turbulent flows (Here the same geometry is assumed, and the Cell Reynolds number in turbulent flow is also increased. This means, there is no circulating zone near the point where the checkerboard oscillation is observed.). In this thesis, the effect of Cell Reynolds number on the magnitude of checkerboard oscillations, especially at the interface between blocks of fluids, is investigated. It is demonstrated that, this checkerboard oscillations are more significant at higher Cell Reynolds numbers.

1.2 Depth-averaged solver

One of the main assumptions in depth-averaged transport equations is the hydrostatic vertical distribution of pressure. In SIMPLE scheme this hydrostatic pressure is linked with water surface elevation through the equation $P = \rho g \xi$. Therefore, an oscillation in pressure field, P, causes oscillation in water surface elevation, ξ. The Rhie and Chow (1983) type pressure interpolation technique is regarded as an efficient technique in order to remove the checkerboard oscillations from pressure field (Darwish et al. 2009, Date 1993, Date 2003, Gao and Liu 2009, Norris et al. 2011). Since in depth-averaged transport equations pressure field is linked with water surface elevation, the Rhie and Chow (1983) type technique will also remove the oscillations from water surface (Minh Duc 1998, Wu 2004, Wu et al. 2005, Wu and Wang 2004).

The water depth appears as numerator in entire terms of the depth-averaged momentum equations except in the term where the bed resistance force is simulated. In this term, water depth appears as denominator and, in turn, the bed resistance force goes to infinity when the water depth goes to zero. A very high bed resistance force can redirect the flow and, as a result, it can cause numerical oscillations. In order to avoid numerical oscillations, Brufau et al. (2004) discretized the bed resistance force in a semi-implicit manner. This method, however, does not avoid infinite bed resistance for very small water depth. In (Brufau et al. 2004) a fraction appeared in discretized momentum equations which at very small water depth its numerator and denominator go to infinity. In this thesis, in order to avoid numerical oscillations, transport equations are multiplied by water depth to the power of a fraction. Thus, the water depth will be removed from the denominator in the source terms due to bed effects and, these terms will be bounded when water depth goes to zero. Since the rest of the terms in transport equations are multiplied by water

depth, they go to zero at very small water depth. In an unsteady solution, the computed variables at new time level then may go to infinity when the water depth goes to zero. It is ilustrated in this thesis that, with an appropriate choice of the implicit part of the discretized source terms, Patankar (1980) suggestion for discretization of source terms resolves this problem.

Ferziger and Peric (Ferziger and Peric 1996) maintained that, in order to calculate the product of dependent variables at the cell face, variables have to be interpolated into the cell face and, their product has to be calculated at the cell face. Another method is: first, calculating the product of variables and then, interpolating these products into the cell face. Mathematically these two expressions are not equal, the first method is less diffusive, and the second method is computationally cheaper. When Riemann solvers, for example the Roe (1997) Riemann solver, are applied to depth-averaged inviscid flows (Castro Diaz et al. 2008, Hernandez-Duenas and Karni 2011, Murillo et al. 2008), dependent variables are interpolated into the cell face with a depth weighted averaging. These interpolated variables then form an approximate Jacobian matrix. In this thesis, two different approaches are adopted in order to interpolate the dependent variables into the cell face. These approaches are then compared in terms of CPU time and numerical accuracy. The first method is, following Ferziger and Peric (1996) and, interpolating the dependent variables into the cell face with a distance weighted averaging. The second method is, integrating the dependent variables over the depth in order to calculate their total values and, interpolating the total values into the cell face with a distance weighted averaging. At the cell face the total value can be divided by water depth in order to obtain the depth averaged variable. The main idea behind the second method lies with the fact that in many simple depth-averaged flows the unit discharge is more linear compared to velocity and, the unit discharge is equal to velocity integrated over the water depth. Thus, a linear interpolation of unit discharge into the cell face is more accurate compared to the linear interpolation of velocity. The preliminary proof of the computational accuracy of this technique lies with the similarity between this technique and the interpolation method used in Roe (1997) Riemann solver.

Independent of whether the bed source terms (e.g. bed resistance source term) are discretized in a point wise manner (Bernard 1993, Fraccarollo et al. 2003, Mohamadian et al. 2005, Soares-Frazao and Zech 2011, Wu 2004, Zhou et al. 2001) or with upwind method (Brufau et al. 2004, Murillo et al. 2008), they have been always integrated over the cell area. Theoretically, the bed source terms have to be integrated over the bed area rather than the cell area. In three-

dimensional simulations cell face lies on geometry and, in turn, with a grid refinement the geometry will be reconstructed more accurately. In depth-averaged simulations where grid lies on a horizontal plan rather than bed topography, grid refinement does not increase the accuracy of the reconstructed bed topography. The effect of integration of bed source terms either over cell area or over bed area on the accuracy of the computed velocity field then is investigated in this thesis.

For a grid independent solution, false diffusion is assumed the main source of inaccuracy in first order schemes (Croft 1998). In depth-averaged simulations when the line connecting the center of two neighboring cells is not perpendicular to flow direction, there may be an additional false numerical flux. The passes where such flux is allowed are called False Channels, FCs. A FC is a direction in which fluid has the tendency to flow due to the combined effect of grid, bed gradient, and bed resistance source term. Murillo et al. (2006) observed that their method for extending the Roe (1997) Riemann solver to a courant number larger than one does not performs in Advanced-Front grids, but it does in Delaunay grids. Murillo et al. (2006) assumed the problem lies with the existence of such directions in Advanced-Front grids. A reason behind Murillo et al. (2006) observations can be addressed through FC effect. In this thesis, the effect of different grids and bed condition on the strength of false currents is investigated and, an appropriate choice of grid is suggested. Numerical simulations performed in this thesis revile that, grid refinement in structured triangular grids cannot reduce the FC effect, but it does in unstructured triangular grids. It suggests that, grid refinement improves a solution only if it breaks FC structures into shorter channels. Strong false currents also produce convergence difficulties.

1.3 Wetting-Drying treatment

Depth-averaged transport equations can be solved either on fixed (Delis and Katsaounis 2005, Di Martino et al. 2011, Knock and Ryrie 1994, Zoppou and Roberts 2000) or moving grids (Chen and Duan 2008). When moving grids are used, the boundaries of the computational domain lie on the water edge. Grid points at the water front then will be shifted with time when the water edges move. On fixed grids an Eulerian technique will be needed for treating the temporal variations in the spatial position of water front (George and Stripling 1995).

When the transport equations are solved on entire computational domain, the effect of wetting-drying algorithm on numerical accuracy is not very significant. The effects of using an efficient

wetting-drying algorithm can be best observed when the transport equations are solved only in wet cells. In (Begnudelli and Sanders 2007) continuity equation is solved in entire computational domain, but, momentum equations are solved only in wet cells. Momentum equations, however, can also be solved in entire computational domain (Nikolos and Delis 2009, Sleigh et al. 1998, Wu 2004). Solving the transport equations only in wet cells is computationally most efficient when the number of wet cells is much smaller than the number of dry cells (Brufau et al. 2004, Lai 2010, Xia et al. 2010). For instance, in a dam-break problem when the initial wet region is where the reservoir is placed, the number of dry cells can be tens of times more than the number of wet cells. In such cases where the floodplain is huge compared with the area of reservoir, solving the transport equations only in wet cells is very efficient.

Since during the time interval between the current and next time level, water front can physically propagate, it is argued that numerical procedure must allow such propagations (Zokagoa and Soulaimani 2010). In order to permit such propagation of water front, the flux at the interface between wet and dry cells has to be calculated; see for instance (Lai 2010, Murillo et al. 2006, Zokagoa and Soulaimani 2010). In three-dimensional simulations when the geometric reconstruction of Volume Of Fluid, VOF, is used for capturing the interface between several fluid phases, such propagation is not permitted. Numerical experiences indicate the accuracy of the computed results when the interface is prevented from propagation during the time interval between current and new time level. An equivalent strategy for depth-averaged simulations is setting the normal component of the front velocity to zero (Liang and Borthwick 2009, Wu 2004). In order to set the flux at the water front to zero, a boundary condition has to be applied. When Saint Venant equations are solved, the boundary condition can be as simple as setting the normal velocity to zero (Liang and Borthwick 2009). In the case of hydrostatic depth-averaged equations, a normal choice can be using wall function approach (Wu 2004). In this thesis, the effect of both calculation of flux and the assumption of zero flux at the water front on numerical accuracy is investigated.

When water flows down a slope, independent of wet or dry condition at the cell downstream of a face, occurrence of a negative water depth at the cell upstream of the face is always possible. In order to avoid negative water depths, local and general water redistribution algorithms seems to be inevitable (Liang and Borthwick 2009, Zokagoa and Soulaimani 2010). With a redistribution algorithm, either local or general, mass will not be fully conserved. Redistribution algorithms

also produce steps at the water surface where distribution of the step's size is very anisotropic. It is observed in this thesis that, steps in water surface produce false currents. As a result, redistribution algorithms are not the best way of treating negative depths. In this thesis, in order to cope with negative water depths, an innovative strategy is developed which is suitable for finite volume SIMPLE algorithm. SIMPLE algorithm is widely used for solving the hydrostatic shallow flow equations (Bennett et al. 2008, Lai 2010, Minh Duc 1998, Wu et al. 2005).

When during time interval between current and future time level, water is allowed to flux at the face between a wet and a dry cell, the order of accuracy of the wetting-drying treatment limits the order of accuracy of the solution near wetting-drying fronts (Liang and Borthwick 2009, Murillo et al. 2008, Nikolos and Delis 2009). For instance, when the wetting-drying treatment is first-order, the order of accuracy of the solution eventually has to be reduced to first-order. When the flux at the face between a wet and a dry cell is set to zero by means of applying a boundary condition, the order of accuracy of the solution near the water front will not be explicitly limited to the order of accuracy of the wetting-drying treatment. In this thesis, a high order wetting-drying treatment is devised which does not explicitly restrict the order of accuracy of the solution near the wetting-drying boundary.

What differentiates wet and dry cells is the threshold water depth (Begnudelli and Sanders 2007, Brufau et al. 2004, Xia et al. 2010). With a two-threshold technique (Sleigh et al. 1998, Zhao et al. 1994) solution will be highly threshold dependent; e.g. the number of the cells where the water depth is between threshold depths will highly depends on the difference between threshold depths. It is observed in this thesis that, a small threshold water depth does not necessarily increase the accuracy of a wetting-drying technique. A conclusion of this finding can be that, decreasing the difference between the magnitudes of two water depths in a two-threshold technique does not necessarily reduce the extent of the semi-wet region. In (Xia et al. 2010), the effect of the threshold depth on numerical simulation of dam-break over shallow wet beds is studied. In this thesis, the effect of threshold water depth on temporal variation of the spatial position of the water front is numerically investigated in several benchmark tests.

1.4   Extension of solver to vegetated channels

Vegetation is normally approximated by rows of equivalent stems and, the flow in a vegetated zone is simulated in the same way as the flow over an array of rods (Sun et al. 2010, Tanino and

Nepf 2008, Wu et al. 2005, Zhang and Su 2008). Similar to the case of flow over array of roads, the double-decomposed depth-averaged equations can be derived through integration of the time-mean depth-averaged equations over a Representative Elementary Volume (REV). Though double-decompose equations are used by Sun et al. (2010), Tanino and Nepf (2008), Wu et al. (2005), and Zhang and Su (2008), more complete techniques are also available in porous media science. The technique which is used in this thesis is mainly based on the works by de Lemos and his co-researchers (de Lemos 2005, de Lemos 2006, Pedras and de Lemos 2008, Saito and de Lemos 2005, Saito and de Lemos 2006, Saito and de Lemos 2009, Saito and de Lemos 2010). A main difference between the works by (de Lemos 2005, de Lemos, 2006, Pedras and de Lemos 2008, Saito and de Lemos 2005, Saito and de Lemos 2006, Saito and de Lemos 2009, Saito and de Lemos 2010) and the research work performed by (Sun et al. 2010, Tanino and Nepf 2008, Wu et al. 2005, Zhang and Su 2008) is in the way porosity appears in transport equations. The porosity of a porous medium should appear in the transport equations in an appropriate way so that in discretized equations the flux area at the face appears as the face area multiplied by water depth and the porosity. In this thesis, compared to the work by (Sun et al. 2010, Tanino and Nepf 2008, Wu et al. 2005, Zhang and Su 2008), the depth-averaged double-decomposed energy equation is also solved over non-flexible partially vegetated porous media.

When transport equations are modified in order to simulate a porous medium, the porosity of the medium will appear in the entire terms of the equations except the terms where porosity effect is simulated. In a vegetated porous medium, for instance, the porosity of the medium appears in entire terms of the momentum equations except the terms which represent the force by porous matrix (Wu et al. 2005). These terms are where the vegetation density will appear in the equations. Thus, either the vegetation density or its porosity should be derivable from the other one. When this criterion is not hold conservation laws will not be satisfied. Wu et al. (2005) and Wu and Wang (2004) proposed the definition of the vegetation density and the relation between vegetation density and its porosity. However, an exact physical and mathematical definition of depth-averaged porosity still remained unclear. Fischer-Antze et al. (2001) assumed there is only one stem at every computational cell. The simple relations for vegetation density and porosity suggested by Fischer-Antze et al. (2001) or Zhang and Su (2008) are hardly extendable to a complicated vegetated porous medium. The porosity defined at the interior of a domain also fails to apply in the region near a macroscopic boundary (Hsu 2005). For a near-wall region, for

example, this problem becomes serious since most of the important transfer process occurs in the boundary layer near the wall. In this thesis, the unit-cell concept which is introduced in (Arquis et al. 1991, Kuwahara and Nakayama 1999, Kuwahara et al. 1996) and further employed in (Pedras and de Lemos 2008, Teruel and Rizwan-Uddin 2009a) is used in order to define the vegetation density and porosity. The vegetation porosity and density which are defined using the unit-cell concept are simply applicable to a complicated vegetated zone. Since either vegetation density or its porosity can be derived from the other one, conservation laws will be satisfied. The vegetation density defined in this thesis can be considered as a more complete form of the vegetation density defined and used before (Choi and Kang 2004, Huai et al. 2009). Three different near-boundary vegetation porosity models are also defined in order to achieve a more accurate boundary treatment. These near-boundary porosities are defined based on percentage of the boundary area which is in contact with vegetation equivalent stems.

Most of turbulence models are not derived for porous media. Though for porous media these models are normally modified by means of space averaging, the experimental constants which are used in these models are not calibrated for porous media. These turbulence models then may no longer perform well (Teruel and Rizwan-uddin 2009b, Teruel and Rizwan-uddin 2010) for simulation of heat (Alshare et al. 2010) and fluid (Saito and de Lemos 2010) flows over an array of roads. The condition will be worse when the domain is partially porous since even a turbulence model which is developed for porous media may not work well in non-porous regions of the domain. For a vegetated porous media, field condition span $R_{e_D} \approx 0 - O(4000)$ (Tanino and Nepf 2008). At the first glance, a high Reynolds number turbulence model should be at least applicable to a vegetated channel with high R_{e_D}. This is used, for example, in (Jang and Shimizu 2007; Wu et al. 2005, Zhang et al. 2010) using the standard $k - \varepsilon$ model, where the wall-function approach is used for the near-wall treatment. In this thesis, flow in a channel with alternate vegetated zones is investigated at high R_{e_D} and, application of standard $k - \varepsilon$ model is examined for two different vegetation densities.

The heat flux between the wall boundary and porous matrix is not the same as the heat flux between the wall and fluid. In the first case the thermal conduction is the main reason behind heat transfer while in the second case heat will be transferred by both conduction and convection. If vegetation stems touch the wall boundary, they will alter the near-wall heat transfer. A technique

then will be required in order to take account of vegetation effects. The term for diffusive heat flux due to porosity gradient does not appear in one-energy equation model when porosity is uniform (de Lemos 2005, de Lemos 2006, Pedras and de Lemos 2008). In a partially vegetated channel the porosity gradient near the vegetation border is not zero. This is where the effect of diffusive heat flux due to porosity gradient can be significant. In a dense porous medium with a low speed flow, $R_{e_d} \leq \sim 300$ and $\sim 1 \leq P_{e_d} \leq \sim 10$, the effect of laminar thermal dispersion on temperature field can be large (Kuwahara and Nakayama 1999, Kuwahara et al. 1996). This condition can be observed in partially vegetated channels with high vegetation density. In this thesis, a model is suggested in order to take account of vegetation material effect on the near-wall heat flux. The diffusive heat flux due to porosity gradient is also calculated and, the effect of this heat flux on temperature filed is investigated at high and low R_{e_D}. At a low R_{e_D} the laminar thermal dispersion effect on temperature filed is examined.

1.5 Vorticity equation for secondary flows

In space averaging process a variable will be considered as sum of its space averaged component and a spatial oscillation. After rearrangement of a space averaged equation, the terms which include spatially fluctuating components form the so-called dispersion terms. In a double-decomposed depth-averaged momentum equation a dispersion term will appear as a result of averaging over water depth. Though this dispersion force can exist even in a straight channel (Blanckaert et al. 2010, Wang and Cheng 2005, Wang and Cheng 2006), the momentum due to this force is most significant in channel bends where the secondary flows are most strong (Begnudelli et al. 2010, Stoesser et al. 2010). This is where the word Dispersion Force can be most meaningfully replaced with the word Secondary Force.

In the literature, the secondary force source term is obtained through different techniques such as solving some algebraic equations (Hsieh and Yang 2005), solving the moment equation (Wu and Wang 2004) or, solving the stream-wise vorticity equation (Bernard 1993, Rodriguez et al. 2004). In none of the mentioned methods, however, the vegetation effect on secondary force is considered. The transport equation for stream-wise vorticity is based on the interaction of the lateral curvature, bottom friction and vertical non-uniformity, to develop a model that reproduces the depth averaged influence of the secondary flow (Bernard 1993). This model is used in this thesis for flume conditions and by Rodriguez et al. (2004) for natural streams in order to simulate

the flow in channel bends. Over predicted stream-wise velocities are, however, observed in this thesis when the secondary force due to depth-averaging process is taken into account.

In vegetated channels the porous matrix resists the secondary flow and, as a result, the magnitude of secondary force in momentum equations has to be reduced. In a partially vegetated channel when vegetation is dense and divides the channel into several sub-channels, the initial secondary flow will be weakened and may be divided into several smaller secondary flows in sub-channels. In this thesis, a dissipation source term is developed and added to the vorticity equation in order to take account of vegetation damping effect on stream-wise vorticity. The reduced stream-wise vorticity then would produce a smaller secondary force. A non-physical shift in velocity profile is observed when the channel was partially vegetated.

Several test cases are performed in order to find circumstances where the secondary force added to momentum equations will actually improve the accuracy of the computed depth-averaged velocity field. In these tests, parameters such as length of the channel bend and depth to width ratio are studied.

CHAPTER 2   METHODOLOGY

In this thesis, the methodology for doing the research work is divided into two parts as: general methodology, and specific methodology. In general methodology, the general aspects of the work were expected to be known. Examples of such aspects are the numerical scheme to be used, and output files format. The general aspects of the work were specified when the main objective of the project was defined. The general methodology of this thesis then was known before starting any of the project steps. The specific methodologies, on the contrary, were not required to be fully known at the beginning of the research work, but the specific methodology of the first step. The specific methodology of every step was clarified at the beginning of that step. The dependency of any future step to preceding steps, however, was observed at preceding steps of the project. Since the specific methodology of this thesis closely relates to its scientific content, it will be explained in more detail.

In Specific methodology, the whole thesis is divided into several steps in order to manage the process of developing the CFD solver. An exact definition of problem, developing new techniques, and design of objects and algorithms are performed almost separately at the beginning of every step. As a result, details of the methodological approaches to research and development at every step are specified at the beginning of that step.

2.1   Two-dimensional solver

As the first step in developing a depth-averaged solver, a simple three-dimensional solver is reduced to a two-dimensional solver. In three-dimensional solver, SIMPLE algorithm is used for the coupling between velocity and pressure field, upwind method is applied to convective terms, central differencing technique is applied to diffusive terms, and source terms are discretized in point-wise manners. Variables are stored at cells' center, and the three-dimensional cells have to be tetrahedron. Following steps are taken in order to develop the two-dimensional solver:

- Reduction of three-dimensional solver into two-dimensional solver: In most of functions and subroutines the reduction process was as simple as reducing the loop over four faces of tetrahedron cells into loop over three edges of triangle cells. A triangle cell is equivalent to a wedge type three-dimensional cell, where the height of the prism is assumed equal to one. Thus, the mathematical relations for calculating geometrical data

such as cells' volume and faces' area are fully changed and, in turn, functions and subroutines which were doing these calculations are significantly altered. Other places where changes are significant include functions and subroutines which perform the required calculations for generating outputs, together with functions and subroutines which export the data to Tecplot. These changes are mainly due to the fact that, every three-dimensional output is reduced to a two-dimensional output, and every two-dimensional output is reduced to a one-dimensional output.

- Modification in two-dimensional solver: The three-dimensional solver was developed for solving the specific problem of external flow around spherical objects. The reduced two-dimensional solver necessarily inherited the same features. Many modifications then were necessary in order to make a general solver out of the two-dimensional solver. These modifications include:

  ➢ Definition of new boundary conditions for the solver. Most of these boundary conditions were required during validation process. The practical application of these boundary conditions for future depth-averaged simulations is also observed. For instance, the no-slip rough wall boundary condition was not required for validation of the solver. It is added to the code and is validated only because it has practical applications in depth-averaged simulations.

  ➢ Definition of new convergence criteria. Any convergence criterion is not applicable to every problem. The existing convergence criterion is replaced with three new criteria which are more general.

  ➢ Rearrangement of steps taken in the coded SIMPLE algorithm. It is tried to strictly follow the computation steps suggested for SIMPLE algorithm in literature.

  ➢ Replacement of the interpolation technique. A distance-based technique is used for interpolating variables from cells' center into the cells' faces.

  ➢ Reduction in the absolute magnitude of the checkerboard oscillations. In order to reduce the checkerboard oscillations in pressure field, a Rhie and Chew type method is applied to the interpolated velocity at the cell face.

- Solution of the standard $k - \varepsilon$ turbulence model: Depth-averaging process limits the turbulent structures to a two-dimensional space and, in turn, the actual cohesive turbulent structures cannot be captured. An isotropic turbulence model based on Boussinesq assumptions then seems adequate for depth-averaged solvers. In this thesis, the standard version of the $k - \varepsilon$ turbulence model is added to the solver for taking the turbulent effects into account. Thus, the Navier-Stokes equations solved by the solver are inevitably Reynolds-averaged.

- Application of a near-wall treatment: In three-dimensional version of the code convective fluxes are set to zero at the wall, but diffusive fluxes are left untouched. In the two-dimensional solver, the same strategy is followed when a flow is laminar. Comparison of results with experimental data and the solutions by Fluent6.3 indicates the accuracy of the computed results. When solving for turbulent flows, the standard wall function approach is used for the near-wall treatment. In this approach, the source terms are added only to the cells adjacent to the wall.

- Application of MBLT grids: When solution domain consists of several blocks of fluid and the data structure is collocated, spurious high checkerboard oscillations may appear in velocity and pressure field at the interface between blocks of fluids. A checkerboard pressure field may appear because of two main reasons: the interpolated velocities at the cell faces are not mass conserving and, the pressure of the cell will not appear in discretized momentum equations when the pressure term is integrated over the cell volume. When Green's theorem is used for converting the integral over cell volume into the integral over cell surface, the pressure of the cell will not appear in discretized momentum equations only if a triangle cell is equilateral. Numerical simulations show that, the mentioned checkerboard velocity and pressure fields will appear at the interface between blocks of fluid only if the triangle cells are not equilateral. Otherwise, both velocity and pressure field will be smooth. The main reason behind having such smooth velocity and pressure fields is found to be due to isotropy in the checkerboard oscillations. This isotropic checkerboard pressure field is in minimum energy state. The isotropic checkerboard pressure field consist of semi-spherical pressure surfaces. Such semi-spherical pressure surfaces need at least four equilateral triangular cells to form. These consist of a central cell and its three neighbouring cells. These four cells form a

bigger triangle which is called a perfect LT. When these four triangular cells are not equilateral, LT is called distorted. Depending upon the distortion of LT, the pressure surface in a distorted LT is not perfectly semi-spherical. Since every LT has three neighbouring LTs, these non-similar pressure surfaces form an anisotropic checkerboard pressure field. Numerical simulations proved that, performance of the Rhie and Chow type pressure correction technique decreases when anisotropy in checkerboard pressure oscillations increases. A technique, MBLT, then is developed in order to apply the desired property of the perfect LTs to unstructured triangular grids. In this technique domain is first meshed with a coarse grid where every cell is assumed to be a block of fluid. LTs then are constructed in every individual cell. This will force an isotropic checkerboard pressure at every initial coarse cell (equivalently, at every block of fluid) and, in turn, increases the effectiveness of a Rhie and Chow type pressure interpolation technique.

- Validation of solver: The two-dimensional solver is first applied to laminar lid-driven cavity. Both first-order and second-order solutions are compared with measured data, and the data computed with Fluent6.3. In the next benchmark test, turbulent flow in a square duct with smooth no-slip walls is simulated and, numerical results are validated with experimental data and the data computed with Fluent6.3. The wall boundary condition is changed to free-slip and rough no-slip and, it is validated with the data from Fluent6.3 software. In the last step of validation, the same square duct is used for simulation of laminar heat and fluid flows. Both first order and second order solutions for the heat transfer are validated with data from Fluent6.3.

2.2 Depth-averaged solver

Since the two-dimensional solver is validated, developing a depth-averaged solver out of this two-dimensional solver reduces the programming error. On the other hand, a copy of the two-dimensional solver is put aside for probable future extension of the code to a three-dimensional solver. The steps taken in developing the depth-averaged solver out of the two-dimensional solver are as follows:

- Modification of transport equations: Water depth to the power of a fraction always appears in the source terms due to channel bed. When the water depth goes to zero, the

source term due to channel bed goes to infinity and solution oscillates. In this thesis, the whole transport equation is multiplied by water depth to the appropriate power of a fraction and, in turn, the source term due to channel bed at very small water depths will be a constant.

- Discretization of source terms: When the transport equations are modified as explained in previous paragraph, every term excluding the bed source term will go to zero at very small water depths. If the bed source term is discretized explicitly, a division by zero will appear in discretized unsteady equations for calculation of variables at new time level. The bed source terms then are discretized with a semi-implicit technique. With this technique the bed source terms will appear in both numerator and denominator of the discretized unsteady equations.

- Performing the depth-averaging process: First, the depth-averaged transport equations are discretized. Then, the discretized depth-averaged equations are compared with discretized two-dimensional equations. Finally, appropriate corrections are made to functions and subroutines of the two-dimensional solver. This includes correction to functions and subroutines for generating outputs.

- Solution of vorticity equation: When streamlines are curved, secondary flows are strong. A source term then is needed for taking account of secondary force in momentum equations. This term can be calculated through solving a transport equation for stream-wise vorticity. In this thesis, before discretization process, vorticity equation is also multiplied by water depth to the appropriate power of a fraction. During discretization, the vorticity damping source term which is due to bed friction is discretized with a semi-implicit technique.

- Development of TV-LI technique: When the data structure is collocated, interpolation of variables from cells' center into the cells' faces will be required during computations. A linear interpolation technique, such as the one used in this thesis, is most accurate when a variable behaves linearly. In many simple shallow flows, such as flow in a wide straight channel with rectangular cross section, unit discharge's behaviour is more linear compared with that of velocity. This fact is used for developing a new interpolation technique which is called Total Value – Linear Interpolation, TV-LI. In this technique,

every variable is integrated over the water depth and its total value is calculated. This total value then is linearly interpolated from cells' center into the cells' faces. At the cell face, the variable is calculated through dividing its total value by interpolated water depth. Exceptions are water depth and water surface elevation where a total value is meaningless. In these cases, a Linear Interpolation technique, LI, is used. Application of TV-LI technique highly reduces the total computational efforts at fine grids.

- Investigation of grid effect on computed velocity field: It is observed during simulations that, solution of transport equations in a structured triangular grid reveals significant spurious currents. Several channels with different bed slope and roughness then are studied in order to investigate the reason behind such spurious currents. False Channels, FCs, are found to be the main reason behind such currents. A FC is one of continues downstream directions in a grid where a numerical flow is permitted, but a physical flow is not allowed. For instance, the physical flux through a face with its normal vector perpendicular to flow direction is always equal to zero, but the numerical flux is not necessarily zero. The path for a false numerical flux, which can appear in a depth-averaged solution but not in the equivalent two-dimensional solution, is part of a FC. Simulations reveal that, such spurious currents do not appear when continues downstream directions do not exist in a grid. It is also observed that, grid refinement in unstructured triangular grids break FCs down and, in turn, it reduces the spurious currents.

- Validation of solver: There are several benchmark tests where the solutions from a two-dimensional solver can be validated with those of a one-dimensional solver. An example of such tests includes flow in a frictionless straight channel with rectangular cross sections. A simple one-dimensional solver then is developed in order to be used, together with several experimental data, for validating the depth-averaged solver. First, flow in a frictionless straight channel is simulated. This test validated the internal accuracy of the solver. Then, flow in a straight channel with smooth walls but rough bed is simulated. In this test, accuracy of the discretized bed source terms is validated. Finally, measured data from a shallow bent channel are used. These data validated the accuracy of the coded discretized wall functions. Some additional tests are also done in order to make sure the results are non-oscillatory at very small water depths.

2.3   Extension of depth-averaged solver to streams with moving water edge

In natural streams the position of water edge is a function of time and space and, in turn, a depth-averaged solver is required to be able to handle problems where the water edge moves. The developed depth-averaged code then is further extended to solve problems including dam-break or flooding phenomenon. The steps taken in this process are as follows:

- Identification of cells: Before starting a solution and also at the beginning of every time level, wet and dry cells are identified. A computational cell is assumed wet if the water level in that cell is above a predefined threshold level, otherwise it is assumed dry. When a wet cell has no dry neighbouring cell, it is called a wet-interior cell. A wet cell which has a dry neighbouring cell is a wet-boundary cell. The identification number assigned to wet-interior and wet-boundary cells is different. A dry cell is an interior dry cell when it has no wet neighbouring cell. When a dry cell has a wet neighbouring cell, it is called a dry-boundary cell. Similar to the case of wet cells, the identification number assigned to dry-interior and dry-boundary cells is different. The identification number of boundary wet and dry cells is used for applying boundary conditions. The identification number of wet cells of either interior or boundary types is used when doing calculations for domain's wet region. A wet cell which has no wet neighbouring cell is called a wet-isolated cell. Calculations are not performed in such wet cells. When every cell neighbouring a dry cell is a wet-boundary cell, it is called a dry-island cell.

- Identification of loops: When a problem includes both wet and dry cells, doing loop over entire cells in order to find wet cells is not computationally efficient. Even though wet and dry cells are identified by identification numbers, an identification number alone adds little value to a wetting-drying algorithm. Assigning an identification number to every cell is a way of marking a computational domain. These marks then have to be used for identifying loops over wet, wet-boundary, and dry-boundary cells. In order to do so, the identification numbers for wet-domain (this includes wet-interior and wet-boundary cells), dry-boundary, and wet-virtual cells are stored in separate arrays. The wet-domain array consists of identification number for cells where computation will be performed. The dry-boundary array consists of identification number for dry cells. This is where boundary conditions at wetting-drying boundaries will be applied. The wet-virtual array

consists of identification number for ghost cells with wet neighbouring cell. The wet-virtual array is used for applying boundary conditions at domain boundaries.

- Treatment for wetting-drying boundaries: Since transport equations are solved at wet cells, a boundary condition is required at wetting-drying boundaries. The tangential component of velocity vectors near a wetting-drying boundary is physically zero, but the normal component can have any magnitudes. Numerical simulations performed in this thesis confirm that, the normal velocity can be set to zero when Courant number is less than one. The wall boundary condition then is applied to wetting-drying boundaries for setting the boundary velocities to zero. Since the position of wetting-drying boundaries is a function of time and space, dynamic ghost cell technique is used for applying the boundary conditions. The dynamic ghost cells are defined where dry-boundary cells exist, and they have the same geometry as the relevant dry-boundary cells. These ghost cells are called dynamic because they will be reallocated at the beginning of every time level and their position will change.

- Treatment for cells with negative water depth: During simulations there is no guaranty that the water depth at a wet cell will remain more than the threshold water depth. The pressure correction to water depth can even produce cells with negative water depth. Even though formation of such cells may not destabilize the solver, it will produce non-physical solutions. A technique then is required to prevent formation of cells with negative or low water depth. The technique developed in this thesis consists of four steps. First, the pressure correction is used for calculating the correction to water depth. Then, the water depth is corrected and the expected new water depth is computed. After that, the computed new water depth is compared with the threshold water depth. Finally, the pressure correction is modified so that the new water depth remains more than the threshold water depth. The modified pressure correction then is used for updating velocities, water surface elevation, and depth.

- Wetting-Drying process: In first order techniques a dry cell can receive water from its neighbouring cells if the water depth at one of the neighbouring cells is more than the threshold water depth, and the flux direction permits the wetting process. This will produce spurious wetted zones with a thin layer of water. These thin layers of water flow

downstream and increase the extent of the spuriously wetted zones. False wet zones, on the other hand, increase the computational efforts since the transport equations are solved only in wet cells. The high order technique which developed in this thesis takes account of the gradient of channel bed and water surface. In this technique, a dry cell will be wetted if the water depth in a neighbouring cell is more than the threshold water depth, the flux direction permits the wetting process, and the reconstructed water surface and channel bed meet in dry cell. This technique prevents formation of spurious thin layers of water. Drying process consists of two main steps: changing the identification of a cell from wet to dry when the water depth at this cell falls below the threshold water depth, and storing the identification number of this cell in the array for dry-boundary cells if applicable.

- Validation of solver: If a wetting-drying algorithm performs well for the problems which include downhill dam-break, uphill dam-break, and dam-break over a flat bet, it will do well for any problem. These test cases then are selected for validating the new wetting-drying algorithm, together with a multidirectional dam-break test. In the multidirectional dam-break test case water can flow uphill, downhill, and over flat regions and, in turn, this test examines the wetting-drying algorithm for combined movements. The results computed with first order and high order techniques then are compared with numerical data which are computed with Fluent6.3. Dam-break over a flat wet bed is also investigated in order to find the optimum threshold water depth.

2.4 Extension of depth-averaged solver to streams in vegetated channels

Vegetations can be well approximated to an equivalent cylindrical stems where, these stems shape a porous matrix. A porous matrix resists the flow, influences the turbulent structures, and alters the temperature field. Very fine grid will be needed if one aims to simulate the exact flow field around a porous matrix. A computationally efficient alternative way of simulating the flow field in a porous medium is the space averaging technique. When the time-mean depth-averaged equations are integrated over a Representative Elementary Volume, REV, the resultant equations are called the double-decomposed depth-averaged equations. These equations then can be solved instead of time-mean depth-averaged equations for simulating heat and fluid flows in a vegetated channel. Following steps then are taken in order to extend the depth-averaged code:

- Definition of vegetation porosity and density: Vegetation porosity appears in entire terms of a transport equation, except the term where the effect of porous matrix is simulated. This is where the vegetation density will appear in equation. Thus, the defined vegetation porosity or its density should be drivable from the other one. If not, the conservation law will not be satisfied. In this thesis, vegetation density and porosity are defined from unit-cells. A unit-cell is assumed to be the simplest equilateral polygon which connects several neighbouring stems. For instance, the unit-cell for staggered arrangement of vegetation stems is an equilateral triangle. The volume of a unit-cell is equal to the area of the unit-cell polygon multiplied by water depth. The cross sectional area of vegetation stems at a unit-cell multiplied by effective stem height is the volume of solid matrix. The area of a unit-cell polygon multiplied by water depth minus the volume of sold matrix is equal to the volume of fluid in that unit-cell. These volumes then are used for defining vegetation porosity as the volume of fluid in a unit-cell divided by volume of unit-cell. Vegetation density is defined as the frontal area of vegetation stems in a unit-cell divided by area of the unit-cell polygon. When this method is used for defining vegetation density and porosity, either the vegetation density or its porosity can be derived from the other one. Vegetation porosity at the domain interior, however, does not necessarily represent the porosity at the domain boundaries. A technique then is required for calculating the near-boundary porosity. When the near-wall arrangement of vegetation stems is not irregular, a near-wall unit-cell can be defined. The near-wall unit-cell consists of a line connecting two near-wall stems. The thickness of this unit-cell normal to the wall is much less than stem diameter. Volumes of porous matrix and fluid in a unit-cell, together with the volume of unit-cell, are defined as the ones of the unit-cell in domain interior. Definition of the near-wall vegetation porosity then is straight forward. When the arrangement of vegetation stems near the wall is very irregular, the near-wall porosity is assumed equal to the porosity at the domain interior.

- Modification of transport equations: the time-mean depth-averaged equations are space averaged in order to take account of spatial oscillations in flow field. As a result of this spatial averaging extra source terms are appeared in transport equations, together with vegetation porosity in other terms. The derived double-decomposed depth-averaged

equations then are discretized, and modifications are made to the coded discretized equations.

- Development of a damping source term for vorticity equation: Vegetation stems resist the flow in any direction, including the secondary flow. This resistance force reduces the strength of the secondary flow and, in turn, it reduces the magnitude of secondary force in momentum equations. Since the secondary force is a function of stream-wise vorticity, a damping source term will be required in vorticity equation in order to reduce the absolute magnitude of the stream-wise vorticity in vegetated zones. For deriving such source term the functional relation between velocity components and stream-wise vorticity is assumed independent of vegetation effects. The derived damping source term is a function of water depth, vegetation effective height, drag coefficient, and vegetation density.

- Development of a macroscopic secondary force: The time-mean depth-averaged secondary force in momentum equations, usually called microscopic secondary force, represents the effect of non-uniformity of flow field in vertical direction. When flow variables are space averaged, the space averaging effect has to be observed in secondary force term; i.e. a macroscopic secondary force has to be used in momentum equations rather than a microscopic force. In order to derive a macroscopic secondary force, the microscopic secondary force model suggested by literature is assumed to represent the actual microscopic force. This microscopic force then is space averaged, and an expression is developed for macroscopic secondary force.

- Implementation of one-energy equation model: The computed temperature field in a porous medium will be most accurate when two energy equations, one for fluid phase and one for porous matrix, are solved. This demands a known temperature or heat flux at the surface of the porous matrix, together with a known interfacial heat transfer coefficient. In a vegetated porous medium the problem is not only an unknown interfacial heat transfer coefficient but also an unknown temperature or heat flux at the surface of the porous matrix. This then leaves no choice but solving a one-energy equation which relies on the assumption of local thermal equilibrium hypothesis. In this hypothesis the porous matrix and its surrounding fluid are assumed in local thermal equilibrium. This assumption reduces the two-energy equation model to a one-energy equation model. The

assumption of local thermal equilibrium remains valid if the porous matrix does not act as a significant source of heat. Regarding the accuracy required for simulating a vegetated zone, the assumption of local thermal equilibrium hypothesis holds in vegetated open waters.

- Modification of diffusion term in energy equation: When the one-energy equation model is applied to the problems with uniform porosity, the thermal diffusion due to porosity gradient can be ignored. In a partially vegetated open channel model where the assumption of uniform porosity does not hold, the diffusive heat flux due to the porosity gradient will be significant at fine grids. In this thesis, the porosity induced thermal diffusion term is developed and added to the one-energy equation model. The effect of this term on the computed temperature field then is examined at different flow Reynolds numbers.

- Modification of wall functions for energy equation: When the porous matrix touches the wall boundary, it affects the heat flux at the wall. The nature of the heat flux between the wall and porous matrix is conductive, and the heat transferred into or out of the porous matrix will be eventually transferred into or out of fluid. This heat immediately affects the temperature field when the local thermal equilibrium hypothesis is assumed. The heat flux at the wall then is assumed equal to the heat flux between wall and fluid plus the conductive heat flux between wall and the porous matrix. In a laminar flow these hypotheses are used for correcting the temperature at ghost cells. The same hypotheses are used in a turbulent flow for modifying the wall functions.

- Investigation of the effect of laminar thermal dispersion: Non-uniformity in temperature field produces thermal diffusion. Space averaging process, however, smooth down any non-uniformity with length scale less than the cube root of the volume of REV. In double-decomposed equations, the effects of these non-uniformities are observed through thermal dispersions. These dispersion terms appear in energy equation by means of equivalent conductivity. In literature, the macroscopic eddy conductivity is assumed to take account of both turbulent diffusive and dispersive conductivities. The laminar thermal dispersion conductivity, on the other hand, is computed for a unit-cell assuming uniform porosity, uniform velocity, uniform thermal gradient, and periodic condition at the boundaries of

the unit-cell. Laminar thermal dispersive fluxes can be comparable to convective fluxes at small Reynolds and Peclet numbers. Whether or not this laminar thermal dispersive flux has to be taken into account in a vegetated zone then is investigated through simulation of low Reynolds and Peclet numbers flow in a partially vegetated open channel.

- Application of high Reynolds number turbulence models to partially vegetated channels: High Reynolds number turbulence models are successfully applied to open channel flows. The application of these turbulence models is even extended to partially vegetated channels. What is most common among all simulated vegetated channels is a small vegetation density. Naturally vegetated channels, however, can exhibit higher vegetation densities. An important question which remains unanswered is: to what extent of vegetation densities are these high Reynolds number turbulence models applicable to partially vegetated channels? Several numerical tests then are made in order to find an answer to this question. In these simulations, high and low Reynolds number flows in partially vegetated channels with high vegetation density are simulated.

- Application of vorticity equation to open channel flows: The source terms for generation and dissipation of stream-wise vorticity are very approximate and, in turn, vorticity equation is more of a balance equation rather than a transport equation. The accuracy of this equation for predicting the stream-wise vorticity then highly relies on the assumptions used for derivation of its source terms. A consequence of an inaccurately computed source term can be a fatal error in computed secondary force and, in turn, inaccuracy in computed velocity field. Among assumptions made in derivation of source terms, a basic but most important assumption is the assumption of shallow flow. Several numerical simulations then are made in order to investigate the effect of channel depth to width ratio on computed velocity field. In derivation of source terms the relation between velocity components and stream-wise vorticity is also assumed known. This assumption may not hold in complex flow regimes. For instance, in the case of a partially vegetated channel or a long channel bend, velocity components may have different functional relation with stream-wise vorticity. Numerical tests then are made in order to investigate the accuracy of the computed velocity field in partially vegetated channels and channels with a long bend.

- Validation of solver: Flow in several partially vegetated channels is simulated, and the computed data are compared with the experimentally measured data. Performance of the solver is additionally investigated through observing the turbulence kinematic energy, stream-wise vorticity, and tangential stress at the border of vegetated zones.

2.5 Development of software for interpolation of geo-data into cells' center

Most channel bed and flood plain consist of very complex geometries and, in turn, functional relationships cannot be used for reconstruction of these geometries. A tool then is needed for interpolation of geo-data into cells' center. The tool which performs this interpolation in Shallow Fluent is called SF-Field. SF-Field supports three different interpolation techniques as follows:

- Old cross sectional data: Old data are measured across channels in several cross sections and, in turn, they have very low resolution. These data are measured to be used in one-dimensional solvers and they are not appropriate for two-dimensional solutions. Such data, however, can be used for preliminary study of a channel flow. In order to interpolate the data, channel is longitudinally divided into several sub-channels where every sub-channel represents a streamline. Sub-channels are also divided by cross sections where every divided part of a sub-channel is quadrilateral and consists of four geo-data lying at its vertices. These four data then are interpolated along streamline into the center of every part of sub-channels.

- Unstructured quadrilateral data arrangement: Field data are not normally measured with unstructured quadrilateral arrangement. Such measurement, however, can be made for flume data. In this case, every quadrilateral structure consists of four data lying at its vertices, and several cells' center lying inside it. The data then is linearly interpolated from the vertices of these quadrilateral structures into the cells' center.

- Unstructured data arrangement: For two-dimensional simulations field morphological data are measured with an unstructured arrangement. In order to interpolate such data into cells' center, the space around every cell center is divided into several sub-spaces. The closest data to the cell center at every sub-space then is found. These data are linearly interpolated into the cell center.

CHAPTER 3   ARTICLE 1: TREATMENT OF CHECKERBOARD PRESSURE IN THE COLLOCATED UNSTRUCTURED FINITE-VOLUME SCHEME

3.1   Presentation of the article

In this section the objective of the article will be presented, as well as a conclusion on this work as part of the thesis. This article presents a new technique for removing the oscillations from pressure and velocity field. It can be used in commercial software to enhance the quality of the simulations. An example of such software which uses the same numerical scheme as this article can be ANSYS/Fluent (http://hpce.iitm.ac.in/website/Manuals/Fluent_6.3/fluent6.3/help/html/ug/ node987.htm).

3.1.1 Objective

When the finite volume method is used together with a collocated data structure, checkerboard oscillations can be observed in both velocity and pressure fields. In depth-averaged simulations, this pressure field is related to the water surface elevation through the expression $P = \rho g \xi$. Thus, the water surface will oscillate if the pressure field is checkerboard. Since in this thesis the depth-averaged solver is derived from a two-dimensional solver, it is considered reasonable to make effort on removing the checkerboard oscillations before extending the code to a depth-averaged solver. In order to achieve this goal, the Rhie and Chow type pressure correction is used, but additional correction to pressure and velocity fields is thought through grid property. This led to a new generation of grids which is called MBLT grids. Another matter which demands concern, when the Rhie and Chow type pressure correction term is used, is the relaxation factor in this term. A hypothesis then is devised in order to choose an appropriate relaxation factor regarding the arguments in the literature.

3.1.2 Conclusion

It is indicated that the relaxation factor in Rhie and Chow type pressure correction term has to be equal to one, and it cannot be equal to the general relaxation factor. It is observed that grid uniformity in triangular grids regulates the oscillations; i.e. checkerboard field will be more

isotropic when grid contains equilateral triangles. It is indicated that, the MBLT grid, which is designed to improve the uniformity property of the grid, reduces the checkerboard oscillations. The MBLT grid is however observed not to perform well near the domain boundaries where the boundaries of the multiple blocks of fluid coincide. It is observed that, to overcome this problem, structured triangular grid can be used near the domain boundary and MBLT right outside the boundaries. This technique is observed to fully remove the checkerboard oscillations.

The article is published with Numerical Heat Transfer; Part B: Fundamentals.

Moradi Larmaei, M., Behzadi, J., and Mahdi, T.-F. (2010). Treatment of checkerboard pressure in the collocated unstructured finite volume scheme. Numerical Heat Transfer; Part B: Fundamentals, 58(2) 121–144.

3.2 Treatment of Checkerboard Pressure in the Collocated Unstructured Finite-Volume Scheme

M. Moradi Larmaei[1], J. Behzadi[2], and Tew-Fik Mahdi[1]

[1]Department of Civil, Geological and Mining Engineering, Ecole Polytechnique de Montreal, Montreal, Quebec, Canada.

[2]Department of Mechanical Engineering, Shahid Chamran University, Ahvaz, Iran.

3.2.1 Abstract

In this article, a new concept, Local Triangle, is described. A smoother pressure field is then obtained through the utilization of Local Triangles in a Multi-Block Local Triangulation method. The cell face velocity is corrected with a pressure correction term which is usually under relaxed. It is demonstrated that this relaxation factor has to be one, and it cannot be the general relaxation factor. It is indicated that the checkerboard oscillations are more significant at high Cell Reynolds numbers and, in turn, in this article, numerical simulations are mainly performed in turbulent flow.

Keywords: Finite volume method, Unstructured grid, Collocated data structure, Checkerboard pressure

3.2.2 Introduction

When the finite volume scheme is used in staggered [1, 2] or lattice [3] grids, the velocity components are stored at the cell face center. The cell face velocity conserves the mass at the scalar cell and, as a result, the computed pressure field will be smooth. On the other hand, when the finite volume SIMPLE algorithm is utilized, a collocated data structure results in a checkerboard pressure field [4-7]. Two main reasons are inferred as the cause of checkerboard pressure: the averaged velocity at the cell face is not mass conserving [6, 8], and when momentum equations are integrated over a control volume, the pressure of the central cell will not appear in discretized equations [4, 6, 7]. In this article, the first reason is held, but it is shown that in triangular grids the second reason does not necessarily cause a checkerboard pressure field.

Nomenclature

a_0, a_j	coefficients in the discretized equations
C_{s_j}	volumetric flux at the cell face s_j
G	the rate of production of k
$h_{c_0\_c_j}$	the normal distance between two neighbor cells
k	turbulence kinematic energy
L	length scale
n	the direction along $\boldsymbol{n}$ or the number of levels in MBLT method
$\boldsymbol{n}$	unit vector normal to the cell face
N_{bcell}	number of the boundary cells in initial grid
N_{bcell_MBLT}	number of the boundary cells in MBLT grid
N_{Cell}	number of the cells (in initial grid considering the MBLT grid)
N_{cell_MBLT}	number of the cells in MBLT grid
N_{node}	number of the nodes in initial grid
N_{node_MBLT}	number of the nodes in MBLT grid
P, P'	pressure and pressure correction, respectively
$\boldsymbol{r}_{c_j\_s_j}, \boldsymbol{r}_{c_0\_s_j}$	distance vectors between the cell's center and the face's center
R	residual at the domain
R_e	Reynolds number

$s_j, \boldsymbol{s}_j$	cell face area and the area vector, respectively
S	source term
t	time
u, v	velocity components in x and y directions, respectively
U	velocity scale
$\boldsymbol{u}$	velocity vector
$\hat{\boldsymbol{u}}$	momentum velocity vector
ϑ°	continuity residual
ϑ°_{in}	volumetric influx at the inlet boundary
x, y	x and y directions

Greek symbols

ε	dissipation rate of k
μ, μ_t	Laminar and turbulent dynamic viscosity, respectively
ρ	fluid density
σ	Prandtl/Schmidt number
φ	general scalar quantity
χ	Prandtl/Schmidt number in general discretized equation for φ
ω, ω_{rc}	general relaxation factor and the relaxation factor in pressure correction term, respectively

Ω volume

Subscripts

d refers to the domain

j refers to the neighboring cell

k refers to turbulence kinematic energy

p_φ refers to the implicit part of the source term in discretized equation for φ

ref refers to reference value

R refers to residual at the domain

s_j refers to cell face s_j

$u_\varphi, u_{\boldsymbol{u}}$ refers to the explicit part of the source term in discretized equation for φ and $\boldsymbol{u}$, respectively

u_P refers to the source term due to pressure gradient in momentum equations

ε refers to dissipation rate of k

φ refers to φ

0 refers to central cell

Superscripts

P refers to pressure

T refers to the transpose of a vector

u refers to $\boldsymbol{u}$

φ refers to φ

..   refers to an initial guess

$*$ refers to the dimensional form of a quantity

In order to have a mass conserving velocity at the cell face, Rhie and Chow [9] have modified the interpolated cell face velocity by the difference between the interpolated pressure gradient and the gradient calculated at the cell face. Two questions, however, were not answered well: how should the pressure gradients be interpolated into the cell face, and how should the cell volume be calculated at the cell face? Davidson [10] has linearly interpolated the pressure gradient into the cell face. Ferziger and Peric [6] have argued that the cell center pressure gradients should be interpolated with a weight of 0.5, since this approximation does not see the grid non-uniformity. Croft [11] has indicated through numerical simulations that the weight in interpolation has to be 0.5. In order to calculate the cell volume at the cell face, Fue-Sang [12] and Davidson [10] have made use of a quadrilateral cell with vertices at the cell centers and the face's vertices. The Rhie and Chow [9] type pressure interpolation technique can be regarded as the most popular technique in research and practical applications [13-16]. Rahman et al. [17] proposed a pressure correction method for a SIMPLE-like algorithm on a vertex based finite volume scheme. Kang and Kim [18] developed a pressure based finite volume scheme on unstructured grid for simulating the reacting flows. Rahman et al. [17] and Kang and Kim [18] applied the Rhie and Chow [9] type pressure interpolation technique in order to obtain a smooth pressure field.

Date [19] has innovated a method for structured grids through the argument that the total pressure correction is in fact a sum of the smoothing and mass conserving pressure corrections. Date [8] has compared this method with Rhie and Chow's [9] momentum interpolation technique and perceived the main difference in the way the pressure gradients were interpolated into the cell face. In Rhie and Chow's [9] method, the pressure gradients were one-dimensionally interpolated while in Date's [19] method a multidimensional averaging was performed. Date's [19] method was later extended to unstructured grids [5, 20].

Touazi et al. [21] have developed a collocated finite volume scheme for incompressible flows on so-called "admissible" unstructured meshes. One of the main difficulties in this method was writing an accurate diffusion approximation. Chenier et al. [22] have developed a new scheme for diffusion terms on general non-conforming grids. Because of restrictions imposed on the grid, this method still has some practical limitations; for more details, see [22].

In this article, the mass conserving velocity at the cell face is obtained through Rhie and Chow [9] type pressure interpolation technique. This velocity, however, does not guarantee a perfectly smooth pressure field. In order to have a smoother pressure field a new concept, Local Triangle (LT), is defined as a triangle containing a triangular cell and its neighboring cells. When the polygon formed by a triangular cell and its neighboring cells is not a triangle, it is called a distorted LT. When there is no distorted LT in the grid, it is indicated that the checkerboard oscillations cannot appear. According to this finding, a Multi-Block Local Triangulation (MBLT) method is devised so that the customary unstructured triangular grid can be considered as a level zero MBLT. In level n MBLT method, an initial triangular cell is divided into $(n + 1)$ levels of triangular cells from level 0 to n, respectively. These smaller cells have the same geometry and, in turn, are similar to the initial cell. A MBLT of any level but more than zero establishes some appropriate LTs into the grid and, as a result, a smoother pressure field can be expected. The performance of MBLT of several levels is then investigated in order to find the best choice.

Since the momentum equations are under-relaxed by general relaxation factor, ω, Date [8] has argued that, in order to have a ω-independent solution, the Rhie and Chow [9] pressure correction term has to be under-relaxed with ω. Ferziger and Peric [6] have maintained that, the difference in the two solutions obtained using different ω is much smaller than the discretization error and, in turn, there is little reason for concern. However, Ferziger and Peric [6] have only discussed the effect of ω on a_0^u. Since in this article Rhie and Chow [9] type pressure interpolation technique is utilized, a hypothesis is established about the proper choice of relaxation factor. It is illustrated that this relaxation factor cannot be ω, and the relaxation factor independency of solutions is then numerically investigated.

If at a cell the magnitude of checkerboard oscillation relative to the gage pressure or pressure gradient increases with Cell Reynolds number, a higher relative oscillation will be expected in turbulent flow (Assuming the same geometry and, that in turbulent flow the Cell Reynolds

number is also increased. This means, there is no circulating zone near the point where the checkerboard oscillation is observed.). In this article, the effect of Cell Reynolds number on the magnitude of checkerboard oscillations is investigated, and it is demonstrated that the checkerboard oscillations are more significant at higher Cell Reynolds numbers. As a result, the numerical simulations are mainly performed in turbulent flow.

The remainder of this article is divided into five sections. In the first section, the relevant details of the developed numerical tool, Shallow Fluent, are presented. These are the dimensionless conservative form of the governing equations, and their discretized form. The theory behind LT and MBLT method are presented in the second section. The third section is devoted to the validation of Shallow Fluent. The fourth section presents the numerical results which are validations for LT concept, and performance analysis for MBLT method.

3.2.3 Details in Shallow Fluent

Shallow Fluent is developed for the 2D and 2D depth averaged simulations. In this section, only the relevant details will be presented.

3.2.3.1 Governing equations

The governing equations for 2D simulation of incompressible flow are continuity and momentum equations. Their dimensionless conservative vector forms can be given by:

$$\boldsymbol{\nabla}.\boldsymbol{u} = 0 \tag{3.1}$$

$$\frac{\partial \boldsymbol{u}}{\partial t} + \boldsymbol{\nabla}.(\boldsymbol{u}\boldsymbol{u}) = -\boldsymbol{\nabla}P + \frac{1}{R_e}\boldsymbol{\nabla}.\left((1+\mu_t)\boldsymbol{\nabla}\boldsymbol{u}^T\right) \tag{3.2}$$

where, $\boldsymbol{u} = \boldsymbol{u}^*/U_{ref}$, $t = t^*U_{ref}/L_{ref}$, $R_e = \rho^*U_{ref}l_{ref}/\mu^*$, $\mu_t = \mu_t^*/\mu^*$, and $P = \left(P^* - P_{ref}\right)/\left(\rho^*U_{ref}^2\right)$.

In Shallow Fluent, when a turbulent flow has to be simulated, the standard $k - \varepsilon$ model is utilized. In the case of laminar flow, the μ_t in Equation (3.2) is left at zero. The dimensionless conservative form of k and ε equations are given by:

$$\frac{\partial k}{\partial t} + \boldsymbol{\nabla}.(k\boldsymbol{u}) = \frac{1}{R_e}\boldsymbol{\nabla}.\left(\left(1+\frac{\mu_t}{\sigma_k}\right)\boldsymbol{\nabla}k\right) + S_k \tag{3.3}$$

$$\frac{\partial \varepsilon}{\partial t} + \nabla.(\varepsilon \boldsymbol{u}) = \frac{1}{R_e} \nabla.\left(\left(1 + \frac{\mu_t}{\sigma_\varepsilon}\right)\nabla \varepsilon\right) + S_\varepsilon \tag{3.4}$$

where $S_k = (G - \varepsilon)$, and $S_\varepsilon = (C_{\varepsilon 1} G \varepsilon/k - C_{\varepsilon 2} \varepsilon^2/k)$. G is given by:

$$G = \frac{\mu_t}{R_e}\left[\left(\frac{\partial u}{\partial y} + \frac{\partial v}{\partial x}\right)^2 + 2\left(\frac{\partial u}{\partial x}\right)^2 + 2\left(\frac{\partial v}{\partial y}\right)^2\right] \tag{3.5}$$

The dimensionless eddy viscosity, μ_t, is expressed as:

$$\mu_t = C_\mu R_e \frac{k^2}{\varepsilon} \tag{3.6}$$

where $k = k^*/U_{ref}^2$, $\varepsilon = \varepsilon^*/(U_{ref}^3/L_{ref})$, and model's constants are $C_\mu = 0.09$, $C_{\varepsilon 1} = 1.44$, $C_{\varepsilon 2} = 1.92$, $\sigma_k = 1.0$ and $\sigma_\varepsilon = 1.3$.

3.2.3.2 Discretized equations

Shallow Fluent uses the SIMPLE algorithm for the coupling between pressure and velocity field. In the SIMPLE algorithm, the continuity equation [Equation (3.1)] is converted into a pressure correction equation. With an initial guess pressure and velocity fields, momentum equations will be solved. The derived velocity field then will be used in a pressure correction equation. The obtained pressure correction modifies pressure and velocity field, other scalars if there are any will be solved, and the solution continues in the next iteration until convergence is attained. The correction to pressure and velocity at any cell is given by:

$$P = \ddot{P} + P' \tag{3.7}$$

$$\boldsymbol{u} = \ddot{u} - \frac{\Omega}{a_0^u}\nabla P' \tag{3.8}$$

In this article convective terms are discretized with the first order upwind scheme, Green's theorem is used for the calculation of the gradient at cell center, and the two point method for the calculation of gradient at cell face. The discretized pressure correction equation then can be expressed as:

$$a_0^P P_0' = \sum_{j=1}^3 a_j^P P_j' - \vartheta^\circ \tag{3.9}$$

$$a_j^P = \frac{s_j}{2h_{c_{0-}c_j}}\left[\left(\frac{\Omega}{a_0^u}\right)_0 + \left(\frac{\Omega}{a_0^u}\right)_j\right] \tag{3.10}$$

$$a_0^P = \sum_{j=1}^{3} a_j^P \tag{3.11}$$

The discretized equation for the conserved variable, φ, in a triangular grid can be written as:

$$a_0^\varphi \varphi_0 = \sum_{j=1}^{3} a_j^\varphi \varphi_j + S_{u_\varphi} \tag{3.12}$$

$$a_0^\varphi = \sum_{j=1}^{3} \left[\!\left[C_{S_j}, 0 \right]\!\right] + \frac{1}{R_e} \sum_{j=1}^{3} \left(\frac{(1+\mu_t/\chi)_{s_j} s_j}{h_{c_0\_c_j}} \right) - S_{p_\varphi} \tag{3.13}$$

$$a_j^\varphi = \left[\!\left[-C_{S_j}, 0 \right]\!\right] + \frac{(1+\mu_t/\chi)_{s_j} s_j}{R_e h_{c_0\_c_j}} \tag{3.14}$$

where, $\left[\!\left[C_{S_j}, 0 \right]\!\right]$ denotes the maximum of C_{S_j} and 0, and χ can be 1.0, σ_k, or σ_ε. Figure 3.1 depicts the geometrical notations.

The Rhie and Chow [9] pressure interpolation technique is applied in order to obtain a mass conserving velocity at the cell face. In Shallow Fluent, the cell face velocities are not linearly interpolated; instead, a momentum-weighted averaging is performed [23]. The utilized Rhie and Chow [9] type pressure interpolation method in laminar and turbulent flows are different from each other. For laminar flow the most used form of the Rhie and Chow [9] type method is utilized [8, 10-12]. In this method the continuity residual can be given by:

$$\vartheta^\circ = \sum_{j=1}^{3} \left\{ \frac{(u a_0^u)_0 + (u a_0^u)_j}{(a_0^u)_0 + (a_0^u)_j} \cdot \mathbf{s}_j + \frac{\omega_{rc} \Omega_{s_j}}{(a_0^u)_{s_j}} \left[\left(\frac{\nabla P_0 + \nabla P_j}{2} \right) \cdot \mathbf{s}_j - \frac{s_j}{h_{c_0\_cj}} (P_j - P_0) \right] \right\} \tag{3.15}$$
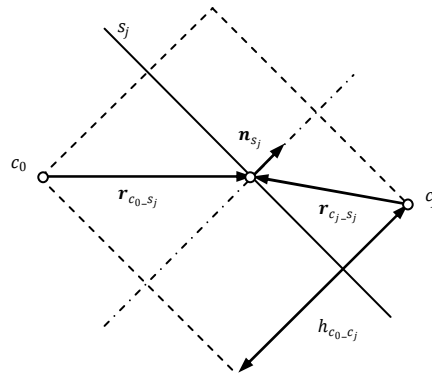
Figure 3.1. Geometrical notations used in discretized equations relevant to a cell and its immediate neighbors: central cell, c_0, neighboring cell, c_j, cell face, s_j, unit vector normal to the cell face, $\mathbf{n}_{s_j}$, distance vector, $\mathbf{r}$, and normal distance between cell centers, $h_{c_0\_c_j}$.

where, Ω_{s_j} is the volume of a quadrilateral cell with vertices on the cells' center (c_0 and c_j in Figure 3.1) and the face's vertices (the vertices of s_j). For the turbulent flow continuity residual is expressed as:

$$\vartheta^{\circ} = \sum_{j=1}^{3} \left\{ \frac{(ua_0^u)_0 + (ua_0^u)_j}{(a_0^u)_0 + (a_0^u)_j} \cdot \mathbf{s}_j - \omega_{rc} a_j^P (P_j - P_0) \right\} \tag{3.16}$$

When Equation (3.16) is used instead of Equation (3.15), convergence rate increases. Since there is a stronger mathematical reasoning behind Equation (3.16), it will be derived. For incompressible flow, continuity residual can be expressed as:

$$\vartheta^{\circ} = \sum_{j=1}^{3} \mathbf{u}_{s_j} \cdot \mathbf{s}_j \tag{3.17}$$

From the momentum equation, the following expression can be derived for velocity:

$$\mathbf{u}_0 = \frac{\sum_{j=1}^{3} a_j^u u_j + (S_{u_u} - S_{u\_P})}{a_0^u} + \frac{S_{u\_P}}{a_0^u} \tag{3.18}$$

The first term in the right hand side of Equation (3.18) is called $\hat{\mathbf{u}}_0$. So, Equation (3.18) can be rewritten as:

$$\mathbf{u}_0 = \hat{\mathbf{u}}_0 + \frac{s_{u\_p}}{a_0^u} \tag{3.19}$$

If pressure gradient is assumed constant throughout the cell, the pressure source term can be expressed as:

$$\mathbf{s}_{u\_p} = -\int_{\Omega_0} \nabla P d\Omega \approx -\nabla P \Omega_0 \tag{3.20}$$

After replacing Equation (3.20) into Equation (3.19), Equation (3.19) is rewritten as:

$$\mathbf{u}_0 = \hat{\mathbf{u}}_0 - \frac{\Omega_0}{a_0^u} \nabla P \tag{3.21}$$

The interpolated cell face velocity is given by:

$$\mathbf{u}_{s_j} = \frac{1}{2} (\mathbf{u}_0 + \mathbf{u}_j) \tag{3.22}$$

When Equation (3.21) is replaced into Equation (3.22), the cell face velocity can be given by:

$$\mathbf{u}_{s_j} = \frac{1}{2} (\hat{\mathbf{u}}_0 + \hat{\mathbf{u}}_j) - \frac{1}{2} \left[\Omega_0 \left(\frac{\nabla P}{a_0^u} \right)_0 + \Omega_j \left(\frac{\nabla P}{a_0^u} \right)_j \right] \tag{3.23}$$

After replacing Equation (3.23) into Equation (3.17), the following expression will be derived for continuity residual:

$$\vartheta^\circ = \frac{1}{2}\sum_{j=1}^{3}\left\{(\hat{\boldsymbol{u}}_0 + \hat{\boldsymbol{u}}_j)\cdot\boldsymbol{s}_j\right\} - \frac{1}{2}\sum_{j=1}^{3}\left\{\left[\Omega_0\left(\frac{\boldsymbol{\nabla}P}{a_0^u}\right)_0 + \Omega_j\left(\frac{\boldsymbol{\nabla}P}{a_0^u}\right)_j\right]\cdot\boldsymbol{s}_j\right\} \tag{3.24}$$

When $\boldsymbol{s}_j = \boldsymbol{n}_j s_j$ is replaced into the last term of Equation (3.24), the pressure gradient normal to the cell face will be obtained.

$$\vartheta^\circ = \sum_{j=1}^{3}\left\{\left(\frac{\hat{\boldsymbol{u}}_0 + \hat{\boldsymbol{u}}_j}{2}\right)\cdot\boldsymbol{s}_j\right\} - \sum_{j=1}^{3}\left\{\left[\left(\frac{\Omega}{2a_0^u}\right)_0\left(\frac{\partial P}{\partial n}\right)_0 + \left(\frac{\Omega}{2a_0^u}\right)_j\left(\frac{\partial P}{\partial n}\right)_j\right]\cdot s_j\right\} \tag{3.25}$$

The first summation in the right hand side of Equation (3.25) is uncorrected flux. This term is the first term in the right hand side of Equation (3.16), but derived with arithmetic averaging. When the pressure gradient at the central cell, c_0, is expanded with forward Taylor's series, and the pressure gradient at the neighboring cell, c_j, is expanded with backward Taylor's series, the second term in the right hand side of Equation (3.16) will be derived.

3.2.3.3 Boundary conditions

The employed boundary conditions are the velocity inlet, the constant pressure boundary, and the no-slip wall condition. Variables have to be known at the inlet. In the constant pressure boundary condition, it is assumed that the gradient of variables is zero. Exceptions are velocity components and pressure. Following Versteeg and Malalasekera [7], in order to derive the velocity components, mass is locally conserved at the cells adjacent to the constant pressure boundary. Pressure is fixed at the boundary's adjacent cells. In a laminar flow, velocity is exactly set to its specified value on the wall. For a turbulent flow the standard wall function approach [24] is applied to the momentum and turbulence model equations.

3.2.3.4 Residuals

In the third and fourth sections, residuals are calculated in two different ways: the scaled residual, and the normalized residual. The continuity residual is given by:

$$\vartheta_R = \frac{\sum_{i=1}^{N_{cell}}|\vartheta^\circ|}{\vartheta_{ref}^\circ} \tag{3.26}$$

For a scaled error, $\overset{\circ}{\vartheta}_{ref}$ is $[\![1, \Omega_d]\!]$ when there is no inlet, and $\overset{\circ}{\vartheta}_{in}$ when there is an inlet. For a normalized error $\overset{\circ}{\vartheta}_{ref}$ is the largest absolute value of the continuity residual in the first five iterations. The residual for any conserved variable, φ, is expressed as:

$$R_\varphi = \frac{\sum_{i=1}^{N_{cell}}\left|\sum_{j=1}^{3} a_j^\varphi \varphi_j + s_{u_\varphi} - a_0^\varphi \varphi_0\right|}{R_{ref}} \tag{3.27}$$

where, for scaled errors $R_{ref} = \sum_{i=1}^{N_{cell}}\left|a_0^\varphi \varphi_0\right|$, and for normalized errors R_{ref} is the largest absolute value of the φ residual in the first five iterations.

3.2.4 LT and MBLT

It is demonstrated through the LT (Local Triangle) concept that, in a triangular grid with perfect LTs, the pressure oscillation has fewer degrees of freedom; i.e. compared with a quadrilateral grid, the checker board pressure field in a triangular grid is much more restricted. The idea of establishing such perfect LTs in a triangular grid then led to the MBLT (Multi-Block Local Triangulation) method.

3.2.4.1 LT concept

A LT is a triangle which contains a central cell and its neighboring cells. When these four cells do not make a triangle, the LT is called distorted. In order to illustrate the LT concept, the central cell is numbered with 4 and its neighboring cells with 1 to 3. When momentum equations are integrated over the central cell, number 4, the application of Green's theorem gives the following expression for the pressure gradient:

$$(\nabla P)_4 = \frac{\left(\frac{P_1+P_4}{2}s_1 + \frac{P_2+P_4}{2}s_2 + \frac{P_3+P_4}{2}s_3\right)}{\Omega_4} \tag{3.28}$$

In a derivation of Equation (3.28), it is assumed that the triangles are equilateral and, in turn, make a perfect LT. s_j, with $j = 1, 2, 3$, is the face area vector. After decomposition, the pressure gradient can be given by:

$$(\nabla P)_4 = \frac{\left(\frac{P_1}{2}s_1 + \frac{P_2}{2}s_2 + \frac{P_3}{2}s_3 + \frac{P_4}{2}(s_1+s_2+s_3)\right)}{\Omega_4} \tag{3.29}$$

In Equation (3.29) the summation at the inner bracket is always zero; i.e. the pressure of central cell, 4, does not appear in the expression for pressure gradient. When the pressure gradient is zero, Equation (3.29) reduces to the following equation:

$$\frac{P_1}{2}\boldsymbol{s}_1 + \frac{P_2}{2}\boldsymbol{s}_2 + \frac{P_3}{2}\boldsymbol{s}_3 = 0 \tag{3.30}$$

Since for any triangle $\boldsymbol{s}_1 = -\boldsymbol{s}_2 - \boldsymbol{s}_3$, Equation (3.30) can be written as:

$$\left(\frac{P_2}{2} - \frac{P_1}{2}\right)\boldsymbol{s}_2 + \left(\frac{P_3}{2} - \frac{P_1}{2}\right)\boldsymbol{s}_3 = 0 \tag{3.31}$$

$\boldsymbol{s}_2$ and $\boldsymbol{s}_3$ has not the same direction and, as a result, the only possibility is:

$$P_1 = P_2 = P_3 \tag{3.32}$$

(a)   (b)   (c)
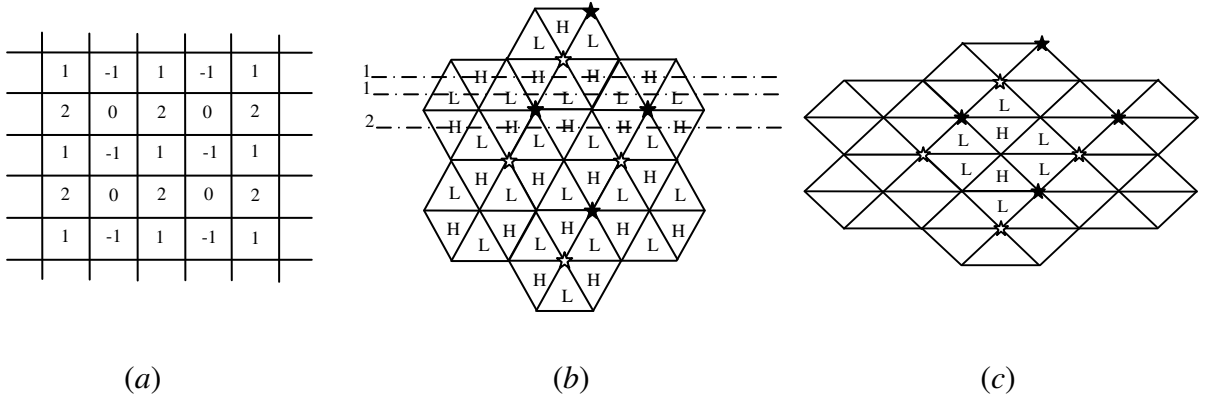
Figure 3.2. Sketch of checkerboard pressure fields in collocated grids; (a) in quadrilateral cells [6], (b) in equilateral triangles, and (c) in quad-split triangles.

Figure 3.2a depicts a possible checkerboard pressure field in a quadrilateral grid. In Figure 3.2-b the only possible checkerboard oscillation in a triangular grid with perfect LTs is sketched. A comparison between Figure 3.2-a and Figure 3.2-b demonstrates that the checkerboard oscillations in a triangular grid with perfect LTs are more restricted. The checkerboard pressure field in Figure 3.2-b is the only possibility. In Figure 3.2-b Points of high/low pressures lying on dash-dote lines have to be the same. If not, a pressure gradient will exist.

It can be indicated from Figure 3.2-b that in every perfect LT the possible checkerboard oscillation is a low/high pressure at the central cell and high/low pressures at the neighboring cells and, in turn, the simplest local oscillation is spherical. When LTs gradually deviate from a

perfect LT, the checkerboard pressure field gradually deviates from its spherical shape, so that the most stable checkerboard system forms. In Figure 3.2-*c* a quad-split grid is sketched. In this figure every two LTs make a square. These two LTs are called neighboring LTs. When the neighboring LTs make a square, a spherical checkerboard oscillation must exist at the square, rather than a single LT (in Figure 3.2-*c* any circle lying on every three *L* points will necessarily lie on the rest of the *L* points in the relevant square). In Figure 3.2-*c* one of these squares is marked with bright stars. Another spherical checkerboard oscillation can exist in a square marked with dark stars (Figure 3.2-*c*). Obviously, the only possibility is that the high and low pressures in Figure 3.2-*c* are the same. It demonstrates that a quad-split grid also imposes a restriction on the checkerboard system.

In Section 3.2.6, it will be shown through numerical simulations that the $\nabla P = 0$ is a necessary criterion for the existence of checkerboard oscillations in a grid with perfect LTs or quad-split grids.

3.2.4.2 MBLT method

If LTs restrict the checkerboard oscillations, establishing such structures into the grid must result in a smoother pressure field. In Figure 3.3 a level four MBLT triangulation is sketched. In this figure an initial triangular cell is divided into five levels of triangular cells. These smaller cells have the same geometry and, in turn, are similar to the initial cell. The sketch of a level n MBLT is same as the sketch of the first n level in a level $(n + 1)$ MBLT. The number of the cells in a level n MBLT can be given by:

$$N_{cell\_MBLT} = f(n) \times N_{cell} \tag{3.33}$$
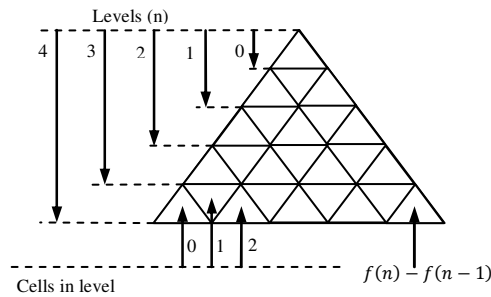
Figure 3.3. A level four MBLT triangulation.

$f(n)$ is a recursive function, expressed as:

$$f(n) = 2(f(n-1) + 1) - f(n-2) \tag{3.34}$$

where, $f(-1) = 0$ and $f(0) = 1$. The Number of the boundary cells can be given by:

$$N_{bcell\_MBLT} = (n+1) \times N_{bcell} \tag{3.35}$$

The number of the nodes can be given by:

$$N_{node\_MBLT} = \left(n + g(n)\right) \times N_{cell} + \frac{n \times (N_{cell} + N_{bcell})}{2} + N_{node} \tag{3.36}$$

$g(n)$ is a recursive function, expressed as:

$$g(n) = (n-1) + g(n-1) \tag{3.37}$$

where, $g(0) = 0$ and $g(1) = 0$.

A MBLT of any level but more than zero establishes some appropriate LTs into the grid and, as a result, a smoother pressure field is expected. In comparison with Figures 3.2-*a* and 3.2-*b*, such a MBLT has two weak regions: where the cell faces of the initial triangular grid exist, and where the vertices of the initial triangular grid exist. In the second weak region the worst distorted LTs are expected. In order to be practical, MBLT must satisfy two main criteria: applicable when the grid is clustered or stretched, and applicable to complicated structures.

3.2.5 Validation of solver

In this section, Shallow Fluent will be validated for laminar and turbulent flows. More validation tests are available in [25].

3.2.5.1 Steady laminar lid-driven cavity

The domain is a square with length $H = 1m$. The boundary conditions contain the upper moving wall, the sides and the lower fixed walls. The upper wall velocity, U_w, is set to unity. On the other walls the no-slip boundary condition is applied. The grid is 20 by 20 on the domain boundaries. Flow Reynolds number is 400, where $L_{ref} = H$ and $U_{ref} = U_w$. Errors are scaled, and the convergence criterion is set to 10^{-3}. Figures 3.4-*a* and 3.4-*b* show the computed longitudinal and transverse velocity profiles. Velocity profiles are in good agreement with the

numerical data of Ghia et al. [26]. The numerical solution of Ghia et al. [26] is related to a 128 by 128 structured grid, and is considered to be the exact solution to the problem. The structured grid, applied by Nobari et al. [2], is coarser and, in turn, the predicted velocity profiles in the structured grid are less developed. The profiles of the pressure coefficient simulated by the present solver and Fluent are also in perfect agreement (Figure 3.4-*c*).

(*a*)   (*b*)   (*c*)
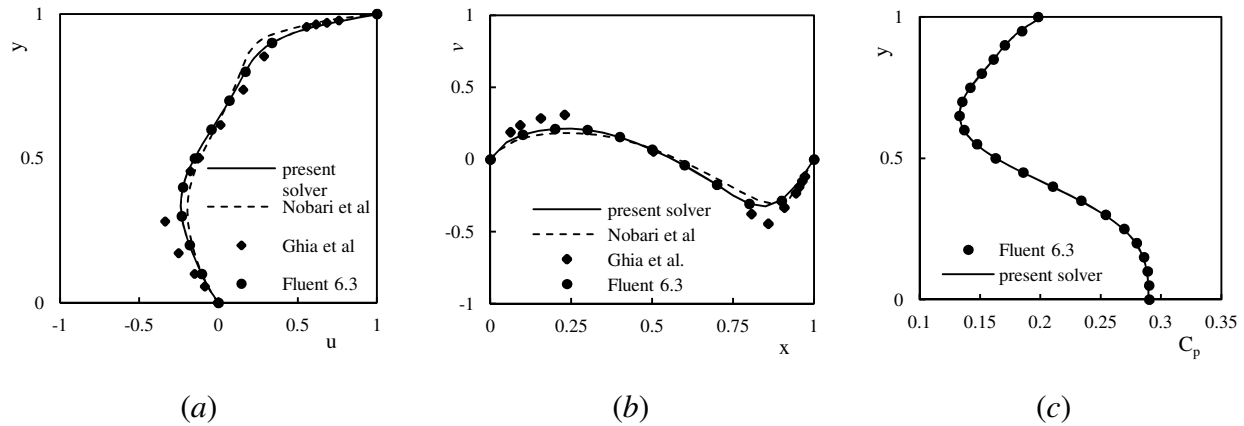
Figure 3.4. Profiles of velocity and pressure coefficient in a laminar lid driven cavity; (*a*) longitudinal component of velocity vector at $x = 0.5$, (*b*) transverse component of velocity vector at $y = 0.5$, and (*c*) pressure coefficient at $x = 0.5$.

3.2.5.2 2D turbulent duct

The computational domain is rectangular, with $L = 5m$ and $H = 1m$. There are two blocks of fluid which are separated with a straight transverse line at $x = 4$ from the inlet. The applied boundary conditions are: velocity inlet with uniform normal velocity, the constant pressure at the outlet, and a no-slip boundary condition on the walls. The grid is 10 by 50 on the domain boundaries. Blocks of fluid are separately meshed, but they are connected at their common interface. Flow Reynolds number is 4410, where $L_{ref} = H$, $U_{ref} = U_{in} = 4.41\,m/s$, and U_{in} is the inlet velocity. The fluid can be assumed SAE30 oil with the specific gravity and dynamic viscosity of $1000\,kg/m^3$ and $1.0\,N.m/s^2$ at $10\,^{0}C$. Errors are scaled, and the convergence criterion is set to 10^{-3}.
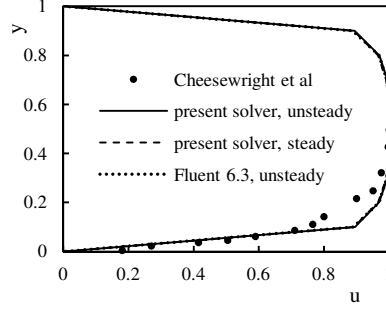
Figure 3.5. Profiles of longitudinal velocity in a 2D turbulent duct at $R_e = 4410$.
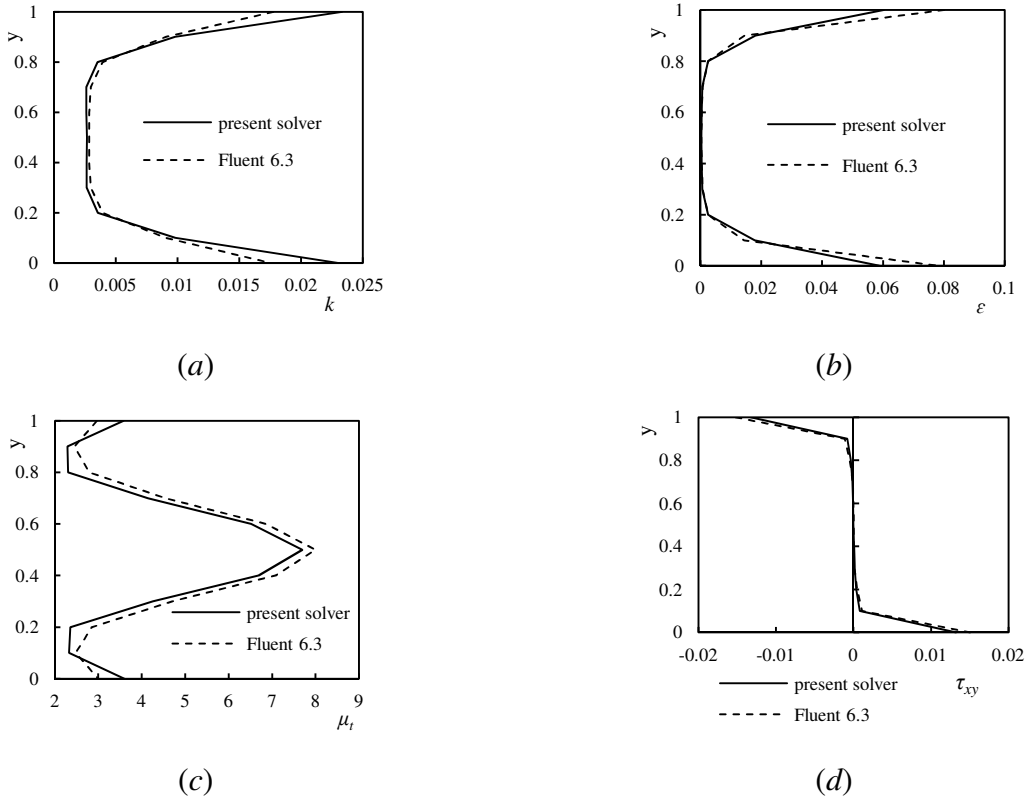
Figure 3.6. Comparison of turbulence related quantities between present solver and Fluent 6.3; (*a*) turbulence kinematic energy, (*b*) turbulence dissipation rate, (*c*) eddy viscosity, and (*d*) tangential stress.

In Figure 3.5, profiles of longitudinal velocity are compared. The numerical solution of the present solver and Fluent match exactly, and they are in good agreement with the experimental data of Cheesewright et al. [27]. When a momentum interpolation technique is applied, it is likely to have discretization dependent solutions [4]. A situation which demands care is the

discretization of transient source terms in an unsteady flow [4]. Figure 3.5 clearly indicates that with the present solver, the numerical results of steady and unsteady solutions are exactly similar.

In Figure 3.6 the turbulence related quantities simulated with the present solver and Fluent are compared. Profiles of turbulence kinematic energy, k, turbulence dissipation rate, ε, eddy viscosity, μ_t, and tangential stress, τ_{xy}, simulated with the present solver and Fluent are in good agreement, respectively.

(a)

(b)

(c)
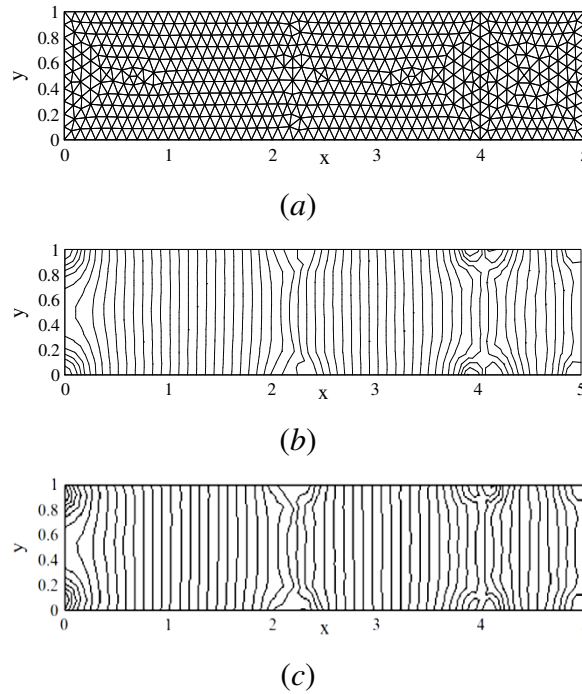
Figure 3.7. Contours of pressure coefficient in a 2D turbulent duct at $R_e = 4410$; (a) the unstructured triangular grid, (b) present solver, and (c) Fluent 6.3 software.

Figure 3.7 compares the contours of the pressure coefficient. The pressure fields simulated with the present solver and Fluent are similar. Oscillations in pressure fields can be observed in two regions: near the longitudinal position at $x = 2.25$, and at $x = 4$. The worst checkerboard oscillation occurs at the second region, where two blocks of fluid meet. The reason behind this oscillation will be discussed in section 3.2.6.

3.2.6 Numerical results

In the first test case of this section, a relaxation factor independent solution is sought. The effects of Cell Reynolds number on the magnitude of checkerboard oscillations are investigated in the second test case. In Section 3.2.4, it was illustrated that a grid with perfect LTs or quad-split grids impose some restrictions on the checkerboard system. The rest of this section is paid to indicate, through numerical simulations, that the restrictions such grids impose are satisfactory enough for a smooth pressure field.

3.2.6.1 Steady laminar lid-driven cavity

Since the momentum equations are under-relaxed, the pressure correction to the cell face velocity has to be under-relaxed [8]. The under-relaxed velocity can be given by: $\boldsymbol{u} = \boldsymbol{u}_{old} + \omega \Delta \boldsymbol{u}$. The new velocity field is multiplied by ω, and the old one with $(1 - \omega)$. The same will apply to the pressure gradients; i.e. the new pressure field is multiplied by ω and the old one with $(1 - \omega)$. It suggests that the relaxation factor in Rhie and Chow's [9] pressure correction, ω_{rc}, has to consider both ω and $(1 - \omega)$. When a solution is converged, there will be no difference between the pressure field in the current and the previous iterations and, in turn, the most meaningful magnitude for ω_{rc} according to the already available pressure field (since the pressure field in the previous iteration is not stored) is one.

Figure 3.8 indicates the effect of ω_{rc} on velocity and pressure fields. Details of the physical domain are similar to those of the test case in Section 3.2.5.1. ω_{rc} has no effect on velocity field (Figure 3.8-a), but its effect on the pressure field is obvious (Figure 3.8-b). In Figures 3.8-a and 3.8-b $\omega = \omega_{rc}$ is applied. Figure 3.8-b indicates that in Fluent software $\omega_{rc} = 0.5$ has been assumed. In the rest of this article, in order to have a meaningful comparison, when results are compared with Fluent, ω_{rc} is set to 0.5. In Figure 3.8-c profiles of pressure coefficient for different ω are compared. In this figure ω_{rc} is set to one, errors are scaled, and the convergence criterion is set to 10^{-3}. Profiles of pressure coefficient in Figure 3.8-c do not exactly match. In order to fix ω_{rc} to one it was assumed that the pressure field in the current iteration is a good approximation of the pressure field in the previous iteration. This assumption demands a strict criterion for mass conservation. In Figure 3.8-d the convergence criterion is set to 10^{-4} and, in turn, a ω_{rc} independent solution is obtained.

3.2.6.2 Steady 2D laminar duct

Details of the physical domain are similar to those of the test case in Section 3.2.5.2 The grid is 10 by 50 on the domain boundaries. The flow Reynolds number is 100, and $U_{in} = 1.0\,m/s$. Errors are scaled, and the convergence criterion is set to 10^{-3}. In a 2D duct with constant inflow and on the same grid, when there is no circulating zone, a change in fluid property can cause an increase in cell and flow Reynolds number. Thus, an increase in flow Reynolds number is equivalent to an increase in Cell Reynolds number. When the flow/Cell Reynolds number increases, the pressure gradient and the gage pressure in the 2D duct decrease. If the magnitude of checkerboard oscillations relative to the pressure gradient or the gage pressure increases with the Reynolds number, checkerboard oscillations are expected to be more significant in turbulent flow. Profiles of pressure coefficient at $x = 4$ from the inlet are presented in Figure 3.9. In Figures 3.9-a, 3.9-b, and 3.9-c the magnitude of oscillations are 0.01, 0.012 and 0.015, and the magnitude of the gage pressures (also absolute gradients) are 0.325, 0.6 and 2.6, respectively. These leave the relative magnitude of 0.0308, 0.02 and 0.00577 for the pressure oscillations and, as a result, higher checkerboard oscillations are expected in turbulent flow.

3.2.6.3 Steady 2D turbulent duct and quad-split grids

Details of the physical domain are similar to those of the test case in section 3.2.5.2. Errors are scaled, and the convergence criterion is set to 10^{-3}. Figure 3.10-a is related to the solution in a uniform quad-split grid. The grid is 10 by 50 on the domain boundaries. There is no oscillation in pressure field. Figure 3.10-a indicates that in a quad-split grid checkerboard oscillations cannot appear. Figure 3.10-b is related to the solution in a multi block quad-split grid. On the domain boundaries the grid is 10 by 40 from $x = 0$ to $x = 4$, and 10 by 20 from $x = 4$ to $x = 5$. The interface between blocks of fluids in Figure 3.10-b is comparable with a cell face of the initial grid in MBLT method. A small non-uniformity can be observed at $x = 4$. But, the pressure field in Figure 3.10-b is smoother than the pressure field in Figure 3.7-b. In Figure 3.10-c the grid is 10 by 50 on the domain boundaries, but clustered with the successive ratio of 1.2 toward the wall at $y = 1$. The pressure field is smooth and, in turn, in a clustered MBLT grid a smooth pressure field can be expected.
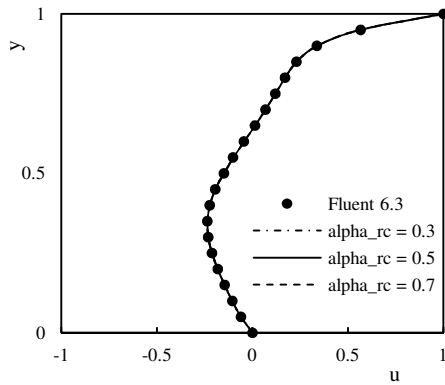
(a)
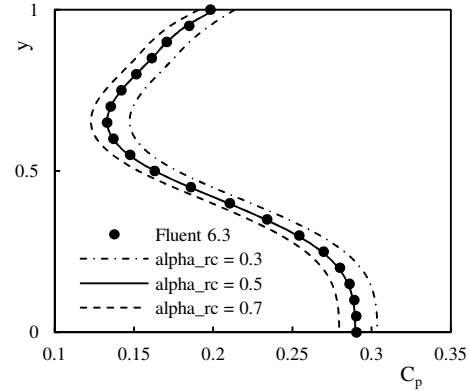
(b)
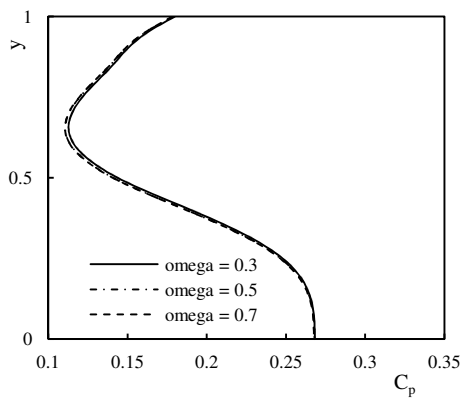
(c)
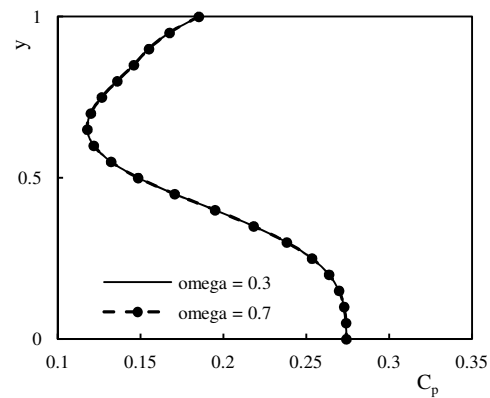
(d)

Figure 3.8. Effect of relaxation factor on velocity and pressure fields in a laminar lid driven cavity; (a) profiles of longitudinal velocity at $x = 0.5$, (b), (c) and (d) profiles of pressure coefficient at $x = 0.5$. "Omega" is the general relaxation factor, and "Omega_rc" is the relaxation factor in [9] pressure correction term. In (a), (b) and (c) the convergence criterion is set to 10^{-3}, and in (d) it is set to 10^{-4}.

In Figure 3.11 surfaces of pressure coefficient, longitudinal velocity and transverse velocity in an unstructured grid (the test case of section 3.2.5.2) and a uniform quad-split grid are compared, respectively. It can be observed in Figure 3.11-a that the checkerboard pressure has a significant effect on transverse velocity. It is also of interest that in surfaces of longitudinal and transverse velocities the checkerboard pressure causes reverse flows. Since in transverse direction there is no pressure gradient, there is no significant driving force to prevent the reverse velocities. On the
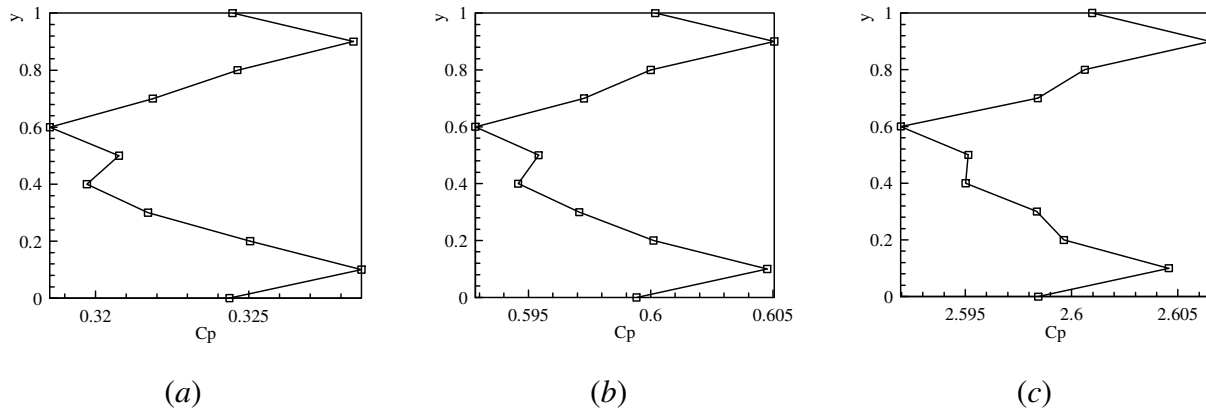
Figure 3.9. Profiles of pressure coefficient in a 2D laminar duct at $x = 4$ from the inlet; (*a*) $R_e = 100$, (*b*) $R_e = 50$, and (*c*) $R_e = 10$.
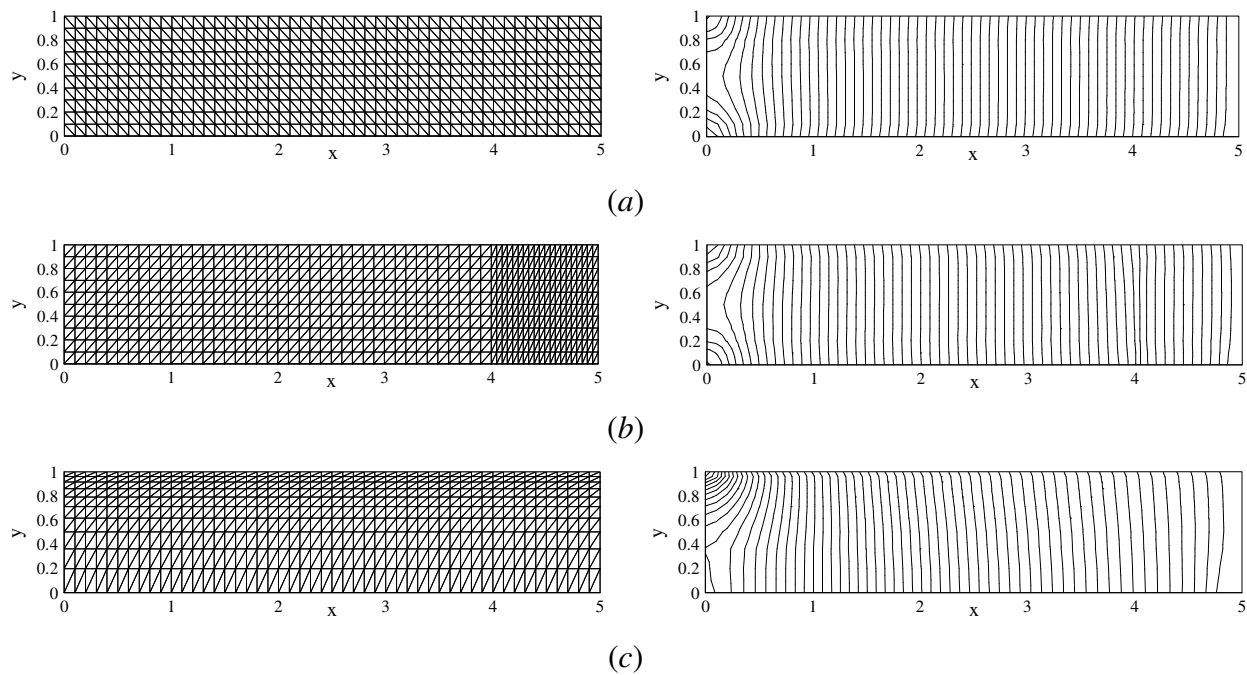
Figure 3.10. Contours of pressure coefficient in a 2D turbulent duct at $R_e = 4410$; (*a*) in a uniform quad-split grid, (*b*) in a two-block quad-split grid, and (*c*) in a non-uniform quad-split grid. The left figures are the grids and the right figures are the pressure contours.

contrary, the pressure gradient in the longitudinal direction efficiently stands the reverse velocities. This indicates that checkerboard oscillations are less likely when the pressure gradient is not zero. Even though the pressure gradient is zero in the transverse direction, the surfaces of

pressure coefficient, longitudinal velocity and transverse velocity are perfectly smooth in a quad-split grid (Figure 3.11-*b*).
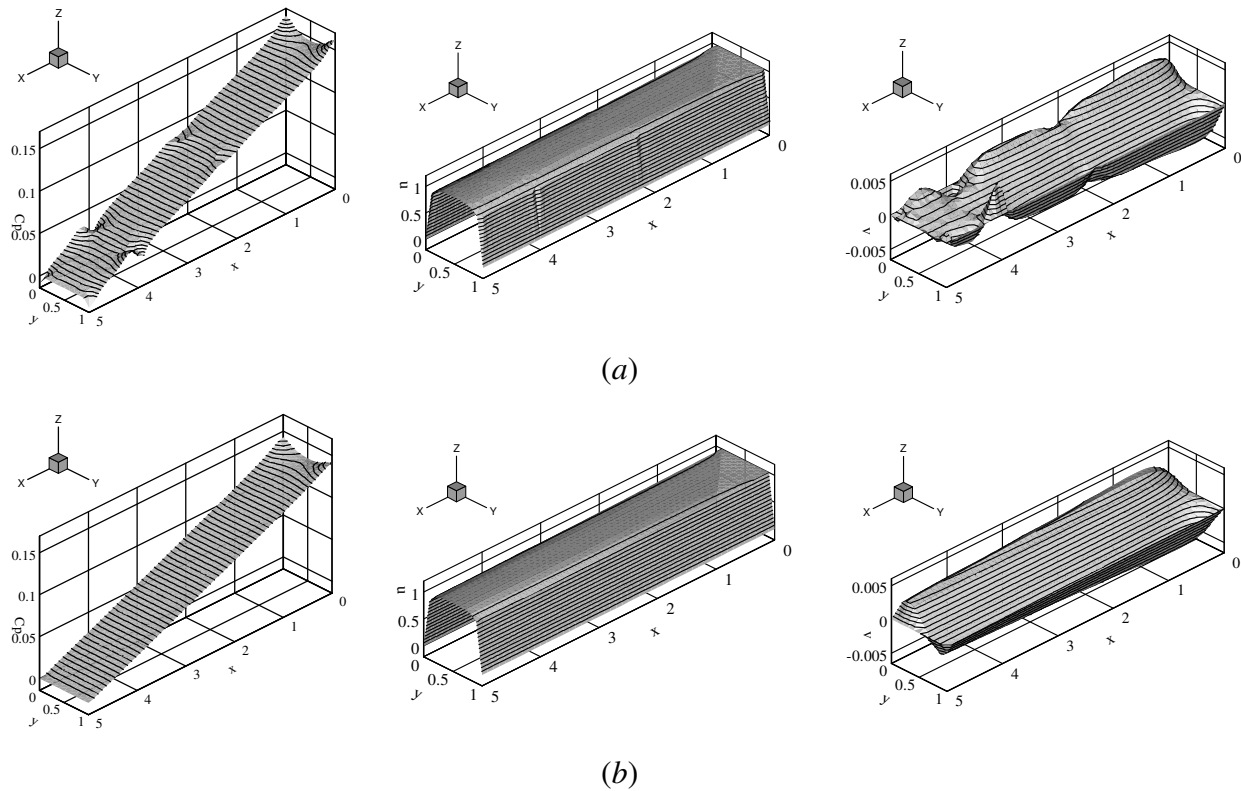
(*a*)

(*b*)

Figure 3.11. Surfaces of pressure coefficient, longitudinal velocity, and transverse velocity in a 2D turbulent duct at $R_e = 4410$; (*a*) in an unstructured grid, and (*b*) in a uniform rectangular quad-split grid. The left figures are the pressure coefficients, the middle ones are the longitudinal velocities, and the right figures are the transverse velocities.

3.2.6.4 Steady 2D turbulent bend with an internal structure

The fluid and inlet velocity are the same as in section 3.2.5.2. Domain geometry is shown in Figure 3.12: the inner curve, the outer curve, and the internal boundaries are no-slip walls. The internal structure is near the constant pressure boundary. At the inlet, flow is perpendicular to the boundary. The width of the domain at the inlet is chosen as the reference length. The Reynolds number is 4410, where $L_{ref} = 1.0m$, and $U_{ref} = U_{in} = 4.41$. Errors are scaled, and the convergence criterion is set to 10^{-3}. In Figure 3.12-*a* the domain is meshed with triangular cells, while in Figure 3.12-*b* the domain is first meshed with quadrilateral cells, then every quadrilateral cell is split into two triangular cells. The quad-split grid generated with this method (Figure 3.12-

b) has very low quality. No straight piece of line exists (except near the constant pressure boundary) in iso-pressure contours and, in turn, no checkerboard oscillation can be observed, even in Figure 3.12-*b*. This indicates that even at low quality grids (regarding the LT concept) when the pressure gradient is not zero, checkerboard oscillations are less likely.

(*a*)

(*b*)
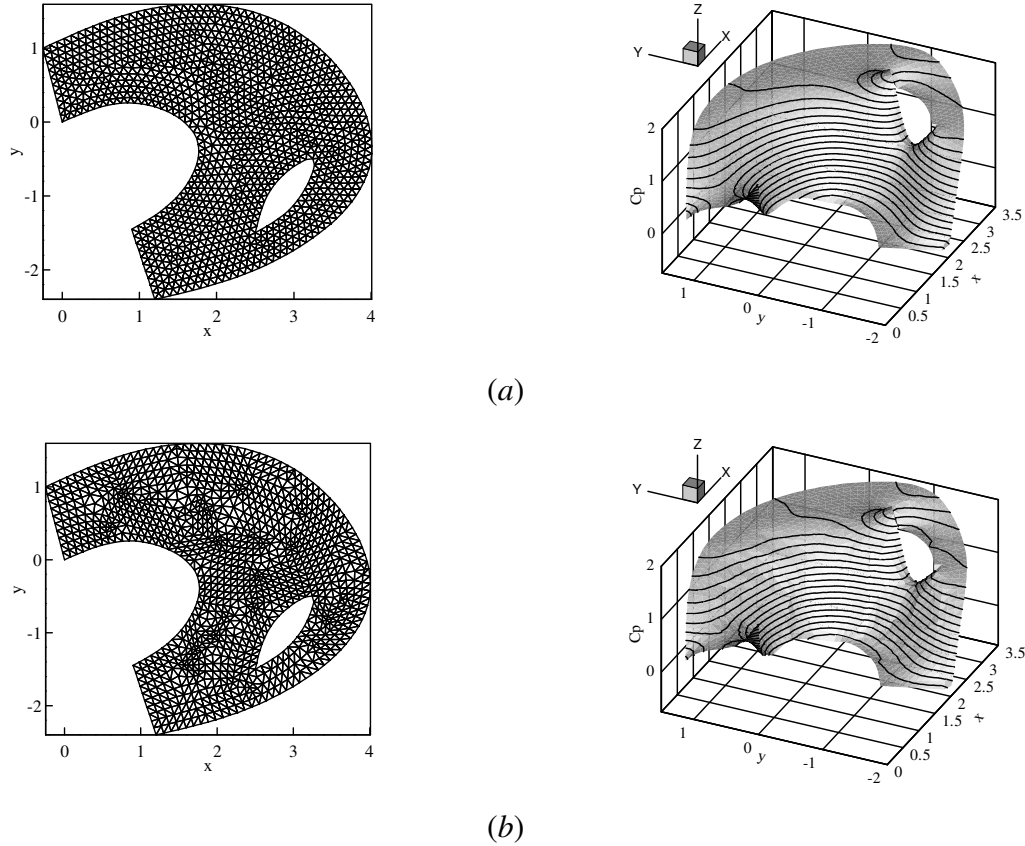
Figure 3.12. Surfaces of pressure coefficient in a 2D turbulent bend with an internal structure at $R_e = 4410$; (*a*) in a uniform unstructured grid, and (*b*) in a non-smooth quad-split grid. The left figures are the grids, and the right figures are the surfaces and the iso-pressure contours.

3.2.6.5 Steady 2D turbulent duct and MBLT grids

Details of the physical domain are similar to those of the test case in Section 3.2.5.2. Fluid is water with the specific gravity and dynamic viscosity of $998.2\ kg/m^3$ and $0.001003\ N.m/s^2$, respectively. Errors are scaled, and the convergence criterion is set to 10^{-3}. In Figure 3.13, surfaces of pressure coefficient in level zero to level two MBLT grids are compared. In level zero and level one MBLT, grids are 10 by 50 on the domain boundaries. In level two MBLT, the grid

is 9 by 48 on the domain boundaries. A checkerboard pressure field can be observed in Figure 3.13-a near $x = 2.5$. At the same longitudinal position there is no checkerboard pressure in Figure 3.13-b and 3.13-c. None of the MBLT methods can remove the checkerboard pressure at $x = 4$. Vertices of initial grids exist at $(x = 4, y = 0)$ and $(x = 4, y = 1)$, and two blocks of fluid are separated with a transverse section at $x = 4$. As a result, MBLT fails to establish nearly perfect LTs.

(*a*)   (*b*)   (*c*)
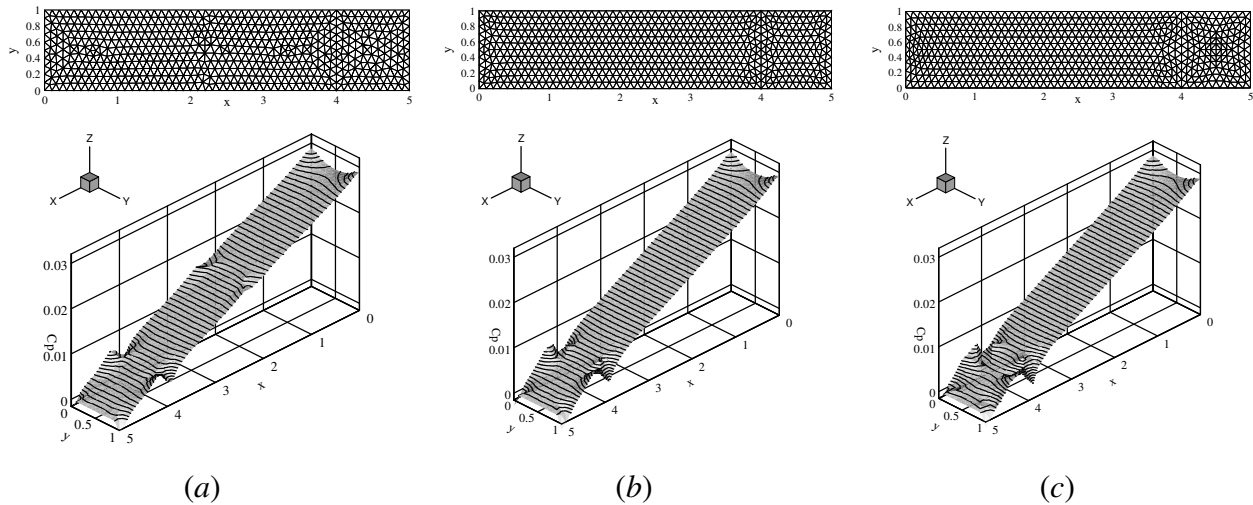
Figure 3.13. Surfaces of pressure coefficient and the iso-pressure contours in a 2D turbulent duct at $R_e = 4.39 \times 10^6$ in; (*a*) level zero MBLT (popular unstructured), (*b*) level one MBLT, and (*c*) level two MBLT grids.

Date [28] has indicated through numerical simulation in structured grids that, the finer the grid, the smoother the pressure field. In Figure 3.14-a the grid is 20 by 100 on the domain boundaries. A comparison of Figure 3.14-b and Figure 3.13-a indicates that a finer triangular grid does not necessarily result in a smoother pressure field. In Figure 3.14-a some distorted LTs exist near $(x = 4.5, y = 0)$ and, in turn, checkerboard pressure occurred in the same area in Figure 3.14-b.

In Figure 3.15-a the wall at $y = 1$ is meshed with a boundary layer quad-split grid, and the rest of the domain is meshed with a level one MBLT grid. The boundary layer grid completely removes the checkerboard oscillations at $(x = 4, y = 1)$, however the level one MBLT grid alone failed to remove the oscillations at $(x = 4, y = 0)$. Figure 3.15-b demonstrates that a level one MBLT grid, combined with a boundary layer quad-split grid on the walls, completely removes the checkerboard oscillations.
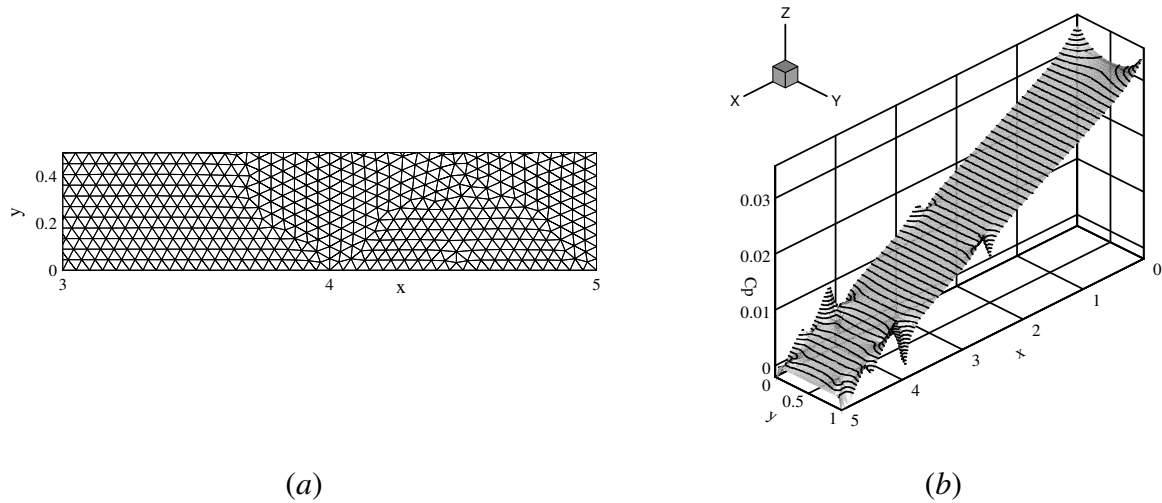
Figure 3.14. Surface of pressure coefficient and iso-pressure contours in a 2D turbulent duct at $R_e = 4.39 \times 10^6$; (*a*) the grid between $x = 3$ and $x = 5$ in half duct width, and (*b*) surface of pressure coefficient.
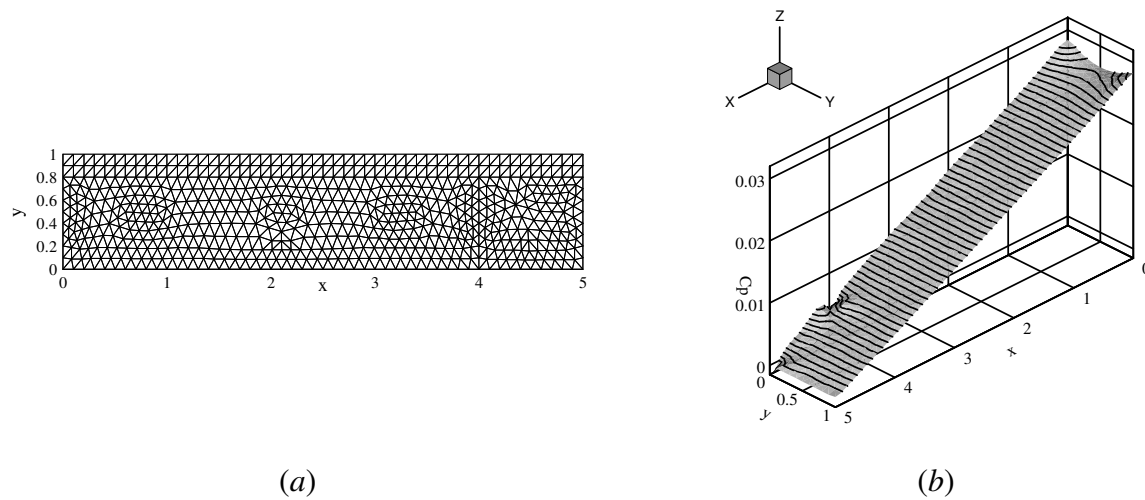
Figure 3.15. Surface of pressure coefficient and iso-pressure contours in a 2D turbulent duct at $R_e = 4.39 \times 10^6$; (*a*) a level one MBLT grid with a quad-split boundary layer grid on the wall at $y = 1$, and (*b*) surface of pressure coefficient.

3.2.6.6 Flow past a cylinder in a 2D duct

Behzadi [29] has simulated the flow around a sphere in a 3D duct at $R_e = 100$. Since Shallow Fluent is a extension of the solver developed by Behzadi [24] (extended to unsteady turbulent

flows), the numerical algorithm and the discretization schemes are almost similar. The exception is the calculation of continuity residual in the pressure correction equation. In [29] the second term on the right hand side of Equation (3.15) [or equivalently Equation (3.16)] was ignored and, in turn, the checkerboard oscillations in the pressure field were obvious. In order to investigate the performance of the level one MBLT method, the same simulation will be performed, but two dimensionally.

(*a*)

(*b*)
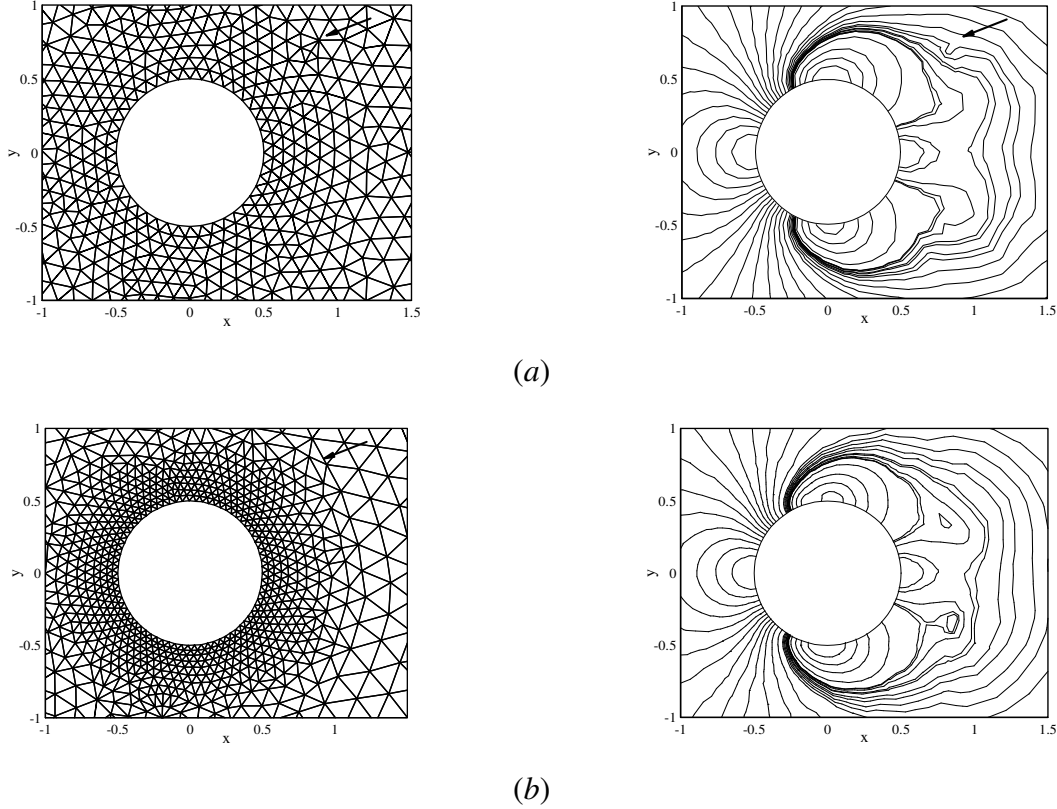
Figure 3.16. Flow past a cylinder in a 2D laminar duct at $R_e = 100$; (*a*) with regular (MBLT level zero) grid, and (*b*) with MBLT level one grid. Arrows mark the same points where an oscillation can be observed in case "*a*".

The computational domain is rectangular, with $L = 7m$ and $H = 5m$. A cylinder with unit diameter, $d_c = 1.0m$, is placed on the center line of the duct at $x = 3$ from the inlet. The applied boundary conditions are: velocity inlet with uniform normal velocity, constant pressure at the outlet, and no-slip boundary conditions on the walls. The flow Reynolds number is 100, where $L_{ref} = d_c$, $U_{ref} = U_{in} = 1.0\,m/s$. Following Behzadi [29] errors are normalized, and the

convergence criterion is set to 10^{-4}. The grid in Figure 3.16-*a* is a level zero MBLT. In Figure 3.16-*a* a region with checkerboard pressure can be observed in the pressure field. In Figures 3.16-*a* and 16*b* the same regions are marked with arrows. The grid in Figure 3.16-*b* is a level one MBLT. In order to resolve the cylinders' geometry with the same resolution, this grid is finer on the cylinder (when the boundary layer grid is applied on the cylinder, and the MBLT grid just outside the boundary layer grid, there will be no extra resolution near the cylinder. This option, however, is not still supported by Shallow Fluent). In order to have a better comparison, cells must have the same size where the pressure field in Figure 3.16-*a* oscillates, and the grid in Figure 3.16-*b* is successively stretched with this end in view. In Figure 3.16-*b*, there is no checkerboard oscillation in the region marked with arrows, and the pressure field is smoother than Figure 3.16-*a*.

3.2.7 Conclusion

In order to obtain a mass conserving velocity at the cell face, the cell face velocity is corrected with a pressure correction term. It is demonstrated that this pressure correction term does not have to be under relaxed. When it is not, it is shown that the solution will be independent of the general relaxation factor. It is indicated that the checkerboard oscillations are more significant at higher Cell Reynolds numbers and, in turn, in this article the numerical simulations are mainly performed in turbulent flow. In all test cases performed in this article, in turbulent flow the Cell Reynolds number in regions where the checkerboard oscillations were observed was more than the equivalent laminar flow. It is demonstrated that Local Triangle (LT) is an important concept in triangular grids. It is indicated that checkerboard oscillations disappear when there is no distorted LT in a grid. It is shown that checkerboard oscillations cause reverse flow and, as a result, they are less likely when there is a pressure gradient. A level n Multi-Block Local Triangulation (MBLT) is defined as a generalized form of the customary unstructured triangular grid. In the test cases performed in this article, the level one MBLT was superior to customary unstructured triangular grids and, in turn, it can be considered as an alternative to such grids. However, more test cases are required in order to investigate the performance of the MBLT grid of different levels. It is shown that a combination of level one MBLT and quad-split boundary layer grids completely remove the checkerboard oscillations. Since it is possible to apply the

MBLT grid of any level just outside the boundary layer, it can be successfully applied to complicated structures.

3.2.8 References

1. M. J. Ketabdari, M. R. H. Nobari, and M. Moradi Larmaei, Simulation of waves group propagation and breaking in coastal zone using a Navier-Stokes solver with an improved VOF free surface treatment, Appl. Ocean Res., vol. 30, pp. 130-143, 2008.

2. M. R. H. Nobari, M. J. Ketabdari, and M. Moradi, A modified volume of fluid advection method for uniform Cartesian grids, Appl. Math. Model., vol. 33, pp. 2298-2310, 2009.

3. K. K. Q. Zhang, B. Rovagnati, Z. Gao, W. J. Minkowycz, and F. Mashayek, An introduction to the lattice grid, Numer. Heat Transf. B, Fundam., vol. 51, pp. 415-431, 2007.

4. S. Acharya, B. R. Baliga, K. Karki, J. Y. Murthy, C. Prakash, and S. P. Vanka, Pressure-based finite-volume methods in computational fluid dynamics, J. Heat Trans., vol. 129, pp. 407-424, 2007.

5. A. W. Date, Solution of transport equations on unstructured meshes with cell-centered colocated variables. Part I: Discretization, Int. J. Heat Mass Tran., vol. 48, pp. 1117-1127, 2005.

6. J. H. Ferziger and M. Peric, Computational methods for fluid dynamics, 3rd ed., pp. 196-202, Springer, Berlin, Germany, 1996.

7. H. K. Versteeg and W. Malalasekera, An introduction to computational fluid dynamics : the finite volume method, 1st ed., ch. 6 and 9, Longman Scientific & Technical, Pearson Prentice Hall, Toronto, 1995.

8. A. W. Date, Fluid dynamical view of pressure checkerboarding problem and smoothing pressure correction on meshes with colocated variables, Int. J. Heat Mass Tran., vol. 46, pp. 4885-4898, 2003.

9. C. M. Rhie and W. L. Chow, Numerical Study of the turbulent flow past an airfoil with trailing edge separation, AIAA J., vol. 21, pp. 1525-1532, 1983.

10. L. Davidson, A pressure correction method for unstructured meshes with arbitrary control volumes, Int. J. Numer. Meth. Fl., vol. 22, pp. 265-81, 1996.

11. T. N. Croft, Unstructured mesh -- finite volume algorithms for swirling turbulent reacting flows, Ph.D. thesis, School of Computing and Mathematical Sciences, University of Greenwich, London, UK, 1998.

12. L. Fue-Sang, A pressure-based unstructured grid method for all-speed flows, Int. J. Numer. Meth. Fl., vol. 33, pp. 355-74, 2000.

13. A. Dalal, V. Eswaran, and G. Biswas, A finite-volume method for Navier-Stokes equations on unstructured meshes, Numer. Heat Transf. B, Fundam., vol. 54, pp. 238-259, 2008.

14. M. Darwish, I. Sraj, and F. Moukalled, A coupled finite volume solver for the solution of incompressible flows on unstructured grids, J. Comput. Phys., vol. 228, pp. 180-201, 2009.

15. W. Gao and R. Liu, A hybrid finite volume/finite element method for incompressible generalized Newtonian fluid flows on unstructured triangular meshes, Acta Mech. Sinica/Lixue Xuebao, vol. 25, pp. 747-760, 2009.

16. W. Z. Shen, J. A. Michelsen, N. N. Srensen, and J. N. Srensen, An improved SIMPLEC method on collocated grids for steady and unsteady flow computations. Numer. Heat Transf. B, Fundam., vol. 43, pp. 221-239, 2003.

17. M. M. Rahman, T. Siikonen, and A. Miettinen, Pressure-correction method for solving fluid flow problems on a collocated grid, Numer. Heat Transf. B, Fundam., vol. 32, pp. 63-84, 1997.

18. S. Kang and Y. Kim, Pressure-based unstructured-grid finite-volume method for simulating laminar reacting flows, Numer. Heat Transf. B, Fundam., vol. 41, pp. 53-72, 2002.

19. A. W. Date, Complete pressure correction algorithm for solution of incompressible Navier-Stokes equations on a nonstaggered grid, Numer. Heat Transf. B, Fundam., vol. 29, pp. 441-458, 1996.

20. S. Pimpalnerkar, M. Kulkarni, and A. W. Date, Solution of transport equations on unstructured meshes with cell-centered colocated variables. Part II: Applications, Int. J. Heat Mass Tran., vol. 48, pp. 1128-1136, 2005.

21. O. Touazi, E. Chenier, and R. Eymard, Simulation of natural convection with the collocated clustered finite volume scheme. Comput. Fluids, vol. 37, pp. 1138-1147, 2008.

22. E. Chenier, R. Eymard, and R. Herbin, A collocated finite volume scheme to solve free convection for general non-conforming grids. J. Comput. Phys., vol. 228, pp. 2296-311, 2009.

23. FLUENT6.3 User's Guide, Fluent Inc: http://my.fit.edu/itresources/manuals/fluent6.3/help/ html/ug/ main_pre.htm, 2010.

24. B. E. Launder and D. B. Spalding, The Numerical Computation of Turbulent Flows. Comput. Method. Appl. M., vol. 3, pp. 269-289, 1974.

25. M. Moradi Larmaei and T.-F. Mahdi, Analysis of SIMPLE algorithm for depth averaged simulations, 6th International Symposium on Environmental Hydraulics, Athens, Greece, 2010, accepted.

26. U. Ghia, K. N. Ghia, and C. T. Shin, High-Re solutions for incompressible flow using the Navier-Stokes equations and a multigrid method, J. Comput. Phys., vol. 48, pp. 387-411, 1982.

27. R. Cheesewright, G. McGrath, and D. G. Petty, LDA measurement of turbulent flow in a duct of square cross section at low Reynolds number, Aeronational Engineering Department, Queen May Westfield College , University of London, Rept. 1011, 1990.

28. A. W. Date, Solution of Navier-Stokes equations on non-staggered grid, Int. J. Heat Mass Tran., vol. 36, pp. 1913-1922, 1993.

29. J. Behzadi, A numerical simulation of incompressible flow past 3D axisymmetric bodies, Ms.C. thesis, Department of Mechanical Engineering, Amirkabir University of Technology, Tehran, Iran, 2007, pp. 119.

CHAPTER 4   ARTICLE 2: GRID-INDEPENDENT DEPTH-AVERAGED SIMULATIONS WITH A COLLOCATED UNSTRUCTURED FINITE VOLUME SCHEME

4.1 Presentation of the article

In this section the objective of the article will be presented, as well as a conclusion on this work as part of the thesis. This article presents new techniques for increasing the computational accuracy and reducing the computational cost. These can be used in commercial software such as Mike21/21C (www.mikebydhi.com) and the solvers used in SMS (www.aquaveo.com/sms). The consequence effect on engineering problems then is evident, since a more accurate simulation of an engineering problem is equivalent to having the chance for providing a better and more cost efficient solution to the problem. For instance, the suggested techniques increase the accuracy of the solutions near the river bank. By "grid-independent" in the article title, the authors thought of a solution independent of every grid property but spacing.

4.1.1 Objective

The word "Numerical Solution", alone, does not represent an acceptable solution to engineering problems. A numerical solution is acceptable if all requirements suitably provided so that the converged solution of a numerical scheme is similar to the actual solution. In order to guaranty this equality, many parameters have to be kept in mind during development and application process. Some of such requirements which are observed to be undermined in the literature are discussed in this article and, their significant effect on computed results is reviled. Some techniques are also introduced in order to increase the numerical accuracy and reduce the computational cost.

4.1.2 Conclusion

It is observed that a depth-averaged solution cannot be grid independent if the grid allows continues downstream directions. These directions permit false numerical flux. It is indicated that the new interpolation technique which is devised for interpolation of variables from cell center into the cell face will highly reduce the computational cost when the number of grid cells is huge.

The technique which is suggested for the integration of bed source term significantly enhance the accuracy of the simulations and, the suggested discretization technique for the bed source term guaranty an oscillation free solution at small water depths.

The article is published with International Journal for Numerical Methods in Fluids.

Moradi Larmaei, M., Behzadi, J., and Mahdi, T.-F. (2012). Grid independent depth-averaged simulations with a collocated unstructured finite volume scheme. International Journal for Numerical Methods in Fluids, 69 (1) 88-109.

4.2 Grid-independent depth-averaged simulations with a collocated unstructured finite volume scheme

M. Moradi Larmaei[1], J. Behzadi[2], and Tew-Fik Mahdi[1]

[1]Department of Civil, Geological and Mining Engineering, Montreal Polytechnic Institute, Montreal, Quebec, Canada.

[2]Department of Mechanical Engineering, Chamran University of Ahvaz, Ahvaz, Iran.

4.2.1 Abstract

In this article, the depth-averaged transport equations are written in a new way so that it is possible to solve the transport equations for very small water depths. Variables are interpolated into the cell face with two different schemes and, the schemes are compared in terms of computational cost and accuracy. The bed source terms are computed using two different assumptions. The effect of these assumptions on numerical simulations is then investigated. Solutions of transport equations on different types of unstructured triangular grids are compared and, an appropriate choice of grid is suggested.

Keywords: Depth-averaged simulation, Finite volume method, Unstructured grid, Collocated data structure

4.2.2 Introduction

Depth-averaged transport equations are obtained through integration of three dimensional transport equations over the water depth. One of the main assumptions in depth-averaged transport equations is that the vertical pressure distribution is hydrostatic. In SIMPLE scheme this hydrostatic pressure is linked with water surface elevation through the equation $P = \rho g \xi$. Therefore, an oscillation in pressure field, P, causes oscillation in water surface elevation, ξ. In this article the Rhie and Chow [1] type pressure interpolation technique is used which has been regarded as an efficient technique in order to remove the checkerboard oscillations from pressure field [2-5] or, equivalently the water surface elevation [6-9].

Nomenclature

a_0, a_j	coefficients in the discretized equations
C_{s_j}	volumetric flux at the cell face s_j
C_f	the bed friction coefficient
F_r	Froude number
g	gravitational acceleration
G	the rate of production in $k - \varepsilon$ model equation
h	water depth
$h_{c_0\_c_j}$	the normal distance between two neighbor cells
k	turbulence kinematic energy
L	length scale
n	the direction along $\boldsymbol{n}$ or Manning's number
$\boldsymbol{n}$	unit vector normal to the cell face
$\hat{\boldsymbol{n}}$	unit vector normal to velocity vector $\boldsymbol{u}$
P, P'	pressure and pressure correction, respectively
r	streamline curvature radius
$\boldsymbol{r}_{c_j\_s_j}, \boldsymbol{r}_{c_0\_s}$	distance vectors between the cell's center and the face's center
R	residual at the domain
R_e	Reynolds number

$s_j, \boldsymbol{s}_j$	cell face area and the area vector, respectively
$S, \boldsymbol{S}$	scalar and vector form of the source terms, respectively
t	time
u, v	velocity components in x and y directions, respectively
U	velocity scale
$\boldsymbol{u}$	velocity vector
x, y	x and y directions
$\mid \ \mid$	for any vector $\boldsymbol{b}$, $\mid\boldsymbol{b}\mid$ refers to the argument of the vector

Greek symbols

ε	dissipation rate of k
ϑ°	continuity residual
ϑ	normalized continuity residual
μ, μ_t	laminar and turbulent dynamic viscosity, respectively
ξ	water surface elevation
ρ	fluid density
σ	Prandtl/Schmidt number
$\tau, \boldsymbol{\tau}$	scalar and vector stresses
φ	general scalar quantity
χ	Prandtl/Schmidt number in general discretized equation for φ

ω_{rc}	relaxation factor in pressure correction term
ϖ	vorticity
ω_s	magnitude of streamwise vorticity vector
Ω	volume

Subscripts

b	refers to the river/channel bed
j	refers to the neighboring cell
k	refers to turbulence kinematic energy
p_φ	refers to the implicit part of the source term in discretized equation for φ
ref	refers to reference value
rb	refers to river/channel bed
R	refers to residual at the domain
ss	refers to secondary shear
sf	refers to secondary force
s_j	refers to cell face s_j
u_φ	refers to the explicit part of the source term in discretized equation for φ
ε	refers to dissipation rate of k
τ	refers to shear
φ	refers to φ

0   refers to central cell

Superscripts

n refers to the current time step

P refers to pressure

T refers to the transpose of a vector

u refers to $\boldsymbol{u}$

φ refers to φ

~   refers to approximate value in Roe's Riemann solver

+   refers to an initial guess (can be from previous iteration)

∗   refers to the dimensional form of a quantity

Some of the most important characteristics of a well established depth-averaged numerical tool are none oscillatory results at very small water depths, small computational cost, accurate discretization scheme, and grid independency of the results. In this article these characteristics are investigated in following research cases:

a. In momentum equations the water depth appears as denominator in bed resistant source term. When the water depth goes to zero, the bed resistance source term goes to infinity. A very high bed resistance source term can redirect the flow and, in turn, it can cause numerical oscillations. In order to avoid numerical oscillations, Brufau et al. [10] discretized the bed resistance source term in a semi-implicit manner. This method however does not avoid infinite bed resistance for very small water depth. In [10] a fraction has appeared in discretized momentum equations which at very small water depth its numerator and denominator go to infinity. In this article, in order to avoid numerical oscillations, the transport equations are multiplied by h^{α} where α depends on the transport equation. As a

result, the bed source term in transport equations will be independent of the water depth. Patankar's [11] suggestion for discretization of source terms is then applied in order to achieve a high, yet stable, convergence rate. Since the rest of the terms in transport equations are multiplied by water depth and, in turn, they tend to zero for a very small depth.

b. Ferziger and Peric [12] maintained that, in order to calculate the product of dependent variables at the cell face, variables have to be interpolated into the cell face and, their product has to be calculated at the cell face. When Riemann solvers, for example the Roe's [13] Riemann solver, are applied to depth-averaged inviscid flow [14-16], dependent variables are interpolated into the cell face with a depth weighted averaging; e.g. $\tilde{\boldsymbol{u}}_{s_j} = \left(\sqrt{h_0}\boldsymbol{u}_0 + \sqrt{h_j}\boldsymbol{u}_j\right)/\left(\sqrt{h_0} + \sqrt{h_j}\right)$ which with an arithmetic averaging is equivalent to $\tilde{\boldsymbol{u}}_{s_j} = \left(\sqrt{h}\boldsymbol{u}\right)_{s_j}/\left(\sqrt{h}\right)_{s_j}$. In this article, two different approaches are adopted in order to interpolate the dependent variables into the cell face. These approaches are then compared in terms of CPU time and numerical accuracy. The first method is, following Ferziger and Peric [12] and, interpolating the dependent variables into the cell face with a distance weighted averaging. The second method is, integrating the dependent variables over the depth in order to calculate their total values and, interpolating the total values into the cell face with a distance weighted averaging. At the cell face the total value can be divided by water depth in order to obtain the depth averaged variable. In this article, the former method is called Linearly Interpolated (LI) and the later method is called Total-Value Linearly Interpolated (TV-LI).

c. Independent of whether the bed source terms (e.g. bed resistance source term) are discretized in a point wise manner [7, 17-19] or with upwind method [10, 20], they have been always integrated over the cell area. Theoretically, the bed source terms have to be integrated over the bed area rather than the cell area. In this article two assumptions are made and, the effect of these assumptions on numerical results is investigated. The first assumption is that, the bed area can be successfully replaced by cell area without any significant error in numerical results. The second assumption is that, the cell area cannot be an appropriate approximation of bed area since even with a grid refinement the cell area is equivalent to the horizontal component of the bed area.

d. Assuming that the grid is refined enough so that a grid independent solution can be inferred, false diffusion is expected to be the main source of inaccuracy in first order schemes [21]. In this article, another significant source of numerical error is recognized which is peculiar to depth-averaged simulations. As far as the authors are aware, this kind of numerical error is not well recognized in depth averaged simulations. Murillo et al. [15] observed that their method for extending the Roe's [13] Riemann solver to a courant number larger than one does not performs in Advanced-Front grids, but it does in Delaunay grids. Murillo et al. [15] hold that, this is perhaps due to existence of such directions in Advanced-Front grids. A reason behind Murillo et al. [15] observations can be addressed through False Channel (FC) effect. A FC is a direction in which fluid has the tendency to flow due to combined effects of grid, bed gradient, and bed resistance source term. In this article, two different types of grids are selected and, the effect of bed gradient, bed resistance source term, and grid resolution on numerical results is examined. Numerical results are then analyzed in order to suggest an appropriate choice of grid.

The remainder of this article is divided into three sections. In the first section, the dimensionless conservative form of the depth-averaged transport equations is presented. In this section, the research case (a) is explained. The second section is devoted to the numerical method where the research cases (a), (b), and (c) are discussed. Numerical results are presented in the third section. In this section, the numerical tool is validated with other numerical and experimental data. Also, the research cases (a) to (d) are examined.

4.2.3 Governing equations

The dimensionless conservative vector form of depth-averaged continuity and momentum equations can be given by:

$$\frac{\partial (P/g)}{\partial t} + \nabla.(h\boldsymbol{u}) = 0 \tag{4.1}$$

$$\frac{\partial (h\boldsymbol{u})}{\partial t} + \nabla.(h\boldsymbol{u}\boldsymbol{u}) = -h\nabla P + \frac{1}{R_e}\nabla.[h(1+\mu_t)\nabla\boldsymbol{u}^T] - \boldsymbol{\tau}_b + \boldsymbol{S}_{sf} \tag{4.2}$$

where, $\boldsymbol{u} = \boldsymbol{u}^*/U_{ref}$, $\quad t = t^*U_{ref}/L_{ref}$, $\quad R_e = \rho^*U_{ref}l_{ref}/\mu^*$, $\quad \mu_t = \mu_t^*/\mu^*$, and $P = (P^* - P_{ref})/(\rho^*U_{ref}^2)$. The dimensionless bed shear stress, $\boldsymbol{\tau}_b$, can be expressed as:

$$\boldsymbol{\tau}_b = c_f|\boldsymbol{u}|\boldsymbol{u} \tag{4.3}$$

$$C_f = g\, n^2 / h^{1/3} \tag{4.4}$$

where, $n = n^* U_{ref} / L_{ref}^{2/3}$. Following Bernard [17], the dimensionless secondary force, $\boldsymbol{S}_{sf}$, is given by:

$$\boldsymbol{S}_{sf} = \frac{\boldsymbol{u}}{|\boldsymbol{u}|}\left[\hat{\boldsymbol{n}}.\nabla(h\tau_{ss}) + \frac{h\tau_{ss}}{2r}\right] \tag{4.5}$$

τ_{ss} is a scalar value, expressed as:

$$\tau_{ss} = h\varpi\sqrt{C_f}|\boldsymbol{u}| \tag{4.6}$$

where, $\varpi = (C_2\omega_s)/12$ is a scalar quantity with C_2 being a constant of proportionality, and $\omega_s = \omega_s^* L_{ref}/U_{ref}$. ω_s is perpendicular to horizontal plane.

In Equation (4.5) $r = r^*/L_{ref}$ is positive for counterclockwise motion and negative for clockwise motion. The normal derivative $\hat{\boldsymbol{n}}.\nabla(h\tau_{ss})$ is positive when $h\tau_{ss}$ increases in the positive radial direction. The unit vector, $\hat{\boldsymbol{n}},$ and the curvature radius, r, are expressed as:

$$\hat{\boldsymbol{n}} = \frac{v}{|\boldsymbol{u}|}\boldsymbol{i} - \frac{u}{|\boldsymbol{u}|}\boldsymbol{j} \tag{4.7}$$

$$r = \frac{|\boldsymbol{u}|^3}{uv((\partial v/\partial y)-(\partial u/\partial x))+u^2(\partial v/\partial x)-v^2(\partial u/\partial y)} \tag{4.8}$$

In Shallow Fluent, the solver which is presented in this article, the standard $k - \varepsilon$ model is selected in order to simulate turbulent flows. The dimensionless conservative form of k and ε equations are given by:

$$\frac{\partial(hk)}{\partial t} + \boldsymbol{\nabla}.(hk\boldsymbol{u}) = \frac{1}{R_e}\boldsymbol{\nabla}.\left[h\left(1+\frac{\mu_t}{\sigma_k}\right)\nabla k\right] + S_k \tag{4.9}$$

$$\frac{\partial(h\varepsilon)}{\partial t} + \boldsymbol{\nabla}.(h\varepsilon\boldsymbol{u}) = \frac{1}{R_e}\boldsymbol{\nabla}.\left[h\left(1+\frac{\mu_t}{\sigma_\varepsilon}\right)\nabla\varepsilon\right] + S_\varepsilon \tag{4.10}$$

where, $S_k = h(G_k - \varepsilon + G_{kb})$, and $S_\varepsilon = h(C_{\varepsilon 1}G_k\,\varepsilon/k - C_{\varepsilon 2}\,\varepsilon^2/k + G_{\varepsilon b})$. G_k, G_{kb}, and $G_{\varepsilon b}$ are given by:

$$G_k = \frac{\mu_t}{R_e}\left[\left(\frac{\partial u}{\partial y}+\frac{\partial v}{\partial x}\right)^2 + 2\left(\frac{\partial u}{\partial x}\right)^2 + 2\left(\frac{\partial v}{\partial y}\right)^2\right] \tag{4.11}$$

$$G_{kb} = C_f^{-1/2}\, U_\tau^3 / h \tag{4.12}$$

$$G_{\varepsilon b} = C_{\varepsilon\Gamma}C_{\varepsilon 2}c_\mu^{1/2}C_f^{-3/4}\, U_\tau^4 / h^2 \tag{4.13}$$

where, $U_\tau = \sqrt{|\tau_b|}$, $\mu_t = C_\mu R_e \frac{k^2}{\varepsilon}$, $k = k^*/U_{ref}^2$, $\varepsilon = \varepsilon^*/(U_{ref}^3/L_{ref})$, and model's constants are $C_\mu = 0.09$, $C_{\varepsilon 1} = 1.44$, $C_{\varepsilon 2} = 1.92$, $\sigma_k = 1.0$ and $\sigma_\varepsilon = 1.3$. Following Rodi [22], the coefficient $C_{\varepsilon\Gamma}$ is set to 3.6 for flumes and 1.8 for rivers.

When streamline is curved, the centrifugal force causes a secondary flow normal to streamline direction. Bed resistance force and gravitational acceleration act on secondary flow and, in turn, a helical flow will form. Bernard [17] has suggested that, in depth-averaged momentum equations the helical flow effect can be accounted for with Equation (4.5). In order to calculate the S_{sf}, the streamwise vorticity, ϖ, has to be known [see Equation (4.6)]. The streamwise vorticity at the domain can be obtained through a transport equation [17].

$$\frac{\partial(h\varpi)}{\partial t} + \nabla \cdot (h\varpi \boldsymbol{u}) = A_s\sqrt{C_f}\frac{|\boldsymbol{u}|^2}{r\psi} - D_s\sqrt{C_f}\varpi|\boldsymbol{u}| + \frac{1}{R_e}\nabla \cdot [(1+\mu_t)h\nabla\varpi] \tag{4.14}$$

where, $A_s = 5.0$, $D_s = 0.5$, and $\psi = (1 + 9\,h^2/r^2)$ are suggested by Bernard [17].

As it is explained in research case (a) of the Section 4.2.2, when the water depth goes to zero, the bed source terms go to infinity. The water depth appears as denominator in bed resistance source term (4.4), in the term for generation of turbulence kinematic energy due to bed effects (4.12), in the term for dissipation of turbulence kinematic energy due to bed effects (4.13) and, in source terms in (4.14). When momentum equations are multiplied by $h^{1/3}$, the turbulence kinematic energy equation by $h^{1/3}$, turbulence dissipation rate equation by $h^{17/12}$, and vorticity equation by $h^{1/6}$, the bed source terms in these equations will be independent of h. In Section 4.2.4.1, it will be discussed that, this modification causes only little increase in computational efforts.

There is a division by the streamline curvature radius in the vorticity generation source term, the first term in the right hand side of Equation (4.14). The lower bound for streamline curvature radius calculated by Equation (4.8) is zero. Grid however filters the streamline curvature so that the actual lower bound for the streamline curvature radius in equilateral triangle cells will be $h_{c_0\_c_n}$ (Figure 4.1-a). In a grid with arbitrary triangular cells the streamline curvature radius can be given by:

$$r = max\left\{r, \frac{\sum_{j=1}^{3} h_{c_0\_c_j}}{3}\right\} \tag{4.15}$$

where, r in the right hand side of Equation (4.15) is obtained through Equation (4.8). Equation (4.15) is also a perfect estimate when the number of the neighboring cells is more than three (in this case the number 3 in Equation (4.15) has to be replaced with the number of the neighboring cells). When streamline curvature radius is modified by means of Equation (4.15), singularity in vorticity generation source term will be removed and, the solver will be stable. However, the secondary force due to high streamline curvature will be ignored.

(a)   (b)
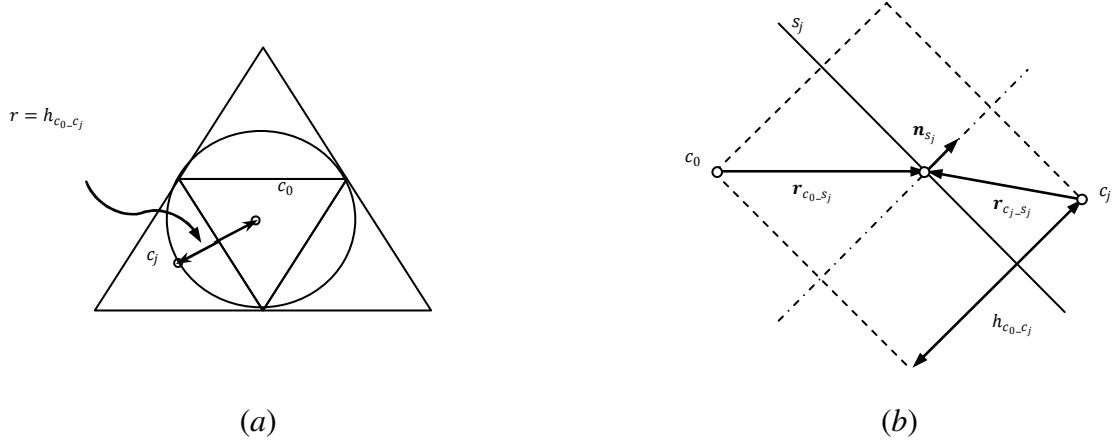
Figure 4.1. Geometrical notations used in; (a) definition of the lower bound for the streamline curvature radius in a triangular grid, r, and, (b) discretized equations relevant to a cell and its immediate neighbors: central cell, c_0, neighboring cell, c_j, cell face, s_j, unit vector normal to the cell face, $\boldsymbol{n}_{s_j}$, distance vector, $\boldsymbol{r}$, and normal distance between cell centers, $h_{c_0\_c_j}$.

4.2.4 Numerical method

In this section, the detail of discretization scheme will be introduced. Also, the boundary conditions and the residual criterion used in this article will be presented.

4.2.4.1 Discretization scheme

In Shallow Fluent, the SIMPLE algorithm is applied for the coupling between pressure and velocity field. In the SIMPLE algorithm continuity equation (4.1) is converted into a pressure correction equation. Momentum equations will be solved with an initial guessed pressure and velocity field. The derived velocity field then will be used in a pressure correction equation. The obtained pressure correction corrects the pressure and velocity field, other scalars if there are any

will be solved, and the solution continues in the next iteration until convergence is attained. The correction to pressure and velocity at any cell is given by:

$$P = P^+ + P'$$ (4.16)

$$\boldsymbol{u} = \boldsymbol{u}^+ - \frac{\Omega h^{4/3}}{a_0^u} \nabla P'$$ (4.17)

In this article, convective terms are discretized with the first order upwind scheme, Green's theorem is used for the calculation of the gradient at cell center, and the two-point method for the calculation of gradient at the cell face. The discretized pressure correction equation then can be expressed as:

$$a_0^P P_0' = \sum_{j=1}^{3} a_j^P P_j' - \vartheta^\circ$$ (4.18)

$$a_j^P = \frac{h_{s_j} s_j}{2h_{c_0\_c_j}} \left[\left(\frac{\Omega h^{4/3}}{a_0^u} \right)_0 + \left(\frac{\Omega h^{4/3}}{a_0^u} \right)_j \right]$$ (4.19)

$$a_0^P = \sum_{j=1}^{3} a_j^P + \frac{\Omega_0}{g\Delta t}$$ (4.20)

The discretized equation for the conserved variable, φ, in a triangular grid can be written as:

$$a_0^\varphi \varphi_0 = \sum_{j=1}^{3} a_j^\varphi \varphi_j + S_{u_\varphi}$$ (4.21)

$$a_0^\varphi = h^\alpha \left[\sum_{j=1}^{3} \llbracket C_{s_j}, 0 \rrbracket + \frac{1}{R_e} \sum_{j=1}^{3} \left(\frac{(h(1+\mu_t/\chi))_{s_j} s_j}{h_{c_0\_c_j}} \right) \right] - S_{p_\varphi}$$ (4.22)

$$a_j^\varphi = h^\alpha \left[\llbracket -C_{s_j}, 0 \rrbracket + \frac{(h(1+\mu_t/\chi))_{s_j} s_j}{R_e h_{c_0\_c_j}} \right]$$ (4.23)

where, $\llbracket C_{s_j}, 0 \rrbracket$ denotes the maximum of C_{s_j} and 0. In Equation (4.22) and Equation (4.23) χ is 1.0, σ_k, σ_ε, and 1.0 for momentum, turbulence kinematic energy, turbulence dissipation rate, and vorticity equations, respectively. In Equation (4.22) and Equation (4.23) α is $1/3$, $1/3$, $17/12$, and $1/6$ for momentum, turbulence kinematic energy, turbulence dissipation rate, and vorticity equations, respectively. Figure 4.1-*b* depicts the geometrical notations. The detail of discretization scheme can be found for example in [3, 4, 12, 23] among others.

The Rhie and Chow [1] pressure interpolation technique is applied in order to obtain a mass conserving velocity at the cell face. In Shallow Fluent, the cell face velocities are not linearly

interpolated; instead, a momentum-weighted averaging is performed [24]. The continuity residual can be expressed as:

$$\vartheta° = \sum_{j=1}^{3} \left\{ \frac{(ua_0^u)_0+(ua_0^u)_j}{(a_0^u)_0+(a_0^u)_j} \cdot \boldsymbol{s}_j - \omega_{rc}a_j^P(P_j - P_0) \right\} + \frac{\Omega_0}{g\Delta t}(P_0^+ - P_0^{n-1}) \tag{4.24}$$

The relaxation factor in Rhie and Chow [1] pressure correction term, ω_{rc}, is set to 1.0 [25].

The modifications the authors made to Equations (4.2), (4.9), (4.10), and (4.14) appeared as h^α in Equations (4.22) and (4.23). These modifications also change the power of h in source terms. For example, in momentum equations the implicit part of the transient source term in an unsteady flow will changes from $\Omega_0 h/\Delta t$ to $\Omega_0 h_0^{4/3}/\Delta t$. As a result, the computational costs will only little increase.

4.2.4.2 LI versus TV-LI method

In order to explain the research case (b), from Section 4.2.2, convective flux is considered. The convective flux, C_{s_j} at the cell face, s_j, can be given by:

$$C_{s_j} = \boldsymbol{u}_{s_j} \cdot \left(h_{s_j} \boldsymbol{s}_j \right) = u_{s_j} \left(h_{s_j} s_{x,j} \right) + v_{s_j} \left(h_{s_j} s_{y,j} \right) \tag{4.25}$$

In Equation (4.25) the normal component of velocity vector is multiplied by flux area. At the cell face the flux area is the cell face area multiplied by water depth. Evidently, Equation (4.25) is in accordance with Ferziger and Peric [12] if every variable is linearly interpolated into the cell face; i.e. Equation (4.25) represents the LI method.

When TV-LI method is used, $\boldsymbol{u}_{s_j}$ has to be calculated as:

$$\boldsymbol{u}_{s_j} = \frac{(h\boldsymbol{u})_{s_j}}{h_{s_j}} = \frac{(|r_{c_{j\_s_j}}|h_0\boldsymbol{u}_0+|r_{c_{0\_s_j}}|h_j\boldsymbol{u}_j)/(|r_{c_{j\_s_j}}|+|r_{c_{0\_s_j}}|)}{(|r_{c_{j\_s_j}}|h_0+|r_{c_{0\_s_j}}|h_j)/(|r_{c_{j\_s_j}}|+|r_{c_{0\_s_j}}|)} = \frac{(|r_{c_{j\_s_j}}|h_0\boldsymbol{u}_0+|r_{c_{0\_s_j}}|h_j\boldsymbol{u}_j)}{(|r_{c_{j\_s_j}}|h_0+|r_{c_{0\_s_j}}|h_j)} \tag{4.26}$$

Now, flux at the cell face can be given by:

$$C_{s_j} = \boldsymbol{u}_{s_j} \cdot \left(h_{s_j} \boldsymbol{s}_j \right) = \frac{(h\boldsymbol{u})_{s_j}}{h_{s_j}} \cdot \left(h_{s_j} \boldsymbol{s}_j \right) = (h\boldsymbol{u})_{s_j} \cdot \boldsymbol{s}_j \tag{4.27}$$

$h\boldsymbol{u}$ in Equation (4.27) is the unit discharge in streamline direction. In Equation (4.27) the streamwise unit discharge at the cell face, $(h\boldsymbol{u})_{s_j}$, is multiplied by cell face area vector, $\boldsymbol{s}_j$, in

order to obtain the flux. When Equation (4.27) is used, more mathematical operation have to be performed in order to calculate the flux compared with Equation (4.25).

4.2.4.3 Bed source terms

In research case (a), from Section 4.2.2, it was discussed that the discretization of bed source terms demands special attention. When a positive velocity field is assumed, the bed resistance source term in modified momentum equations (i.e. Equation (4.2) multiplied by $h^{1/3}$) can be given by:

$$\boldsymbol{\tau}_b = gn^2\boldsymbol{u}^2 \tag{4.18}$$

In order to achieve a high, yet stable, convergence rate, Patankar [11] suggested a semi implicit discretization of the source terms.

$$S = S^+ + \frac{\partial S^+}{\partial \varphi^+}(\varphi - \varphi^+) \tag{4.19}$$

When Equation (4.19) is applied to Equation (4.18), the bed resistance can be given by:

$$\boldsymbol{\tau}_b = gn^2\boldsymbol{u}^{+2} + 2gn^2\boldsymbol{u}^+(\boldsymbol{u} - \boldsymbol{u}^+) \tag{4.20}$$

The direction of the bed resistance, $\boldsymbol{\tau}_b$, changes when the flow direction changes. In order to take the flow direction into account, Equation (4.20) has to be expressed as:

$$\boldsymbol{\tau}_b = 2gn^2|\boldsymbol{u}^+|\boldsymbol{u} - gn^2|\boldsymbol{u}^+|\boldsymbol{u}^+ \tag{4.21}$$

The bed resistance source term is the only depth independent term in momentum equations. When the water depth goes to zero, the contribution from other terms is ignorable and, in turn, momentum equations can be written as:

$$\frac{h^{4/3}\boldsymbol{u} - h^{1/3}(h\boldsymbol{u})^{n-1}}{\Delta t} = -[2gn^2|\boldsymbol{u}^+|\boldsymbol{u} - gn^2|\boldsymbol{u}^+|\boldsymbol{u}^+]$$

or, after rearrangement:

$$\boldsymbol{u} = \frac{(h^{1/3}(h\boldsymbol{u})^{n-1})/\Delta t + gn^2|\boldsymbol{u}^+|\boldsymbol{u}^+}{(h^{4/3})/\Delta t + 2gn^2|\boldsymbol{u}^+|} \tag{4.22}$$

Equation (4.22) has three main properties. Firstly, when the water depth goes to zero Equation (4.22) reduces to $\boldsymbol{u} = \boldsymbol{u}^+/2.$ When a solution converged, the velocity field in previous and current iterations are identical and, in turn, $\boldsymbol{u} = \boldsymbol{u}/2$ which is in fact $\boldsymbol{u} - \boldsymbol{u}/2 = 0.0$ or

equivalently, $\boldsymbol{u} = 0.0$. Therefore, the bed shear stress stops the flow but it does not change the direction of the flow. Secondly, velocity only gradually tends to zero; i.e., there will be no sudden changes in the flow field. For a reduction of about 10^{-3} by order of magnitude, the reduction to zero will be achieved in ten iterations. Ten iterations is an acceptable number of iterations in an iterative method. Thirdly, in Equation (4.22) both terms in the denominator are always positive. This guaranties a diagonally dominant coefficient matrix.

The same procedure as applied to the bed resistance source term can be applied to the other bed source terms. The discretized bed source term in turbulence kinematic energy equation is given by:

$$G_{kb} = 2gn^2|\boldsymbol{u}|^3 - gn^2|\boldsymbol{u}|^3 \frac{k}{k^+} \tag{4.23}$$

Since in this article the wall function approach is applied to the near wall cells, the turbulence kinematic energy is always positive and, as a result, the second term in the right hand side of Equation (4.23) never goes to infinity. The discretized bed source term in turbulence dissipation rate equation is expressed as:

$$G_{\varepsilon b} = 2c_{\varepsilon\Gamma}c_{\varepsilon 2}c_\mu^{1/2}g^{5/4}n^{5/2}|\boldsymbol{u}|^4 - c_{\varepsilon\Gamma}c_{\varepsilon 2}c_\mu^{1/2}g^{5/4}n^{5/2}|\boldsymbol{u}|^4 \frac{\varepsilon}{\varepsilon^+} \tag{4.24}$$

When φ is assumed one of the k or ε, for a very small water depth, Equations (4.23) and (4.24) reduce to $\varphi = 2\varphi$. If it happens, the $k - \varepsilon$ model equations will diverge. It will be shown In Section 4.2.5.5 that, this problem at least does not appear when the dimensional water depth is as large as 10^{-3} m. A smaller water depth does not have any practical application in river/channel hydraulic engineering. According to [11] the discretization of vorticity dissipation source term which is due to bed effects has to be done in a fully implicit manner and is straight forward.

4.2.4.4 BA versus CA

In research case (c), in Section 4.2.2, it was discussed that the bed source terms has to be integrated over the bed area rather than the cell area. In Figure 4.2 a sinus-type bed form which is reconstructed by cell and bed area schemes is compared on coarse and fine grids. When the cell area scheme is used, a grid refinement has no effect on reconstructed bed form. But, in the case of the bed area scheme, the reconstructed bed form in finer grid is better.

The depth averaged transport equations are integrated over the cell area. When it is done, the bed source terms will be automatically integrated over the cell area. At every computational cell, in order to integrate the bed source terms over the bed area, Equations (4.3), (4.12), and (4.13) together with the dissipation source term in Equation (4.14) have to be multiplied by $(\Omega_{rb}/\Omega)_0$. Bed elevation has to be interpolated from cell-centers into the cell-vertices in order to reconstruct the bed topography. The reconstructed bed topography will be smooth and accurate as far as grid resolution and smoothness permit. In Section 4.2.5.4 the effect of such modification on numerical results will be examined through numerical simulations.

(*a*)   (*b*)
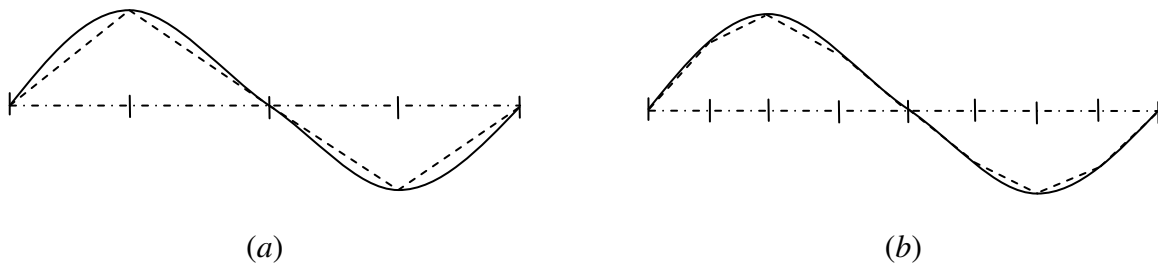
Figure 4.2. Comparison of the reconstructed bed area (dash lines) with the cell area (dash-dot lines) for sinus type bed form (solid lines); (*a*) in coarse grid and, (*b*) in fine grid.

4.2.4.5 Boundary conditions

The employed boundary conditions are the velocity inlet, the constant pressure boundary, and the wall condition. Variables have to be known at the inlet. At the constant pressure boundary, it is assumed that the gradient of variables is zero. Exceptions are velocity components and pressure. Following Versteeg and Malalasekera [26], in order to derive the velocity components, mass is locally conserved at the cells adjacent to the constant pressure boundary where pressure is fixed. The standard wall function approach [27] is applied to the momentum and turbulence model equations.

4.2.4.6 Residuals

The normalized continuity residual is given by:

$$\vartheta_R = \frac{\sum_{i=1}^{N_{cell}}|\vartheta^\circ|}{\vartheta_{ref}^\circ} \tag{4.25}$$

where, ϑ_{ref}° is the largest absolute value of the continuity residual in the first five iterations. The residual for any conserved variable, φ, is expressed as:

$$R_\varphi = \frac{\sum_{i=1}^{N_{cell}} \left| \sum_{j=1}^{3} a_j^\varphi \varphi_j + s_{u\varphi} - a_0^\varphi \varphi_0 \right|}{R_{ref}} \tag{4.26}$$

where, R_{ref} is the largest absolute value of the φ residual in the first five iterations.

4.2.5 Numerical results

The depth-averaged version of Shallow Fluent is developed through extension of its 2D version [28] into depth-averaged cases. The depth-averaged version is valid if the solver itself performs well and, if the applied depth-averaged boundary conditions are valid. In the first test case there is no source term and, the boundary conditions are as simple as possible. This test case will validate the internal accuracy of the solver. In the second test case the bed source terms are added to the problem. This test case validates the discretization method applied to the source terms. The third test case validates both the solver and the depth averaged smooth but no-slip wall boundary condition. In the fourth test case the bed area scheme is compared with the cell area scheme; i.e. the research case (c). The fifth test case is mainly designed in order to examine the research case (a). The research case (d) is also examined in the first and second test cases. The research case (b) is examined in the first to fifth test cases.

At the first two test cases a 1D tool will be used in order to validate Shallow Fluent. This 1D tool uses the inlet velocity and the water depth obtained from Shallow Fluent and, marches in space in positive x direction. Following equations are applied in order to develop the 1D tool:

$$\frac{\partial h}{\partial x} = \frac{-\partial Z_b/\partial x - \tau_{b\_1D}}{1 - F_r^2} \tag{4.27}$$

$$uh = constant \tag{4.28}$$

where, $F_r = \sqrt{u^2/gh}$, and $\tau_{b\_1D} = n^2 u^2/h^{4/3}$.

4.2.5.1 Loose flow: shear free channels

The computational domain is rectangular, with $L = 5\,m$ and $H = 1\,m$. The applied boundary conditions are: velocity inlet with uniform normal velocity, the constant water surface elevation (i.e. a constant pressure boundary condition) at the outlet, and the free-slip boundary condition on

the walls. Channel cross section is rectangular, Manning's number is assumed zero, and the water surface elevation at the outlet is $0.3\ m$. Flow Reynolds number is 4.98×10^5, where $L_{ref} = H$, $U_{ref} = U_{in} = 0.5\ m/s$, and U_{in} is the inlet velocity. The water specific gravity and dynamic viscosity are $998.2\ kg/m^3$ and $0.001003\ N.m/s^2$, respectively. The gravitational acceleration is $9.806\ m/s^2$. Errors are normalized, and the convergence criterion is set to 10^{-3}. For this test, two different types of grids with two different resolutions are selected; see Fig. 4. In this article, a grid as in Figures 4.3-a and 4.3-b is called a quad-split grid and, a grid as in Figures 4.3-c and 4.3-d is called an unstructured grid. When the bed gradient is negative and the gradient of the water surface (equivalently, the pressure gradient) is positive the flow is called loose flow. Such flow shows special behavior which will be discussed here (note that in this article channels with positive bed gradient are not studied).
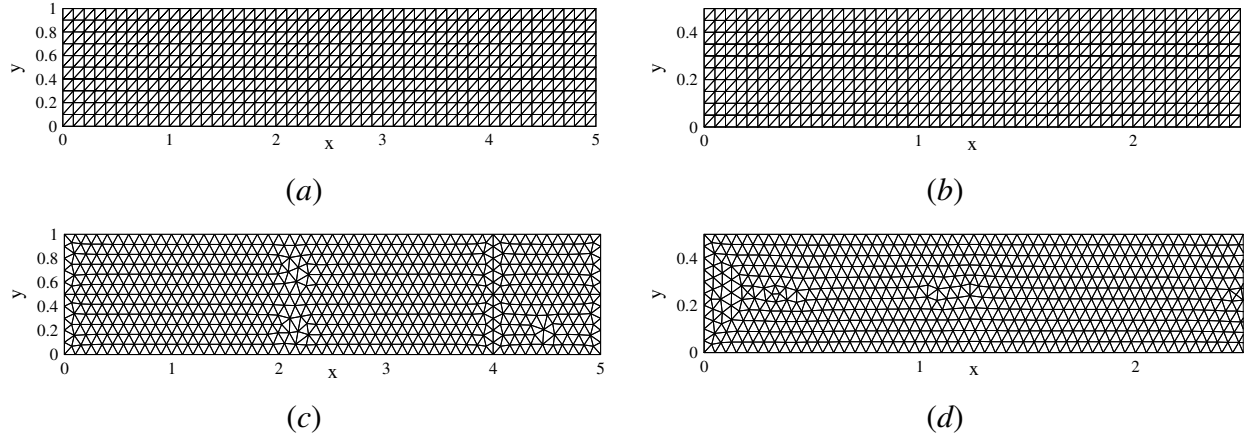
Figure 4.3. The grids used in Section 4.2.5.1 and 4.2.5.2; (a) and (c) are 10 by 50 on the domain boundaries, and (b) and (d) are 20 by 100 on the domain boundaries.

For the first test case (Figure 4.4-a) the bed gradient in x directions is zero. In the second test case (Figure 4.4-b) the bed gradient in x direction is assumed -0.01. For the third test case (Figure 4.4-c) the bed gradient in x direction is -0.03. In entire test cases the bed gradient in y direction is zero. The grid used in these test cases is 10 by 50 on the domain boundaries (Figure 4.3-a). The longitudinal profiles of water surface elevation and, the velocity components at $x = 4$ are shown in Figure 4.4. The numerical results obtained from LI and TV-LI methods are exactly similar. At the channel centerline, the profile of water surface elevation simulated with Shallow Fluent is in good agreement with 1D tool. The predicted longitudinal velocity, u, in

Figure 4.4-*a* is 1.0 as it has to be and, the transverse velocity, v, is perfectly zero. When the magnitude of the bed gradient increases, the agreement between the water surface elevations predicted with Shallow Fluent and 1D tool reduces. This can be due to the vertical expansion in channel cross section. Since Shallow Fluent solve for turbulent flow and the 1D tool for laminar flow, this little disagreement is expected. The predicted transverse velocity, v, increases when the magnitude of bed gradient increases. This causes a transverse discharge and, in turn, changes the profile of u velocity.

(*a*)

(*b*)

(*c*)
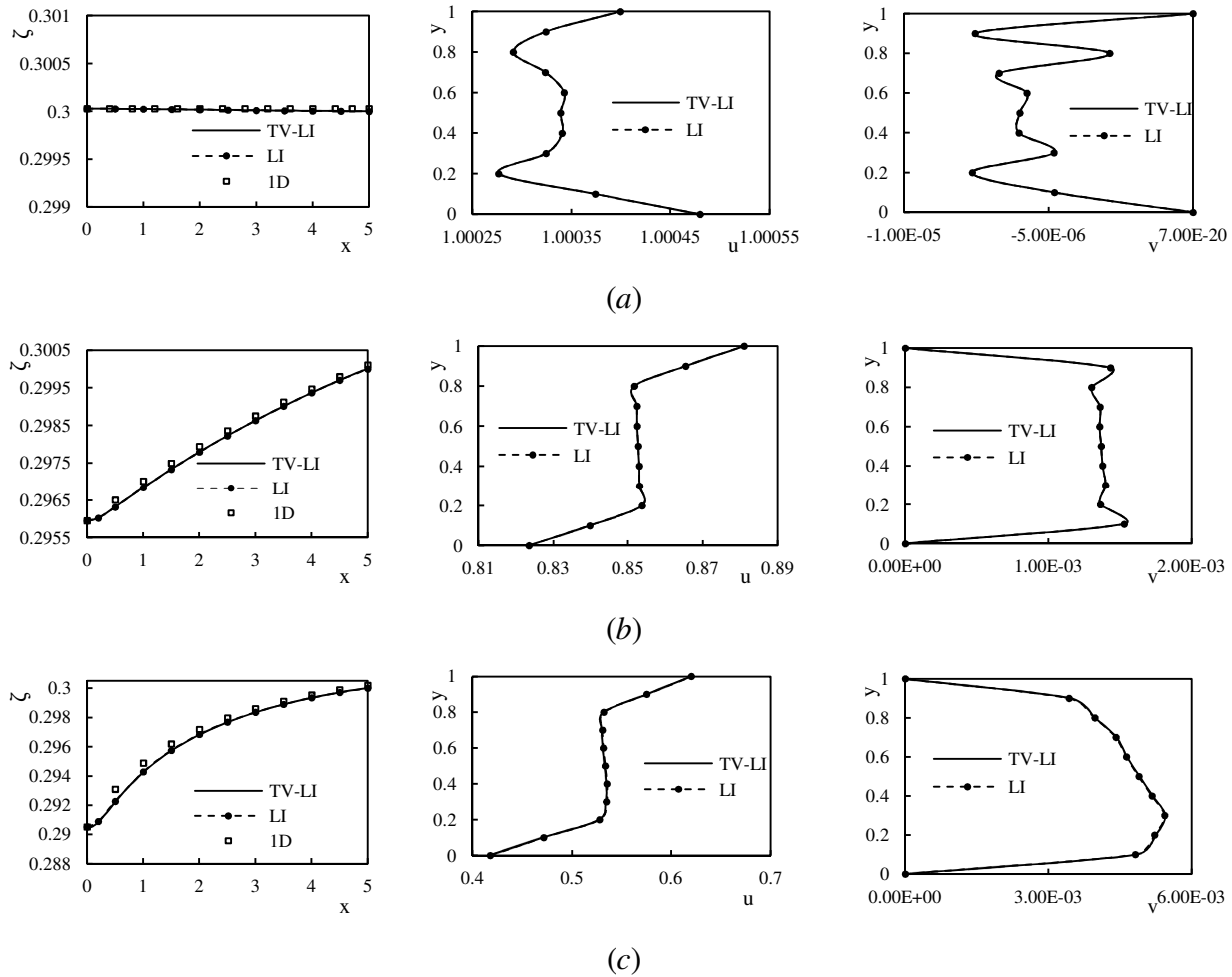
Figure 4.4. Profiles of water surface elevation, longitudinal, and transverse velocity in a straight channel with rectangular cross section; (*a*) $\partial Z_b/\partial x = 0.0$, (*b*) $\partial Z_b/\partial x = -0.01$, and (*c*) $\partial Z_b/\partial x = -0.03$. The left figures are the water surface elevation at the channel centerline, the middle figures are the u velocity at $x = 4$ from the inlet, and the right figures are the v velocity at the same position as u velocity.

The reason behind such behavior can be addressed through False Channel (FC) effect of the first type. In Figure 4.5-*a* the sketch of the false currents of the first type in a quad-split grid is shown. When the bed gradient is not zero, the bed elevation at the center of the cells at points A and B are not the same and, in turn, there will be a local slope from A toward B. The pressure at the cell A is also less than the pressure at the cell B. In the other hand, there is a local channel from cell A toward cell B with the same characteristics as a loose flow (negative bed gradient and positive pressure gradient). Such local channel where a false current exists is called FC. In Figure 4.5-*a*, the flux enters at the face 1 causes false currents which exit through face 3. The directions of these false currents are marked with dashed arrows. Since the flux enters at face 2 will also cause a false current at face 3, the near wall u velocity at $y \approx 1$ must gradually increase with the distance from the inlet. This can be observed in Figure 4.6-*a* through the contours of u velocity for the third test case (Figure 4.4-*c*). If the grid does not permit continuous downstream directions, there will not be continuous FCs and, in turn, the FC effect of the first type will reduce.

(*a*) (*b*)
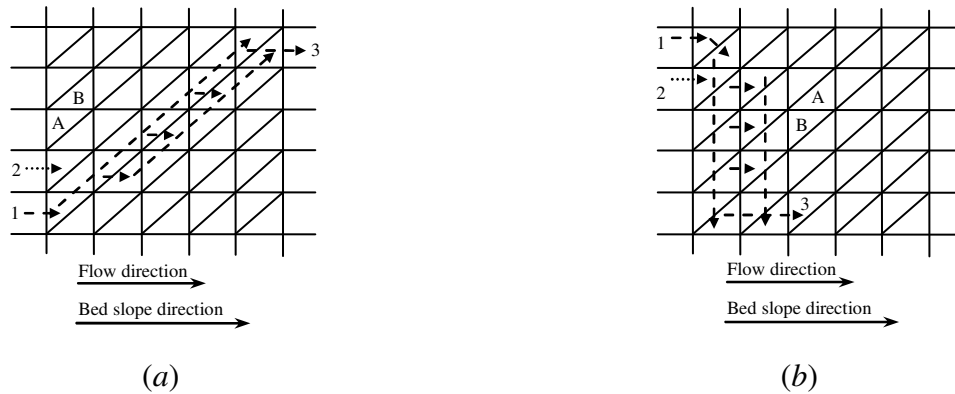
Figure 4.5. Sketch of the FCs and the false currents in a quad-split grid; (*a*) loose flow with a positive pressure gradient in x direction and, (*b*) pressurized flow with a negative pressure gradient in x direction.

The FC effect of the first type is expected to be independent of the grid resolution. Figure 4.7 is relevant to the second test case (Figure 4.4-*b*), but, different grids are used. Figure 4.7-*a* is related to the grid in Figure 4.3-*b*, Figure 4.7-*b* is related to the grid in Figure 4.3-*c* and, Figure 4.7-*c* is related to the grid in Figure 4.3-*d*. When Figure 4.7-*a* is compared with Figure 4.4-*b*, it can be observed that the spurious current in x direction is limited to the first two near wall cells. Though

in Figure 4.7-*a* the magnitude of the *v* velocity is reduced, since the spurious *u* velocity is limited to the first two near wall cells, the absolute magnitude of the spurious *u* velocity in fine (Figure 4.7-*a*) and coarse (Figure 4.4-*b*) quad-split grids is similar. In the unstructured grids (Figures 4.3-*c* and 4.3-*d*) the neighboring cells (same as the cell A and B in Figure 4.5-*a*) have the same bed and water surface elevations and, in turn, FC effect of the first type is not expected. An unstructured grid highly reduces the spurious currents (Figure 4.7-*b*). When the unstructured grid is two times finer, the spurious currents will be reduced two times by order of magnitude (Figure 4.7-*c*).

(*a*)   (*b*)
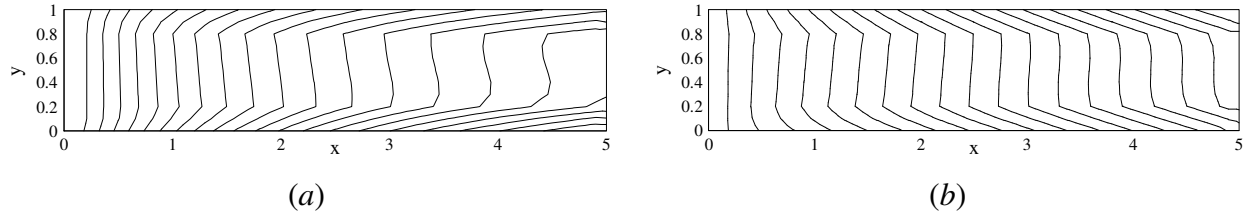
Figure 4.6. Contours of *u* velocity in a straight channel with rectangular cross section and without transverse slope; (*a*) $\partial Z_b/\partial x = -0.03$, $n = 0.0$ (Figure 4.4-*c*) and, (*b*) $\partial Z_b/\partial x = -0.01$, $n = 0.04$ (Figure 4.8-*c*).

(*a*)   (*b*)   (*c*)
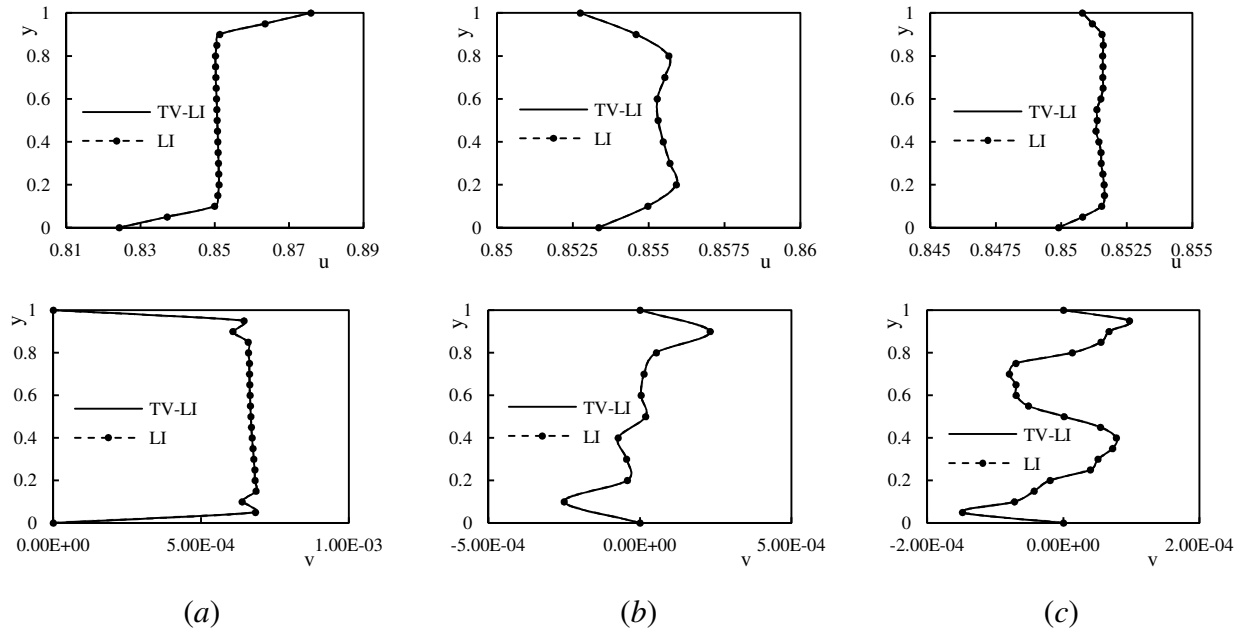
Figure 4.7. Velocity profiles in shear free channels with $\partial Z_b/\partial x = -0.01$; (*a*) 20 by 100 quad-split grid, (*b*) 10 by 50 unstructured grid and, (*c*) 20 by 100 unstructured grid.

In Table 4.1, TV-LI and LI methods are compared in terms of number of the iterations and the CPU time. The computer is a XPS M1330, the processor is an Intel(R) Core(TM) 2 Duo CPU T5800 @ 2.00GHz and, the memory is 3.00 GB. In Section 4.2.4.2 it is discussed that, more mathematical operations have to be performed in a TV-LI method compared to a LI method. Table 4.1 however indicates that TV-LI method reduces the computational efforts and, more reduction in computational effort can be expected on finer grids.

Table 4.1. Comparison of computational cost when TV-LI and LI methods are applied.

Grid type	Bed slope	Spacing at the domain boundaries	Interpolation method	Number of iterations	CPU time (s)
Quad-split	$\frac{\partial z_b}{\partial x} = 0.0$, $\frac{\partial z_b}{\partial y} = 0.0$	10×50	TV-LI	377	5.819
			LI	377	6.286
Quad-split	$\frac{\partial z_b}{\partial x} = 0.0$, $\frac{\partial z_b}{\partial y} = 0.0$	10×50	TV-LI	434	6.490
			LI	434	7.363
Quad-split	$\frac{\partial z_b}{\partial x} = 0.0$, $\frac{\partial z_b}{\partial y} = 0.0$	10×50	TV-LI	557	9.095
			LI	557	9.578
Quad-split	$\frac{\partial z_b}{\partial x} = 0.0$, $\frac{\partial z_b}{\partial y} = 0.0$	20×100	TV-LI	1302	70.606
			LI	1302	77.642
Unstructured	$\frac{\partial z_b}{\partial x} = 0.0$, $\frac{\partial z_b}{\partial y} = 0.0$	10×50	TV-LI	167	2.746
			LI	167	2.902
Unstructured	$\frac{\partial z_b}{\partial x} = 0.0$, $\frac{\partial z_b}{\partial y} = 0.0$	20×100	TV-LI	1085	65.661
			LI	1085	72.041

4.2.5.2 Pressurized flow: channels with bed resistance

Details of the test cases and the computational domain are similar to those in Section 4.2.5.1. The exceptions are Manning's number which is not zero and, the bed gradient which is set to -0.01. When the gradient of water surface (equivalently, pressure gradient) is negative, the flow is called pressurized flow. Such flow shows behaviors which differ from a loose flow.

For the first test case (Figure 4.8-*a*) Manning's number is 0.01. In the second test case (Figure 4.8-*b*) Manning's number is assumed 0.0225. For the third test case (Figure 4.8-*c*) Manning's number is 0.04. The grid used in these test cases is 10 by 50 on the domain boundaries (Figure 4.3-*a*). The longitudinal profiles of water surface elevation and, the velocity components at $x = 4$ are shown in Figure 4.8. The numerical results obtained from LI and TV-LI methods are exactly similar. At the channel centerline, the profile of water surface elevation simulated with Shallow Fluent is in good agreement with 1D tool. When Manning's number increases the spurious current reduces until horizontal water surface is attained (Figure 4.8-*b*). An addiotional increase in Manning's number causes a spurious current in opposite direction.

The reason behind such behavior can be addressed through FC effect of the second type. In Figure 4.5-*b* the sketch of the pressurized false currents in a quad-split grid is shown. When Manning's number is not zero, there will be a force at the cells A and B which acts in negative streamline direction. With increase in Manning's number this force increases and reduces the pressure gradient. At a threshold Manning's number the water surface will be horizontal (Figure 4.8-*b*). The horizontal water surface is characteristic of a shear free channel with zero bed slop and, as a result, there will be no false current (Figure 4.8-*b*). With more increase in Manning's number the flow will be pressurized. In pressurized flow, both the bed and water surface gradient from A toward B are positive. This is characteristic of a subcritical flow over a bed with positive bed gradient and, in turn, there will be a small subcritical flow from A toward B. This is called the FC effect of the second type. In a pressurized flow, the FC effect of the second type runs the spurious current (Figure 4.8-*c*). In Figure 4.5-*b*, the flux enters at the face 1 causes false currents which exit through face 3. The directions of these false currents are marked with dashed arrows. Since the flux enters at face 2 will also cause a false current at face 3, the near wall u velocity at $y \approx 0$ must gradually increase with the distance from the inlet. This can be observed in Figure 4.6-*b* through the contours of u velocity for the third test case (Figure 4.8-*c*). The FC effect of the second type is also expected to be independent of the grid resolution. If the grid does not permit continuous downstream directions, there will not be continuous FCs and, in turn, the FC effect of the second type will reduce.
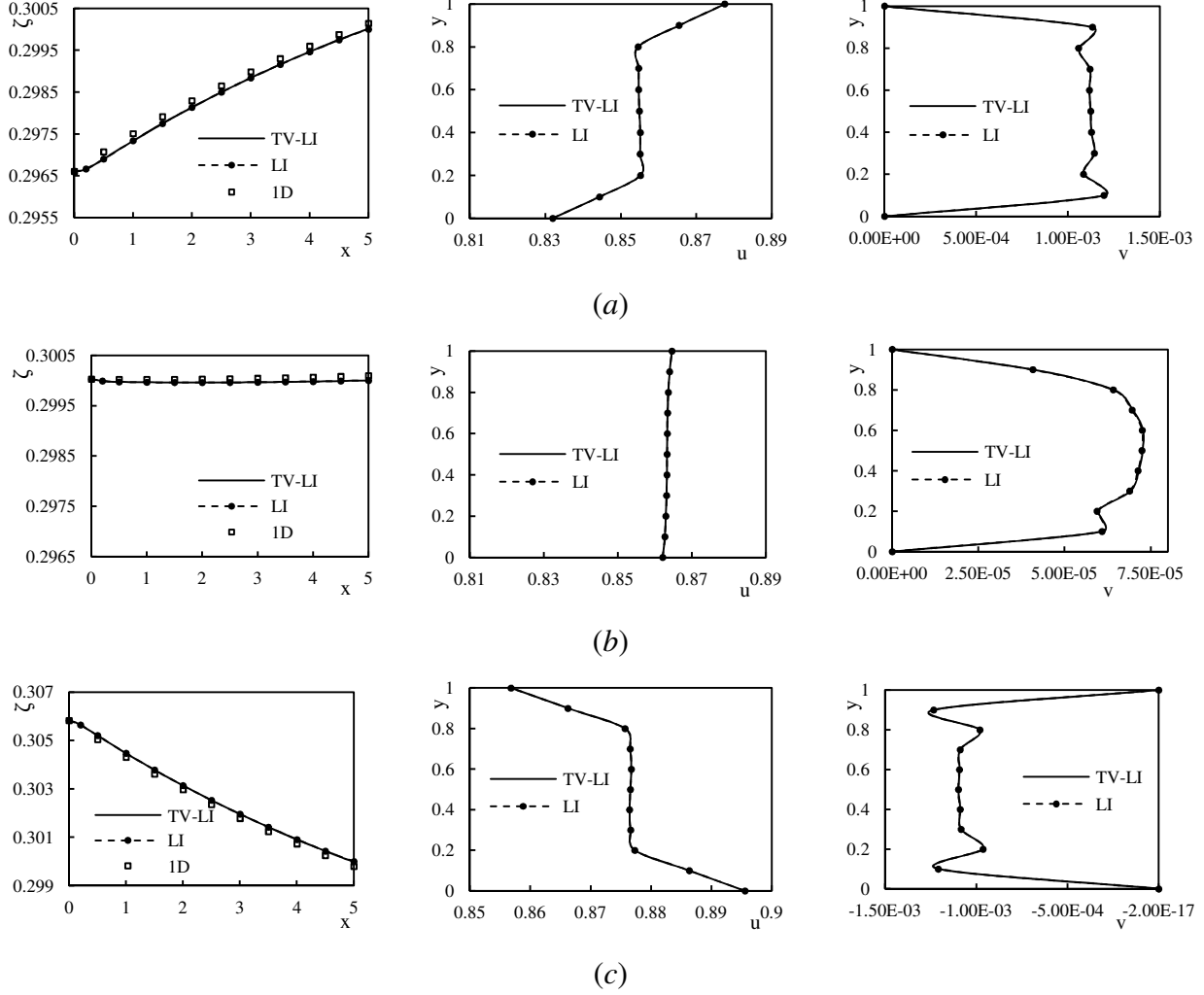
Figure 4.8. Profiles of water surface elevation, longitudinal, and transverse velocity in a straight channel with rectangular cross section and $\partial Z_b/\partial x = -0.01$; (*a*) $n = 0.01$, (*b*) $n = 0.0225$, and (*c*) $n = 0.04$. The left figures are the water surface elevation at the channel centerline, the middle figures are the u velocity at $x = 4$ from the inlet, and the right figures are the v velocity at the same position as u velocity.

Figure 4.9 is relevant to the third test case (Figure 4.8-*c*), but, an unstructured 10 by 50 grid (Figure 4.3-*c*) is used. When Figure 4.9 is compared with Figure 4.8-*c*, it can be observed that the spurious current has almost disappeared. Since in the unstructured grid (Figure 4.3-*c*) the neighboring cells (same as the cell A and B in Figure 4.5-*b*) have the same longitudinal position, the bed and water surface elevation in these cells are equal. In such condition, there will not be a FC effect of the second type. As it is expected from a high quality numerical code [29], in Figure

4.9 the numerical results obtained by means of a steady simulation and an unsteady simulation at steady-state are similar (regarding that the convergence criterion is set to 10^{-3}).

(a) (b) (c)
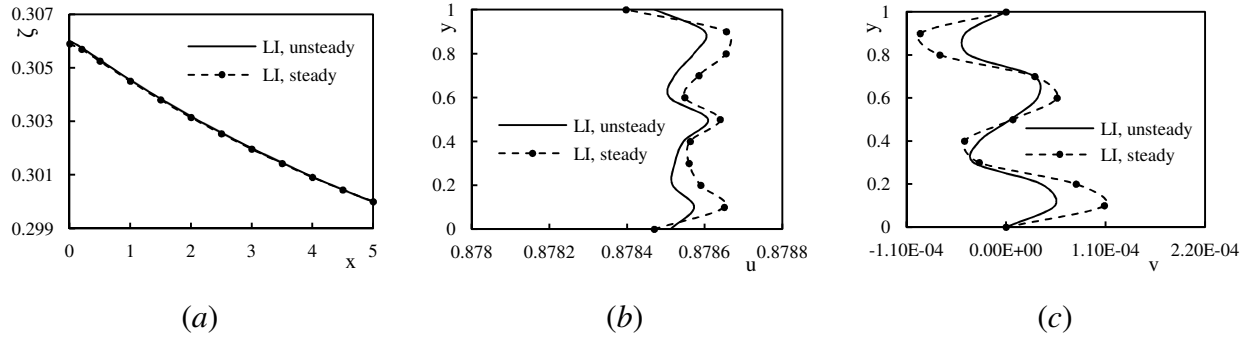
Figure 4.9. Steady flow and unsteady flow at steady-state in a straight channel with rectangular cross section; $\partial Z_b / \partial x = -0.01$, $n = 0.04$; (a) water surface elevation at the channel centerline, (b) u velocity at $x = 4$ from the inlet, and (c) v velocity at the same position as u velocity.

Table 4.2. Comparison of computational cost when TV-LI and LI methods are applied.

Grid type	Manning's n	Spacing at the domain boundaries	Interpolation method	Number of iterations	CPU time (s)
Quad-split	0.01	10×50	TV-LI	412	6.131
			LI	412	6.942
Quad-split	0.03	10×50	TV-LI	316	5.008
			LI	316	5.335
Quad-split	0.0259	10×50	TV-LI	345	5.179
			LI	345	5.944
Quad-split	0.04	10×50	TV-LI	260	4.072
			LI	260	4.415
Unstructured	0.04	10×50	TV-LI	253	4.774
			LI	253	5.070

In Table 4.2, the TV-LI and LI methods are compared in terms of number of the iterations and the CPU time. Table 4.2 indicates that the TV-LI method reduces the computational efforts compared with the LI method.

4.2.5.3 Steffler's bend

The geometrical details are shown in Figure 4.10. In the experiment [30] the side walls were galvanized sheet metal. Therefore, the smooth but no-slip condition is assumed on side walls.

Manning's number is 0.0125, the water depth at the outlet is 0.061 m, the total discharge at the inlet is 0.0235 m^3/s, and the bed gradient is -0.00083. The reference length, L_{ref}, is 0.061 m and, the reference velocity, U_{ref}, is 0.36 m/s. The water physical properties are same as in Section 4.2.5.1. Errors are normalized and, the convergence criterion is set to 10^{-3}. The grid contains 18398 nearly uniform unstructured triangular elements and, the number of the cells in channel cross section is about 20.

At the first test case the vorticity equation, Equation (4.14), is not solved. Profile of streamwise velocity is shown in Figure 4.11. In Figure 4.11 the origin of the sections, sec, is at the inner bank of the channel. In Figure 4.11 the numerical results are in good agreement with experimental data and, the results obtained from LI and TV-LI methods are exactly similar. The elapsed CPU times for the LI and TV-LI methods are 490 s and 449 s, respectively. The application of TV-LI method caused a 9% reduction in elapsed CPU time.
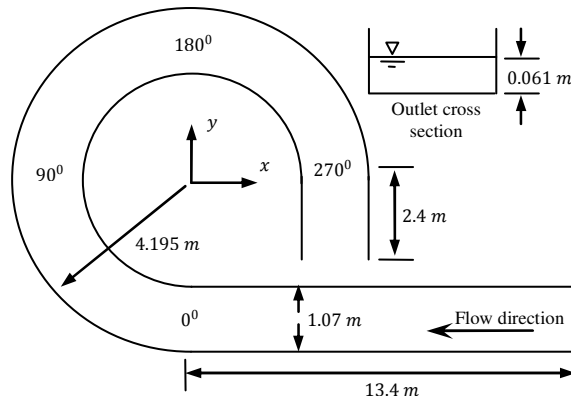
Figure 4.10. Geometrical details of the Steffler's bend.

At the second test case the vorticity equation is also solved. The numerical results obtained with and without solving the vorticity equation are presented in Figure 4.12. In Figure 4.12, the numerical results are also compared with measured data from [30] and, the numerical data from [9]. The hypothesis behind applying Equation (4.14) is that, the streamline curvature accelerates the streamwise velocity [17]. In Steffler's bend the inner bank has smaller curvature radius compared with the outer bank and, in turn, when Equation (4.14) is solved, the velocity near the inner bank is expected to increase. Such increase in near bank velocity causes a flatter velocity profile; see Figure 4.12. The numerical data of Wu and Wang [9] are the less accurate one. The

grid used by Wu and Wang [9] had 31 nodes in transverse direction and, in turn, its transverse resolution was 1.5 times more than the grid used in Shallow Fluent. According to Figure 4.12 it can be mentioned that, not the grid resolution alone, neither any modification which take account of the secondary flow effect, but the internal accuracy of a solver is the most important characteristic of the solver for having an accurate simulation.
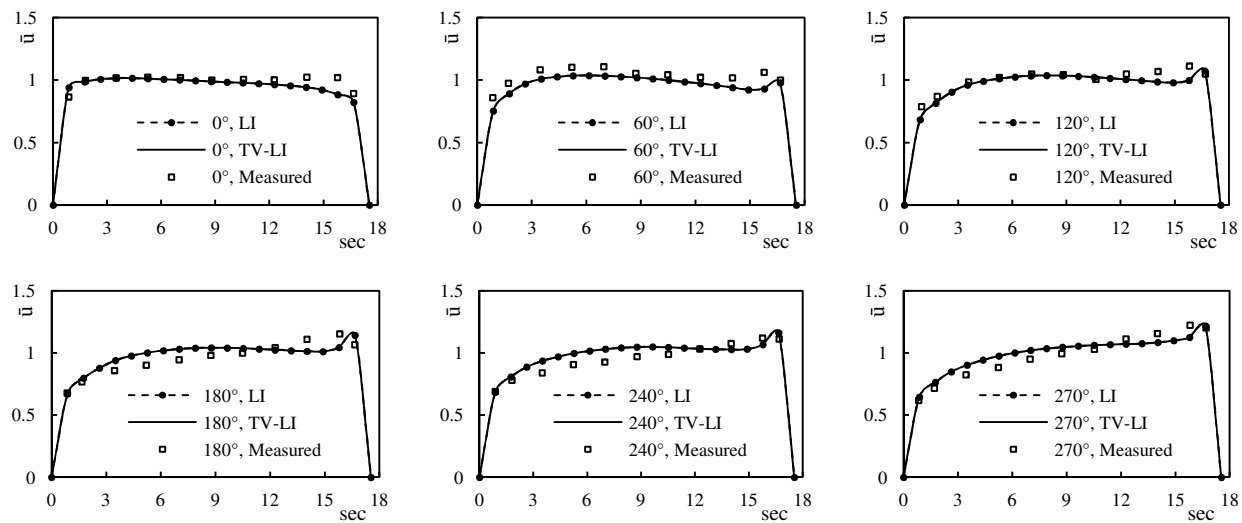
Figure 4.11. Profile of streamwise velocity in Steffler's bend at different sections, sec; measured data are from [30].
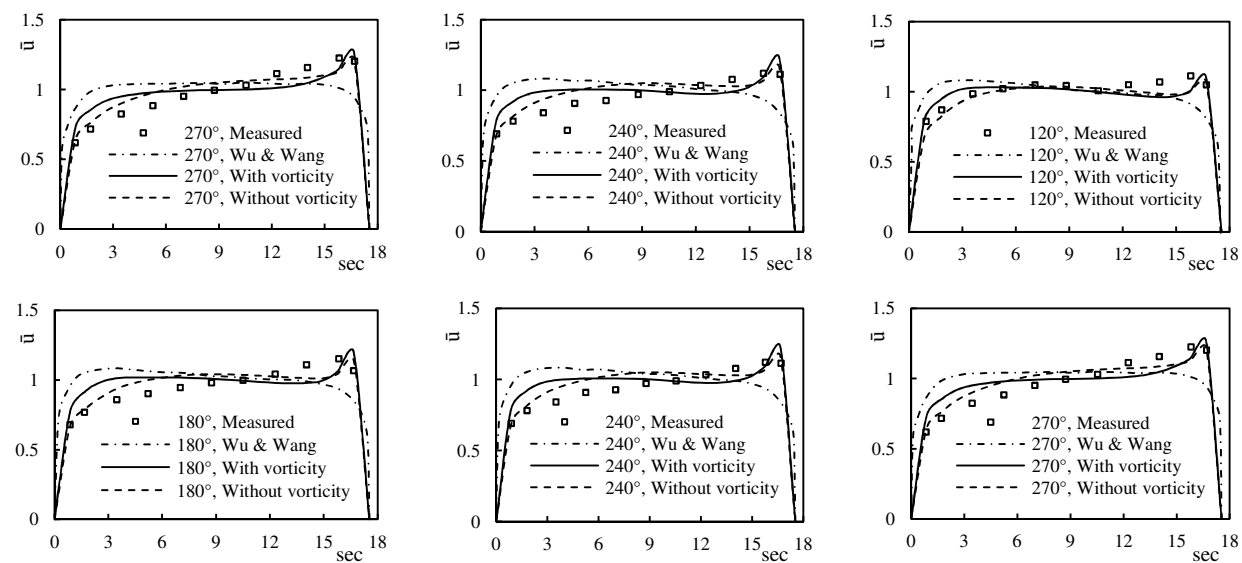
Figure 4.12. Profile of streamwise velocity in Steffler's bend at different sections, sec; measured data are from [30], and the Wu & Wang numerical data is from [9].

4.2.5.4 Double bend-way

The geometrical details are shown in Figure 4.13. In order to study the pure bed resistance effect the side walls are assumed free-slip. Manning's number is 0.03, the water depth at the outlet is $0.5\ m$, the total discharge at the inlet is $0.44587\ m^3/s$, and the bed gradient is zero. The reference length, L_{ref}, is $2.0\ m$ and, the reference velocity, U_{ref}, is $0.5\ m/s$. The water physical properties are the same as in Section 4.2.5.1. Errors are normalized and, the convergence criterion is set to 10^{-3}. The grid contains 19026 nearly uniform unstructured triangular elements and, the number of the cells in channel cross section is about 20. For the double bend-way test cases the vorticity equation, Equation (4.14), is not solved.

At the first test case the bed area scheme, as explained in the research case (c), is chosen. Profiles of streamwise velocity and water surface elevation are shown in Figure 4.14. In Figure 4.14 the position of $sec = 0.0$ is at the bank line which starts from $(x = -5, y = 4)$ and ends at $(x = 15, y = -11)$. In Figure 4.14 the results obtained from LI and TV-LI methods are exactly similar. The elapsed CPU times for the LI and TV-LI methods are $273\ s$ and $250\ s$, respectively. The application of TV-LI method caused a 9.2% reduction in the elapsed CPU time.
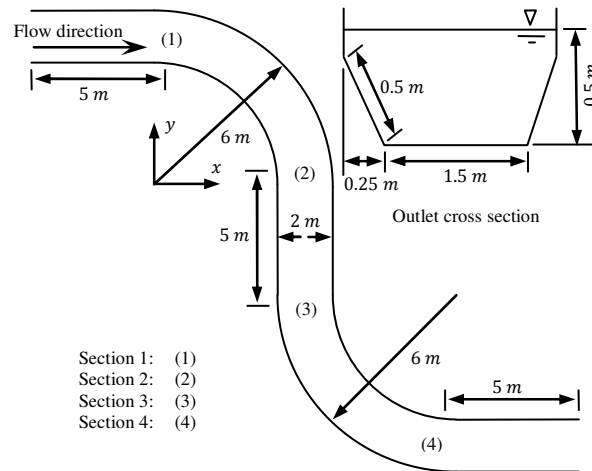
Figure 4.13. Geometrical details of the double bend-way.

At the second test case the bed area scheme is compared with the cell area scheme (Figure 4.15). At the sloped part of the bed, near the banks, the bed resistance calculated with the Bed Area (BA) scheme is two times more than the bed resistance calculated with the Cell Area (CA)

scheme. When the velocity at the sloped bed is high, the difference between the resisting forces calculated with the BA and CA schemes will be significant. In the case of CA scheme, the under predicted bed resistance causes an erroneous velocity profile especially near the banks with high near bank velocity (Figure 4.15). Since the BA scheme increases the computed averaged cross sectional bed resistance, the simulated water surface elevation using the BA scheme is more than the simulated water surface elevation using the CA scheme (Figure 4.15).
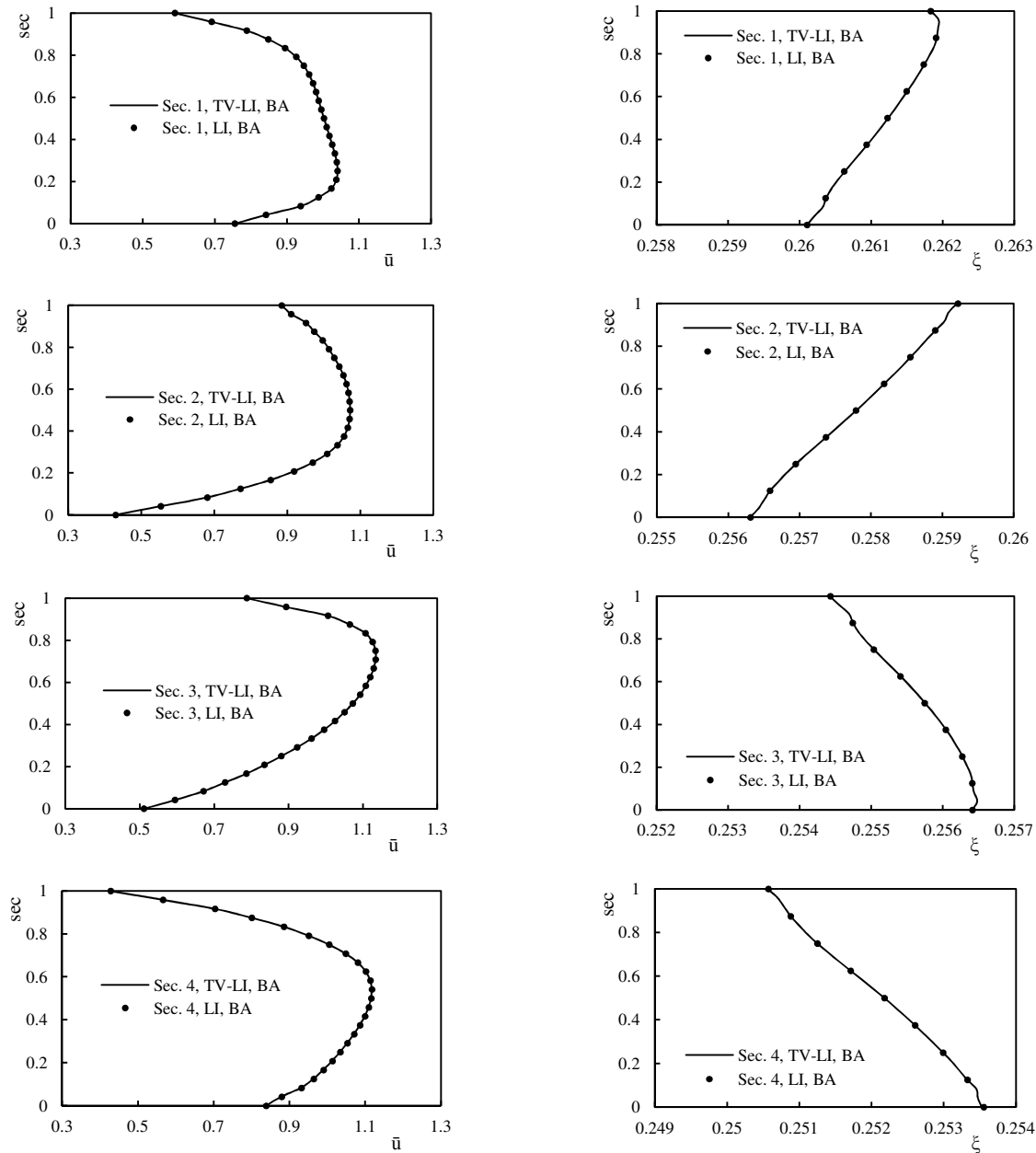
Figure 4.14. Profiles of streamwise velocity and water surface elevation in double bend-way test; a comparison between TV-LI and LI methods.
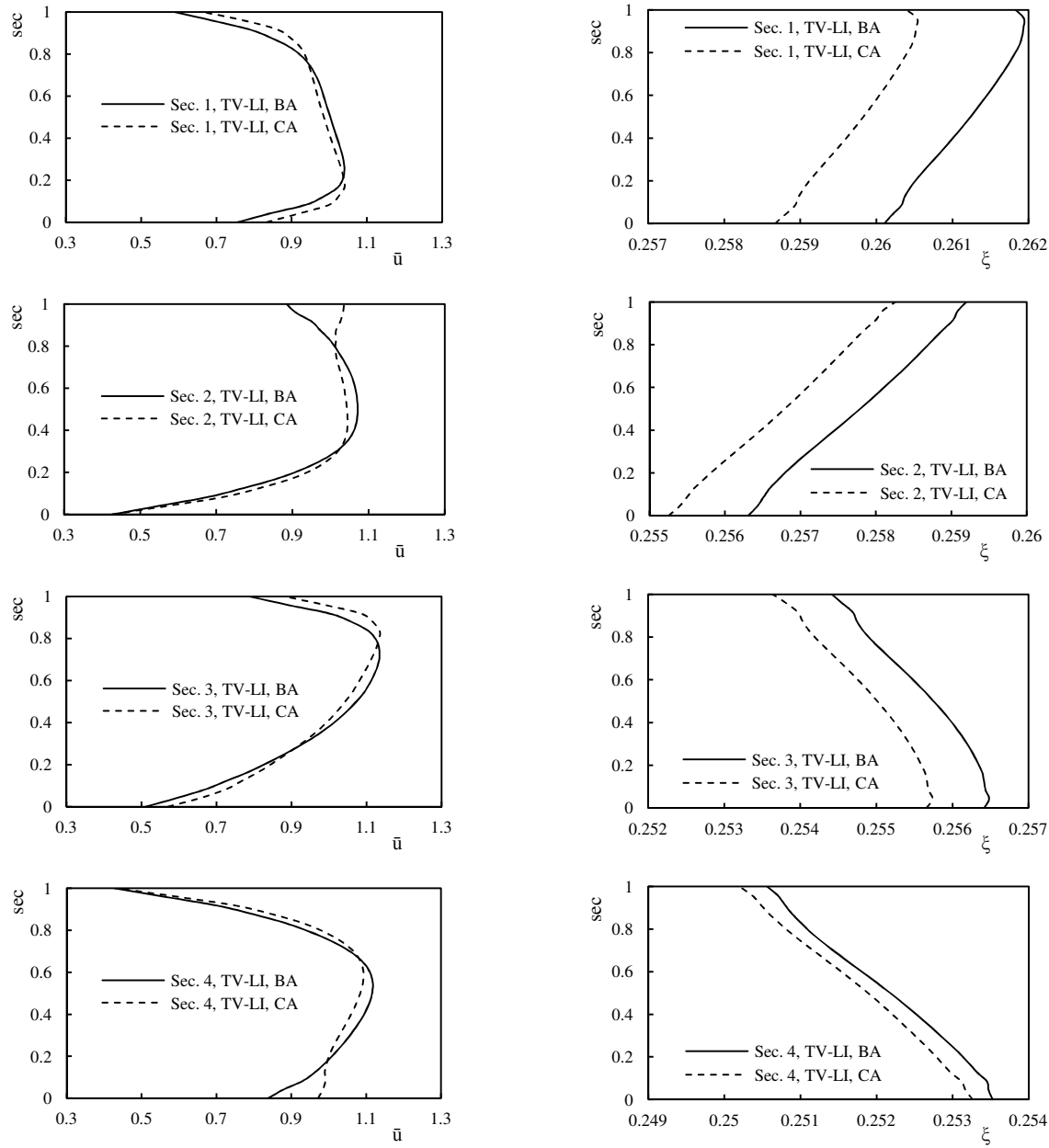
Figure 4.15. Profiles of streamwise velocity and water surface elevation in double bend-way test; a comparison between bed area, BA, and cell area, CA, schemes.

4.2.5.5 Dam break over a very shallow wet bed

Since in a dam break problem flow variables experience discontinuity, a dam break problem is a challenging test for numerical schemes. In this test, the computational domain is rectangular, with $L = 5\,m$ and $H = 1\,m$. The grid used in this test is shown in Figure 4.3-d. The physical domain is assumed a quadrilateral pool with free-slip wall boundaries. The pool's cross section is

rectangular, Manning's number is assumed 0.03, and the water surface elevation is $1.0\,m$ at $x \leq 1\,m$ and $0.001\,m$ at $x > 1\,m$. The water specific gravity and dynamic viscosity are $998.2\,kg/m^3$ and $0.001003\,N.m/s^2$. The gravitational acceleration is assumed $9.806\,m/s^2$, the initial velocity at the domain is zero, and the time step is $0.002823\,s$. The reference length and velocity are $1.0\,m$ and $4.4285\,m/s$, respectively. Errors are normalized and, the convergence criterion is set to 10^{-3}.
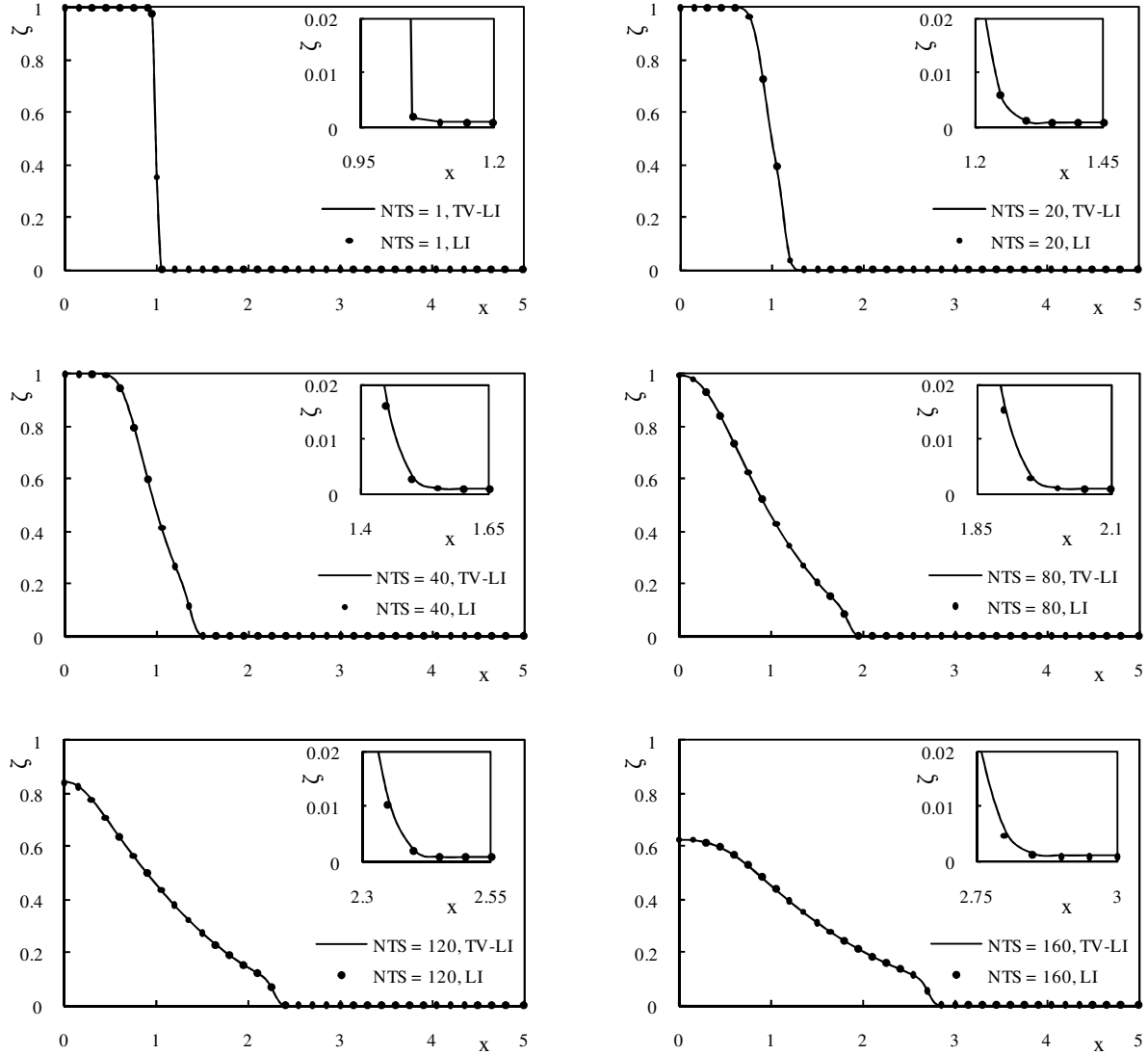
Figure 4.16. Comparison of TV-LI and LI method in a dam break problem.

In Figure 4.16 the numerical solutions at $y = 0.5$ at six different times are shown. When the Number of Time Steps, NTS, are less than 40, the numerical results are the same as the dam

break over a dry bed. But, for the number of time steps more than 80, a step which its height is about 1.5 can be observed. As the velocity experiences a jump at the front, numerical methods tend to produce spurious oscillations in the vicinity of the front [31]. It can be observed in Figure 4.16 that, there is no oscillation in the vicinity of the front and, in turn, the strategy devised in this article for treating the bed source terms is successful.

In Figure 4.16 the numerical results obtained with TV-LI and LI methods show ignorable differences and, as a result, it can be mentioned that these methods have the same accuracy in capturing discontinuities. The elapsed CPU times for TV-LI and LI methods are $690\,s$ and $749\,s$, respectively. The application of TV-LI method caused a 8.6% reduction in the elapsed CPU time.

4.2.6 Conclusion

In this article, four research cases were introduced and investigated:

- Research case (a): the transport equations were multiplied by appropriate power of the water depth in order to avoid numerical oscillations due to small water depths. The numerical tool was then applied to a dam break problem where the water depth in shallow region was as small as $0.001\,m$. The simulated water surface was smooth (without any oscillation), even near the discontinuity.

- Research case (b): in the entire test cases the TV-LI scheme was compared with LI scheme. Numerical results indicated that, the TV-LI scheme is as accurate as LI scheme, but, the TV-LI scheme reduces the computational efforts 9% by order of magnitude.

- Research case (c): the bed area scheme was compared with cell area scheme and, it is shown that the cell area scheme can cause significant error in numerical results.

- Research case (d): the occurrence of a non physical phenomenon, FC effects, was recognized in quad-split grids. It is shown that, an unstructured grid reduces the false currents and, the finer the unstructured grid the smaller the false current. False currents are likely when grid permits continuous downstream directions. As a result, in depth averaged simulations, Delaunay grids which do not permit such continuous downstream directions are more appropriate.

Since there is no general technique in order to take account of the secondary flow effects, a depth-averaged simulation is better to achieve through an appropriate numerical scheme and discretization technique.

4.2.7 References

1. Rhie CM, Chow WL. Numerical study of the turbulent flow past an airfoil with trailing edge separation. AIAA Journal 1983; 21 : 1525-1532.

2. Darwish M, Sraj I, Moukalled F. A coupled finite volume solver for the solution of incompressible flows on unstructured grids. Journal of Computational Physics 2009; 228 : 180-201.

3. Date AW. Solution of Navier-Stokes equations on non-staggered grid. International Journal of Heat and Mass Transfer 1993; 36 : 1913-1922.

4. Date AW. Fluid dynamical view of pressure checkerboarding problem and smoothing pressure correction on meshes with colocated variables. International Journal of Heat and Mass Transfer 2003; 46 : 4885-4898.

5. Gao W. Liu R. A hybrid finite volume/finite element method for incompressible generalized Newtonian fluid flows on unstructured triangular meshes. Acta Mechanica Sinica/Lixue Xuebao 2009; 25 : 747-760.

6. Minh Duc B. Berechnung der stroemung und des sedimenttransorts in fluessen mit einem tieffengemittelten numerischen verfahren. PhD thesis. The University of Karlsruhe: Karlsruhe, Germany. 1998.

7. Wu W. Depth-averaged two-dimensional numerical modeling of unsteady flow and nonuniform sediment transport in open channels. Journal of Hydraulic Engineering 2004; 130 : 1013-1024.

8. Wu W, Shields Jr FD, Bennett SJ, Wang SSY. A depth-averaged two-dimensional model for flow, sediment transport, and bed topography in curved channels with riparian vegetation. Water Resources Research 2005; 41 : W03015.

9. Wu W, Wang SSY. Depth-averaged 2-D calculation of flow and sediment transport in curved channels. International Journal of Sediment Research 2004; 19 : 241-257.

10. Brufau P, Garcia-Navarro P, Vazquez-Cendon ME. Zero mass error using unsteady wetting-drying conditions in shallow flows over dry irregular topography. International Journal for Numerical Methods in Fluids 2004; 45 : 1047-82.

11. Patankar SV. Numerical heat transfer and fluid flow. Hemisphere: New York, 1980.

12. Ferziger JH, Peric M. Computational methods for fluid dynamics. Springer: Berlin, Germany, 1996.

13. Roe PL. Approximate Riemann solvers, parameter vectors, and difference schemes. Journal of Computational Physics 1997; 135 : 250.

14. Castro Diaz MJ, Fernandez-Nieto ED, Ferreiro AM. Sediment transport models in Shallow Water equations and numerical approach by high order finite volume methods. Computers and Fluids 2008; 37 : 299-316.

15. Murillo J, Garcia-Navarro P, Brufau P, Burguete J. Extension of an explicit finite volume method to large time steps (CFL > 1): Application to shallow water flows. International Journal for Numerical Methods in Fluids 2006; 50 : 63-102.

16. Murillo J, Garcia-Navarro P, Brufau P, Burguete J. 2D modelling of erosion/deposition processes with suspended load using upwind finite volumes. Journal of Hydraulic Research 2008; 46 : 99-112.

17. Bernard RS. STREMR: Numerical model for depth-averaged incompressible flow. U.S. Army Engineer Waterway Experiment Station: Vicksburg, MS, 1993, pp. A4-A5 and C1-C6.

18. Mohamadian A, Le Roux DY, Tajrishi M, Mazaheri K. A mass conservative scheme for simulating shallow flows over variable topographies using unstructured grid,.Advances in Water Resources 2005; 28 : 523-539.

19. Zhou JG, Causon DM, Mingham CG, Ingram DM. The surface gradient method for the treatment of source terms in the shallow-water equations. Journal of Computational Physics 2001; 168 : 1-25.

20. Murillo J, Garcia-Navarro P, Burguete J. Analysis of a second-order upwind method for the simulation of solute transport in 2D shallow water flow. International Journal for Numerical Methods in Fluids 2008; 56 : 661-86.

21. Croft TN. Unstructured mesh - finite volume algorithms for swirling, turbulent, reacting flows. PhD thesis. School of Computing and Mathematical Sciences: University of Greenwich, 1998.

22. Rodi W. Turbulence models and their application in hydraulics. IAHR Monograph, Balkema, Rotterdam: Netherlands, 1993.

23. Date AW. Solution of transport equations on unstructured meshes with cell-centered colocated variables. Part I: Discretization. International Journal of Heat and Mass Transfer 2005; 48 : 1117-1127.

24. Fluent6.3_user's_guide, Fluent Inc: http://my.fit.edu/itresources/manuals/fluent6.3/ help/html/ug// main_pre.htm, 2010.

25. Moradi Larmaei M, Behzadi J, Mahdi T-F. Treatment of checkerboard pressure in the collocated unstructured finite-volume scheme. Numerical Heat Transfer, Part B: Fundamentals 2010; 58 : 121-144.

26. Versteeg HK, Malalasekera W. An introduction to computational fluid dynamics: the finite volume method. Pearson Prentice Hall: Toronto, 1995, ch. 6, 9.

27. Launder BE, Spalding DB. The numerical computation of turbulent flows. Computer Methods in Applied Mechanics and Engineering 1974; 3 : 269-289.

28. Moradi Larmaei M, Mahdi T-F. Analysis of SIMPLE algorithm for depth averaged simulations. 6th International Symposium on Environmental Hydraulics. Athens: Greece, 2010, June 23-25.

29. Acharya S, Baliga BR, Karki K, Murthy JY, Prakash C, Vanka SP. Pressure-based finite-volume methods in computational fluid dynamics. Journal of Heat Transfer 2007; 129 : 407-424.

30. Steffler PM. Turbulent flow in a curved rectangular channel. PhD thesis. Department of civil engineering, University of Alberta: Alberta, Canada, 1984.

31. Toro EF. Shock-capturing methods for free-surface shallow flows. John Wiley & Sons: Chichester, England, 2001, ch. 7.

CHAPTER 5   ARTICLE 3: A NEW METHOD FOR THE TREATMENT OF WETTING-DRYING FRONTS

5.1 Presentation of the article

In this section the objective of the article will be presented, as well as a conclusion on this work as part of the thesis. The wetting-drying treatment is an unavoidable part of any depth-averaged software either commercial such as Mike21/21C and solvers used in SMS (this can be verified by taking a look at the user's manual of these tools. In the case of MIKE21 the reader can download a demo from the site where the user's manual can be found in the demo. The download can be started at: www.mikebydhi.com/Download/MIKEByDHI2011.aspx and for the SMS the reader can look at www.aquaveo.com/sms) or, research such as CCHE2D (www.ncche.olemiss.edu/cche2d). The consequence effect of an improvement in this technique on engineering problems is a more accurate simulation of water front, and reduced computational cost. This can be important when, for instance, predicting the water front in a dam break problem.

5.1.1 Objective

When wetting-drying front exists in a model, what matters most in depth-averaged simulations is: whether the equations have to be solved on entire domain or only on wet region, how should one differentiate wet and dry cells, what should be the threshold depth, should one compute the flux at the interface between wet and dry cells, and if not, how should the wetting-drying front advance, and how to control the formation of cells with negative water depths. This article provides answer to these questions. When these questions are well answered, the developed solver can well handle any problem which include wetting-drying front. Before this step, the solver which is presented in this thesis was not able to handle such problems.

5.1.2 Conclusion

Since solution of transport equations only on wet region potentially reduces the computational cost, it will be recommended to do so. It is recommended in this thesis to use a one-threshold technique rather than a two-threshold technique, since a two-threshold technique can lead to a threshold dependent solution. Contrary to what the literature suggest about choosing an

appropriate threshold depth, it is indicated in this article that a smaller threshold does not guaranty a more accurate solution. Also, for the scheme suggested in this thesis, the threshold depth of about 10^{-4} is considered the best option. It is indicated that the flux at the interface between wet and dry cell can be computed if and only if the applied technique does not reduce the order of accuracy of the solution near the wetting-drying front. The wetting-drying front can advance with simple on-off logic without any effect on the computed results. A new technique is also suggested in order to prevent formation of cells with negative water depth.

The article is published at Applied Mathematical Modelling.

Moradi Larmaei, M., and Mahdi, T.-F. (2012). A new method for the treatment of wetting-drying fronts. Applied Mathematical Modelling, 36, 2286-2302.

5.2 A new method for the treatment of wetting-drying fronts

M. Moradi Larmaei and Tew-Fik Mahdi

Department of Civil, Geological and Mining Engineering, Montreal Polytechnic Institute, Montreal, Quebec, Canada.

5.2.1 Abstract

In this article, a new method is developed for the treatment of wetting-drying fronts in depth-averaged simulations. Some benchmark tests are devised in order to examine the performance of the new method at extreme conditions. The depth-averaged tool with two different wetting-drying process and Fluent6.3 are then applied to the benchmark tests. It is assumed that a solution by Fluent6.3 is the realistic solution and, a depth-averaged solution which is more similar to the solution by Fluent6.3 is more accurate.

Keywords: Depth-averaged simulation, Finite volume method, Unstructured grid, Wetting-Drying front

5.2.2 Introduction

Depth-averaged transport equations can be solved either on fixed [1-4] or moving grids [5]. In the case of moving grids the domain boundaries move so that computational domain exactly covers the physical domain. When a fixed grid is used, an appropriate strategy for moving the wetting-drying fronts on computational domain will be necessary [6]. In order to have a well established strategy for moving the wetting-drying fronts on fixed grids, some crucial cases have to be considered.

a) Whether the transport equations are solved on entire computational domain or only on wet cells, affects the way wetting-drying fronts are treated. In [7] continuity equation is solved on entire computational domain, but, momentum equations are solved only on wet cells. However, there is no constraint on solving the momentum equations on entire computational domain [8-10]. When the number of the wet cells is much smaller than the number of the dry cells, solving the transport equations only on wet cells is computationally efficient [11-13]. In

Nomenclature

a_0, a_j coefficients in the discretized equations

C_{s_j} volumetric flux at the cell face s_j

C_f the bed friction coefficient

g gravitational acceleration

G the rate of production in $k - \varepsilon$ model equation

h water depth

$h_{c_0\_c_j}$ the normal distance between two neighbor cells

k turbulence kinematic energy

L length scale

n the direction along $\boldsymbol{n}$ or Manning's number

$\boldsymbol{n}$ unit vector normal to the cell face

P, P' pressure and pressure correction, respectively

$\boldsymbol{r}_{c_j\_s_j}, \boldsymbol{r}_{c_0\_s}$ distance vectors between the cell's center and the face's center

R residual at the domain

R_e Reynolds number

$s_j, \boldsymbol{s}_j$ cell face area and the area vector, respectively

$S, \boldsymbol{S}$ Scalar and vector form of the source terms, respectively

t time

u, v velocity components in x and y directions, respectively

U velocity scale

$\boldsymbol{u}$ velocity vector

x, y x and y directions

Z_b bed elevation

$|\ \ |$ for any vector $\boldsymbol{b}$, $|\boldsymbol{b}|$ refers to the argument of the vector

Greek symbols

α general relaxation factor

ε dissipation rate of k

ϑ° continuity residual

ϑ normalized continuity residual

μ, μ_t laminar and turbulent dynamic viscosity, respectively

ξ water surface elevation

ρ fluid density

σ Prandtl/Schmidt number

$\tau, \boldsymbol{\tau}$ scalar and vector stresses

φ general scalar quantity

χ Prandtl/Schmidt number in general discretized equation for φ

ω_{rc} relaxation factor in pressure correction term

Ω volume

Subscripts

b refers to the river/channel bed

j refers to the neighboring cell

k refers to turbulence kinematic energy

p_φ refers to the implicit part of the source term in discretized equation for φ

ref refers to reference value

R refers to residual at the domain

s_j refers to cell face s_j

th refers to threshold

ε refers to dissipation rate of k

τ refers to shear

φ refers to φ

0 refers to central cell

Superscripts

n refers to the current time step

P refers to pressure

T refers to the transpose of a vector

u refers to $\boldsymbol{u}$

φ refers to φ

$+$ refers to an initial guess (can be from previous iteration)

$*$ refers to the dimensional form of a quantity

this article, the transport equations are solved on double-sided symmetric test cases. At one side, the transport equations are solved on the entire domain; at the other side, the transport equations are solved only on wet cells. The numerical results are then compared and discussed.

b) It is possible to calculate the flux at the face between wet and dry cells [12,14,15] or, set it to zero [10,16]. In order to set the flux to zero, a boundary condition has to be applied. When Saint Venant equations are solved, the boundary condition can be as simple as setting the normal velocity to zero [16]. In the case of hydrostatic depth-averaged equations, a normal choice can be using wall function aproach [10]. In this article, it will be discussed whether calculation of flux at the face between wet and dry cells or, applying a boundary condition which sets the flux to zero significantly affect the solution or not.

c) When a down-slope fluid flow, independent of wet or dry condition at the cell downstream of a face, a negative water depth at the cell upstream of the face is always possible. In order to avoid negative water depths, local and general water redistribution algorithms seems to be inevitable [15,16]. In this article, in order to cope with negative water depth, a new strategy is developed which is suitable for finite volume SIMPLE algorithm. Currently, SIMPLE algorithm is widely used for solving the hydrostatic shallow flow equations [12,17-19].

d) When fluid flux at the cell face is calculated, the order of accuracy of the wetting-drying treatment explicitly affects the order of accuracy of the solution near wetting-drying fronts [8,16,20]; i.e. the order of accuracy of the solution near wetting-drying fronts is limited to the order of accuracy of wetting-drying treatment. If a boundary condition is applied to wetting-drying fronts, the order of accuracy of the solution only implicitly depends to the order of accuracy of the wetting-drying treatment. In this article, a high order wetting-drying treatment is devised which does not explicitly restrict the order of accuracy of the solution.

e) What differentiates wet and dry cells is the threshold water depth [7,11,21]. With a two-threshold technique [9,22] solution will be highly threshold dependent; e.g. number of the cells where the water depth is between threshold depths will highly depends to the difference between threshold depths. Thus, using only one threshold depth is significantly important. In [21], the effect of the threshold depth is studied on numerical simulation of dam break over shallow wed bed. In this article, the effect of threshold water depth on numerical simulations is also examined.

The remainder of this article is divided into three sections. In the first section, the hydrostatic shallow flow model is presented. This section contains the dimensionless conservative form of the depth-averaged transport equations and their discretized form. The second section is devoted to the new treatment for wetting-drying fronts. The research cases (a) to (d) are also discussed in this section. Numerical results are presented in the third section.

5.2.3 Shallow Fluent: hydrostatic shallow flow model

Shallow Fluent is a tool the authors are developing in Montreal Polytechnic Institute. The code, Shallow Fluent, is extensively validated [23-26]. In this section, the governing equations and the detail of discretization scheme will be introduced. Also, the boundary conditions and the residual criterion used in this article will be presented.

5.2.3.1 Governing equations

The dimensionless conservative vector form of the depth-averaged continuity and momentum equations can be given by:

$$\frac{\partial (P/g)}{\partial t} + \boldsymbol{\nabla}.(h\boldsymbol{u}) = 0 \tag{5.1}$$

$$\frac{\partial (h\boldsymbol{u})}{\partial t} + \boldsymbol{\nabla}.(h\boldsymbol{u}\boldsymbol{u}) = -h\nabla P + \frac{1}{R_e}\boldsymbol{\nabla}.[h(1+\mu_t)\boldsymbol{\nabla}\boldsymbol{u}^T] - \boldsymbol{\tau}_b \tag{5.2}$$

where, $\boldsymbol{u} = \boldsymbol{u}^*/U_{ref}$, $t = t^*U_{ref}/L_{ref}$, $R_e = \rho^*U_{ref}l_{ref}/\mu^*$, $\mu_t = \mu_t^*/\mu^*$, and $P = (P^* - P_{ref})/(\rho^*U_{ref}^2)$. In Equation (5.2) the effect of secondary forces is ignored. The dimensionless bed shear stress, $\boldsymbol{\tau}_b$, can be expressed as:

$$\boldsymbol{\tau}_b = c_f|\boldsymbol{u}|\boldsymbol{u} \tag{5.3}$$

$$C_f = g\,n^2/h^{1/3} \tag{5.4}$$

where, $n = n^* U_{ref}/L_{ref}^{2/3}$.

In Shallow Fluent, the solver which is presented in this article, the standard $k - \varepsilon$ model is selected in order to simulate turbulent flows. The dimensionless conservative form of k and ε equations are given by:

$$\frac{\partial(hk)}{\partial t} + \nabla.(hk\boldsymbol{u}) = \frac{1}{R_e}\nabla.\left[h\left(1 + \frac{\mu_t}{\sigma_k}\right)\nabla k\right] + S_k \tag{5.5}$$

$$\frac{\partial(h\varepsilon)}{\partial t} + \nabla.(h\varepsilon\boldsymbol{u}) = \frac{1}{R_e}\nabla.\left[h\left(1 + \frac{\mu_t}{\sigma_\varepsilon}\right)\nabla\varepsilon\right] + S_\varepsilon \tag{5.6}$$

where, $S_k = h(G_k - \varepsilon + G_{kb})$, and $S_\varepsilon = h(C_{\varepsilon 1}G_k\,\varepsilon/k - C_{\varepsilon 2}\,\varepsilon^2/k + G_{\varepsilon b})$. G_k, G_{kb}, and $G_{\varepsilon b}$ are given by:

$$G_k = \frac{\mu_t}{R_e}\left[\left(\frac{\partial u}{\partial y} + \frac{\partial v}{\partial x}\right)^2 + 2\left(\frac{\partial u}{\partial x}\right)^2 + 2\left(\frac{\partial v}{\partial y}\right)^2\right] \tag{5.7}$$

$$G_{kb} = C_f^{-1/2}\,U_\tau^3/h \tag{5.8}$$

$$G_{\varepsilon b} = C_{\varepsilon\Gamma}C_{\varepsilon 2}c_\mu^{1/2}C_f^{-3/4}\,U_\tau^4/h^2 \tag{5.9}$$

where, $U_\tau = \sqrt{|\boldsymbol{\tau}_b|}$, $\mu_t = C_\mu R_e \frac{k^2}{\varepsilon}$, $k = k^*/U_{ref}^2$, $\varepsilon = \varepsilon^*/\left(U_{ref}^3/L_{ref}\right)$, and the model's constants are $C_\mu = 0.09$, $C_{\varepsilon 1} = 1.44$, $C_{\varepsilon 2} = 1.92$, $\sigma_k = 1.0$ and $\sigma_\varepsilon = 1.3$. Following Rodi [27], the coefficient $C_{\varepsilon\Gamma}$ is set to 3.6 for flumes and 1.8 for rivers.

5.2.3.2 Discretization scheme

In Shallow Fluent, SIMPLE algorithm is applied for the coupling between pressure and velocity field. In SIMPLE algorithm continuity equation [Equation (5.1)] is converted into a pressure correction equation. Momentum equations are solved with an initial guessed pressure and velocity field. The derived velocity field then is used in the pressure correction equation. The obtained pressure correction corrects the pressure and velocity field, other scalars if there are any will be solved, and the solution continues in the next iteration until convergence is attained. The correction to pressure and velocity at any cell is given by:

$$P = P^+ + \alpha P' \tag{5.10}$$

$$\boldsymbol{u} = \boldsymbol{u}^+ - \frac{\alpha \Omega h^{4/3}}{a_0^u} \nabla P' \tag{5.11}$$

In this article, convective terms are discretized with the first order upwind scheme, Green's theorem is used for the calculation of the gradient at cell center, and the two point method for the calculation of gradient at the cell face. The discretized pressure correction equation then can be expressed as:

$$a_0^P P_0' = \sum_{j=1}^{3} a_j^P P_j' - \vartheta^\circ \tag{5.12}$$

$$a_j^P = \frac{h_{s_j} s_j}{2 h_{c_0\_c_j}} \left[\left(\frac{\Omega h^{4/3}}{a_0^u} \right)_0 + \left(\frac{\Omega h^{4/3}}{a_0^u} \right)_j \right] \tag{5.13}$$

$$a_0^P = \sum_{j=1}^{3} a_j^P + \frac{\Omega_0}{g \Delta t} \tag{5.14}$$

The discretized equation for the conserved variable, φ, in a triangular grid can be written as [23]:

$$a_0^\varphi \varphi_0 = \sum_{j=1}^{3} a_j^\varphi \varphi_j + S_{u_\varphi} \tag{5.15}$$

$$a_0^\varphi = h^\beta \left[\sum_{j=1}^{3} \left[\!\left[C_{S_j}, 0 \right]\!\right] + \frac{1}{Re} \sum_{j=1}^{3} \left(\frac{\left(h(1 + \mu_t/\chi) \right)_{s_j} s_j}{h_{c_0\_c_j}} \right) \right] - S_{p_\varphi} \tag{5.16}$$

$$a_j^\varphi = h^\beta \left[\left[\!\left[-C_{S_j}, 0 \right]\!\right] + \frac{\left(h(1 + \mu_t/\chi) \right)_{s_j} s_j}{Re h_{c_0\_c_j}} \right] \tag{5.17}$$

where, $\left[\!\left[C_{S_j}, 0 \right]\!\right]$ denotes the maximum of C_{S_j} and 0. In Equations (5.16) and (5.17) χ is 1.0, σ_k and σ_ε for momentum, turbulence kinematic energy, and turbulence dissipation rate equations, respectively. In Equations (5.16) and (5.17) β is 1/3, 1/3, and 17/12 for momentum, turbulence kinematic energy, and turbulence dissipation rate equations, respectively. Figure 5.1 depicts the geometrical notations.

The Rhie and Chow [28] pressure interpolation technique is applied in order to obtain a mass conserving velocity at the cell face. In Shallow Fluent, the cell face velocities are not linearly interpolated; instead, a momentum-weighted averaging is performed [29]. The continuity residual can be expressed as:

$$\vartheta^\circ = \sum_{j=1}^{3} \left\{ \frac{(u a_0^u)_0 + (u a_0^u)_j}{(a_0^u)_0 + (a_0^u)_j} \cdot \boldsymbol{s}_j - \omega_{rc} a_j^P (P_j - P_0) \right\} + \frac{\Omega_0}{g \Delta t} (P_0^+ - P_0^{n-1}) \tag{5.18}$$
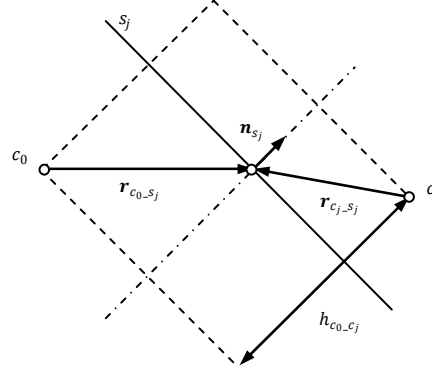
Figure 5.1. Geometrical notations used in discretized equations relevant to a cell and its immediate neighbors: central cell, c_0, neighboring cell, c_j, cell face, s_j, unit vector normal to the cell face, $\boldsymbol{n}_{s_j}$, distance vector, $\boldsymbol{r}$, and normal distance between cell centers, $h_{c_0\_c_j}$.

The relaxation factor in Rhie and Chow [28] pressure correction term, ω_{rc}, is set to 1.0 [24]. Following [23], the discretized bed source terms can be written as:

$$\boldsymbol{\tau}_b = 2gn^2|\boldsymbol{u}^+|\boldsymbol{u} - gn^2|\boldsymbol{u}^+|\boldsymbol{u}^+ \tag{5.19}$$

$$G_{kb} = 2gn^2|\boldsymbol{u}|^3 - gn^2|\boldsymbol{u}|^3\frac{k}{k^+} \tag{5.20}$$

$$G_{\varepsilon b} = 2c_{\varepsilon\Gamma}c_{\varepsilon2}c_\mu^{1/2}g^{5/4}n^{5/2}|\boldsymbol{u}|^4 - c_{\varepsilon\Gamma}c_{\varepsilon2}c_\mu^{1/2}g^{5/4}n^{5/2}|\boldsymbol{u}|^4\frac{\varepsilon}{\varepsilon^+} \tag{5.21}$$

5.2.3.3 Boundary conditions

The boundary condition used on the entire domain boundaries is the wall boundary. For the near wall treatment, the standard wall function approach [30] is applied to the momentum and turbulence model equations.

5.2.3.4 Residuals

The normalized continuity residual is given by:

$$\vartheta_R = \frac{\sum_{i=1}^{N_{cell}}|\vartheta^\circ|}{\vartheta_{ref}^\circ} \tag{5.22}$$

where, ϑ_{ref}° is the largest absolute value of the continuity residual in the first five iterations. The residual for any conserved variable, φ, is expressed as:

$$R_\varphi = \frac{\sum_{i=1}^{N_{cell}} \left| \sum_{j=1}^{3} a_j^\varphi \varphi_j + s_{u_\varphi} - a_0^\varphi \varphi_0 \right|}{R_{ref}} \tag{5.23}$$

where, R_{ref} is the largest absolute value of the φ residual in the first five iterations. Depending upon the unsteady problem, the ϑ_{ref}° and R_{ref} can be set only at the first time step or independently at every time step. This issue will be discussed, in Section 5.2.5.

5.2.4 Wetting-Drying treatment

In this section the research cases (a) to (e) (see Section 5.2.2) are discussed and, for every case, a solution is suggested. After having an appropriate strategy, a second order accurate wetting-drying treatment is developed.

5.2.4.1 Solution on entire computational domain versus solution on wet cells

In a dam break over a dry bed, when the dry region is initially wetted to a small threshold depth, the numerical solution can be very erroneous [31]. Thus, since the transport equations cannot be solved on absolutely dry cells, they have to be solved only on wet cells. On the other hand, solving the transport equations only on wet cells has not to affect the solution.

Volume Of Fluid (VOF) is a technique for capturing the interface between two fluids. Since this technique can capture the sharp interface between two fluids, it is used in many research works [32-34]. In [35] translation of a square block of fluid by a steady uniform flow on a Cartesian square domain is simulated using the Hirt and Nichols [36] and several other VOF methods. The domain had dimensions of 1.0 m^2 and was composed of 10,000 equally sized cells. A square block of fluid with dimensions 0.1 m^2 moved with equal horizontal and vertical velocities of 1.0 m/s from bottom left-had corner of the computational domain toward the top right-hand corner. In this test, the geometric shape had to remain intact In Hirt and Nichols [36] algorithm equations are solved only in water phase while in the rest of the algorithms equations are solved in both water and air. All VOF methods, presented in [35], perfectly predict the spatial position of the center of the block of fluid (note that the distortion of the square block of fluid is a consequence of the error in geometrically reconstructed flux polygon). Thus, a successful solution of depth-averaged transport equations only on wet cells is potentially possible. This issue is numerically investigated in section 5.2.5.

5.2.4.2 Flux at the face between wet and dry cells

The calculated flux at the cell face [11,15] is a bounded flux which guarantees the stability of the solver. This calculated flux is an approximation, not the exact flux. Another approximation of the flux is a zero flux at the cell face. This approximation is acceptable if the numerical solution of a physical problem (e.g. dam break over dry bed) is accurate.

In VOF method the volume of water is fixed at every time step. When the solution has converged, the VOF fraction at the cells adjacent to the interface will be updated (see [35-37] for example). This is the strategy which is used in this article; i.e. the wet region is fixed at every time step and, when the solution is converged the status (i.e. wet or dry condition) of cells near the wetting-drying fronts is updated. Since the depth-averaged transport equations are only solved on wet cells, applying such strategy demands application of a boundary condition on wetting-drying fronts. In order to have a zero flux at the face between wet and dry cells, the wall boundary condition [30] is applied. The success of this approach is numerically examined in Section 5.2.5.

5.2.4.3 Down-slope fluid flow

In shallow Fluent, the dependent variables are the velocity components and the water surface elevation. The water depth is calculated as a difference between the water surface and bed elevations. The solver internally works with hydrostatic pressure field. When required, the hydrostatic pressure will be converted to water surface elevation with $\xi = P/g$. Thus, in order to prevent a negative water depth, the water surface elevation at a cell has to be always more than bed elevation. A mass and momentum conservative technique can be achieved through modification of pressure correction when the water depth falls below the threshold depth. The temporary pressure and water depth are expressed as:

$$P_{tmp_0} = P_0^+ + \alpha P_0'$$

$$h_{tmp_0} = \frac{P_{tmp_0}}{g} - Z_{b_0}$$

When the water depth at the central cell, c_0, is more than the threshold depth, the temporary pressure and depth are accepted, otherwise the pressure correction, P_0', water depth, h_0, and pressure, P_0, are corrected as:

$$h_0 = h_{th} \tag{5.24}$$

$$P_0 = \left(h_0 + Z_{b_0}\right)/g \tag{5.25}$$

$$P_0' = (P_0 - P_0^+)/\alpha \tag{5.26}$$

This pressure correction is then used in Equation (5.11) in order to update the velocity field. When a dry cell receives fluid, it has to be initialized with zero velocity. This minimizes the flux through the faces of an already wetted cell and, in turn, prevents extension of errors.

5.2.4.4 A second order wetting-drying method

In Figure 5.2 the Simple Line Interface Calculation (SLIC) type VOF method of Nobari et al. [35], the Piecewise Linear Interface Calculation (PLIC) type VOF method of Harvie and Feletcher [37] and, the experimental work by Martin and Moyce [38] on a dam break over a dry flat bed are compared (note that in Figure 5.2, simulation of dam break using PLIC method is done by Hieu et al. [39]). In Figure 5.2, the SLIC type VOF, which is a first order technique, significantly over predicts the position of the leading edge of water. Near the bed, a SLIC method permits flux of water to a downstream cell as soon as the VOF at the upstream cell is above a predefined threshold. But, in PLIC method the gradient of the interface is calculated and, interface is reconstructed. Thus, a PLIC method prevents extension of thin layers of fluid. The same strategy can be used in order to reconstruct the water surface near wetting-drying fronts.
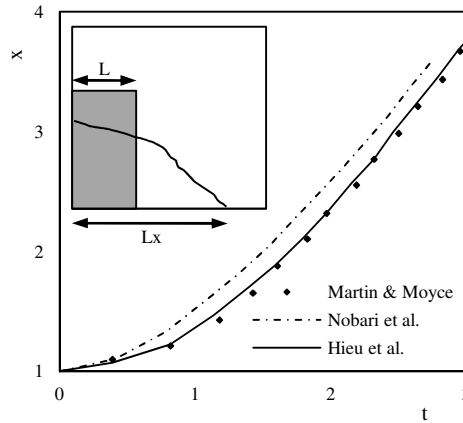
Figure 5.2. Time history of the position of the leading edge of water.

In Figure 5.3, a quarter of a disk is schematically reconstructed with first order wetting/drying treatment, second order wetting/drying treatment, and PLIC VOF method. Compared to a depth-averaged simulation, in a 2D vertical simulation, grid has more resolution in vertical direction. As a result, the disk reconstructed by PLIC method has the best resolution. In Figure 5.3, if the dash-dot line is assumed the bed, the first order depth-averaged method permits flux of fluid from cell "A" to cell "B". But, the second order method does not allow flux of fluid since the face between cells "A" and "B" is dry (Figure 5.3-*b*). In practice, the order of accuracy of wetting-drying treatment is independent of the order of accuracy of the solution. Thus, only the water surface at cell "A", where fluid can flux from a wet cell to a dry cell, has to be reconstructed. The solution can have any order of accuracy independent of the order of accuracy of the wetting-drying process. The proposed wetting-drying process contains three main steps as follows:

(*a*) (*b*) (*c*)
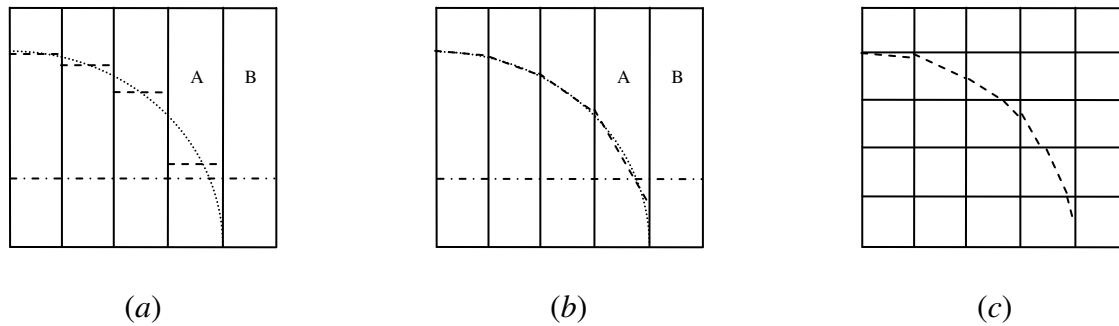
Figure 5.3. Reconstructed quarter of a disk; (*a*) first order, depth-averaged; (*b*) second order, depth-averaged; (*c*) PLIC, 2D vertical. Dot line is the actual water surface; Dash line is the reconstructed water surface; Dash-dot line is the assumed flat bed.

5.2.4.4.1 Cell marking

A cell is marked as wet-interior if the water depth at cell center is above a predefined threshold and, all neighboring cells are wet. If a wet cell has a dry neighboring cell, it is marked as wet-boundary cell. When the entire neighboring cells are dry, the cell is marked as wet isolated. During simulation, a wet-isolated cell is treated as a dry cell; i.e. the transport equations are not solved on wet-isolated cells. A dry-exterior cell is a dry cell which has no wet neighboring cell. If any of the neighboring cells are wet, a dry cell is marked as dry-boundary cell. When all neighboring cells are wet, a dry cell is marked as dry-island.

5.2.4.4.2 Dry cell wetting

In general, any wetting-drying front can be categorized as flooding condition (Figure 5.4) or dam-break condition (Figure 5.5). In Figures 5.4 and 5.5 the cell "L" is a wet cell and, the cell "R" is a dry cell. In this article, the definition of dam-break or flooding is independent of the velocity direction. For example, in Figure 5.5 the velocity vector at cell "L" can have any direction. But, a flux through the face between cells "L" and "R" can be prevented if the direction of the velocity is from "R" to "L".
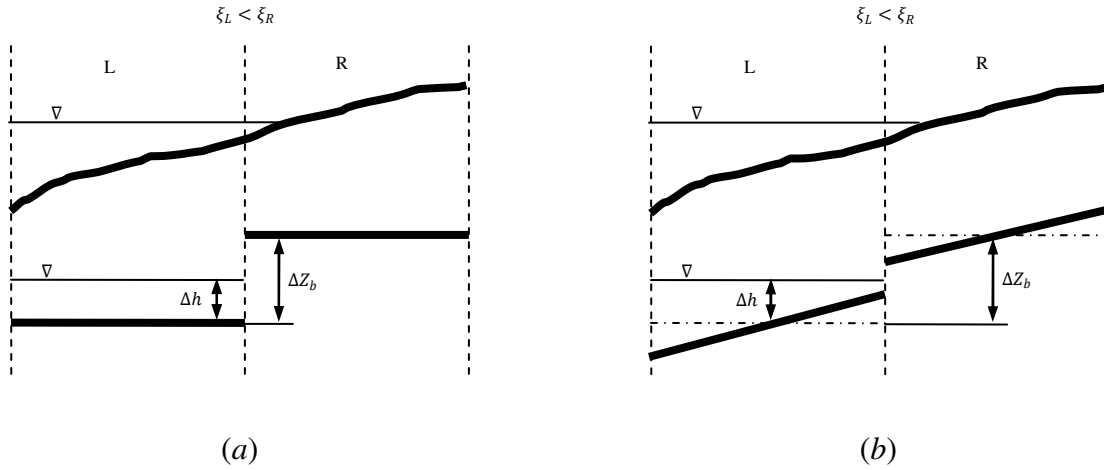
Figure 5.4. Reconstruction of flooding wetting-drying front; (*a*) first order; (*b*) second order.

In a second order accurate wetting-drying process, the gradient of bed and water surface elevation has to be calculated at wet-boundary cells. Assuming a permeable bed in Figure 5.4, when the water run up/down, the water surface elevation in "R", ξ_R, is less/more than the water surface elevation in "L", ξ_L. But, the water surface elevation in "R" is always limited to the bed elevation in this cell, Z_{b_R} (since the cell "R" is assumed dry). Thus, the most realistic assumption for the gradient of water surface elevation at the face between cells "R" and "L" is a zero gradient; i.e. $\xi_R = \xi_L$. Having this boundary condition, the gradient of water surface in "L" can be calculated. In Figure 5.5, the most realistic value for the water surface elevation in "R" is $\xi_R = Z_{b_R}$. During wetting process, program turns over dry-boundary and dry-island cells and, in turn, the cell "R" will be the central cell, c_0, and the cell "L" will be the neighboring cell, c_j. In a two dimensional grid, the average of the boundary conditions forced by wet neighboring cells is applied.

A dry-boundary/island cell is wetted if:

$$\begin{cases} \xi_{j\_s_j} > max\left[Z_{b_{j\_s_j}}, Z_{b_{0\_s_j}} \right] + h_{th} \\ \boldsymbol{u}_j . \boldsymbol{n} \geq 0.0 \end{cases} \tag{5.27}$$

In a first order wetting-drying process $\xi_{j\_s_j} = \xi_j$, $Z_{b_{j\_s_j}} = Z_{b_j}$, and $Z_{b_{0\_s_j}} = Z_{b_0}$. In a second order wetting-drying process $\xi_{j\_s_j} = \left[\xi + \boldsymbol{\nabla}\xi . r_{c_{j\_s_j}} \right]_j$, $Z_{b_{j\_s_j}} = \left[Z_b + \boldsymbol{\nabla}Z_b . r_{c_{j\_s_j}} \right]_j$, and $Z_{b_{0\_s_j}} = \left[Z_b + \boldsymbol{\nabla}Z_b . r_{c_{0\_s_j}} \right]_0$. Since the wall boundary condition is applied on wetting-drying fronts, the normal velocity at the cell face is zero. In Shallow Fluent, the term $\boldsymbol{u}_j . \boldsymbol{n} \geq 0.0$ in Equation (5.27) is an optional term which takes the velocity direction into account (it is optional since in some cases $\boldsymbol{u}_j . \boldsymbol{n} \geq 0.0$ is always true; thus, there will be no need for checking this criterion).
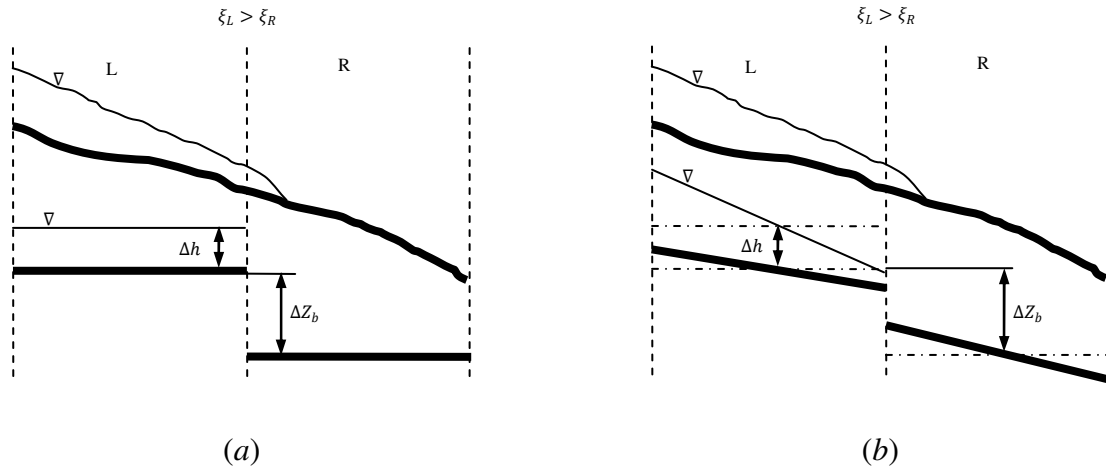
Figure 5.5. Reconstruction of dam-break wetting-drying front; (*a*) first order; (*b*) second order.

5.2.4.4.3 Wet cell drying

Equation (5.24) limits the water depth at very shallow cells. During wetting-drying process, these shallow cells are identified and marked as dry cells; i.e. dry-exterior, dry-boundary or, dry-island regarding the wet-dry condition at the neighboring cells. A dry cell is deactivated, but, the water depth at a dry cell is kept untouched. When a dry cell is wetted, its condition changes from inactivate (dry) to active (wet). The water depth at the cell is not touched in this process. Thus, the process is completely mass conserving, no mass redistribution is required and, in turn, the process does not cause any local spurious current. It has to be pointed out that, this process

conserves the mass on entire computational domain; i.e. on iterative solutions the continuity residual criterion has to be chosen in accordance (always bigger) with the threshold depth. In the entire test cases in Section 5.2.5, convergence is attained for $h_{th} = 10^{-4}$ and $\vartheta_R \leq 10^{-3}$.

5.2.5 Numerical results

Dam break over a very shallow wet bed is simulated in the first test case. The aim of this test is seeking a threshold depth for the shallow wet bed where below this threshold the solution is independent of water depth at shallow region. In the second test case, dam break over flat dry bed is simulated. Two different depths, smaller than the threshold depth obtained in the first test case, are examined in the second test case in order to find an appropriate threshold depth for wetting-drying process. In the third test case, dam break over down-slope dry bed is investigated. The fourth test case is paid to dam break over up-slope dry bed. Test cases three and four are devised for investigating the performance of the wetting-drying treatment on sloping bed conditions. In the fifth test case, a multidirectional dam break over compound dry bed is examined. This test case is devised in order to compare the accuracy of a solution with second order wetting-drying treatment with a case when first order treatment is applied. In test cases two to five first order and second order wetting-drying treatments are compared.

The hydrostatic vertical distribution of pressure field is one of the main assumptions in a depth averaged simulation. Thus, simulation of dam break using a high order VOF technique, where the vertical distribution of pressure field is hydrodynamic, is always more accurate. Such accuracy can never be achieved when the vertical distribution of pressure field is assumed hydrostatic [31]. In the test cases where simulations are compared with those from Fluent6.3 software, a depth averaged simulation using first or second order treatment of wetting-drying fronts which is more similar to the solution by Fluent6.3 is logically more accurate.

5.2.5.1 Dam break over shallow wet bed

In [21], dam break over shallow wet bed is simulated. Various water depths, from $0.1m$ to $10^{-3}m$, are examined in shallow region. In [21], numerical solutions significantly change when the water depth in shallow region is changed, but, the absolute magnitude of the difference in numerical solutions reduces for shallower water depths; i.e. near $10^{-3}m$. Thus, there has to be a

threshold depth where below this threshold numerical solutions are independent of the water depth in shallow wet bed.
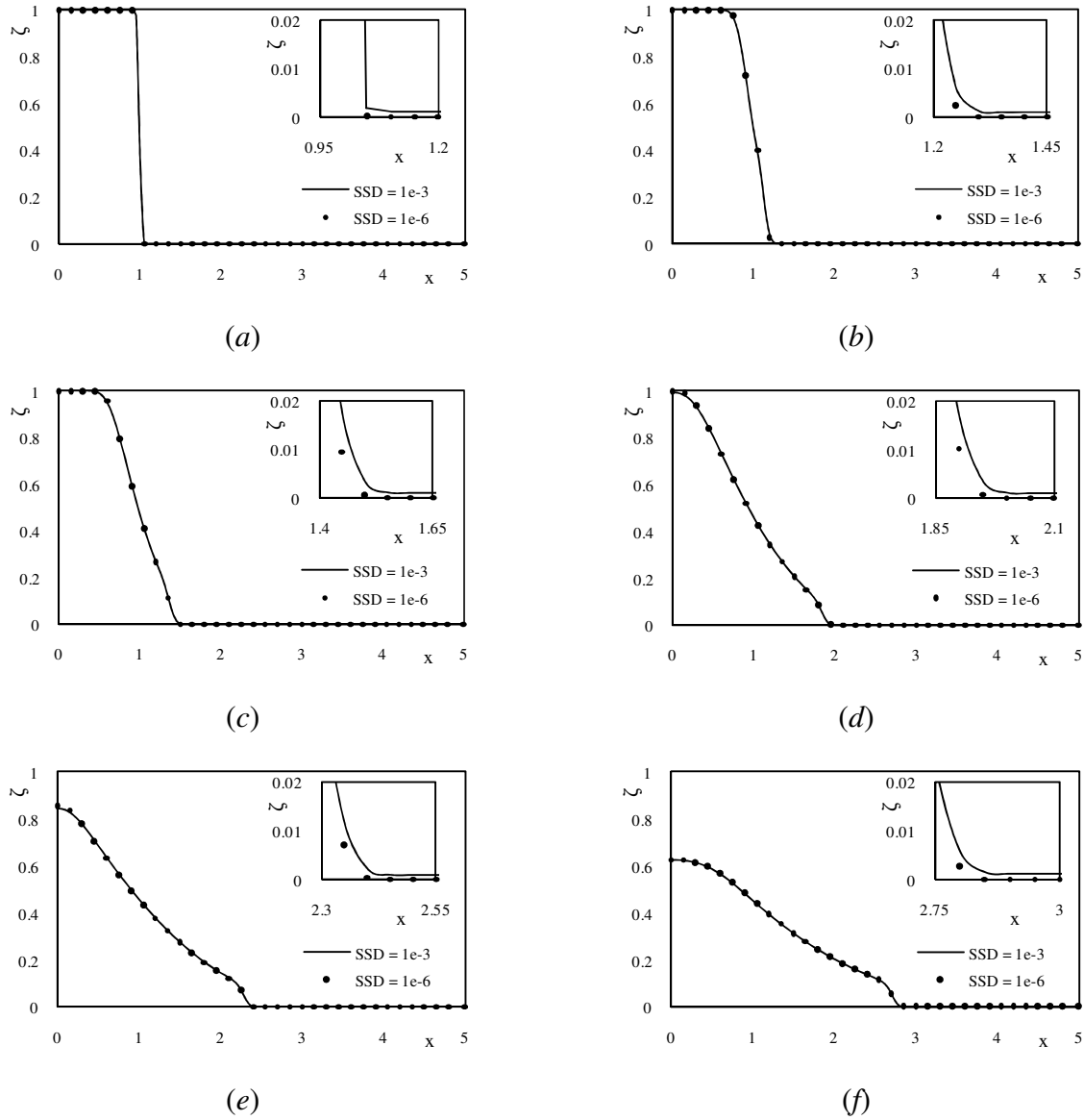
Figure 5.6. Dam break over shallow wet bed; (*a*) $t = 0.0125$; (*b*) $t = 0.2500$; (*c*) $t = 0.5001$; (*d*) $t = 1.000$; (*e*) $t = 1.500$; (*f*) $t = 2.000$; SSD = Shallow Side Depth.

The computational domain is rectangular, with $L = 5\,m$ and $H = 1\,m$. Grid contains nearly uniform triangular cells with 100×20 grid spacing on domain boundaries. The physical domain is assumed a quadrilateral pool with free-slip wall boundaries. The pool cross section is rectangular and, Manning's number is assumed 0.03. The water surface elevation is $1.0\,m$ at

$x \leq 1\,m$ and, $10^{-3}\,m$ and $10^{-6}\,m$ at $x > 1\,m$ in every test, respectively. The water specific gravity and dynamic viscosity are $998.2\,kg/m^3$ and $0.001003\,N.m/s^2$, respectively. The gravitational acceleration is assumed $9.806\,m/s^2$, the initial velocity at the domain is zero, and the time step is $0.002823\,s$. The reference length and velocity are $1.0\,m$ and $4.4285\,m/s$, respectively. Errors are normalized with the maximum error at the first five iterations in the first time step and, the convergence criterion is set to 10^{-3}.

In Figure 5.6 the numerical solutions at $y = 0.5$ at six different times are shown. The numerical results obtained with different shallow side depths, 10^{-3} and 10^{-6}, show ignorable differences (about 10^{-3} near the wave front). This difference is due to the difference in shallow side depths and, it does not increase with time. Thus, solutions can be regarded shallow-side-depth independent and, the shallow side depth 10^{-3} can be considered as the threshold depth.

5.2.5.2 Dam break over flat dry bed

The computational domain is rectangular, with $L = 8\,m$ and $H = 1\,m$. The grid contains nearly uniform triangular cells with 160×20 grid spacing on domain boundaries. The water surface elevation is $1.0\,m$ at $3 \leq x \leq 5\,m$, $10^{-3}\,m$ at $x < 3\,m$, and $0.0\,m$ at $x > 5\,m$. Other settings are same as in Section 5.2.5.1. The initial condition is sketched in Figure 5.7-a.

(*a*)   (*b*)

Figure 5.7. Dam break over flat free-slip bed; (*a*) initial condition; (*b*) time history of the position of the leading edge of water.

Time history of the position of the leading edge of water is shown in Figure 5.7-*b*. In Figure 5.7-*b*, The threshold water depth for wetting-drying treatment is set to 10^{-4}. Numerical solutions of the depth-averaged model are compared with the solution by Fluent6.3. In Fluent6.3, PLIC VOF

method is used in order to capture the interface between air and water. Same as in Figure 5.2, the first order method over predicts the position of the leading edge of water. In Figure 5.8, 2D and 3D view of the solutions with first order and second order wetting-drying treatment at $t = 2.000$ are compared. As it is expected in a dam break over dry bed, there is no step in profile of water surface near $x = 7$. A step however can be observed near $x = 1$, the side where dam breaks over the shallow wet bed. The position of the wave front in Figures 5.8-a and 5.8-b is the same; i.e. the
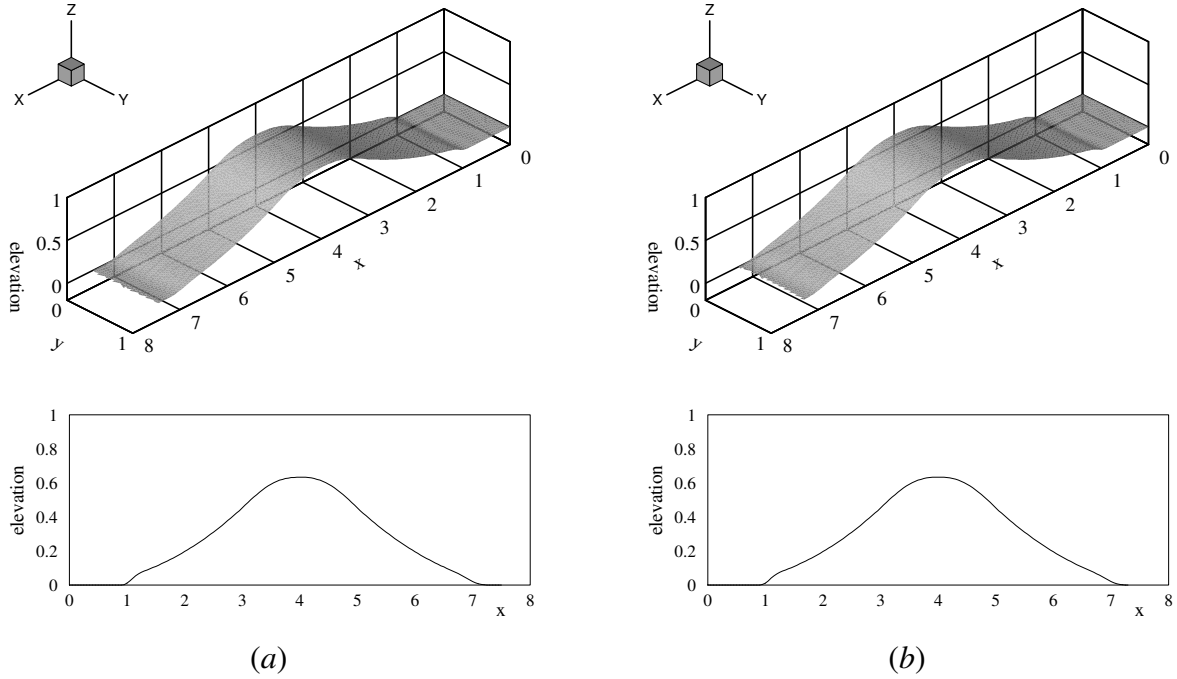
Figure 5.8. Water surface in a dam break over a flat free-slip bed; (a) first order; (b) second order.

difference between the numerical solutions obtained with first order and second order wetting-drying method is extension of a thin layer of water when the first order method is used. For the region with $x < 3$ the dam breaks over wet bed; i.e. flux is calculated at every cell face. But, for the region with $x > 5$ the dam breaks over dry bed; i.e. flux at the face between wet and dry cell is set to zero. In the research cases (a) and (b) in Section 5.2.2 (equivalently Section 5.2.4.1 and 5.2.4.2) it is stated that, neither solving the transport equations only on wet cells, nor setting the flux at the face between a wet and dry cell to zero can affect the numerical solution (it has to be pointed out that there are some criteria; e.g. the CFL number must be always less than one). This hypothesis is confirmed since in Figure 5.8 the wave fronts displace the same distance over both wet and dry beds.

In the literature, the threshold depth of 10^{-6} is regarded as an appropriate threshold depth for wetting-drying treatment [7,8,16]. As far as the authors are aware, a smaller threshold is considered more appropriate. In Figure 5.9 two different threshold water depths are used in wetting-drying treatment. It can be observed in Figure 5.9-*a* that, the error increases when the threshold depth decreases. The magnitude of the increase in error is the same in both first order and second order treatments. At very shallow wet-boundary cells, the gradient of the water surface is almost zero and, as a result, the performance of the second order scheme significantly decreases for very small threshold depths. Thus, a very small threshold depth is not the most appropriate choice.

(*a*)   (*b*)   (*c*)
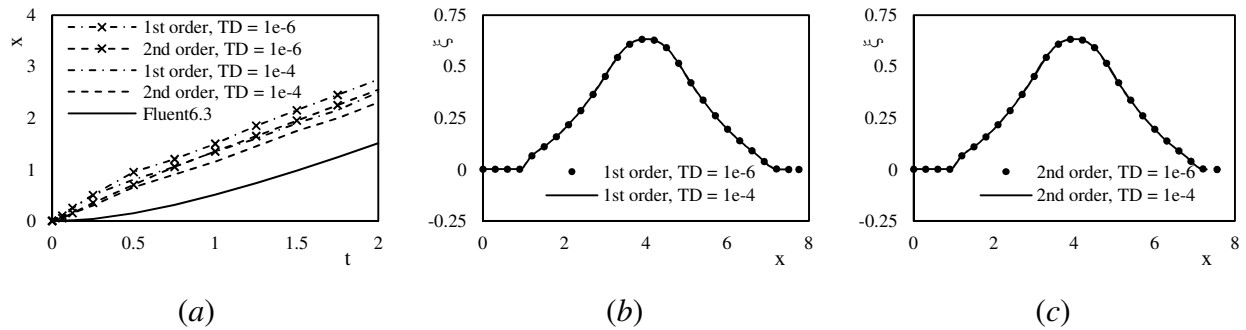
Figure 5.9. Threshold depth effect on simulation of dam break over a shear-free flat bed; (*a*) time history of the position of the leading edge of water; (*b*) and (*c*) profile of water surface at $t = 2.000$; (*b*) first order method; (*c*) second order method; TD = Threshold Depth.
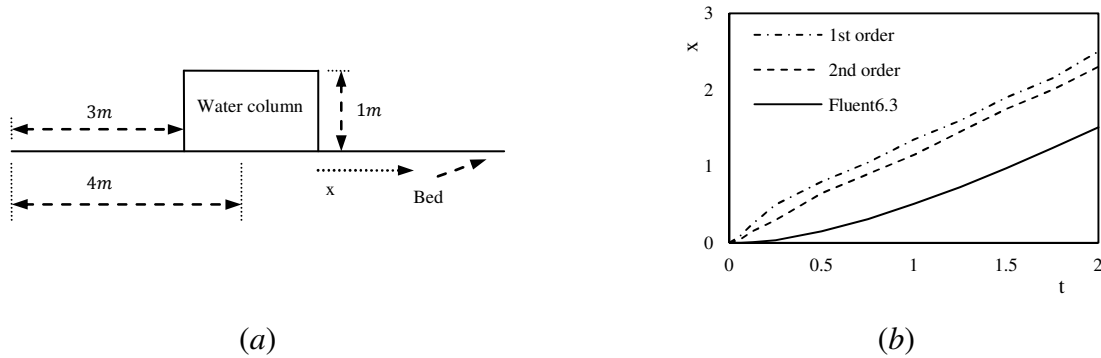

(*a*)   (*b*)
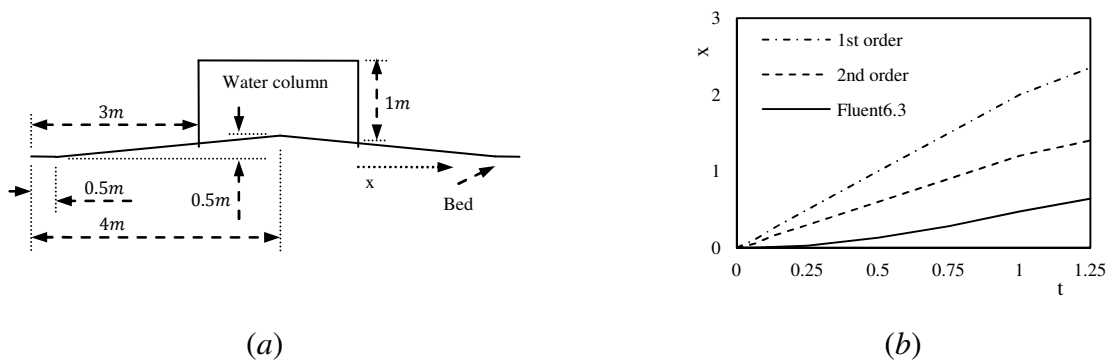
Figure 5.10. Dam break over down-slope free-slip bed; (*a*) initial condition; (*b*) time history of the position of the leading edge of water.

5.2.5.3 Dam break over down-slope bed

The computational domain is rectangular, with $L = 8\,m$ and $H = 1\,m$. Errors are normalized with the maximum error at the first five iterations in every time step and, the convergence criterion is set to 10^{-3}. When a dry cell is wetted, it will be initialized. Thus, the convergence criterion defined in Section 5.2.5.2 is not necessarily sufficient enough for every test case. While the convergence criterion defined in Section 5.2.5.2 is not satisfactory enough for dam break over down-slope bed, the convergence criterion defined here is very strict for the test case in Section 5.2.5.2. Other settings are same as in Section 5.2.5.2. The bed topography and the initial condition are depicted in Figure 5.10-*a*.

(a) $\qquad\qquad\qquad\qquad\qquad$ (b)
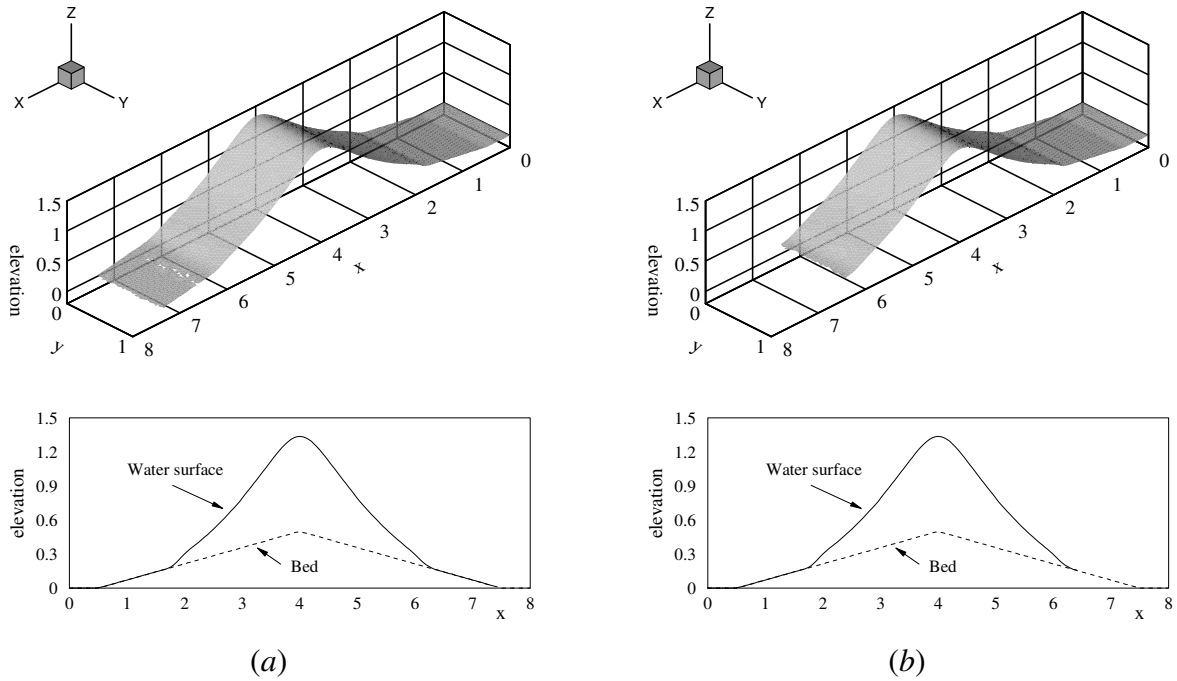
Figure 5.11. Water surface in dam break over down-slope free-slip bed; (*a*) first order; (*b*) second order.

In Figure 5.10-*b* the position of the leading edge of water predicted with the first order method is very erroneous. In Figure 5.10-*b* contrary to Figure 5.7-*b*, the difference between first order and second order wetting-drying treatments is big. This difference increases with time and, in turn, a thin layer of water quickly extends throughout the computational domain. Since one of the main goals of solving the transport equations only on wet cells is reducing the computational efforts,

the non-physical extension of a thin layer of water throughout the computational domain is very undesirable. In Figure 5.11, 2D and 3D views of the solutions with first order and second order wetting-drying method at $t = 1.188$ are compared. The extension of a thin layer of water is evident in Figure 5.11-*a*.

5.2.5.4 Dam break over up-slope bed

The computational domain is rectangular, with $L = 8\,m$ and $H = 1\,m$. Errors are normalized with the maximum error at the first five iterations in every time step and, the convergence criterion is set to 10^{-3}. Other settings are same as in Section 5.2.5.2. The bed topography and the initial condition are depicted in Figure 5.12-*a*.

(a) (b)
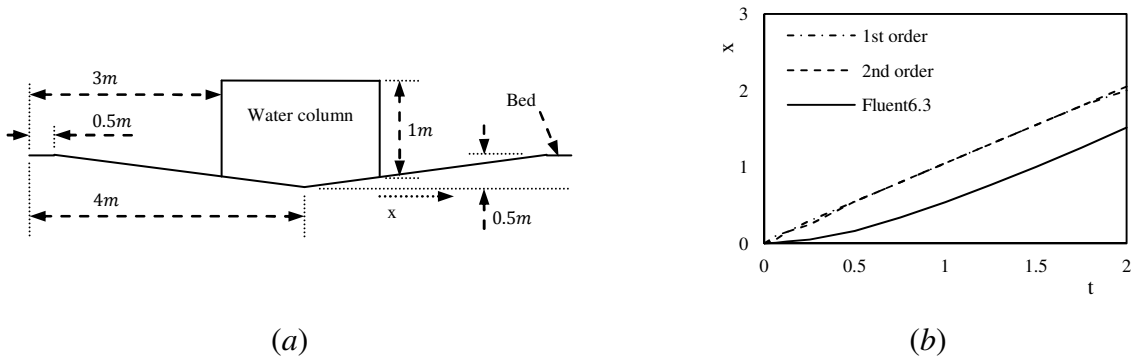
Figure 5.12. Dam break over up-slope free-slip bed; (*a*) initial condition; (*b*) time history of the position of the leading edge of water.

Time history of the position of the leading edge of water is shown in Figure 5.12-*b*. It can be observed that the difference between first order and second order wetting-drying treatments is ignorable. In dam break over up-slop bed, presented here, after a short period the wetting-drying condition will be the flooding case (see Figure 5.4). Since in the flooding case the water surface in wet-boundary cells is almost horizontal, the solution is independent of the order of accuracy of the wetting-drying treatment (the maximum difference is about one grid spacing since with a second order method the bed is more accurately reconstructed). In Figure 5.13, 2D and 3D views of the solutions with first order and second order wetting-drying method at $t = 2.000$ are compared. It can be observed that, there is no extension of thin fluid layer and the solutions are the same.
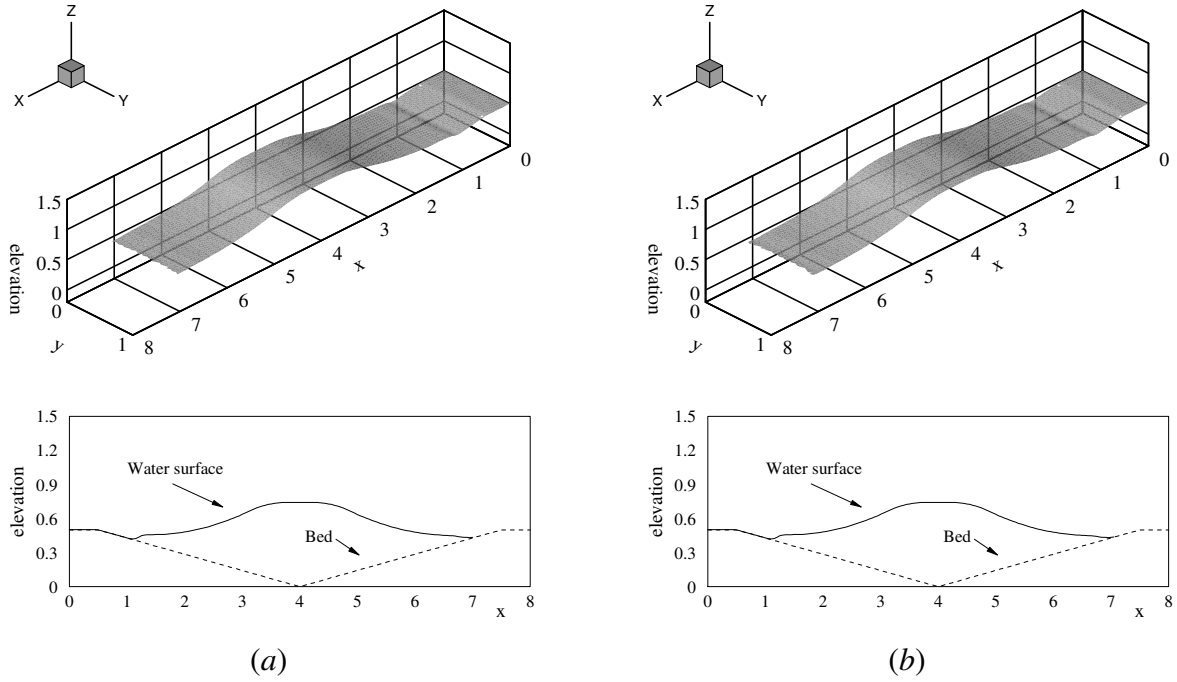
Figure 5.13. Water surface in dam break over up-slope free-slip bed; (*a*) first order; (*b*) second order.

5.2.5.5 Multidirectional dam break over compound dry bed

The computational domain is rectangular, with $L = 8\,m$ and $H = 1\,m$. Errors are normalized with the maximum error at the first five iterations in the first time step and, the convergence criterion is set to 10^{-3}. Other settings are same as in Section 5.2.5.2. The analytical functions for the bed topography are given as:

$$
\begin{cases}
Z_b = (0.6x - 0.84y + 1.26)/4.2 & x < 2.8 \; and \; y \le 1.5 \\
Z_b = \big(0.6x + 0.84(y - 1.5)\big)/4.2 & x < 2.8 \; and \; y > 1.5 \\
Z_b = -0.3y/1.5 + 0.7 & (x \ge 2.8 \; and \; x \le 5.2) and \; y \le 1.5 \\
Z_b = 0.3(y - 1.5)/1.5 + 0.4 & (x \ge 2.8 \; and \; x \le 5.2) and \; y > 1.5 \\
Z_b = (-0.6(x - 5.2) - 0.84y + 2.94)/4.2 & x > 5.2 \; and \; y \le 1.5 \\
Z_b = (-0.6(x - 5.2) + 0.84(y - 1.5) + 1.68)/4.2 & x > 5.2 \; and \; y > 1.5
\end{cases}
$$

The bed topography is depicted in Figure 5.14. The water surface elevation is given by the following analytical functions:

$$\begin{cases} \xi = (0.6x - 0.84y + 1.26)/4.2 + 0.001 & x < 2.8 \ and \ y \leq 1.5 \\ \xi = \big(0.6x + 0.84(y - 1.5)\big)/4.2 + 0.001 & x < 2.8 \ and \ y > 1.5 \\ \xi = 1.4 & (x \geq 2.8 \ and \ x \leq 5.2) and \ y \leq 1.5 \\ \xi = 1.4 & (x \geq 2.8 \ and \ x \leq 5.2) and \ y > 1.5 \\ \xi = (-0.6(x - 5.2) - 0.84y + 2.94)/4.2 & x > 5.2 \ and \ y \leq 1.5 \\ \xi = (-0.6(x - 5.2) + 0.84(y - 1.5) + 1.68)/4.2 & x > 5.2 \ and \ y > 1.5 \end{cases}$$

This test case is both realistic and challenging. It is realistic since the bed topography represents what one can expect in nature and, it is challenging since the wave front moves both in the directions normal to the initial dam (down-slope of the valley) and parallel to it (due to the transverse slope in the valley).
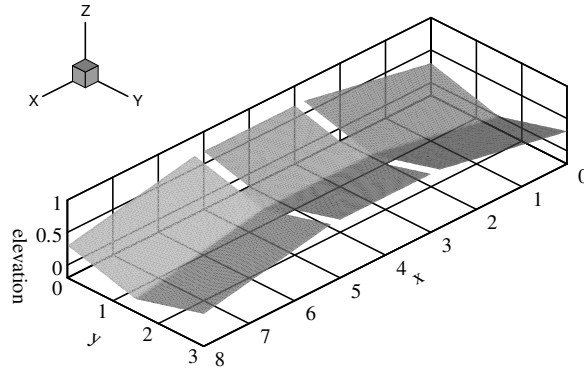
Figure 5.14. Bed topography in multidirectional dam break test.

In Figure 5.15 first order and second order wetting-drying treatments are compared at three different times. A thin layer of water extends throughout the talweg when the first order wetting-drying treatment is used. The position of the leading edge of water is shown in Figure 5.16. The difference between the solutions with first order and second order methods is too much and rapidly increases with time. The difference in Figure 5.16 increases much faster than the difference in Figure 5.10-*b*. In Figure 5.15, the wave front which is moved in x direction will slip down-slope in y direction toward the talweg and, as a result, the water depth at higher bed elevations diminishes. The down-slope movement of water in y direction increases the water depth near the talweg and, in turn, it amplifies down-slope extension of the thin layer of water in x direction. The fact that the thin layer of water in Figure 5.15 contains separated bodies of water confirms this hypothesis. In Figure 5.17 the numerical solution with second order wetting-drying

treatment is continued further ahead in time. There is no extension of thin layers of fluid and, the wave front is as it is expected to be, without any step formation.

(*a*)

(*b*)

(*c*)
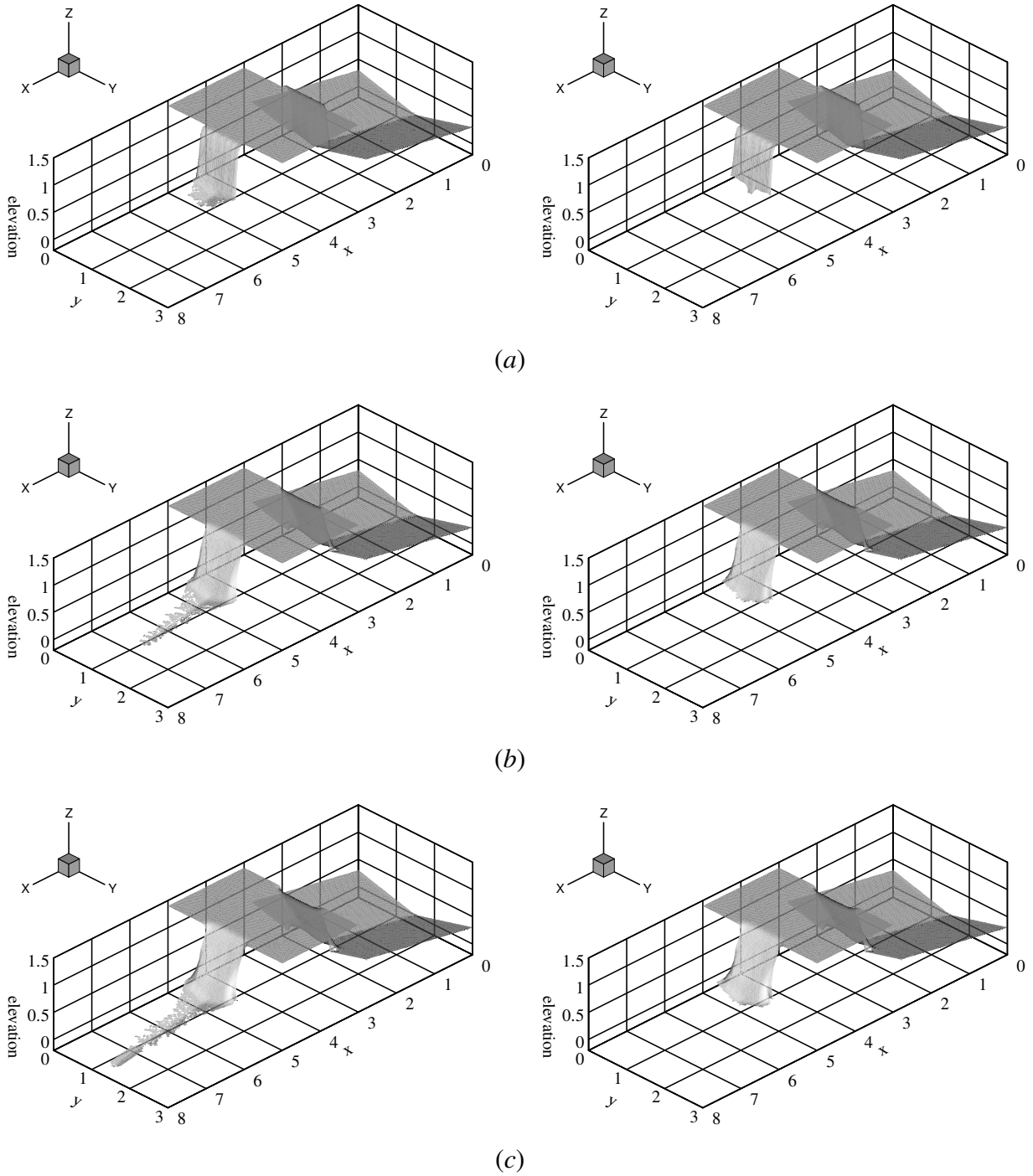
Figure 5.15. Multi-directional dam break; (*a*) $t = 0.062508$; (*b*) $t = 0.250033$; (*c*) $t = 0.350046$. Left figures: first order method; right figures: second order method.
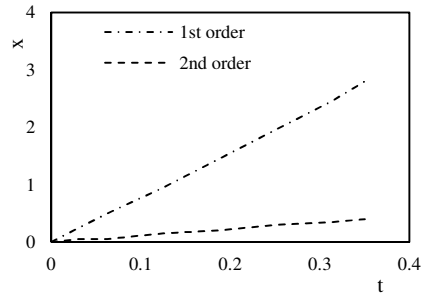
Figure 5.16. Time history of the position of the leading edge of water in multi-directional dam break.
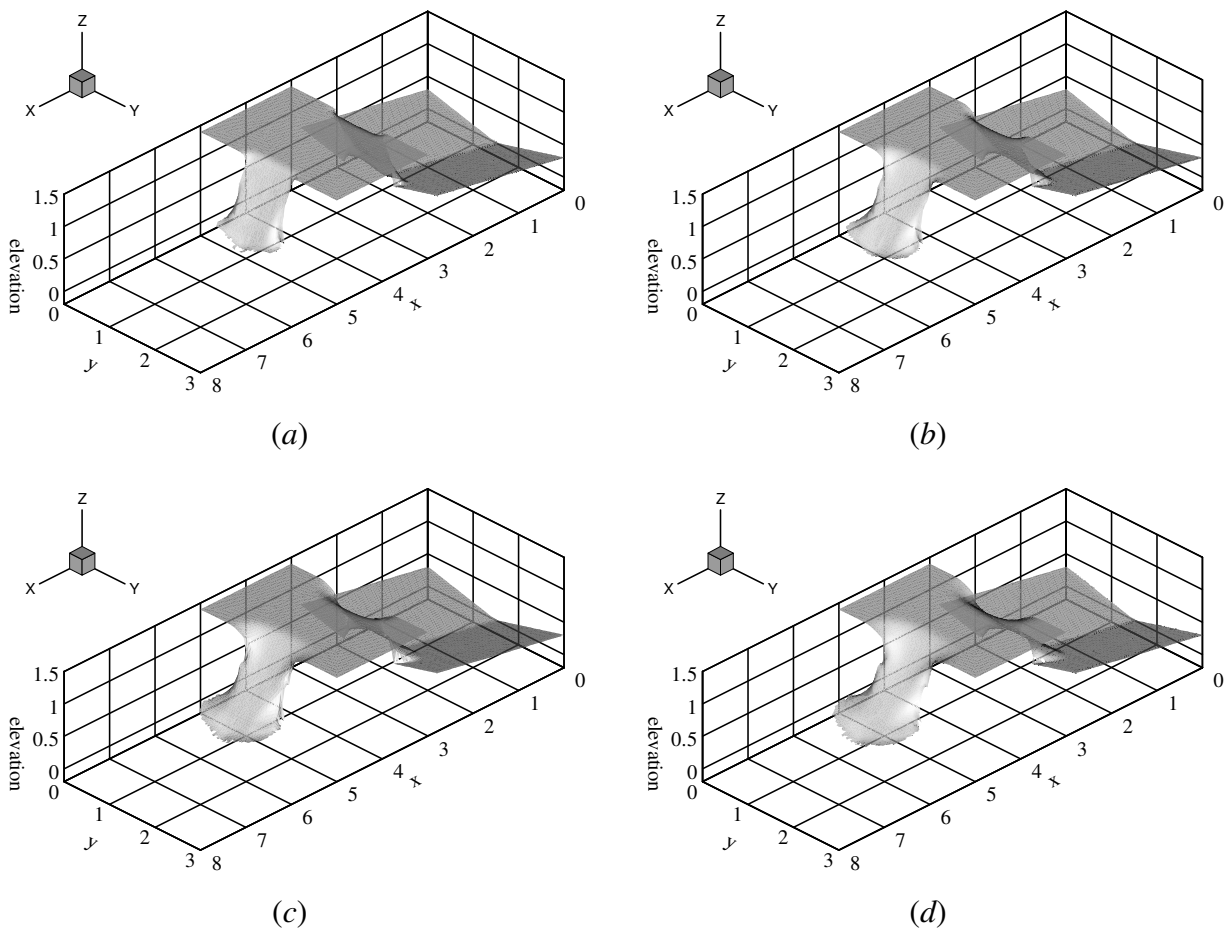
Figure 5.17. Multi-directional dam break; (*a*) $t = 0.37505$; (*b*) $t = 0.562574$; (*c*) $t = 0.750099$; (*d*) $t = 0.846987$.

5.2.6 Conclusion

In this article, five research cases are introduced and investigated:

- Research cases (a, b); (a) solution on wet cells versus solution on entire computational domain, (b) zero flux versus calculation of flux at the cell face: in order to reduce the computational effort, the transport equations are solved only on wet cells (i.e. the solver is designed in this way), the flux at the face between wet and dry cells is set to zero and, the solver is then applied to dam break cases. The simulated wave front over dry bed is not hindered. Also, as it can be observed in a real case, there is no step at the wave front.

- Research case (c); treatment of negative water depths: the water depth at the domain is monitored during the iterations. As soon as the water depth fell below a threshold depth, the pressure correction is modified so that the minimum water depth at wet region is limited to the threshold depth.

- Research case (d); development of a high order wetting-drying treatment: The devised second order accurate wetting-drying process only implicitly affects the order of accuracy of the solution. It also efficiently prevents undesired extension of thin layer of fluid throughout the computational domain.

- Research case (e); finding an appropriate threshold depth: In a dam break over a shallow wet bed, the solution is independent of the water depth at shallow wet bed when the water depth at the shallow side is less than 10^{-3}. The devised wetting-drying process is also more efficient when bigger threshold depths are used; i.e. about 10^{-3} to 10^{-4}. This property is very desirable since the solution of many numerical schemes oscillates at very small water depths.

In terms of the required computation time, solving only for wet region will be suggested since fewer computational cells will be involved. The assumption of zero mass flux at the face between wet can dry cells will be suggested when there is no solution for both calculating the flux and, at the same time, having a high order wetting-drying treatment. When SIMPLE algorithm is used, it is suggested to monitor and correct the pressure correction in order to prevent negative water depths. A high order treatment of wetting-drying fronts is suggested since it prevents extension of

the spurious thin layers of fluid. When the wetting-drying treatment which is suggested in this article is used, the appropriate threshold water depth is 10^{-4} $[m]$.

5.2.7 References

[1] A.I. Delis, T. Katsaounis, Numerical solution of the two-dimensional shallow water equations by the application of relaxation methods, Appl. Math. Modell. 29 (2005) 754-783.

[2] B. Di Martino, C. Giacomoni, J. Martin Paoli, P. Simonnet, Simulation of the spread of a viscous fluid using a bidimensional shallow water model, Appl. Math. Modell. 35 (2011) 3387-3395.

[3] C. Knock, S.C. Ryrie, Parameterization of dispersion in the depth-averaged transport equation, Appl. Math. Modell. 18 (1994) 582-587.

[4] C. Zoppou, S. Roberts, Numerical solution of the two-dimensional unsteady dam break, Appl. Math. Modell. 24 (2000) 457-475.

[5] D. Chen, J.G. Duan, Case study: Two-dimensional model simulation of channel migration processes in West Jordan River, Utah, J. Hydraul. Eng. 134 (2008) 315-327.

[6] K.J. George, S. Stripling, Improving the simulation of drying and wetting in a two-dimensional tidal numerical model, Appl. Math. Modell. 19 (1995) 2.

[7] L. Begnudelli, B.F. Sanders, Conservative wetting and drying methodology for quadrilateral grid finite-volume models, J. Hydraul. Eng. 133 (2007) 312-322.

[8] I.K. Nikolos, A.I. Delis, An unstructured node-centered finite volume scheme for shallow water flows with wet/dry fronts over complex topography, Comput. Meth. Appl. Mech. Eng. 198 (2009) 3723-3750.

[9] P.A. Sleigh, P.H. Gaskell, M. Berzins, N.G. Wright, An unstructured finite-volume algorithm for predicting flow in rivers and estuaries, Comput. Fluids 27 (1998) 479-508.

[10] W. Wu, Depth-averaged two-dimensional numerical modeling of unsteady flow and nonuniform sediment transport in open channels, J. Hydraul. Eng. 130 (2004) 1013-1024.

[11] P. Brufau, P. Garcia-Navarro, M.E. Vazquez-Cendon, Zero mass error using unsteady wetting-drying conditions in shallow flows over dry irregular topography, Int. J. Numer. Methods Fluids 45 (2004) 1047-82.

[12] Y.G. Lai, Two-dimensional depth-averaged flow modeling with an unstructured hybrid mesh, J. Hydraul. Eng. 136 (2010) 12-23.

[13] J. Xia, B. Lin, R.A. Falconer, G. Wang, Modelling dam-break flows over mobile beds using a 2D coupled approach, Adv. Water Res. 33 (2010) 171-183.

[14] J. Murillo, P. Garcia-Navarro, J. Burguete, P. Brufau, A conservative 2D model of inundation flow with solute transport over dry bed, Int. J. Numer. Methods Fluids 52 (2006) 1059-1092.

[15] J.-M. Zokagoa, A. Soulaimani, Modeling of wetting-drying transitions in free surface flows over complex topographies, Comput. Meth. Appl. Mech. Eng. 199 (2010) 2281-2304.

[16] Q. Liang, A.G.L. Borthwick, Adaptive quadtree simulation of shallow flows with wet-dry fronts over complex topography, Comput. Fluids 38 (2009) 221-234.

[17] S.J. Bennett, W. Wu, C.V. Alonso, S.S.Y. Wang, Modeling fluvial response to in-stream woody vegetation: Implications for stream corridor restoration, Earth Surf. Processes Landforms 33 (2008) 890-909.

[18] B. Minh Duc, Berechnung der stroemung und des sedimenttransorts in fluessen mit einem tieffengemittelten numerischen verfahren, PhD thesis, The University of Karlsruhe, Karlsruhe, Germany, 1998.

[19] W. Wu, F.D. Shields Jr, S.J. Bennett, S.S.Y. Wang, A depth-averaged two-dimensional model for flow, sediment transport, and bed topography in curved channels with riparian vegetation, Water Resour. Res. 41 (2005) W03015.

[20] J. Murillo, P. Garcia-Navarro, J. Burguete, Analysis of a second-order upwind method for the simulation of solute transport in 2D shallow water flow, Int. J. Numer. Methods Fluids 56 (2008) 661-86.

[21] J. Xia, R.A. Falconer, B. Lin, G. Tan, Modelling flood routing on initially dry beds with the refined treatment of wetting and drying, Int. J. River Basin Management 9 (2010) 1-19.

[22] D.H. Zhao, H.W. Shen, G.Q. Tabios, J.S. Lai, W.Y. Tan, Finite-volume two-dimensional unsteady-flow model for river basins, J. Hydraul. Eng. 120 (1994) 863-882.

[23] M. Moradi Larmaei, J. Behzadi, T.-F. Mahdi, Grid independent depth-averaged simulations with a collocated unstructured finite volume scheme, Int. J. Numer. Methods Fluids, Article first published online: 22 MAR 2011, DOI: 10.1002/fld.2538.

[24] M. Moradi Larmaei, J. Behzadi, T.-F. Mahdi, Treatment of checkerboard pressure in the collocated unstructured finite-volume scheme, Numer. Heat Transfer, Part B: fundamentals 58 (2010) 121–144.

[25] M. Moradi Larmaei, and T.-F. Mahdi, Analysis of SIMPLE algorithm for depth averaged simulations, 6th International Symposium on Environmental Hydraulics, Athens, Greece, June 23-25 (2010).

[26] M. Moradi Larmaei, and T.-F. Mahdi, Effect of interpolation technique on numerical accuracy and computational cost, 34th IAHR World Congress, International Association of Hydraulic Engineering & Research (IAHR), Brisbane, Australia, (2011), accepted.

[27] W. Rodi, Turbulence models and their application in hydraulics, IAHR Monograph, Balkema, Rotterdam, Netherlands, 1993.

[28] C.M. Rhie, W.L. Chow, Numerical Study of the turbulent flow past an airfoil with trailing edge separation, AIAA Journal 21 (1983) 1525-1532.

[29] Fluent6.3_user's_guide, Fluent Inc: http://my.fit.edu/itresources/manuals/fluent6.3/help/html /ug// main_pre.htm, 2010.

[30] B.E. Launder, D.B. Spalding, The Numerical Computation of Turbulent Flows, Comput. Meth. Appl. Mech. Eng. 3 (1974) 269-289.

[31] E.F. Toro, Shock-capturing methods for free-surface shallow flows, John Wiley & Sons, Chichester, England 2001.

[32] M.F. Karim, K. Tanimoto, P.D. Hieu, Modelling and simulation of wave transformation in porous structures using VOF based two-phase flow model, Appl. Math. Modell. 33 (2009) 343-360.

[33] J. Solórzano-López, R. Zenit, M.A. Ramírez-Argáez, Mathematical and physical simulation of the interaction between a gas jet and a liquid free surface, Appl. Math. Modell. Article in Press (2011).

[34] V. Srinivasan, A.J. Salazar, K. Saito, Modeling the disintegration of modulated liquid jets using volume-of-fluid (VOF) methodology, Appl. Math. Modell. 35 (2011) 3710-3730.

[35] M.R.H. Nobari, M.J. Ketabdari, M. Moradi, A modified volume of fluid advection method for uniform Cartesian grids, Appl. Math. Modell. 33 (2009) 2298-2310.

[36] C.W. Hirt, B.D. Nichols, Volume of fluid (VOF) method for the dynamics of free boundaries, J. Comput. Phys. 39 (1981) 201-25.

[37] D.J.E. Harvie, D.F. Fletcher, A new volume of fluid advection algorithm: the defined donating region scheme, Int. J. Numer. Methods Fluids 35 (2001) 151-72.

[38] J.C. Martin, W.J. Moyce, An experimental study of the collapse of liquid columns on a rigid horizontal plane, Philos. Trans. R. Soc. London, Ser. A 244 (1952) 325-334.

[39] P.D. Hieu, T. Katsutoshi, V.T. Ca, Numerical simulation of breaking waves using a two-phase flow model, Appl. Math. Modell. 28 (2004) 983-1005.

CHAPTER 6 ARTICLE 4: VORTICITY EQUATION FOR THE SECONDARY FLOW EFFECT IN DEPTH-AVERAGED SIMULATIONS

6.1 Presentation of the article

In this section the objective of the article will be presented, as well as a conclusion on this work as part of the thesis. This article investigates the applicability of technique which can be used for taking account of the secondary flow effect in depth-averaged momentum equations. When this technique is used in commercial depth-averaged solvers, together with the insights provided in this article, a more accurate prediction of depth-averaged velocity field will be possible. This significantly affects the computed results when for instance the software is used for investigation of sediment transport phenomenon in a river and all parameters are fixed except the effect of the secondary force. By the word "affect" the author means any positive or negative influence.

6.1.1 Objective

There are several techniques for taking account of depth-averaged secondary flow effect in momentum equations, from simple algebraic equations to moment equations and vorticity equations. None of these equations could take the vegetation effect on secondary flow into account, there was no criterion expressing clearly under which criteria these techniques are applicable and, some of them are function of case-dependent constants. In this research the vorticity equation is chosen among others, in order to take account of the secondary flow effect in depth-averaged simulation, since it relys on a transport equation and the constants in this equation are case independent. The equation is then extended in order to take account of vegetation effect on stream-wise vorticity, and the depth-averaged secondary force in momentum equations is modified for this reason. After applying this technique to several test cases, by comparing the computed and measured data, the criterion under which the calculated vorticity based secondary force actually increases the accuracy of the computed velocity field is identified. Before taking this step in this thesis, the solver was not able to take account of secondary flow in vegetated channels. Also, there was no criterion under which the correction, by secondary force, to velocity field could be considered acceptable.

6.1.2 Conclusion

In a vegetated zone both the steam-wise vorticity and velocity are small and, in turn, modification of the stream-wise vorticity and depth-averaged secondary force does not significantly affect the computed velocity field. The vorticity-based depth-averaged secondary force can actually increase the accuracy of the computed velocity field but, some condition has to hold. This condition consists of limited depth to width and depth to bend-curvature radius ratio for a known degree of curvature in channel bend.

The article is submitted to Journal of Hydro-Environment Research.

Moradi Larmaei, M. (2012). Vorticity equation for the secondary flow effect in depth-averaged simulations. Journal of Hydro-Environment Research, Submitted.

6.2 Vorticity equation for the secondary flow effect in depth-averaged simulations

M. Moradi Larmaei

Department of Civil, Geological and Mining Engineering, Montreal Polytechnic Institute, Montreal, Quebec, Canada.

6.2.1 Abstract

In this article, a transport equation for stream-wise vorticity is solved. The secondary force is then calculated using the computed stream-wise vorticity. Several numerical tests are performed in order to investigate the effect of the calculated secondary force on the accuracy of the computed velocity field. The velocity fields computed with and without considering the secondary force effect then are compared with measured data. According to these comparisons, the conditions where the secondary force calculated through solving a vorticity equation will actually increase the accuracy of the computed velocity field are identified.

Keywords: Depth-averaged simulation, Secondary flow, Streamwise vorticity, Vegetation

6.2.2 Introduction

When a microscopic transport equation is integrated over the water depth, its depth-averaged form will be derived. A time-mean microscopic depth averaged equation will be obtained when the microscopic depth-averaged equation is integrated over a time interval. Further integration of a time-mean depth-averaged equation over a Representative Elementary Volume (REV) will produce a time-mean macroscopic depth averaged equation. A transport equation which underwent all the mentioned integrations is called a double-decomposed depth-averaged equation (Moradi Larmaei and Mahdi, 2012).

Nomenclature

a_0, a_j coefficients in the discretized equations

C_{s_j} volumetric flux at the cell face s_j

C_{fr}, C_d bed friction coefficient and vegetation drag coefficient, respectively

d_v stem diameter

g gravitational acceleration

G rate of production in $k - \varepsilon$ model equation

h, h_v water depth and vegetation effective height, respectively

$h_{c_0\_c_j}$ normal distance between two neighbor cells

k turbulence kinematic energy

L length scale

n direction along $\boldsymbol{n}$ or Manning's number

$\boldsymbol{n}$ unit vector normal to the cell face when there is no subscript, any unit normal otherwise

$\hat{\boldsymbol{n}}$ unit vector normal to velocity vector $\boldsymbol{u}$

P, P' pressure and pressure correction, respectively

r streamline curvature radius

R residual at the domain

R_e flow Reynolds number, defined as $R_e = \rho_f^* U_{ref} l_{ref} / \mu_f^*$

R_{e_D} stem Reynolds number based on reference velocity, defined as $R_{e_D} = \rho_f^* U_{ref} d_v / \mu_f^*$

$s_j, \boldsymbol{s}_j, s$ cell face area, the area vector, and the area of an arbitrary surface, respectively

$S, \boldsymbol{S}$ scalar and vector form of the source terms, respectively

t time

u, v velocity components in x and y directions, respectively

U velocity scale

$\boldsymbol{u}$ velocity vector

x, y x and y directions

$|\boldsymbol{\varrho}|$ for any vector $\boldsymbol{\varrho}$, $|\boldsymbol{\varrho}|$ refers to the argument of the vector

$\langle \varrho \rangle^i$ for any variable ϱ, $\langle \varrho \rangle^i$ refers to its average over the volume of the fluid phase in REV

$\langle \varrho \rangle^v$ for any variable ϱ, $\langle \varrho \rangle^v$ refers to its average over the volume of REV

$\bar{\varrho}$ for any depth-averaged variable ϱ, $\bar{\varrho}$ refers to its time-mean depth-averaged form

Greek symbols

α dimensionless constant of about 1.0 for cylindrical vegetation stems

ε dissipation rate of k

η a dimensionless constant of about 1.0

ϑ° continuity residual

ϑ normalized continuity residua

λ vegetation density

μ, μ_{t_ϕ} laminar and macroscopic turbulent dynamic viscosity, respectively

ξ water surface elevation

ρ density

σ Prandtl/Schmidt number

$\tau, \boldsymbol{\tau}$ scalar and vector stresses

φ general scalar quantity

ϕ porosity

χ Prandtl/Schmidt number in general discretized equation for φ

ω_{rc} relaxation factor in pressure correction term

ϖ vorticity

ω_s magnitude of streamwise vorticity vector

Ω volume

Subscripts

b refers to the channel bed

f refers to fluid phase

fs refers to the interface between fluid and solid phase, directed from fluid toward solid

j refers to neighboring cell

k refers to turbulence kinematic energy

p_φ refers to the implicit part of the source term in discretized equation for φ

ref refers to reference value

R refers to residual at the domain

REV, REV_f refer to REV and the fluid in REV, respectively

ss refers to secondary shear

sf Refer to secondary force

s_j refers to cell face s_j

t refers to turbulence

u_φ refers to the explicit part of the source term in discretized equation for φ

v refers to vegetation

vd refers to vegetation drag force

w refers to wall

ε refers to dissipation rate of k

τ refers to shear

φ refers to φ

0 refers to central cell

Superscripts

n refers to the current time step

P refers to pressure

T	refers to the transpose of a vector
u	refers to $\boldsymbol{u}$
φ	refers to φ
$+$	refers to an initial guess (can be from previous iteration)
$*$	refers to the dimensional form of a quantity

Secondary currents are widely studied in literature and have significant importance since they affect flow and morphology characteristics. Nezu and Sanjou (2008) observed that, coherent structures are related to the large-scale secondary flows. They also observed, when vegetated and non-vegetated zones exist partially, time-averaged secondary currents will be generated due to anisotropy. Dulal and Shimizu (2010) experimentally investigated the meandering in clay mixed sediments. They observed that, bank erosion leads to high sediment transport rate which passes downstream and, due to the secondary flow effects near the channel bend, partially toward bar. Cieślik, Kamp et al. (2010) observed the secondary flow as the significant mechanism behind vertical motion in shallow fluid layers. Since secondary currents decrease the magnitude of the stream-wise velocity from the beginning of a meandering, meandering slows down the longitudinal dispersion (Dongsu, 2012). Kimura, Onda et al. (2010) observed that, secondary flow has significant effect on suspended sediment transport and its deposition pattern in a shallow side-cavity.

When the depth-averaging process is performed on momentum equations, dispersion forces will appear in these equations. Though the dispersion forces can exist even in a straight channel (Choi et al., 2007; Hyeongsik and Sung-Uk, 2009; Omran and Knight, 2010; Wang and Cheng, 2008), the momentum due to these forces is most significant in channel bends where the secondary flows are most strong (Hsieh and Yang, 2005; Shiono et al., 2008). This is where the word Dispersion Force can be most meaningfully replaced with the word Secondary Force. The secondary force source term is normally obtained through solving some algebraic equations (Duan and Julien, 2005; Hsieh and Yang, 2005; Sun et al., 2001; Tang and Knight, 2008), solving

the moment equation (Wu and Wang, 2004) or, solving the stream-wise vorticity equation (Bernard, 1993; Rodriguez et al., 2004). Irrespective of the method used for computing the secondary force, the derived secondary force has to be sensitive to irregularity of the lateral boundaries, variation in bed topography, presence of vegetated zones, and turbulence structures.

Among the mentioned methods, the transport equation for stream-wise vorticity is based on the interaction of the lateral curvature, bottom friction and vertical non-uniformity, to develop a model that reproduces the depth averaged influence of the secondary flow (Bernard, 1993). The method is later used in order to simulate the flow in channel bends, both in flume conditions (Moradi Larmaei et al., 2011; Moradi Larmaei and Mahdi, 2012) and natural streams (Rodriguez et al., 2004). Moradi Larmaei et al. (2011) observed that, the secondary force calculated using the stream-wise vorticity may cause an over predicted magnitude for the stream-wise velocity. Moradi Larmaei and Mahdi (2012) added an extra source term to the right hand side of the vorticity equation in order to take account of vegetation damping effect on secondary flows. In one of the tests cases in (Moradi Larmaei and Mahdi, 2012) where the channel was partially vegetated, the computed secondary force non-physically shifted the velocity profile toward the inner wall of the channel bend. In this article, several test cases are performed in order to find circumstances where the secondary force added to momentum equations will actually improve the accuracy of the computed depth-averaged velocity field.

The main objective of this article consists of finding circumstances where the secondary force calculated through solving a vorticity equation [i.e. Equations (5)-(8) and (17)-(20)] will actually increase the accuracy of the computed velocity field. The remainder of this article is divided into two major sections. In the first section, the hydrostatic shallow flow model is presented. This section contains the dimensionless conservative form of the double-decomposed depth-averaged transport equations and their discretized form. The second section is devoted to numerical tests and investigation of the secondary force effect on velocity field.

6.2.3 Numerical model

In this section, the governing equations and the discretization scheme will be introduced. Also, the boundary conditions and the residual criteria used in this article will be presented.

6.2.3.1 Governing equations

The dimensionless conservative vector form of the double-decomposed depth-averaged continuity and momentum equations can be given by:

$$\frac{\partial(\langle \bar{P} \rangle^i \phi/g)}{\partial t} + \nabla.\left(\phi \langle \bar{h} \rangle^i \langle \bar{u} \rangle^i\right) = 0 \tag{6.1}$$

$$\frac{\partial(\phi \langle \bar{h} \rangle^i \langle \bar{u} \rangle^i)}{\partial t} + \nabla.\left(\phi \langle \bar{h} \rangle^i \langle \bar{u} \rangle^i \langle \bar{u} \rangle^i\right) = -\langle \bar{h} \rangle^i \nabla\left(\phi \langle \bar{P} \rangle^i\right) + \frac{1}{Re} \nabla.\left[\langle \bar{h} \rangle^i \left(1 + \mu_{t_\phi}\right) \nabla\left(\phi \langle \bar{u} \rangle^{i^T}\right)\right] -$$

$$\phi_b \langle \overline{\tau_b} \rangle^i + \langle \overline{S_{sf}} \rangle^v - \langle \overline{S_{vd}} \rangle^v \tag{6.2}$$

where, $\langle \bar{u} \rangle^i = \langle \bar{u} \rangle^{i^*}/U_{ref}$, $t = t^* U_{ref}/L_{ref}$, $\mu_{t_\phi} = \mu_{t_\phi}^*/\mu_f^*$, $\phi = \Omega_{REV_f}/\Omega_{REV}$, and $\langle \bar{P} \rangle^i = \left(\langle \bar{P} \rangle^{i^*} - P_{ref}\right)/\left(\rho_f^* U_{ref}^2\right)$. Since the dimensionless fluid density is equal to 1.0, the relation between the pressure and water surface elevation is $\langle \bar{P} \rangle^i = g\langle \bar{\xi} \rangle^i$. The dimensionless bed shear stress, $\langle \overline{\tau_b} \rangle^i$, can be expressed as:

$$\langle \overline{\tau_b} \rangle^i = \langle C_{fr} \rangle^i \left|\langle \bar{u} \rangle^i\right| \langle \bar{u} \rangle^i \tag{6.3}$$

$$\langle C_{fr} \rangle^i = g \langle n \rangle^{i^2}/\langle \bar{h} \rangle^{i^{1/3}} \tag{6.4}$$

where, $\langle n \rangle^i = \langle n \rangle^{i^*} U_{ref}/L_{ref}^{2/3}$. In shallow flow hydraulics, Manning's number is usually assumed constant over an area much larger than a cell area. Thus, for a practical application $\langle n \rangle^i \approx n$ is an acceptable assumption. Following Bernard [16], the dimensionless secondary force, $\langle \overline{S_{sf}} \rangle^v$, is given by:

$$\langle \overline{S_{sf}} \rangle^v = \frac{\langle \bar{u} \rangle^i}{|\langle \bar{u} \rangle^i|}\left[\langle \widehat{\bar{n}} \rangle^i \cdot \nabla\left(\phi \langle \bar{h} \rangle^i \langle \overline{\tau_{ss}} \rangle^i\right) + \frac{\phi \langle \bar{h} \rangle^i \langle \overline{\tau_{ss}} \rangle^i}{2\langle \bar{r} \rangle^i}\right] \tag{6.5}$$

In [1], Equation (6.5) is derived from $\overline{S_{sf}}$. $\langle \overline{\tau_{ss}} \rangle^i$ is a scalar value, expressed as:

$$\langle \overline{\tau_{ss}} \rangle^i = \langle \bar{h} \rangle^i \langle \bar{\varpi} \rangle^i \sqrt{\langle C_{fr} \rangle^i}\left|\langle \bar{u} \rangle^i\right| \tag{6.6}$$

where, $\langle \bar{\varpi} \rangle^i = \left(C_2 \langle \overline{\omega_s} \rangle^i\right)/12$ is a scalar quantity with C_2 being a constant of proportionality, and $\langle \overline{\omega_s} \rangle^i = \langle \overline{\omega_s} \rangle^{i^*} L_{ref}/U_{ref}$. $\langle \overline{\omega_s} \rangle^i$ is perpendicular to cross section.

In Equation (6.5) $\langle \bar{r} \rangle^i = \langle \bar{r} \rangle^{i^*}/L_{ref}$ is positive for counterclockwise motion and negative for clockwise motion. The normal derivative $\langle \widehat{\bar{n}} \rangle^i . \nabla\left(\phi \langle \bar{h} \rangle^i \langle \overline{\tau_{ss}} \rangle^i\right)$ is positive when $\phi \langle \bar{h} \rangle^i \langle \overline{\tau_{ss}} \rangle^i$

increases in the positive radial direction. The unit vector, $\langle\widehat{\bar{n}}\rangle^i$, and the curvature radius, $\langle\bar{r}\rangle^i$, are expressed as:

$$\langle\widehat{\bar{n}}\rangle^i = \frac{\langle\bar{v}\rangle^i}{|\langle\bar{u}\rangle^i|}\boldsymbol{i} - \frac{\langle\bar{u}\rangle^i}{|\langle\bar{u}\rangle^i|}\boldsymbol{j} \tag{6.7}$$

$$\langle\bar{r}\rangle^i = \frac{|\langle\bar{u}\rangle^i|^3}{\langle\bar{u}\rangle^i\langle\bar{v}\rangle^i\left((\partial\langle\bar{v}\rangle^i/\partial y)-(\partial\langle\bar{u}\rangle^i/\partial x)\right)+\langle\bar{u}\rangle^{i^2}(\partial\langle\bar{v}\rangle^i/\partial x)-\langle\bar{v}\rangle^{i^2}(\partial\langle\bar{u}\rangle^i/\partial y)} \tag{6.8}$$

The dimensionless vegetation drag force can be given by:

$$\langle\overline{S_{vd}}\rangle^v = \frac{1}{\Omega_{REV}R_e}\int_{S_{fs}}\boldsymbol{n}_{fs}\cdot\left(\bar{\mu}\bar{h}\nabla\bar{\boldsymbol{u}}^T\right)ds - \frac{h}{\Omega_{REV}}\int_{S_{fs}}\boldsymbol{n}_{fs}\bar{P}\,ds = 0.5\langle\overline{C_d}\rangle^i\lambda\langle\overline{u_v}\rangle^i|\langle\overline{u_v}\rangle^i| \tag{6.9}$$

Equation (6.9) takes account of total drag force, it is valid for turbulent flow regime, its validity reduces in Forchheimer flow regime (since viscous effects will be significant and a linear expression has to be applied for the drag force) and, it is invalid for Darcy flow regime [19,20]. The macroscopic drag coefficient, $\langle\overline{C_d}\rangle^i$, is derived from temporally and spatially averaged microscopic drag coefficient [21]. The resultant flow velocity, $\langle\overline{u_v}\rangle^i$, can be given by [22]:

$$\langle\overline{u_v}\rangle^i = \eta_v\langle\bar{u}\rangle^i\left(\frac{\langle\overline{h_v'}\rangle^i}{\langle\bar{h}\rangle^i}\right)^{1/2} \tag{6.10}$$

where, η_v is a dimensionless coefficient of about 1.0 [22] and $\langle\overline{h_v'}\rangle^i = min\left(\langle\overline{h_v}\rangle^i, \langle\bar{h}\rangle^i\right)$.

In this article the high Reynolds number standard $k - \varepsilon$ model is used. The dimensionless conservative form of the k and ε equations are given by:

$$\frac{\partial(\phi\langle\bar{h}\rangle^i\langle\bar{k}\rangle^i)}{\partial t} + \nabla.\left(\phi\langle\bar{h}\rangle^i\langle\bar{k}\rangle^i\langle\bar{u}\rangle^i\right) = \frac{1}{R_e}\nabla.\left[\langle\bar{h}\rangle^i\left(1 + \frac{\mu_{t_\phi}}{\sigma_k}\right)\nabla(\phi\langle\bar{k}\rangle^i)\right] + \langle\overline{S_k}\rangle^i \tag{6.11}$$

$$\frac{\partial(\phi\langle\bar{h}\rangle^i\langle\bar{\varepsilon}\rangle^i)}{\partial t} + \nabla.\left(\phi\langle\bar{h}\rangle^i\langle\bar{\varepsilon}\rangle^i\langle\bar{u}\rangle^i\right) = \frac{1}{R_e}\nabla.\left[\langle\bar{h}\rangle^i\left(1 + \frac{\mu_{t_\phi}}{\sigma_\varepsilon}\right)\nabla(\phi\langle\bar{\varepsilon}\rangle^i)\right] + \langle\overline{S_\varepsilon}\rangle^i \tag{6.12}$$

where, $\langle\overline{S_k}\rangle^i = \langle\bar{h}\rangle^i\left(\langle\overline{G_k}\rangle^i - \phi\langle\bar{\varepsilon}\rangle^i + \phi\langle\overline{G_{kb}}\rangle^i + C_{fr_k}\langle\overline{G_{kv}}\rangle^i\right)$, and $\langle\overline{S_\varepsilon}\rangle^i = \langle\bar{h}\rangle^i C_{\varepsilon1}\langle\overline{G_k}\rangle^i\langle\bar{\varepsilon}\rangle^i/\langle\bar{k}\rangle^i$

$+\langle\bar{h}\rangle^i\left(-C_{\varepsilon2}\phi\langle\bar{\varepsilon}\rangle^{i^2}/\langle\bar{k}\rangle^i + \phi\langle\overline{G_{\varepsilon b}}\rangle^i + C_{\varepsilon1}C_{fr_\varepsilon}\langle\overline{G_{kv}}\rangle^i\langle\bar{\varepsilon}\rangle^i/\langle\bar{k}\rangle^i\right)$. $\langle\overline{G_k}\rangle^i$, $\langle\overline{G_{kv}}\rangle^i$, $\langle\overline{G_{kb}}\rangle^i$, and $\langle\overline{G_{\varepsilon b}}\rangle^i$ are given by:

$$\langle\overline{G_k}\rangle^i = \frac{\mu_{t_\phi}}{\phi R_e}\left[\left(\frac{\partial(\phi\langle\bar{u}\rangle^i)}{\partial y} + \frac{\partial(\phi\langle\bar{v}\rangle^i)}{\partial x}\right)^2 + 2\left(\frac{\partial(\phi\langle\bar{u}\rangle^i)}{\partial x}\right)^2 + 2\left(\frac{\partial(\phi\langle\bar{v}\rangle^i)}{\partial y}\right)^2\right] \tag{6.13}$$

$$\langle \overline{G_{kv}} \rangle^i = \langle \overline{S_{vd_x}} \rangle^v \langle \overline{u_v} \rangle^i + \langle \overline{S_{vd_y}} \rangle^v \langle \overline{v_v} \rangle^i \tag{6.14}$$

$$\langle \overline{G_{kb}} \rangle^i = C_{fr}^{-1/2} \langle \overline{U_\tau} \rangle^{i^3} / \langle \bar{h} \rangle^i \tag{6.15}$$

$$\langle \overline{G_{\varepsilon b}} \rangle^i = C_{\varepsilon\Gamma} C_{\varepsilon 2} C_\mu^{1/2} C_{fr}^{-3/4} \langle \overline{U_\tau} \rangle^{i^4} / \langle \bar{h} \rangle^{i^2} \tag{6.16}$$

where, $\langle \overline{U_\tau} \rangle^i = \sqrt{|\langle \overline{\tau_b} \rangle^i|}$, $\mu_{t_\phi} = C_\mu R_e \langle \bar{k} \rangle^{i^2} / \langle \bar{\varepsilon} \rangle^i$, $\langle \bar{k} \rangle^i = \langle \bar{k} \rangle^{i^*} / U_{ref}^2$, $\langle \bar{\varepsilon} \rangle^i = \langle \bar{\varepsilon} \rangle^{i^*} / (U_{ref}^3 / L_{ref})$, and the model constants are $C_\mu = 0.09$, $C_{\varepsilon 1} = 1.44$, $C_{\varepsilon 2} = 1.92$, $\sigma_k = 1.0$ and $\sigma_\varepsilon = 1.3$. Following Rodi [23], the coefficient $C_{\varepsilon\Gamma}$ is set to 3.6 for flumes and 1.8 for rivers. According to [24], $C_{fr_k} = 1.0$ and $C_{fr_\varepsilon} = 1.33$ are used.

When streamline is curved, the centrifugal force causes a secondary flow normal to streamline direction. Bed resistance force and gravitational acceleration act on secondary flow and, in turn, a helical flow will form. Bernard [16] has suggested that, in depth-averaged momentum equations the helical flow effect can be accounted for with Equation (6.5). In order to calculate the $\langle \overline{S_{sf}} \rangle^v$, the streamwise vorticity, $\langle \overline{\varpi} \rangle^i$, has to be known [see Equation (6.6)]. The streamwise vorticity at the domain can be obtained through a transport equation [16]:

$$\frac{\partial(\phi \langle \bar{h} \rangle^i \langle \overline{\varpi} \rangle^i)}{\partial t} + \nabla \cdot \left(\phi \langle \bar{h} \rangle^i \langle \overline{\varpi} \rangle^i \langle \overline{u} \rangle^i \right) = \phi A_s \sqrt{C_{fr}} \frac{|\langle \overline{u} \rangle^i|^2}{\langle \bar{r} \rangle^i \psi} - \phi_b D_s \sqrt{C_{fr}} \langle \overline{\varpi} \rangle^i |\langle \overline{u} \rangle^i| + \langle \overline{G_{\varpi v}} \rangle^v +$$

$$\frac{1}{R_e} \nabla \cdot \left[\langle \bar{h} \rangle^i \left(1 + \frac{\mu_{t_\phi}}{\sigma_\varpi} \right) \nabla (\phi \langle \overline{\varpi} \rangle^i) \right] \tag{6.17}$$

where, $\langle \overline{\varpi} \rangle^i = \langle \overline{\varpi} \rangle^{i^*} L_{ref} / U_{ref}$, $A_s = 5.0$, $D_s = 0.5$, $\sigma_\varpi = 1.0$, and $\psi = \left(1 + 9 \langle \bar{h} \rangle^{i^2} / \langle \bar{r} \rangle^{i^2} \right)$ are suggested by Bernard [16]. The vegetation dissipation source term, $\langle \overline{G_{\varpi v}} \rangle^v$, can be given by [1]:

$$\langle \overline{G_{\varpi v}} \rangle^v = \aleph \langle \overline{\varpi} \rangle^i |\langle \overline{\varpi} \rangle^i| \tag{6.18}$$

$$\aleph = 3 \sqrt{\frac{6}{A_s}} \langle \overline{C_d} \rangle^i \lambda \begin{cases} \left(\frac{\langle \overline{h_v''} \rangle^{i^4}}{\langle \overline{h_v'} \rangle^i \langle \bar{h} \rangle^{i^2}} - \frac{2 \langle \overline{h_v''} \rangle^{i^3}}{\langle \overline{h_v'} \rangle^i \langle \bar{h} \rangle^i} + \frac{3 \langle \overline{h_v''} \rangle^{i^2}}{2 \langle \overline{h_v'} \rangle^i} - \frac{\langle \overline{h_v''} \rangle^i \langle \bar{h} \rangle^i}{2 \langle \overline{h_v'} \rangle^i} \right) - & always \\[2ex] \left(\frac{\langle \overline{h_v'} \rangle^{i^3}}{\langle \bar{h} \rangle^{i^2}} - \frac{2 \langle \overline{h_v'} \rangle^{i^2}}{\langle \bar{h} \rangle^i} + \frac{3 \langle \overline{h_v'} \rangle^i}{2} - \frac{\langle \bar{h} \rangle^i}{2} + \frac{\langle \bar{h} \rangle^{i^2}}{16 \langle \overline{h_v'} \rangle^i} \right) & when \ \langle \overline{h_v'} \rangle^i > \frac{\langle \bar{h} \rangle^i}{2} \end{cases} \tag{6.19}$$

In Equation (6.19), $\langle \overline{h_v''} \rangle^i = \min \left(\langle \overline{h_v} \rangle^i, \langle \bar{h} \rangle^i / 2 \right)$ and, the second most right hand side bracket will be calculated only if $\langle \overline{h_v'} \rangle^i > \langle \bar{h} \rangle^i / 2$.

There is a division by streamline curvature radius in vorticity generation source term, the first term in the right hand side of Equation (6.17). The lower bound for streamline curvature radius calculated by Equation (6.8) is zero. Grid however filters the streamline curvature so that the actual lower bound for the streamline curvature radius in an equilateral triangle cell will be the normal distance between the neighboring cells, $h_{c_0\_c_n}$. In a grid with arbitrary triangular cells the streamline curvature radius can be given by [18]:

$$\langle \bar{r} \rangle^i = max \left\{ \langle \bar{r} \rangle^i, \frac{\sum_{j=1}^{3} h_{c_0\_c_j}}{3} \right\}$$
(6.20)

where, $\langle \bar{r} \rangle^i$ in the right hand side of Equation (6.20) is given by Equation (6.8).

6.2.3.2 Discretization scheme

SIMPLE algorithm is used for the coupling between pressure and velocity field. In SIMPLE algorithm continuity equation [Equation (6.1)] is converted into a pressure correction equation. Momentum equations are solved with an initial guessed pressure and velocity field. The derived velocity field is then used in the pressure correction equation. The obtained pressure correction corrects the pressure and velocity field, other scalars will be solved, and the solution continues in the next iteration until convergence is attained. The correction to pressure and velocity at any cell is given by:

$$\langle \bar{P} \rangle^i = \langle \overline{P^+} \rangle^i + \langle \bar{P}' \rangle^i$$
(6.21)

$$\langle \bar{u} \rangle^i = \langle \overline{u^+} \rangle^i - \frac{\Omega \langle \bar{h} \rangle^{i\,4/3}}{a_0^u} \nabla \left(\phi \langle \bar{P}' \rangle^i \right)$$
(6.22)

Convective terms are discretized using first order upwind scheme, Green's theorem is used for the calculation of the gradient at cell-center, and the two point method for the calculation of gradient at the cell face. The discretized pressure correction equation then can be expressed as:

$$a_0^P \langle \bar{P}' \rangle_0^i = \sum_{j=1}^{3} a_j^P \langle \bar{P}' \rangle_j^i - \langle \bar{\vartheta}^\circ \rangle^i$$
(6.23)

$$a_j^P = \frac{\phi_{s_j} \langle \bar{h} \rangle_{s_j}^i s_j}{2 h_{c_0\_c_j}} \left[\left(\frac{\Omega \langle \bar{h} \rangle^{i\,4/3}}{a_0^u} \right)_0 + \left(\frac{\Omega \langle \bar{h} \rangle^{i\,4/3}}{a_0^u} \right)_j \right] \phi_j$$
(6.24)

$$a_0^P = \phi_0 \sum_{j=1}^{3} \left\{ \frac{\phi_{s_j} \langle \bar{h} \rangle_{s_j}^i s_j}{2 h_{c_0\_c_j}} \left[\left(\frac{\Omega \langle \bar{h} \rangle^{i\,4/3}}{a_0^u} \right)_0 + \left(\frac{\Omega \langle \bar{h} \rangle^{i\,4/3}}{a_0^u} \right)_j \right] \right\} + \frac{\Omega_0 \phi_0}{g \Delta t}$$
(6.25)

In a triangular grid the discretized equation for the variable $\langle\bar{\varphi}\rangle^i$ can be written as:

$$a_0^\varphi \langle\bar{\varphi}\rangle_0^i = \sum_{j=1}^3 a_j^\varphi \langle\bar{\varphi}\rangle_j^i + \langle\overline{S_{u_\varphi}}\rangle^i \tag{6.26}$$

$$a_0^\varphi = \langle\bar{h}\rangle_0^i{}^{\alpha_1} \left\{ \sum_{j=1}^3 \left[\!\!\left[\langle\bar{C}\rangle_{s_j}^i, 0\right]\!\!\right] + \frac{\phi_0}{Re} \sum_{j=1}^3 \left[\frac{\left[\langle\bar{h}\rangle^i\left(1+\mu_{t_\phi}/\chi\right)\right]_{s_j} s_j}{h_{c_0\_c_j}} \right] \right\} - \langle\overline{S_{p_\varphi}}\rangle^i \tag{6.27}$$

$$a_j^\varphi = \langle\bar{h}\rangle_0^i{}^{\alpha_1} \left\{ \left[\!\!\left[-\langle\bar{C}\rangle_{s_j}^i, 0\right]\!\!\right] + \frac{\phi_j\left[\langle\bar{h}\rangle^i\left(1+\mu_{t_\phi}/\chi\right)\right]_{s_j} s_j}{Re h_{c_0\_c_j}} \right\} \tag{6.28}$$

where, $\left[\!\!\left[\langle\bar{C}\rangle_{s_j}^i, 0\right]\!\!\right]$ denotes the maximum of $\langle\bar{C}\rangle_{s_j}^i$ and 0. In Equations (6.27) and (6.28) χ takes the values 1.0, σ_k, σ_ε, and 1.0 for momentum, turbulence kinematic energy, turbulence dissipation rate, and vorticity equations, respectively. In Equations. (6.27) and (6.28) α_1 takes the values 1/3, 1/3, 17/12, and 1/6 for momentum, turbulence kinematic energy, turbulence dissipation rate, and vorticity equations, respectively.

A Rhie and Chow [25] type pressure interpolation technique is applied in order to obtain a mass conserving velocity at the cell face. Thus, the continuity residual can be expressed as:

$$\langle\bar{\vartheta}^\circ\rangle^i = \sum_{j=1}^3 \left\{ \frac{\left(\langle\bar{u}\rangle^i a_0^u\right)_0 + \left(\langle\bar{u}\rangle^i a_0^u\right)_j}{\left(a_0^u\right)_0 + \left(a_0^u\right)_j} \phi_{s_j}\langle\bar{h}\rangle_{s_j}^i \cdot \boldsymbol{s}_j - \omega_{rc} a_j^P\left(\langle\bar{P}\rangle_j^i - \frac{\phi_0}{\phi_j}\langle\bar{P}\rangle_0^i\right) \right\} + \frac{\Omega_0}{g\Delta t}\left[\phi\langle\overline{P^+}\rangle^i - \left(\phi\langle\bar{P}\rangle^i\right)^{n-1}\right]_0 \tag{6.29}$$

In Equation (6.29), the relaxation factor, ω_{rc}, is set to 1.0 [26]. Source terms are discretized according to [18].

6.2.3.3 Boundary conditions

The employed boundary conditions are the velocity inlet, the constant pressure (or equivalently, the water surface elevation) boundary, and the wall condition. Variables have to be known at the inlet. At the constant pressure boundary, it is assumed that the gradient of variables is zero, except for velocity components and pressure. Following Versteeg and Malalasekera [27], in order to derive the velocity components, mass is locally conserved at the cells adjacent to the constant pressure boundary where pressure is fixed. The standard wall function approach [28] is applied to the momentum and turbulence model equations.

6.2.3.4 Residuals

In Section 6.2.4, residuals are calculated in two different ways: the scaled residual, and the normalized residual. The continuity residual is given by:

$$\langle \overline{\vartheta_R} \rangle^i = \frac{\sum_{i=1}^{N_{cell}} |\langle \overline{\vartheta^\circ} \rangle^i|}{\langle \overline{\vartheta_{ref}^\circ} \rangle^i} \tag{6.30}$$

For a scaled error, $\langle \overline{\vartheta_{ref}^\circ} \rangle^i$ is the volumetric inlet discharge. For a normalized error, $\langle \overline{\vartheta_{ref}^\circ} \rangle^i$ is the largest absolute magnitude of the continuity residual in the first five iterations. The residual for any variable, $\langle \bar{\varphi} \rangle^i$, is expressed as:

$$\langle \overline{R_\varphi} \rangle^i = \frac{\sum_{i=1}^{N_{cell}} \left| \sum_{j=1}^{3} a_j^\varphi \langle \bar{\varphi} \rangle_j^i + s_{u_\varphi} - a_0^\varphi \langle \bar{\varphi} \rangle_0^i \right|}{\langle \overline{R_{ref}} \rangle^i} \tag{6.31}$$

where, for scaled errors, $\langle \overline{R_{ref}} \rangle^i = \sum_{i=1}^{N_{cell}} \left| a_0^\varphi \langle \bar{\varphi} \rangle_0^i \right|$, and for normalized errors, $\langle \overline{R_{ref}} \rangle^i$ is the largest absolute magnitude of the φ residual in the first five iterations.

6.2.4 Numerical results

This section contains five different test cases in order to investigate the conditions where the calculated secondary force improves the accuracy of the computed velocity field.

6.2.4.1 Steffler (1984) test

In the experiment performed in [29], the side walls were galvanized sheet metal. Therefore, the smooth but no-slip condition is assumed on side walls. Manning's number is $0.0125 \, s/m^{1/3}$, the water depth at the outlet is 0.061 m, the total discharge at the inlet is $0.0235 \, m^3/s$, and the bed slope is 0.00083. The reference length, L_{ref}, is $0.061 \, m$ and, the reference velocity, U_{ref}, is $0.36 \, m/s$. The water specific gravity and dynamic viscosity are $998.2 \, kg/m^3$ and $0.001003 \, N.m/s^2$, respectively. Errors are normalized and, the convergence criterion is set to 10^{-3}. The grid contains 18398 nearly uniform unstructured triangular elements and, the number of the cells in channel cross section is about 20. The geometrical details together with some hydraulic parameters of the channel are depicted in Figure 6.1.

Profile of stream-wise velocity at different sections is presented in Figure 6.2. Section 0° is at the straight part of the channel. At this section, the computed velocity profiles with and without

considering the secondary force effect are exactly similar. At section $60^{°}$, the computed velocity profile is more accurate when the secondary force effect is considered. At section $120^{°}$, the accuracy of the computed velocity profiles are nearly the same. At other sections, when the secondary force effect is considered, the magnitude of the stream-wise velocity near the inner wall is highly over predicted.
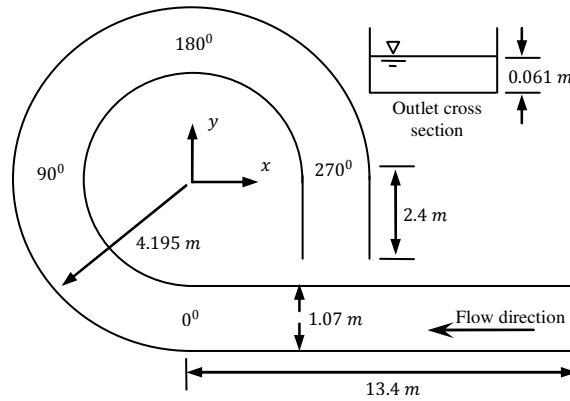
Figure 6.1. Geometrical detail in Steffler's [29] test.
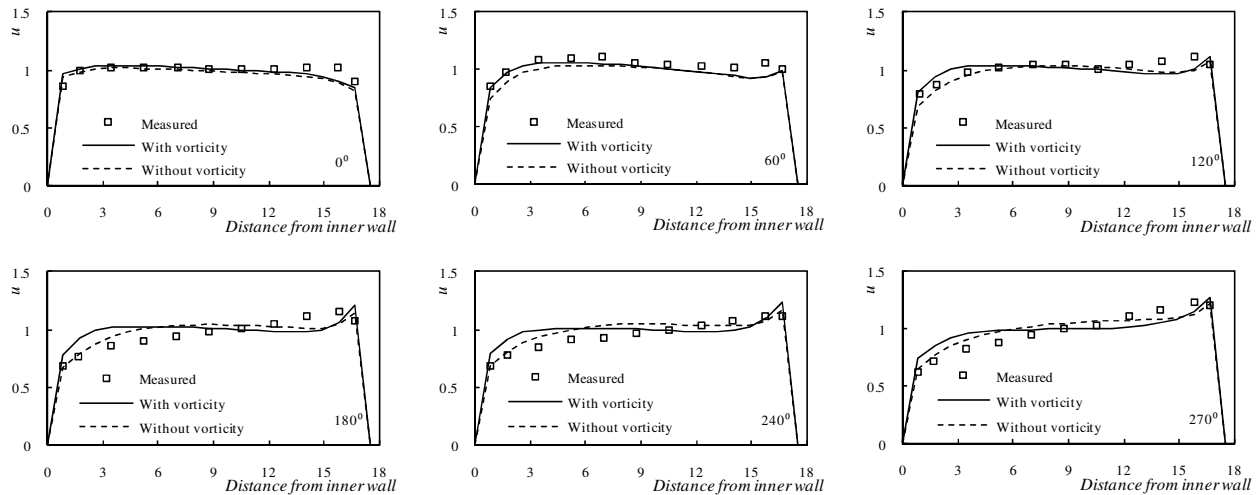
Figure 6.2. Profile of streamwise velocity in Steffler [29] bend at different sections.

6.2.4.2 De Vriend (1981) test

In this test, the flow in a smooth bend, measured by De Vriend [30], is simulated. The smooth but no-slip condition is assumed on side walls. Manning's number is $0.024\ s/m^{1/3}$, the water depth at the outlet is $0.1412\ m$, the total discharge at the inlet is $0.19\ m^{3}/s$, and the bed slope is zero.

The reference length, L_{ref}, is $0.1412\,m$ and, the reference velocity, U_{ref}, is $0.5198\,m/s$. The water physical properties are same as in Section 6.2.4.1. Errors are normalized and, the convergence criterion is set to 10^{-3}. The grid contains 10496 nearly uniform unstructured triangular elements, the number of the cells in channel cross section is about 17, and the average grid spacing is 0.71. The geometrical details together with some hydraulic parameters of the channel are depicted in Figure 6.3.
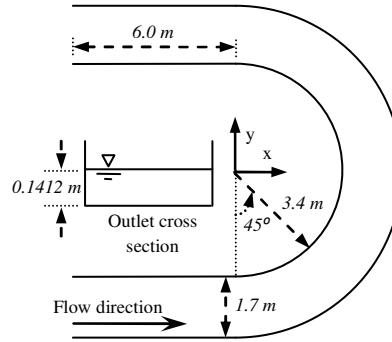
Figure 6.3. Geometrical detail in De Vriend's [30] test.

Profiles of stream-wise velocity are presented in Figure 6.4. In entire sections except section 45°, the computed velocity profile without considering the secondary force effect in momentum equations is more accurate compared with the cases where the secondary force effect is considered. Regarding the density of the measurement points near the inner wall at section 45°, the velocity profiles computed with and without considering the secondary force effect have nearly the same accuracy. A simple comparison between the channel in this test case and the channel in Section 6.2.4.1 reveals that, the main difference is in the magnitude of the water depths. In Section 6.2.4.1, the water depth is very small and the channel width to depth ratio is very high. Thus, the assumption of a shallow flow is more valid in Steffler's test compared with the De Vriend's test.
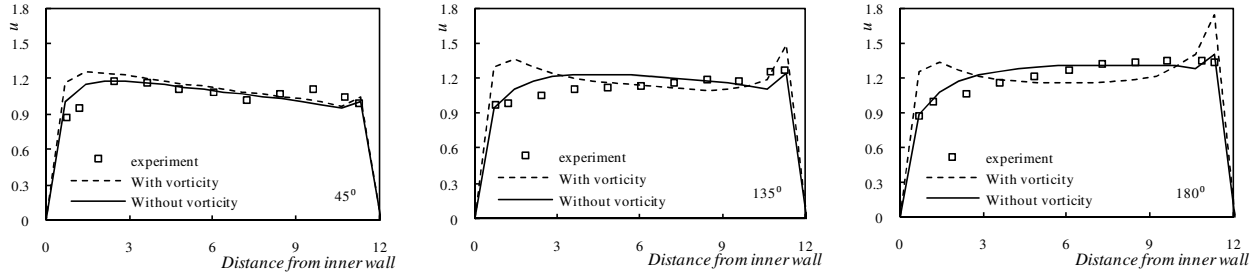
Figure 6.4. Profiles of streamwise velocity in De Vriend's [30] bend at different sections.

6.2.4.3 Tominaga et al. (1998) type tests

The experimental test is performed by Tominaga et al. [31]. The flow Reynolds number is 2.65×10^5 with $L_{ref} = 0.9\,m$ and $U_{ref} = 0.296296\,m/s$. Bed slope is assumed zero, vegetation stem diameter is $0.005\,m$, and the emergent stems are uniformly arranged with a spacing equal to $0.05\,m$. Manning's number is $0.015\,s/m^{1/3}$, and the total inlet discharge is $0.04\,m^3/s$. Errors are scaled, and the convergence criterion is set to 10^{-3}. Other details are as in Section 6.2.4.1. Following [31] the drag coefficient is calculated as:

$$\langle \overline{C_d} \rangle^i \approx \begin{cases} (10^3/R_e)^{0.25} & for\ R_{e_d} \leq 10^3 \\ min(0.79 + [(10^{-3}R_e - 2)/20.5]^2, 1.15) & for\ 10^3 \leq R_{e_d} \leq 4 \times 10^4 \end{cases}$$

Test cases include the channel in Figure 6.5 where only a narrow band at the centerline of the channel bend is vegetated and, the same channel as the one in Figure 6.5 where the width of the vegetated zone is assumed equal to the width of the channel.
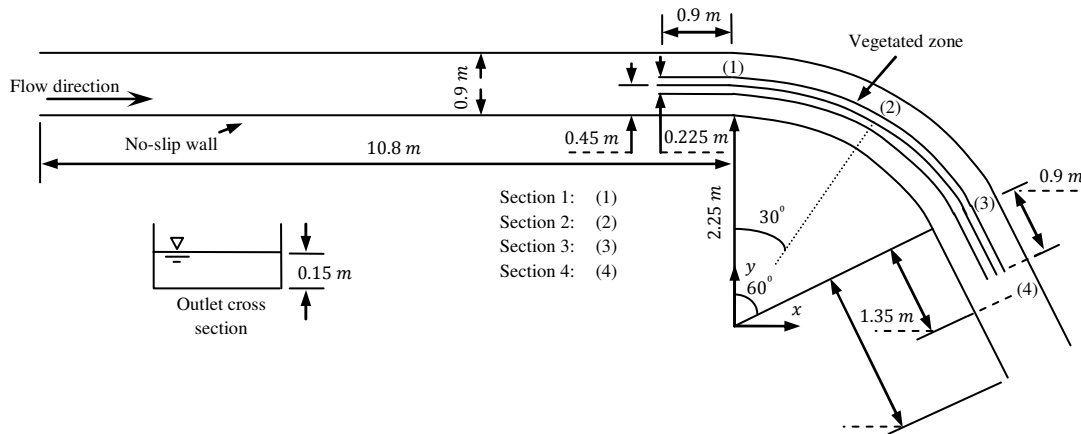
Figure 6.5. Geometrical detail in Tominaga et al. [31] test.

6.2.4.3.1 Partially vegetated channel bend

In this test, the number of grid points in transverse direction is about 40. The velocity profiles at four different sections are shown in Figure 6.6. When the secondary force is computed, the magnitude of the stream-wise velocity in section 2 is slightly more accurate. In sections 3 and 4, calculation of the secondary force highly shifts the velocity profiles toward the inner wall. In Figure 6.6, damping of stream-wise vorticity by vegetation has no effect on velocity profiles. It can be due to the small thickness of the vegetated zone or the small magnitude of the streamwise velocity in vegetated band. In order to investigate the effect of these parameters the whole channel cross section in Section 6.2.4.3.2 is vegetated.
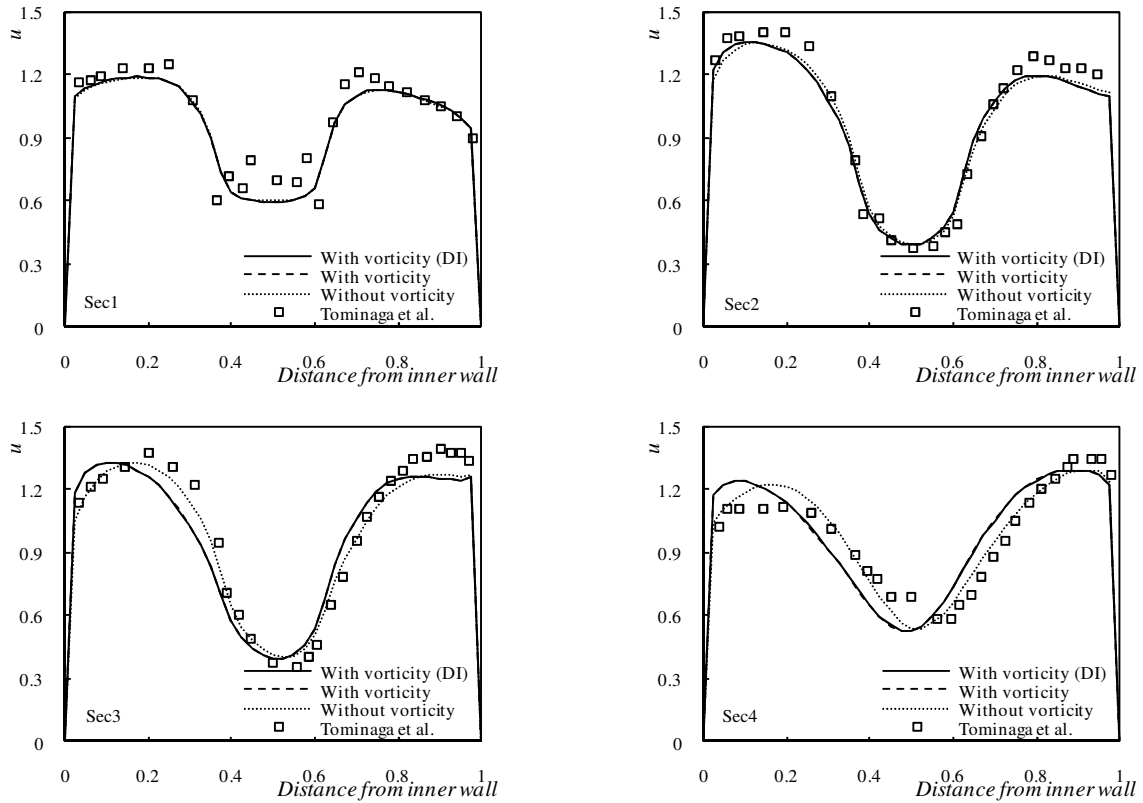
Figure 6.6. Secondary force effect on velocity profile in Tominaga et al. [31] test; DI means, damping of vorticity due to vegetation zone is included.

6.2.4.3.2 Fully vegetated channel bend

In this test, the number of grid points in transverse direction is about 20. The magnitude of the streamwise velocities in Figure 6.7 is about three times bigger than the magnitude of the

streamwise velocity in vegetated zones in Figure 6.6. Even though, the computed velocity profiles in Figure 6.7 are exactly similar. The profile of water surface is presented in Figure 6.8. In this figure a high drop in the magnitude of the water surface elevation can be observed at the channel bend in streamwise direction. The consequence of this drop in water surface elevation is acceleration of water. This streamwise acceleration of water can be clearly observed in Figure 6.7 where the velocity magnitude in section 4 is more than the velocity magnitude in section 1. Since the force due to the hydrostatic pressure gradient is much bigger than the force due to the secondary force, the computed velocity profiles in Figure 6.7 are similar; i.e. the secondary force effect is ignorable.
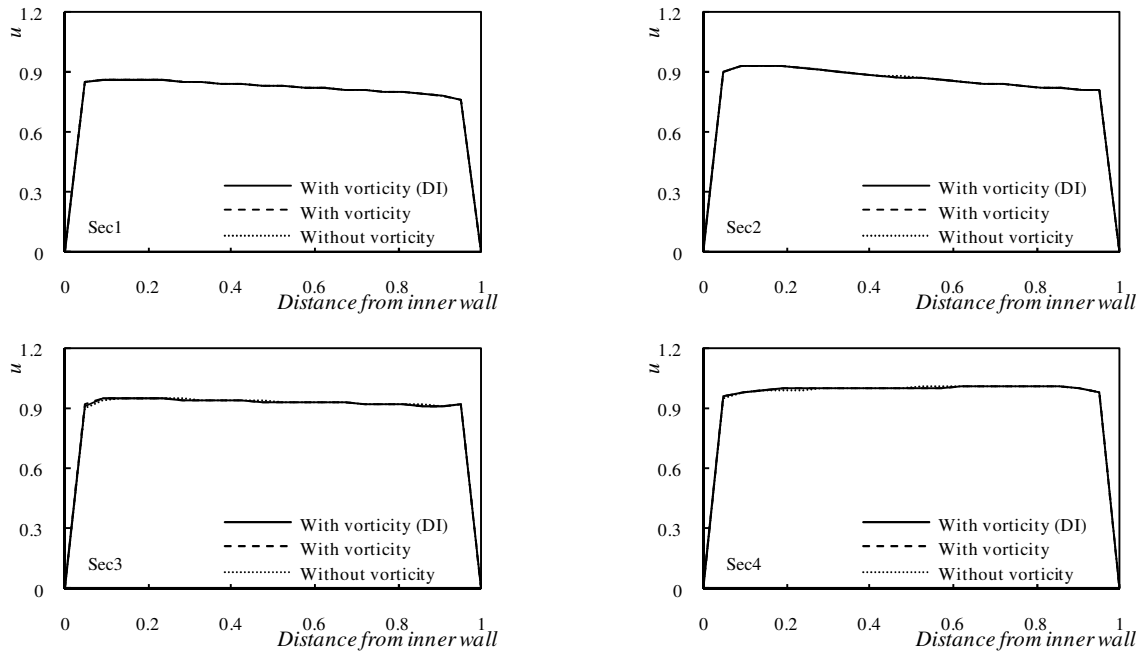
Figure 6.7. Secondary force effect on velocity profile in Tominaga et al. [31] channel where, the width of vegetation zone is assumed equal to the width of the channel; DI means, damping of vorticity due to vegetation zone is included.

6.2.4.4 Alternate vegetated zones

In this test case, the flow Reynolds number is 4.98×10^5 with $L_{ref} = 1\ m$ and $U_{ref} = 0.5\ m/s$. Bed slope is 0.001, stem diameter is 0.01 m, and the spacing between stems is 0.1 m. Manning's number is 0.01 $s/m^{1/3}$, drag coefficient is assumed 1.0, and the total inlet discharge is 0.1 m^3/s. The side walls are assumed smooth but no-slip, and the emergent vegetation stems are

arranged in a staggered manner. The number of grid points in transverse direction is about 40. Errors are scaled, and the convergence criterion is set to 10^{-3}. The geometrical details together with some hydraulic parameters of the channel are depicted in Figure 6.9. Other details are as in Section 6.2.4.1.
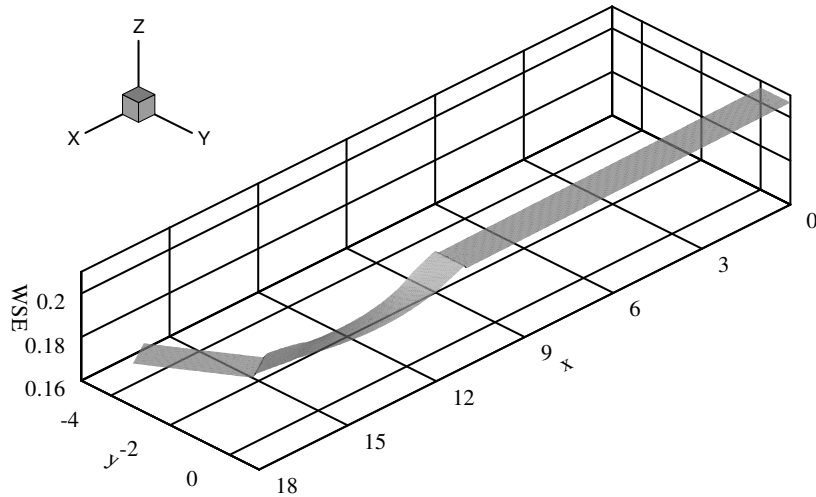
Figure 6.8. Profile of water surface for a Tominaga et al. [31] type channel where the whole cross section at channel bend is vegetated.
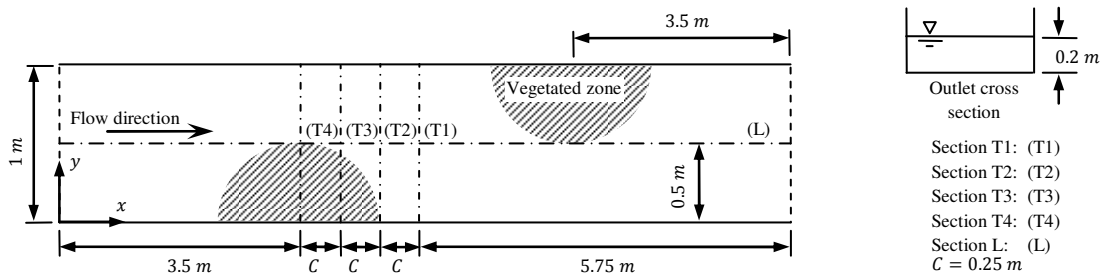
Figure 6.9. Geometrical detail in alternate vegetated zones test case.

The velocity profiles computed with and without solving for vorticity equation are presented in Fig. 10. In vegetated zone where the flow is slower, the computed velocity profiles are quite similar. More differences can be observed in velocity profiles, computed with and without solving for vorticity equation, right outside the vegetated zone. When the flow velocity is high enough, the streamline curvature due to the presence of a vegetated zone produces a secondary force strong enough to influence the velocity field.
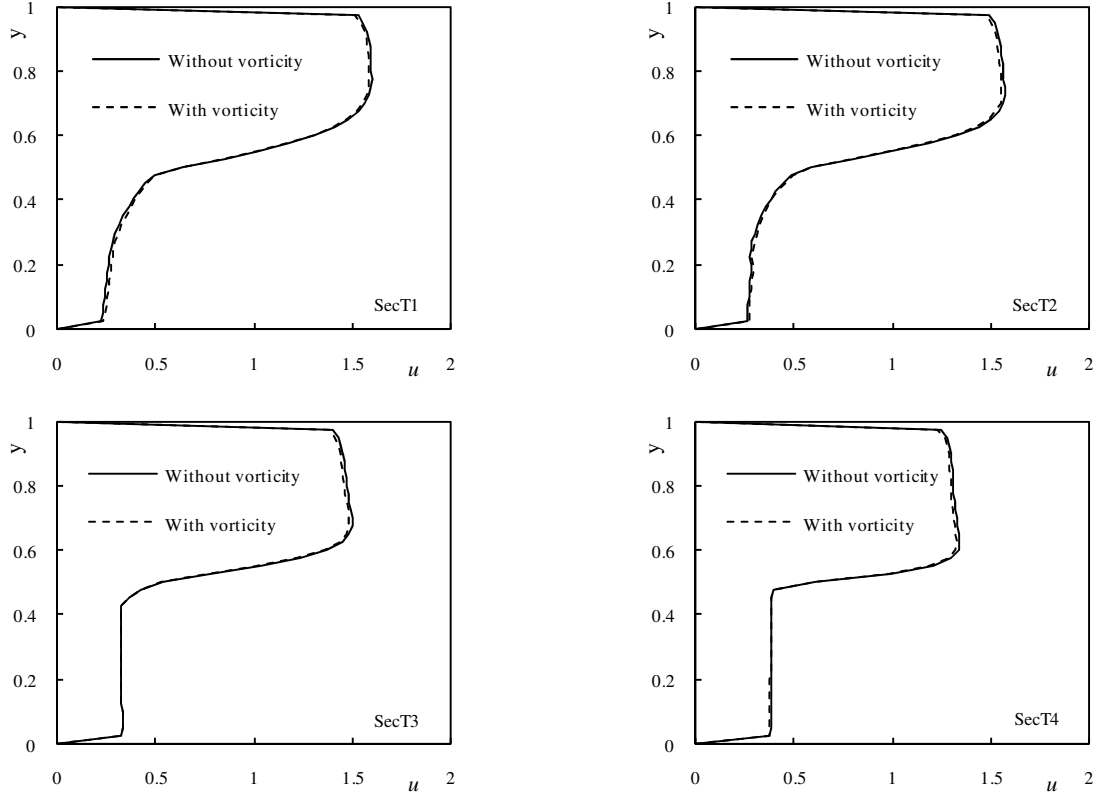
Figure 6.10. Velocity profiles in the channel with alternate vegetated zones at $R_{e_D} = 5000$.

6.2.5 Discussion of results

On entire simulations where a bend is involved, the vorticity based secondary force increases the accuracy of the computed velocity field only when the depth to width and depth to bend radius ratios are small. This can be observed in Figure 6.11 where the data available in this article are put together in order to quantify the results. Regarding the gradient of variations, the vorticity based secondary force can be safely used when depth to width ratio is less than 0.055 and depth to bend radius ratio is less than 0.015.
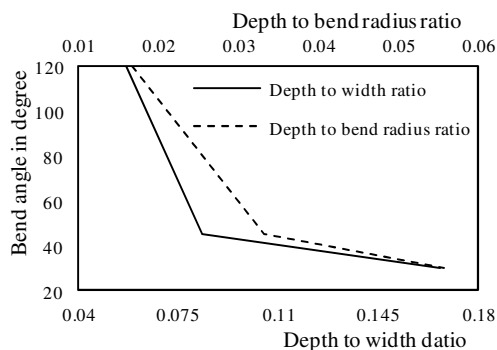
Figure 6.11. Maximum bend angles in degree, where the application of vorticity based secondary force will actually increase the accuracy of the computed velocity field.

6.2.6 Conclusion

In this article, vorticity equation is solved in order to compute the stream-wise vorticity. The computed stream-wise vorticity is then used for calculating the secondary force. It is indicated that, the calculated secondary force improves the accuracy of the computed velocity field where both the depth to width and depth to bend radius ratios are very small. It is shown that, even for a higher magnitude of the depth to width ratio, the calculated secondary force improves the accuracy of the computed velocity field if the channel bend is short. Though the vegetation induced damping source term in vorticity equation reduces the absolute magnitude of the stream-wise vorticity, its consequent effect on secondary force has little effect on a depth-averaged simulation. It is indicated that, in a channel with fully vegetated cross section where the extent of the vegetated zone in stream-wise direction is less than the channel length, the gradient of water surface elevation in vegetated zone will be high. In such cases, since the magnitude of the secondary force will not be comparable with hydrostatic pressure force, the secondary force effect can be ignored. It is shown that, the calculated secondary force even alters the velocity field when the streamline is curved through the presence of a vegetated zone. The secondary force due to the presence of a vegetated zone is found to have less influence on velocity profile compared with the cases where the secondary force is due to channel bends.

6.2.7 Acknowledgments

6.2.8 References

Bernard, R.S., 1993. STREMR: Numerical model for Depth-averaged incompressible Flow, U.S. Army Engineer Waterway Experiment Station, Vicksburg, MS.

Choi, S.-U., Park, M., Kang, H., 2007. Numerical simulations of cellular secondary currents and suspended sediment transport in open-channel flows over smooth-rough bed strips. J. Hydraul. Res. 45, 829-840.

Cieślik, A.R., Kamp, L.P.J., Clercx, H.J.H., van Heijst, G.J.F., 2010. Three-dimensional structures in a shallow flow. J. Hydro-environ. Res. 4, 89-101.

de Lemos, M.J.S., 2006. Turbulence in porous media: modeling and applications. Elsevier, London, UK, 335 pp.

De Vriend, H.J., 1981. Flow measurments in a curved rectangular channel, Part II: rough bottom. 9-79, Laboratory of Fluid Mechanics, Delft University of Technology, Delft, Netherlands.

Dongsu, K., 2012. Assessment of longitudinal dispersion coefficients using Acoustic Doppler Current Profilers in large river. J. Hydro-environ. Res. 6, 29-39.

Duan, J.G., Julien, P.Y., 2005. Numerical simulation of the inception of channel meandering. Earth Surf. Process. Landf. (UK), 30, 1093-1110.

Dulal, K.P., Shimizu, Y., 2010. Experimental simulation of meandering in clay mixed sediments. J. Hydro-environ. Res. 4, 329-343.

Hsieh, T.-Y., Yang, J.-C., 2005. Numerical examination on the secondary-current effect for contaminant transport in curved channel. J. Hydraul. Res. 43, 644-659.

Hyeongsik, K., Sung-Uk, C., 2009. Scalar flux modeling of solute transport in open channel flows: Numerical tests and effects of secondary currents. J. Hydraul. Res. 47, 643-655.

Kimura, I., Onda, S., Hosoda, T., Shimizu, Y., 2010. Computations of suspended sediment transport in a shallow side-cavity using depth-averaged 2D models with effects of secondary currents. J. Hydro-environ. Res. 4, 153-161.

Launder, B.E., Spalding, D.B., 1974. The Numerical Computation of Turbulent Flows. Comput. Meth. Appl. Mech. Eng. 3, 269-289.

Lopez, F., Garcia, M., 1997. Open-channel flow through simulated vegetation: turbulence modeling and sediment transport. WRP-CP-10, US Army Corps of Engineers, Waterw. Exp. Stn., Vicksburg.

Moradi Larmaei, M., Behzadi , J., Mahdi, T.-F., 2010. Treatment of checkerboard pressure in the collocated unstructured finite-volume scheme. Numer. Heat Transfer. Part B Fundam. 58, 121–144.

Moradi Larmaei, M., Behzadi , J., Mahdi, T.-F., 2011. Grid-independent depth-averaged simulations with a collocated unstructured finite volume scheme. Int. J. Numer. Methods Fluids: Article first published online: 22 MAR 2011.

Moradi Larmaei, M., Mahdi, T.-F., 2012. Depth-averaged turbulent heat and fluid flow in a vegetated porous media. Int J Heat Mass Transfer. 55, 848-863.

Nezu, I., Sanjou, M., 2008. Turburence structure and coherent motion in vegetated canopy open-channel flows. J. Hydro-environ. Res. 2, 62-90.

Omran, M., Knight, D.W., 2010. Modelling secondary cells and sediment transport in rectangular channels. J. Hydraul. Res. 48, 205-212.

Rhie, C.M., Chow, W.L., 1983. Numerical Study of the turbulent flow past an airfoil with trailing edge separation. Aiaa J. 21, 1525-1532.

Rodi, W., 1993. Turbulence models and their application in hydraulics. IAHR Monograph, Balkema, Rotterdam, Netherlands.

Rodriguez, J.F. et al., 2004. High-resolution numerical simulation of flow through a highly sinuous river reach. Water Resour. Manage. 18, 177-199.

Shiono, K., Spooner, J., Chan, T., Rameshwaran, P., Chandler, J., 2008. Flow characteristics in meandering channels with non-mobile and mobile beds for overbank flows. J. Hydraul. Res. 46, 113-132.

Steffler, P.M., 1984. Turbulent flow in a curved rectangular channel, University of Alberta, Alberta, Canada, 262 pp.

Sun, T., Meakin, P., Jossang, T., 2001. A computer model for meandering rivers with multiple bed load sediment sizes 1. Theory. Water Resour. Res. 37, 2227-2241.

Tang, X., Knight, D.W., 2008. A general model of lateral depth-averaged velocity distributions for open channel flows. Adv. Water Resour. 31, 846-857.

Tanino, Y., Nepf, H.M., 2008. Laboratory investigation of mean drag in a random array of rigid, emergent cylinders. J. Hydraul. Eng. 134, 34-41.

Tominaga, A., Nagao, M., Nezu, I., 1998. Effects of vegetation on flow structures and bed profiles in curved open channels. In: Lee, J.H.W., Jayawardena, A.W., Wang, Z.Y. (Eds.), Second international symposium on environmental hydraulics. A.A. Balkema, Hong Kong, China, pp. 329-334.

Versteeg, H.K., Malalasekera, W., 1995. An introduction to computational fluid dynamics : the finite volume method. Pearson Prentice Hall, Toronto, 257 pp.

Wang, Z.-Q., Cheng, N.-S., 2008. Influence of secondary flow on distribution of suspended sediment concentration. J. Hydraul. Res. 46, 548-552.

Wu, W., Shields Jr, F.D., Bennett, S.J., Wang, S.S.Y., 2005. A depth-averaged two-dimensional model for flow, sediment transport, and bed topography in curved channels with riparian vegetation. Water Resour. Res. 41, W03015.

Wu, W., Wang, S.S.Y., 2004. Depth-averaged 2-D calculation of flow and sediment transport in curved channels. Int. J. Sediment Res. 19, 241-257.

Zhang, M.-L., Li, C.W., Shen, Y.-M., 2010. A 3D non-linear k-epsilon turbulent model for prediction of flow and mass transport in channel with vegetation. Appl. Math. Modelling. 34, 1021-1031.

Zhang, X., Nepf, H.M., 2009. Thermally driven exchange flow between open water and an aquatic canopy. J. Fluid Mech. 632, 227-243.

CHAPTER 7   ARTICLE 5: DEPTH-AVERAGED TURBULENT HEAT AND FLUID FLOW IN A VEGETATED POROUS MEDIUM

7.1   Presentation of the article

In this section the objective of the article will be presented, as well as a conclusion on this work as part of the thesis. In this research, the most recent advances in porous media science are applied to partially vegetated channels. Together with the authors' scientific contributions in this field, which are presented in this chapter, an accurate prediction of thermal and hydrodynamic fields in vegetated zones now is possible. This can be used, for instance, for the investigation of thermal pollution due to a power plant near a river or lake.

7.1.1   Objective

As far as the authors are aware, the heat transfer under forced convection has never been numerically investigated in partially vegetated channels using porous media science. Even in porous media science there are still many numerical aspects which demand attention. For instance, several researchers made efforts to improve the near wall treatment in porous zones. In this research several numerical models are suggested which can be used in the general field of porous media as well as vegetated zones. Efforts are also made in this research to investigate the effect of discontinuity in porosity on temperature field, as well as the effect of laminar thermal dispersion, and applicability of a high Reynolds number turbulence model to partially vegetated porous zones. An important problem in partially porous media is that, the turbulence strength in the porous zone hardly follows the turbulence characteristics in the main channel. Though, there are several turbulence models which are developed for uniformly porous media, neither these models nor the high Reynolds number turbulence models (regarding the fact that, in any customary turbulence model the model constants are not calibrated for porous media) are applicable to a partially porous media. As a result, it will be a valuable research to investigate the conditions under which a high Reynolds number turbulence model which is usually used in conjunction with shallow flow equations can be applied. After this research, the solver which is developed in this thesis can be applied to problems which include heat transfer in vegetated zones such as the thermal pollution in a river.

7.1.2 Conclusion

Neither the laminar thermal dispersion, nor the heat flux due to porosity gradient has significant effect on temperature field when a high Reynolds number turbulence model can be applied. There is a region right downstream of every vegetated zone where the turbulence kinematic energy has its minimum magnitude. Such regions are where the universal wall normal distance has its minimum value, and a high Reynolds number turbulence model may not be applicable if vegetation density is high. It is observed that, application of porous media science to partially vegetated channels highly increases the accuracy of the computed velocity field.

The article published with International Journal of Heat and Mass Transfer.

Moradi Larmaei, M., and Mahdi, T.-F. (2012). Depth-averaged turbulent heat and fluid flow in a vegetated porous medium. International Journal of Heat and Mass Transfer, 55 (4) 848-863.

7.2 Depth-averaged turbulent heat and fluid flow in a vegetated porous medium

M. Moradi Larmaei and Tew-Fik Mahdi

Department of Civil, Geological and Mining Engineering, Montreal Polytechnic Institute, Montreal, Quebec, Canada.

7.2.1 Abstract

In this article, the latest developments of porous media science are used in order to simulate heat and fluid flow in a non-flexible vegetated porous media. Vegetation porosity and density at the domain interior are redefined. The same strategy is then applied in order to define the boundary porosity near the bed and water surface. Regarding the vegetation arrangement in natural streams and flumes, three different models are suggested for calculating the porosity near other boundaries. The microscopic time-mean secondary force in momentum equations is modified for a vegetated porous media and its macroscopic form is derived. A dissipation source term is derived and, it is added to vorticity equation in order to take account of vegetation damping effect on secondary flows. The effect of this dissipation source term on the absolute magnitude of vorticity and velocity field is then investigated. Application of a high Reynolds number turbulence model to turbulent flow in partially vegetated open channels is numerically examined. A model is suggested for taking account of vegetation material on heat flux through walls in a vegetated porous media. The thermal diffusion due to the porosity gradient is modeled and, the contribution of this porosity-induced heat flux on temperature field is investigated. The effect of laminar thermal dispersion on temperature field is also investigated at low stem Reynolds number.

Keywords: Double-decomposition, Depth-averaged simulation, Vegetation, Porous media, Heat transfer

Nomenclature

a_0, a_j	coefficients in the discretized equations
c_p	specific heat capacity
C_{s_j}	volumetric flux at the cell face s_j
C_{fr}, C_d	bed friction coefficient and vegetation drag coefficient, respectively
d_v	stem diameter
g	gravitational acceleration
G	rate of production in $k - \varepsilon$ model equation
h, h_v	water depth and vegetation effective height, respectively
$h_{c_0\_c_j}$	normal distance between two neighbor cells
H_v	spacing between vegetation stems
k	turbulence kinematic energy
$K, \boldsymbol{K}$	thermal conductivity and the thermal conductivity tensor
L	length scale
n	direction along $\boldsymbol{n}$ or Manning's number
$\boldsymbol{n}$	unit vector normal to the cell face when there is no subscript, any unit normal otherwise
$\hat{\boldsymbol{n}}$	unit vector normal to velocity vector $\boldsymbol{u}$
P, P'	pressure and pressure correction, respectively

P_{e_d} stem Peclet number, defined as $P_{e_d} = c_{p_f}^* \phi |\langle \overline{\boldsymbol{u_v}} \rangle^{i^*}| d_v^* / K_f^*$

P_{e_H} cavity Peclet number, defined as $P_{e_H} = c_{p_f}^* \phi |\langle \overline{\boldsymbol{u_v}} \rangle^{i^*}| H_v^* / K_f^*$

P_r Prandtl number, defined as $P_r = c_{p_f}^* \mu_f^* / K_f^*$

P_{r_t} Turbulent Prandtl number, defined as $P_{r_t} = c_{p_f}^* \mu_{t_\phi}^* / K_t^* = 0.85$

r streamline curvature radius

R residual at the domain

R_e flow Reynolds number, defined as $R_e = \rho_f^* U_{ref} l_{ref} / \mu_f^*$

R_{e_D} stem Reynolds number based on reference velocity, defined as $R_{e_D} = \rho_f^* U_{ref} d_v / \mu_f^*$

R_{e_d} stem Reynolds number based on resultant velocity, defined as $R_{e_d} = \rho_f^* \langle \overline{\boldsymbol{u_v}} \rangle^{i^*} d_v^* / \mu_f^*$.

$s_j, \boldsymbol{s}_j, s$ cell face area, the area vector, and the area of an arbitrary surface, respectively

$S, \boldsymbol{S}$ Scalar and vector form of the source terms, respectively

t time

T temperature

u, v velocity components in x and y directions, respectively

U velocity scale

$\boldsymbol{u}$ velocity vector

x, y x and y directions

$[-]$ in figures, it refers to a dimensionless solution

$\lvert \boldsymbol{\varrho} \rvert$	for any vector $\boldsymbol{\varrho}$, $\lvert \boldsymbol{\varrho} \rvert$ refers to the argument of the vector
$\langle \varrho \rangle^i$	for any variable ϱ, $\langle \varrho \rangle^i$ refers to its average over the volume of the fluid phase in REV
$\langle \varrho \rangle^v$	for any variable ϱ, $\langle \varrho \rangle^v$ refers to its average over the volume of REV
$\bar{\varrho}$	for any depth-averaged variable ϱ, $\bar{\varrho}$ refers to its time-mean depth-averaged form

Greek symbols

α	dimensionless constant of about 1.0 for cylindrical vegetation stems
ε	dissipation rate of k
η	a dimensionless constant of about 1.0
ϑ°	continuity residual
ϑ	normalized continuity residua
λ	vegetation density
μ, μ_{t_ϕ}	laminar and macroscopic turbulent dynamic viscosity, respectively
ξ	water surface elevation
ρ	density
σ	Prandtl/Schmidt number
ς	porosity-induced flux equivalent
$\tau, \boldsymbol{\tau}$	scalar and vector stresses
φ	general scalar quantity

ϕ	porosity
χ	Prandtl/Schmidt number in general discretized equation for φ
ω_{rc}	relaxation factor in pressure correction term
ϖ	vorticity
ω_s	magnitude of streamwise vorticity vector
Ω	volume

Subscripts

b	refers to the channel bed
bo	refers to boundaries
f	refers to fluid phase
fs	Refers to the interface between fluid and solid phase, directed from fluid toward solid
j	refers to neighboring cell
k	refers to turbulence kinematic energy
p_φ	refers to the implicit part of the source term in discretized equation for φ
P	refers to the nearest point (cell-center) to the wall
ref	refers to reference value
R	refers to residual at the domain
REV, REV_f	refer to REV and the fluid in REV, respectively
ss	refers to secondary shear

sf	Refers to secondary force
s_j	refers to cell face s_j
t	refers to turbulence
u_φ	refers to the explicit part of the source term in discretized equation for φ
v	refers to vegetation
vd	refers to vegetation drag force
w	refers to wall
ε	refers to dissipation rate of k
τ	refers to shear
φ	refers to φ
0	refers to central cell

Superscripts

n	refers to the current time step
P	refers to pressure
T	refers to the transpose of a vector
u	refers to $\boldsymbol{u}$
φ	refers to φ
$=$	refers to discretized form
$+$	refers to an initial guess (can be from previous iteration)

∗   refers to the dimensional form of a quantity

7.2.2 Introduction

When a microscopic transport equation is integrated over the water depth, its depth-averaged form will be derived. A time-mean microscopic depth averaged equation will be obtained when the microscopic depth-averaged equation is integrated over a time interval. Further integration of a time-mean depth-averaged equation over a Representative Elementary Volume (REV) will produce a time-mean macroscopic depth averaged equation. A transport equation which underwent all the mentioned integrations is called a double-decomposed depth-averaged equation. The equations which will be introduced in this article underwent the sequential integration process as presented.

Double-decomposed depth-averaged flow in a non-flexible vegetated porous media can be simulated in the same way as the double-decomposed two-dimensional flow over an array of rods [1-4]. After the research work by [1-4] more advancements in porous media science is achieved. The technique the authors are using in this article is mainly based on the works by De Lemos and his co-researchers [5-11]. A main difference between the works by [5-11] and the research work performed by [1-4] is in the way porosity appears in transport equations. This, for example, will affect the definition of the flux at the face between two neighbouring cells. In this article, compared to the work by [1-4], the depth-averaged double-decomposed energy equation is also solved over a non-flexible partially vegetated porous media.

An appropriate solution for heat and fluid flow in a vegetated porous media will be achieved when the domain porosity is well defined, vegetation damping effect on secondary flows is considered, an appropriate turbulence model is used, heat flux through walls is accurately calculated and, thermal diffusion is well modeled. In this article, the mentioned characteristics of such solution are investigated in the following research cases:

a) The porosity of a vegetated porous media will appear in the entire terms of a transport equation, except the term where vegetation effect is formulated; e.g. the vegetation drag force in momentum equations [3]. This term is where the vegetation density will appear in the

equation. Thus, either the vegetation density or its porosity should be derivable from the other one. When this criterion is not held, the conservation of the relevant fluid property will not be satisfied; e.g. momentum in momentum equations. In [3,12] either the defined vegetation density or its porosity can be derived from the other one but, an exact expression for the definition of vegetation porosity is not presented. Fischer-Antze et al. [13] assumed there is only one stem at every computational cell. The vegetation density and porosity which are derived using this assumption, or their more complete form as suggested in [4], are hardly extendable to a complicated vegetated porous media. The porosity defined at the interior of a domain fails to apply in the region near a macroscopic boundary [14]. For a near-wall region, for example, this problem becomes serious since most of the important transfer process occurs in the boundary layer near the wall. In this article, vegetation density and its porosity are defined from a unit-cell. The two-dimensional form of such unit-cell was first introduced in [15-17] in order to study the thermal dispersion over an array of rods. Such unit-cell is regarded as a basic concept and, it is used in future research works [7,18]. The defined vegetation density and porosity are simply applicable to a complicated vegetated zone and, either the vegetation density or its porosity can be derived from one another. In the case of vegetation density, such definition can be considered as a more complete form of the vegetation density defined in [19,20]. Three different near-boundary vegetation porosity models are also defined in order to achieve a more accurate boundary treatment.

b) In order to take account of the secondary flow effect in depth-averaged momentum equations, a secondary force source term has to be added to the right hand side of the momentum equations. When a channel is vegetated, vegetation will resist the secondary flow. Thus, vegetation reduces the magnitude of the secondary force in depth-averaged momentum equations; i.e. vegetation damps the secondary force. The secondary force source term can be obtained through solving some algebraic equations [21], solving the moment equation [22] or, solving the streamwise vorticity equation [23,24]. In none of the mentioned methods the vegetation effect on secondary force is considered. In this article, the double-decomposed depth-averaged streamwise vorticity equation is solved in order to obtain the secondary force. A dissipation source term is developed and added to the vorticity equation for reducing the absolute magnitude of the streamwise vorticity in vegetated zone. The effect of this source

term on the absolute magnitude of vorticity and velocity field in a partially vegetated channel bend is then investigated.

c) When simulating a two-dimensional heat [25] or fluid [11] flow over an array of roads, the available turbulence models may no longer perform well [26,27]. This condition can be worse when the domain is partially porous. For a vegetated porous media, field condition span $R_{e_D} \approx 0 - O(4000)$ [2]. At the first glance, a high Reynolds number turbulence model should be at least applicable (though the accuracy may be reduced) to a vegetated channel with high R_{e_D}. This is practiced, for example, in [3,28,29] using the standard $k - \varepsilon$ model, where the wall-function approach is used for the near-wall treatment. In this article, flow in a channel with alternate vegetated zones is investigated at high R_{e_D} and, application of standard $k - \varepsilon$ model is examined for two different vegetation densities.

d) When in a near-wall vegetated zone vegetation touches the wall, the difference between the thermal property of vegetation and water affects the heat exchange between the wall and fluid. In a uniform porous media the porosity gradient is zero and, in turn, it does not appear in double-decomposed one-energy equation model [5-7]. When a channel is partially vegetated, the porosity gradient near the vegetation border is not zero. Thus, the porosity gradient may alter the diffusive heat flux near the vegetation border at high vegetation density. In a partially vegetated channel with dens canopies, flow can be very slow at vegetated zones. When $R_{e_d} \leq \sim 300$ and $\sim 1 \leq P_{e_d} \leq \sim 10$, the effect of laminar thermal dispersion on temperature field will be most significant [16,17]. In this article, a model is suggested in order to take account of vegetation material effect on the heat flux through the wall. This effect is important when vegetation touches the wall and the near wall porosity is less than one. The porosity-induced heat flux due to the porosity gradient is calculated and, the effect of this heat flux on temperature filed is investigated near the border of a dense vegetation zone at high and low R_{e_D}. At a low R_{e_D} the laminar thermal dispersion effect on temperature filed near the border of a dense vegetation zone is also examined.

Among all aspects of this work, it is especially unique because of simulating turbulent heat transfer in a partially vegetated channel using the porous media science. All equations and expressions presented in this article are developed for both emergent and submerged vegetations but, only the heat and fluid flow in emergent vegetated zones are numerically investigated. The

reminder of this article is divided into four sections. In the first section, the dimensionless conservative form of the double-decomposed depth-averaged transport equations is presented. The second section is devoted to the numerical methods, where the research cases (a), (b), and (d) are discussed. Numerical results are presented in the third section. In this section, the numerical tool is validated with experimental data. Also, the research cases (b) to (d) are examined.

7.2.3 Governing equations

The dimensionless conservative vector form of the double-decomposed depth-averaged continuity and momentum equations can be given by:

$$\frac{\partial(\langle \bar{P} \rangle^i \phi/g)}{\partial t} + \nabla.\left(\phi \langle \bar{h} \rangle^i \langle \bar{u} \rangle^i\right) = 0 \tag{7.1}$$

$$\frac{\partial(\phi \langle \bar{h} \rangle^i \langle \bar{u} \rangle^i)}{\partial t} + \nabla.\left(\phi \langle \bar{h} \rangle^i \langle \bar{u} \rangle^i \langle \bar{u} \rangle^i\right) = -\langle \bar{h} \rangle^i \nabla\left(\phi \langle \bar{P} \rangle^i\right) + \frac{1}{R_e}\nabla.\left[\langle \bar{h} \rangle^i \left(1 + \mu_{t_\phi}\right)\nabla\left(\phi \langle \bar{u} \rangle^{i^T}\right)\right] -$$
$$\phi_b \langle \overline{\tau_b} \rangle^i + \langle \overline{S_{sf}} \rangle^v - \langle \overline{S_{vd}} \rangle^v \tag{7.2}$$

where, $\langle \bar{u} \rangle^i = \langle \bar{u} \rangle^{i^*}/U_{ref}$, $t = t^* U_{ref}/L_{ref}$, $\mu_{t_\phi} = \mu_{t_\phi}^*/\mu_f^*$, $\phi = \Omega_{REV_f}/\Omega_{REV}$, and $\langle \bar{P} \rangle^i = \left(\langle \bar{P} \rangle^{i^*} - P_{ref}\right)/\left(\rho_f^* U_{ref}^2\right)$. Since the dimensionless fluid density is equal to 1.0, the relation between the pressure and water surface elevation is $\langle \bar{P} \rangle^i = g\langle \bar{\xi} \rangle^i$. The dimensionless bed shear stress, $\langle \overline{\tau_b} \rangle^i$, can be expressed as:

$$\langle \overline{\tau_b} \rangle^i = \langle C_{fr} \rangle^i \left|\langle \bar{u} \rangle^i\right|\langle \bar{u} \rangle^i \tag{7.3}$$

$$\langle C_{fr} \rangle^i = g \langle n \rangle^{i^2}/\langle \bar{h} \rangle^{i^{1/3}} \tag{7.4}$$

where, $\langle n \rangle^i = \langle n \rangle^{i^*} U_{ref}/L_{ref}^{2/3}$. In shallow flow hydraulics, Manning's number is usually assumed constant over an area much larger than a cell area. Thus, for a practical application $\langle n \rangle^i \approx n$ is an acceptable assumption. Following Bernard [23], the dimensionless secondary force, $\langle \overline{S_{sf}} \rangle^v$, is given by:

$$\langle \overline{S_{sf}} \rangle^v = \frac{\langle \bar{u} \rangle^i}{\left|\langle \bar{u} \rangle^i\right|}\left[\langle \hat{\bar{n}} \rangle^i \cdot \nabla\left(\phi \langle \bar{h} \rangle^i \langle \overline{\tau_{ss}} \rangle^i\right) + \frac{\phi \langle \bar{h} \rangle^i \langle \overline{\tau_{ss}} \rangle^i}{2\langle \bar{r} \rangle^i}\right] \tag{7.5}$$

In Section 7.2.4.3, Equation (7.5) will be derived from $\overline{S_{sf}}$. $\langle \overline{\tau_{ss}} \rangle^i$ is a scalar value, expressed as:

$$\langle \overline{\tau_{ss}} \rangle^i = \langle \bar{h} \rangle^i \langle \bar{\varpi} \rangle^i \sqrt{\langle C_{fr} \rangle^i}\left|\langle \bar{u} \rangle^i\right| \tag{7.6}$$

where, $\langle\bar{\varpi}\rangle^i = \left(C_2\langle\overline{\omega_s}\rangle^i\right)/12$ is a scalar quantity with C_2 being a constant of proportionality, and $\langle\overline{\omega_s}\rangle^i = \langle\overline{\omega_s}\rangle^{i^*}L_{ref}/U_{ref}$. $\langle\overline{\omega_s}\rangle^i$ is perpendicular to horizontal plane.

In Equation (7.5) $\langle\bar{r}\rangle^i = \langle\bar{r}\rangle^{i^*}/L_{ref}$ is positive for counterclockwise motion and negative for clockwise motion. The normal derivative $\langle\widehat{\overline{n}}\rangle^i.\boldsymbol{\nabla}\left(\phi\langle\bar{h}\rangle^i\langle\overline{\tau_{ss}}\rangle^i\right)$ is positive when $\phi\langle\bar{h}\rangle^i\langle\overline{\tau_{ss}}\rangle^i$ increases in the positive radial direction. The unit vector, $\langle\widehat{\overline{n}}\rangle^i$, and the curvature radius, $\langle\bar{r}\rangle^i$, are expressed as:

$$\langle\widehat{\overline{n}}\rangle^i = \frac{\langle\bar{v}\rangle^i}{|\langle\overline{u}\rangle^i|}\boldsymbol{i} - \frac{\langle\overline{u}\rangle^i}{|\langle\overline{u}\rangle^i|}\boldsymbol{j} \tag{7.7}$$

$$\langle\bar{r}\rangle^i = \frac{|\langle\overline{u}\rangle^i|^3}{\langle\overline{u}\rangle^i\langle\bar{v}\rangle^i\left((\partial\langle\bar{v}\rangle^i/\partial y)-(\partial\langle\overline{u}\rangle^i/\partial x)\right)+\langle\overline{u}\rangle^{i^2}(\partial\langle\bar{v}\rangle^i/\partial x)-\langle\bar{v}\rangle^{i^2}(\partial\langle\overline{u}\rangle^i/\partial y)} \tag{7.8}$$

The dimensionless vegetation drag force can be given by:

$$\langle\overline{\boldsymbol{S}_{vd}}\rangle^v = \frac{1}{\Omega_{REV}R_e}\int_{S_{fs}}\boldsymbol{n}_{fs}\cdot\left(\bar{\mu}\bar{h}\nabla\overline{\boldsymbol{u}}^T\right)ds - \frac{h}{\Omega_{REV}}\int_{S_{fs}}\boldsymbol{n}_{fs}\bar{P}\,ds = 0.5\langle\overline{C_d}\rangle^i\lambda\langle\overline{\boldsymbol{u}_v}\rangle^i|\langle\overline{\boldsymbol{u}_v}\rangle^i| \tag{7.9}$$

Equation (7.9) takes account of total drag force, it is valid for turbulent flow regime, its validity reduces in Forchheimer flow regime (since viscous effects will be significant and a linear expression has to be applied for the drag force) and, it is invalid for Darcy flow regime [6,30]. The macroscopic drag coefficient, $\langle\overline{C_d}\rangle^i$, is derived from temporally and spatially averaged microscopic drag coefficient [2]. The resultant flow velocity, $\langle\overline{\boldsymbol{u}_v}\rangle^i$, can be given by [3]:

$$\langle\overline{\boldsymbol{u}_v}\rangle^i = \eta_v\langle\overline{\boldsymbol{u}}\rangle^i\left(\frac{\langle\overline{h_v'}\rangle^i}{\langle\bar{h}\rangle^i}\right)^{1/2} \tag{7.10}$$

where, η_v is a dimensionless coefficient of about 1.0 [3] and $\langle\overline{h_v'}\rangle^i = min\left(\langle\overline{h_v}\rangle^i,\langle\bar{h}\rangle^i\right)$.

In this article the high Reynolds number standard $k-\varepsilon$ model is used. The dimensionless conservative form of the k and ε equations are given by:

$$\frac{\partial\left(\phi\langle\bar{h}\rangle^i\langle\bar{k}\rangle^i\right)}{\partial t} + \boldsymbol{\nabla}.\left(\phi\langle\bar{h}\rangle^i\langle\bar{k}\rangle^i\langle\overline{\boldsymbol{u}}\rangle^i\right) = \frac{1}{R_e}\boldsymbol{\nabla}.\left[\langle\bar{h}\rangle^i\left(1+\frac{\mu_{t\phi}}{\sigma_k}\right)\boldsymbol{\nabla}\left(\phi\langle\bar{k}\rangle^i\right)\right] + \langle\overline{S_k}\rangle^i \tag{7.11}$$

$$\frac{\partial\left(\phi\langle\bar{h}\rangle^i\langle\bar{\varepsilon}\rangle^i\right)}{\partial t} + \boldsymbol{\nabla}.\left(\phi\langle\bar{h}\rangle^i\langle\bar{\varepsilon}\rangle^i\langle\overline{\boldsymbol{u}}\rangle^i\right) = \frac{1}{R_e}\boldsymbol{\nabla}.\left[h\left(1+\frac{\mu_{t\phi}}{\sigma_\varepsilon}\right)\boldsymbol{\nabla}\left(\phi\langle\bar{\varepsilon}\rangle^i\right)\right] + \langle\overline{S_\varepsilon}\rangle^i \tag{7.12}$$

where, $\langle\overline{S_k}\rangle^i = \langle\bar{h}\rangle^i\left(\langle\overline{G_k}\rangle^i - \phi\langle\bar{\varepsilon}\rangle^i + \phi\langle\overline{G_{kb}}\rangle^i + C_{fr_k}\langle\overline{G_{kv}}\rangle^i\right)$, and $\langle\overline{S_\varepsilon}\rangle^i = \langle\bar{h}\rangle^iC_{\varepsilon 1}\langle\overline{G_k}\rangle^i\langle\bar{\varepsilon}\rangle^i/\langle\bar{k}\rangle^i$

$+\langle \bar{h}\rangle^i \left(-C_{\varepsilon 2}\phi \langle \bar{\varepsilon}\rangle^{i\,2}/\langle \bar{k}\rangle^i + \phi\langle \overline{G_{\varepsilon b}}\rangle^i + C_{\varepsilon 1}\,C_{fr_\varepsilon}\langle \overline{G_{kv}}\rangle^i \langle \bar{\varepsilon}\rangle^i/\langle \bar{k}\rangle^i \right).$ $\langle \overline{G_k}\rangle^i$, $\langle \overline{G_{kv}}\rangle^i$, $\langle \overline{G_{kb}}\rangle^i$, and $\langle \overline{G_{\varepsilon b}}\rangle^i$ are given by:

$$\langle \overline{G_k}\rangle^i = \frac{\mu_{t\phi}}{\phi R_e}\left[\left(\frac{\partial(\phi\langle \bar{u}\rangle^i)}{\partial y} + \frac{\partial(\phi\langle \bar{v}\rangle^i)}{\partial x}\right)^2 + 2\left(\frac{\partial(\phi\langle \bar{u}\rangle^i)}{\partial x}\right)^2 + 2\left(\frac{\partial(\phi\langle \bar{v}\rangle^i)}{\partial y}\right)^2\right] \tag{7.13}$$

$$\langle \overline{G_{kv}}\rangle^i = \langle \overline{S_{vd_x}}\rangle^v \langle \overline{u_v}\rangle^i + \langle \overline{S_{vd_y}}\rangle^v \langle \overline{v_v}\rangle^i \tag{7.14}$$

$$\langle \overline{G_{kb}}\rangle^i = C_{fr}^{-1/2}\langle \overline{U_\tau}\rangle^{i\,3}/\langle \bar{h}\rangle^i \tag{7.15}$$

$$\langle \overline{G_{\varepsilon b}}\rangle^i = C_{\varepsilon \Gamma}C_{\varepsilon 2}C_\mu^{1/2}C_{fr}^{-3/4}\langle \overline{U_\tau}\rangle^{i\,4}/\langle \bar{h}\rangle^{i\,2} \tag{7.16}$$

where, $\langle \overline{U_\tau}\rangle^i = \sqrt{|\langle \overline{\tau_b}\rangle^i|}$, $\mu_{t\phi} = C_\mu R_e \langle \bar{k}\rangle^{i\,2}/\langle \bar{\varepsilon}\rangle^i$, $\langle \bar{k}\rangle^i = \langle \bar{k}\rangle^{i*}/U_{ref}^2$, $\langle \bar{\varepsilon}\rangle^i = \langle \bar{\varepsilon}\rangle^{i*}/(U_{ref}^3/L_{ref})$, and the model constants are $C_\mu = 0.09$, $C_{\varepsilon 1} = 1.44$, $C_{\varepsilon 2} = 1.92$, $\sigma_k = 1.0$ and $\sigma_\varepsilon = 1.3$. Following Rodi [31], the coefficient $C_{\varepsilon \Gamma}$ is set to 3.6 for flumes and 1.8 for rivers. According to [32], $C_{fr_k} = 1.0$ and $C_{fr_\varepsilon} = 1.33$ are used.

When streamline is curved, the centrifugal force causes a secondary flow normal to streamline direction. Bed resistance force and gravitational acceleration act on secondary flow and, in turn, a helical flow will form. As suggested by Bernard [23], in depth-averaged momentum equations the helical flow effect can be accounted for with Equation (7.5). In order to calculate $\langle \overline{S_{sf}}\rangle^v$, the streamwise vorticity, $\langle \bar{\varpi}\rangle^i$, has to be known [see Equation (7.6)]. The streamwise vorticity at the domain can be obtained through a transport equation [23].

$$\frac{\partial(\phi\langle \bar{h}\rangle^i\langle \bar{\varpi}\rangle^i)}{\partial t} + \nabla.\left(\phi\langle \bar{h}\rangle^i\langle \bar{\varpi}\rangle^i\langle \bar{u}\rangle^i\right) = \phi A_s\sqrt{C_{fr}}\frac{|\langle \bar{u}\rangle^i|^2}{\langle \bar{r}\rangle^i\psi} - \phi_b D_s\sqrt{C_{fr}}\langle \bar{\varpi}\rangle^i|\langle \bar{u}\rangle^i| + \langle \overline{G_{\varpi v}}\rangle^v +$$
$$\frac{1}{R_e}\nabla.\left[\langle \bar{h}\rangle^i\left(1 + \frac{\mu_{t\phi}}{\sigma_\varpi}\right)\nabla(\phi\langle \bar{\varpi}\rangle^i)\right] \tag{7.17}$$

where, $\langle \bar{\varpi}\rangle^i = \langle \bar{\varpi}\rangle^{i*}L_{ref}/U_{ref}$, $A_s = 5.0$, $D_s = 0.5$, $\sigma_\varpi = 1.0$, and $\psi = \left(1 + 9\langle \bar{h}\rangle^{i\,2}/\langle \bar{r}\rangle^{i\,2}\right)$ are suggested by Bernard [23]. The vegetation dissipation source term, $\langle \overline{G_{\varpi v}}\rangle^v$, can be given by (see Section 7.2.4.3 for detail of derivation):

$$\langle \overline{G_{\varpi v}}\rangle^v = \aleph\langle \bar{\varpi}\rangle^i|\langle \bar{\varpi}\rangle^i| \tag{7.18}$$

$$\aleph = 3\sqrt{\frac{6}{A_s}}\langle \overline{C_d}\rangle^i \lambda \begin{cases} \left(\dfrac{\langle \overline{h_v''}\rangle^{i^4}}{\langle h_v'\rangle^i \langle \overline{h}\rangle^{i^2}} - \dfrac{2\langle \overline{h_v''}\rangle^{i^3}}{\langle h_v'\rangle^i \langle \overline{h}\rangle^i} + \dfrac{3\langle \overline{h_v''}\rangle^{i^2}}{2\langle h_v'\rangle^i} - \dfrac{\langle \overline{h_v''}\rangle^i \langle \overline{h}\rangle^i}{2\langle h_v'\rangle^i}\right) - & always \\[2ex] \left(\dfrac{\langle \overline{h_v'}\rangle^{i^3}}{\langle \overline{h}\rangle^{i^2}} - \dfrac{2\langle \overline{h_v'}\rangle^{i^2}}{\langle \overline{h}\rangle^i} + \dfrac{3\langle \overline{h_v'}\rangle^i}{2} - \dfrac{\langle \overline{h}\rangle^i}{2} + \dfrac{\langle \overline{h}\rangle^{i^2}}{16\langle \overline{h_v'}\rangle^i}\right) & when\ \langle \overline{h_v'}\rangle^i > \dfrac{\langle \overline{h}\rangle^i}{2} \end{cases} \tag{7.19}$$

In Equation (7.19), $\langle \overline{h_v''}\rangle^i = \min\left(\langle \overline{h_v}\rangle^i, \langle \overline{h}\rangle^i/2\right)$ and, the second most right hand side bracket will be calculated only if $\langle \overline{h_v'}\rangle^i > \langle \overline{h}\rangle^i/2$.

There is a division by streamline curvature radius in vorticity generation source term, the first term in the right hand side of Equation (7.17). The lower bound for streamline curvature radius calculated by Equation (7.8) is zero. Grid however filters the streamline curvature so that the actual lower bound for the streamline curvature radius in an equilateral triangle cell will be the normal distance between the neighboring cells, $h_{c_0\_c_n}$. In a grid with arbitrary triangular cells the streamline curvature radius can be given by [33]:

$$\langle \bar{r}\rangle^i = max\left\{\langle \bar{r}\rangle^i, \frac{\sum_{j=1}^{3} h_{c_0\_c_j}}{3}\right\} \tag{7.20}$$

where, $\langle \bar{r}\rangle^i$ in the right hand side of Equation (7.20) is given by Equation (7.8).

The temperature or the heat flux at the stem surface is a function of time and space and, it is almost impossible to measure it for every individual stem. Thus, application of local thermal equilibrium hypothesis to vegetated porous media seems to be unavoidable but adequate. With the assumption of local thermal equilibrium between vegetation and water, the dimensionless conservative form of the double-decomposed depth-averaged energy equation can be expressed as:

$$\frac{\partial\{[\phi + c_{p_v}(1-\phi)]\langle \overline{h}\rangle^i \langle \overline{T}\rangle^i\}}{\partial t} + \nabla \cdot \left(\phi \langle \overline{h}\rangle^i \langle \overline{T}\rangle^i \langle \overline{\mathbf{u}}\rangle^i\right) = \frac{1}{Re Pr}\nabla \cdot \left\{\langle \overline{h}\rangle^i \mathbf{K}_{eff}\nabla\langle \overline{T}\rangle^i + \langle \overline{h}\rangle^i \langle \overline{T}\rangle^i(1-K_v)\nabla\phi\right\} \tag{7.21}$$

where, $c_{p_v} = c_{p_v}^*/c_{p_f}^*$, and $\langle \overline{T}\rangle^i = \langle \overline{T}\rangle^{i^*}/T_{ref}$. The last term in the right hand side of Equation (7.21) is the porosity-induced heat flux. In the literature a uniform porosity is assumed and, in turn, the porosity gradient term is ignored; e.g. [5-7]. The effective conductivity is given by:

$$\mathbf{K}_{eff} = \left[\{\phi + K_v(1-\phi)\} + \phi\frac{\mu_{t_\phi}Pr}{Pr_t}\right]\mathbf{I} + \mathbf{K}_{disp} \tag{7.22}$$

and, $K_v = K_v^*/K_f^*$, $\phi + K_v(1 - \phi)$ represents the effective laminar conductivity, and $\phi \, \mu_{t_\phi} P_r/P_{r_t}$ takes account of turbulent thermal diffusion plus turbulent thermal dispersion [34]. The laminar thermal dispersion is approximated by [16,17,35]:

$$\begin{cases} (\boldsymbol{K}_{disp})_{XX} = 2.1(1 - \phi)^{0.4} P_{e_H} & for\ flow\ direction \\ (\boldsymbol{K}_{disp})_{YY} = 0.052(1 - \phi) P_{e_H} & normal\ to\ flow\ direction \end{cases} \quad (7.23)$$

where, $\boldsymbol{K}_{eff} = \boldsymbol{K}_{eff}^*/K_f^*$. In a depth averaged flow, variables are assumed uniform over the water depth. Thus, the laminar thermal dispersion in a double-decomposed depth-averaged flow is quite similar to the one in a two dimensional flow. What make a difference are the fluctuations at the water surface. Since such fluctuations are ignored in Equation (7.23), the laminar thermal dispersion calculated using Equation (7.23) under-predicts the actual laminar thermal dispersion. The magnitude of under-prediction decreases when the water depth increases or, when the flow velocity decreases. Since laminar thermal dispersion effect is significant at low P_{e_H}, application of Equation (7.23) in a depth-averaged simulation is acceptable.

7.2.4 Numerical method

In this section, the detail of the discretization scheme will be introduced in Section 7.2.4.1, research case (a) will be discussed in Section 7.2.4.2, research case (b) will be investigated in Section 7.2.4.3, and the research case (c) will be discussed in Sections 7.2.4.4 and 7.2.4.5. The boundary conditions and the residual criteria used in this article will be presented in Sections 7.2.4.6 and 7.2.4.7.

7.2.4.1 Discretization scheme

SIMPLE algorithm is used for the coupling between pressure and velocity field. In SIMPLE algorithm continuity equation [Eq. (7.1)] is converted into a pressure correction equation. Momentum equations are solved with an initial guessed pressure and velocity field. The derived velocity field is then used in the pressure correction equation. The obtained pressure correction corrects the pressure and velocity field, other scalars will be solved, and the solution continues in the next iteration until convergence is attained. Convective terms are discretized using first order upwind scheme, Green's theorem is used for the calculation of the gradient at cell-center, and the two point method for the calculation of gradient at the cell face.

A Rhie and Chow [36] type pressure interpolation technique is applied in order to obtain a mass conserving velocity at the cell face. Thus, the continuity residual can be expressed as.

$$\langle\bar{\vartheta}^\circ\rangle^i = \sum_{j=1}^{3}\left\{\frac{(\langle\bar{u}\rangle^i a_0^u)_0 + (\langle\bar{u}\rangle^i a_0^u)_j}{(a_0^u)_0 + (a_0^u)_j}\phi_{s_j}\langle\bar{h}\rangle_{s_j}^i.\,s_j - \omega_{rc}a_j^P\left(\langle\bar{P}\rangle_j^i - \frac{\phi_0}{\phi_j}\langle\bar{P}\rangle_0^i\right)\right\} + \frac{\Omega_0}{g\Delta t}\left[\phi\langle\overline{P^+}\rangle^i - \right.$$
$$\left.\left(\phi\langle\bar{P}\rangle^i\right)^{n-1}\right]_0 \tag{7.24}$$

In Eq. (7.24), the relaxation factor, ω_{rc}, is set to 1.0 [37]. Source terms are discretized following [33]. This prevents oscillation of relevant variables when the water depth goes to zero. In [39] a dam-break over shallow wet bed is simulated using the technique introduced in [33] for discretization of source terms. The simulated profile of water surface remained clear of any oscillation even when the water depth in shallow side was as small as $10^{-6}\ m$. According to [38] the discretization of vorticity dissipation source term due to bed effects has to be done in a fully implicit manner and is straight forward.

7.2.4.2 Porosity and vegetation density in a vegetated porous medium

The porosity of a vegetated porous media may change during simulation if vegetation is emerged. Regardless of whether vegetation is emergent or submerged, its density will change if the water depth changes. A well-defined porosity must take account of such variations.
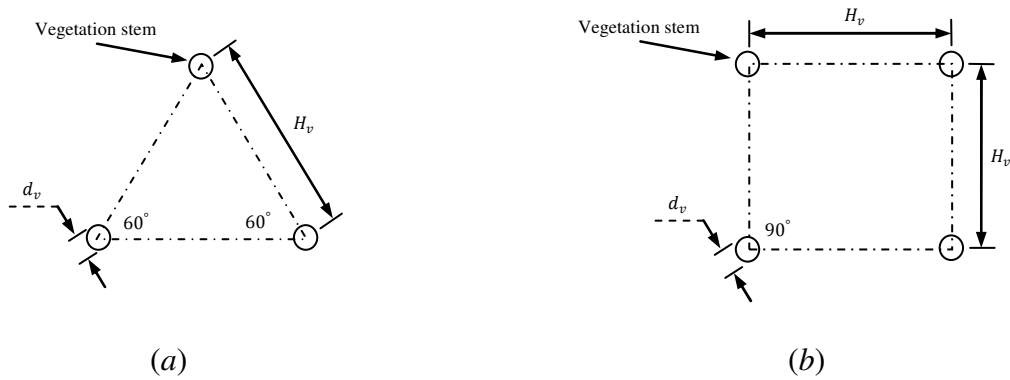

Figure 7.1. Unit-cell; (*a*) staggered arrangement, (*b*) uniform arrangement.

The unit-cell for vegetation zones with staggered and uniform arrangements is presented in Figure 7.1. According to this figure, the porosity at the interior of a computational domain can be given by:

$$\phi = \begin{cases} 1 - \dfrac{\pi d_v^2 \langle \overline{h_v'} \rangle^i}{4\langle \overline{h} \rangle^i H_v^2 cos(\pi/6)} & for\ staggered\ arrangement \\[4mm] 1 - \dfrac{\pi d_v^2 \langle \overline{h_v'} \rangle^i}{4\langle \overline{h} \rangle^i H_v^2} & for\ uniform\ arrangement \end{cases} \tag{7.25}$$

In order to calculate the vegetation density, vegetation frontal area has to be known. In [3,4,40,41] vegetation frontal area is assumed to be the sum of the frontal area of stems and, macroscopic drag coefficient is derived from temporally and spatially averaged microscopic drag coefficient [2]. Thus, vegetation density can be expressed as:

$$\lambda = \begin{cases} \dfrac{\alpha_v d_v \langle \overline{h_v'} \rangle^i}{H_v^2 cos(\pi/6)} & for\ staggered\ arrangement \\[4mm] \dfrac{\alpha_v d_v \langle \overline{h_v'} \rangle^i}{H_v^2} & for\ uniform\ arrangement \end{cases} \tag{7.26}$$

where, α_v is a dimensionless coefficient. α_v is 1.0 when vegetation is approximated with cylindrical stems [3]. According to Equations (7.25) and (7.26) either ϕ or λ can be derived from the other one; for example: $\lambda = \left(4\alpha_v(1-\phi)\langle \overline{h} \rangle^i\right)/(\pi d_v)$. The near-bed porosity can be given by:

$$\phi_b = \begin{cases} 1 - \dfrac{\pi d_v^2}{4H_v^2 cos(\pi/6)} & for\ staggered\ arrangement \\[4mm] 1 - \dfrac{\pi d_v^2}{4H_v^2} & for\ uniform\ arrangement \end{cases} \tag{7.27}$$

In derivation of Equation (7.27), water depth is assumed at the limit going toward zero. Thus, vegetation is assumed essentially emerged. Three different near-boundary porosities can be assumed; i.e. fully rod-touching condition, rod-free conditions, and partially rod-touching condition. In Figure 7.2 these conditions are shown for both staggered and uniform vegetation arrangements. A near-boundary condition is assumed rod-toughing if by average the biggest chord of half of stems lies on the boundary, it is assumed rod-free if none of the stems touch the boundary and, it is assumed partially rod-touching if stems partially (irregularly) touch the boundary. Thus, the near-boundary porosity for a fully rod-touching condition can be expressed as:

$$\phi_{bo} = \begin{cases} 1 - \dfrac{d_v \langle \overline{h_v'} \rangle^i}{2\langle \overline{h} \rangle^i H_v cos(\pi/6)} & for\ staggered\ arrangement \\[4mm] 1 - \dfrac{d_v \langle \overline{h_v'} \rangle^i}{\langle \overline{h} \rangle^i H_v} & for\ uniform\ arrangement \end{cases} \tag{7.28}$$

In derivation of Equation (7.28) it is assumed that, the thickness of near-boundary REV is much smaller than the gap between stems and the boundary; e.g. in Figure 7.2, $\delta_n \ll H_w$. The near-boundary porosity for the other conditions can be given by:

$$\phi_{bo} = \begin{cases} 1 & rod - free\ condition \\ \phi\ at\ the\ boundary & partially\ rod - touching\ condition \end{cases} \quad (7.44)$$
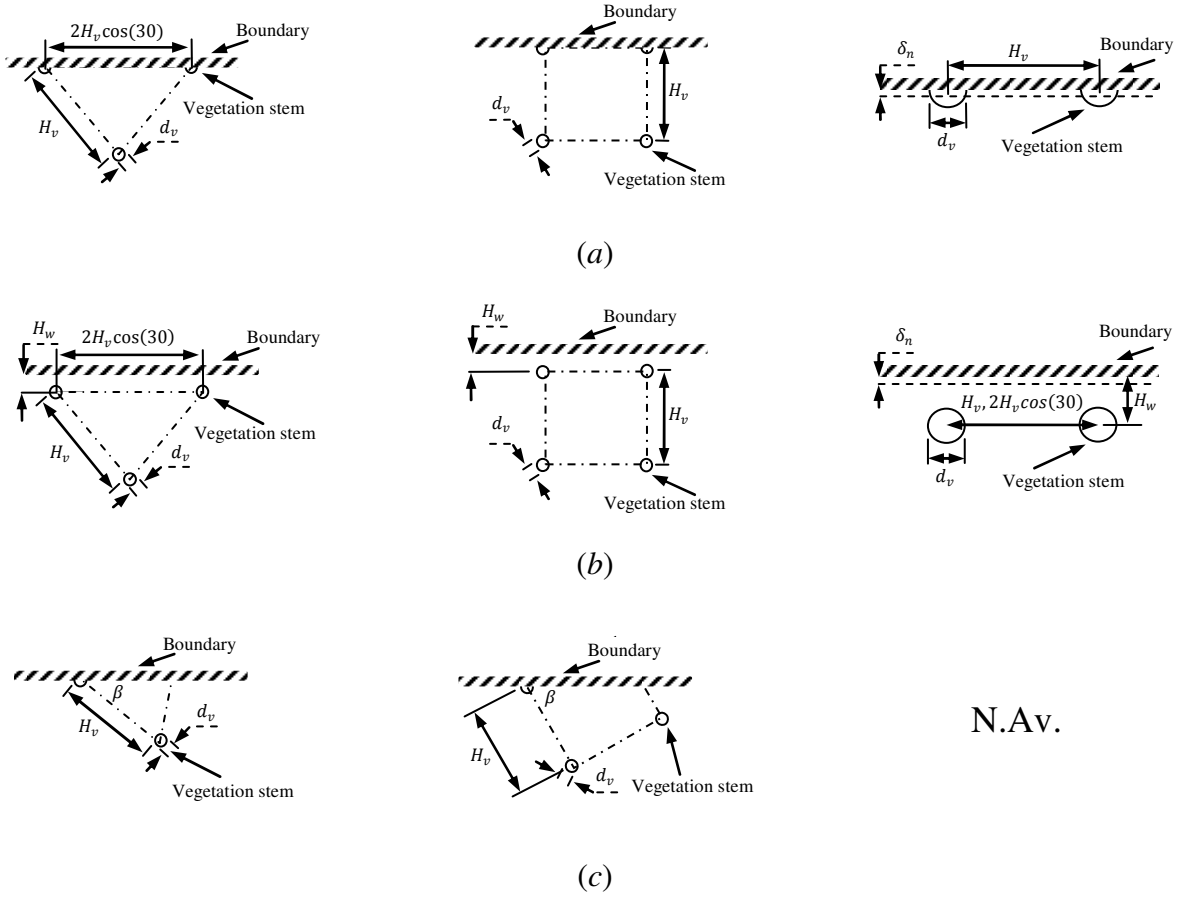

(*a*)

(*b*)

(*c*)

Figure 7.2. Definition of the boundary porosity; (*a*) fully rod-touching condition, (*b*) rod-free condition, (*c*) partially rod-touching condition. Left figures represent a staggered arrangement, middle figures represent a uniform arrangement and, the right figures represent the boundary unit-cell.

Vegetation effect on flow momentum is simulated by means of a body-force; see Equation (7.2). When stems do not touch a boundary, their near-wall effect is simulated only through assuming such body-force. If stems are in touch with a boundary, they actually reduce the wetted area of the boundary. These hypotheses are used when Equations (7.28) and (7.29) are derived.

7.2.4.3 Vegetation dissipation source term and the secondary force

The force acting on a unit height of vegetation can be given by:

$$\langle \overline{S_z} \rangle^v = -0.5 \langle \overline{C_d} \rangle^i \frac{\lambda}{\langle h'_v \rangle^i} \langle \overline{u_v} \rangle^i |\langle \overline{u_v} \rangle^i|$$

When the origin of the vertical axis, z, is fixed at $\langle \bar{h} \rangle^i / 2$ from the channel bed, one may assume the radial component of velocity vector as $\langle \overline{u_{v_r}} \rangle^i = \langle \overline{\omega_s} \rangle^i z$ [23]. Thus, the radial component of the drag force can be given by:

$$\langle \overline{S_{z_r}} \rangle^v = -0.5 \langle \overline{C_d} \rangle^i \frac{\lambda}{\langle h'_v \rangle^i} \langle \overline{\omega_s} \rangle^{i^2} z|z|$$

The moment acting on unit height of a column of fluid due to this force can be given by:

$$\langle \overline{S_{z_r}} \rangle^v z = -0.5 \langle \overline{C_d} \rangle^i \frac{\lambda}{\langle h'_v \rangle^i} \langle \overline{\omega_s} \rangle^{i^2} |z^3|$$

The total moment can be derived as:

$$\langle \overline{M_r} \rangle^v = \int_{-\langle \bar{h} \rangle^i /2}^{\langle \overline{h'_v} \rangle^i - \langle \bar{h} \rangle^i /2} \langle \overline{S_{z_r}} \rangle^v z \, dz = \int_{-\langle \bar{h} \rangle^i /2}^{\langle \overline{h'_v} \rangle^i - \langle \bar{h} \rangle^i /2} -0.5 \langle \overline{C_d} \rangle^i \frac{\lambda}{\langle h'_v \rangle^i} \langle \overline{\omega_s} \rangle^{i^2} |z^3| \, dz =$$

$$0.5 \langle \overline{C_d} \rangle^i \frac{\lambda}{\langle \overline{h_v} \rangle^i} \langle \overline{\omega_s} \rangle^{i^2} \begin{cases} \int_{-\langle \bar{h} \rangle^i /2}^{\langle \overline{h''_v} \rangle^i - \langle \bar{h} \rangle^i /2} z^3 \, dz - & always \\ \int_0^{\langle \overline{h''_v} \rangle^i - \langle \bar{h} \rangle^i /2} z^3 \, dz & when \ \langle \overline{h'_v} \rangle^i > \frac{\langle \bar{h} \rangle^i}{2} \end{cases}$$

After some algebra, the total moment can be expressed as:

$$\langle \overline{M_r} \rangle^v =$$

$$\frac{1}{8} \langle \overline{C_d} \rangle^i \frac{\lambda}{\langle h'_v \rangle^i} \langle \overline{\omega_s} \rangle^{i^2} \begin{cases} \left(\langle \overline{h''_v} \rangle^{i^4} - 2 \langle \overline{h''_v} \rangle^{i^3} \langle \bar{h} \rangle^i + \frac{3}{2} \langle \overline{h''_v} \rangle^{i^2} \langle \overline{h'_v} \rangle^{i^2} - \frac{\langle \overline{h''_v} \rangle^i \langle \bar{h} \rangle^{i^3}}{2} \right) - & always \\ \left(\langle \overline{h'_v} \rangle^{i^4} - 2 \langle \overline{h'_v} \rangle^{i^3} \langle \bar{h} \rangle^i + \frac{3}{2} \langle \overline{h'_v} \rangle^{i^2} \langle \bar{h} \rangle^{i^2} - \frac{\langle \overline{h'_v} \rangle^i \langle \bar{h} \rangle^{i^3}}{2} + \frac{\langle \bar{h} \rangle^{i^4}}{16} \right) & when \ \langle \overline{h'_v} \rangle^i > \frac{\langle \bar{h} \rangle^i}{2} \end{cases}$$

Following the method used by Bernard [23] in order to derive the vorticity equation and, multiplying the moment by $12/\langle \bar{h} \rangle^{i^2}$, replacing $\langle \overline{\omega_s} \rangle^i$ with $12 \langle \overline{\omega} \rangle^i / C_2$, and multiplying the moment by $C_2/12$, moment formula can be given by:

$$\frac{C_2 \langle \overline{M_r} \rangle^v}{\langle \bar{h} \rangle^{i^2}} = 3 \frac{6}{C_2} \langle \overline{C_d} \rangle^i \lambda \langle \overline{\omega} \rangle^{i^2} \begin{cases} \left(\frac{\langle \overline{h''_v} \rangle^{i^4}}{\langle h'_v \rangle^i \langle \bar{h} \rangle^{i^2}} - \frac{2 \langle \overline{h''_v} \rangle^{i^3}}{\langle h'_v \rangle^i \langle \bar{h} \rangle^i} + \frac{3 \langle \overline{h''_v} \rangle^{i^2}}{2 \langle h'_v \rangle^i} - \frac{\langle \overline{h''_v} \rangle^i \langle \bar{h} \rangle^i}{2 \langle h'_v \rangle^i} \right) - & always \\ \left(\frac{\langle \overline{h'_v} \rangle^{i^3}}{\langle \bar{h} \rangle^{i^2}} - \frac{2 \langle \overline{h'_v} \rangle^{i^2}}{\langle \bar{h} \rangle^i} + \frac{3 \langle \overline{h'_v} \rangle^i}{2} - \frac{\langle \bar{h} \rangle^i}{2} + \frac{\langle \bar{h} \rangle^{i^2}}{16 \langle h'_v \rangle^i} \right) & when \ \langle \overline{h'_v} \rangle^i > \frac{\langle \bar{h} \rangle^i}{2} \end{cases}$$

(7.30)

According to [23], $C_2/6 = A_s \Rightarrow C_2 = \sqrt{6A_s}$. In Figure 7.3-*a* a sketch of secondary flow in a channel bend is depicted. The vegetation damping effect as a function of vegetation height is shown in Figure 7.3-*b*. For a positive vorticity, as it can be observed in Figure 7.3, vegetation damping source term is always negative. When the vorticity term in Equation (7.30), $\langle\bar{\varpi}\rangle^{i^2}$, is replaced with $\langle\bar{\varpi}\rangle^i|\langle\bar{\varpi}\rangle^i|$, Equation (7.30) can dissipate both positive and negative vorticity.
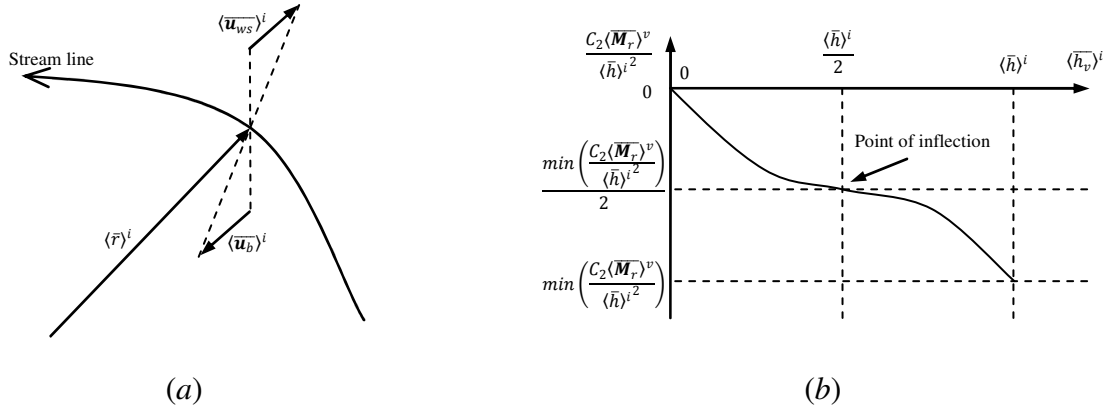

(a) (b)

Figure 7.3. Vegetation effect on vorticity equation; (a) an imaginary streamline with a positive vorticity and the assumed linear secondary flow in radial direction, (b) schematic of the relevant vegetation damping effect.

If one assumes that the depth-averaged time-mean secondary force is known and it can be derived following Bernard [23], the double-decomposed depth-averaged secondary force can be derived if one integrates the depth-averaged time-mean secondary force over REV.

$$\langle\overline{S_{sf}}\rangle^v = \phi\langle\overline{S_{sf}}\rangle^i = \phi\langle\frac{\overline{u}}{|\overline{u}|}\left[\widehat{\overline{n}}\cdot\nabla(\overline{h\tau_{ss}}) + \frac{\overline{h\tau_{ss}}}{2\overline{r}}\right]\rangle^i = \phi\langle\frac{\overline{u}}{|\overline{u}|}\rangle^i \langle\widehat{\overline{n}}\cdot\nabla(\overline{h\tau_{ss}})\rangle^i + \phi\langle\frac{\overline{u}}{|\overline{u}|}\rangle^i \langle\frac{\overline{h\tau_{ss}}}{2\overline{r}}\rangle^i =$$

$$\frac{\langle\overline{u}\rangle^i}{|\langle\overline{u}\rangle^i|}\langle\widehat{\overline{n}}\rangle^i \cdot \phi\langle\nabla(\overline{h\tau_{ss}})\rangle^i + \phi\frac{\langle\overline{u}\rangle^i}{|\langle\overline{u}\rangle^i|}\frac{\langle\overline{h}\rangle^i\langle\overline{\tau_{ss}}\rangle^i}{2\langle\overline{r}\rangle^i} \tag{7.31}$$

If for variables φ and ψ conditions $\bar{\varphi} = \langle\bar{\varphi}\rangle^i + {}^i\bar{\varphi}$ and $\overline{\varphi\psi} = \langle\bar{\varphi}\rangle^i\langle\bar{\psi}\rangle^i + \langle\bar{\varphi}\rangle^i{}^i\bar{\psi} + {}^i\bar{\varphi}\langle\bar{\psi}\rangle^i + {}^i\bar{\varphi}{}^i\bar{\psi}$ hold, the gradient term in the last right hand side part of Equation (7.31) can be written as:

$$\phi\langle\nabla(\overline{h\tau_{ss}})\rangle^i = \nabla(\phi\langle\overline{h\tau_{ss}}\rangle^i) + \frac{1}{\Omega_{REV}}\int_{S_{fs}} \boldsymbol{n}_{fs} \cdot (\overline{h\tau_{ss}})\,ds \tag{7.32}$$

If one ignores the second right hand side term in Equation (7.32), since there is no expression for that, the gradient term can be given by:

$$\phi\langle\nabla(\bar{h}\overline{\tau_{ss}})\rangle^i = \nabla(\phi\langle\bar{h}\rangle^i\langle\overline{\tau_{ss}}\rangle^i) \tag{7.33}$$

And, the secondary force can be expressed as in Equation (7.5). In ignored expression:

$$\frac{\langle\overline{u}\rangle^i}{|\langle\overline{u}\rangle^i|}\langle\widehat{\overline{n}}\rangle^i \cdot \frac{1}{\Omega_{REV}}\int_{S_{fs}} \boldsymbol{n}_{fs} \cdot (\bar{h}\overline{\tau_{ss}})\, ds \tag{7.34}$$

is the secondary force due to spatial oscillation of total time-mean secondary shear, $\bar{h}\overline{\tau_{ss}}$.

7.2.4.4 Porosity-induced heat flux

When the porosity of a vegetated porous media is not uniform, a porosity-induced diffusive term will appear in the right hand side of a one-energy equation model; see the last term in the right hand side of Equation (7.21). When this term, $\nabla \cdot (\langle\bar{h}\rangle^i\langle\bar{T}\rangle^i(1 - K_v)\nabla\phi)$, is integrated over the cell volume using Green's theorem, it can be expressed as:

$$\frac{1}{R_e P_r}\sum_{j=1}^{3}\langle\bar{h}\rangle^i\langle\bar{T}\rangle^i(1 - K_v)\nabla\phi \cdot \boldsymbol{s}_j = -\frac{1}{R_e P_r}\sum_{j=1}^{3}\langle\bar{\varsigma}\rangle^i_{s_j}\frac{\langle\bar{T}\rangle^i_{s_j}}{\phi_{s_j}} \tag{7.35}$$

where, the porosity-induced flux can be given by:

$$\langle\bar{\varsigma}\rangle^i_{s_j} = -(1 - K_v)\nabla\phi \cdot (\phi_{s_j}\langle\bar{h}\rangle^i_{s_j}\boldsymbol{s}_j) \tag{7.36}$$

In Equation (7.36), the flux mechanism (which can be compared with velocity vector) is $-(1 - K_v)\nabla\phi$, and the flux area is $\phi_{s_j}\langle\bar{h}\rangle^i_{s_j}\boldsymbol{s}_j$. When the upwind method is used, the following simplification will have no effect on the accuracy of the discretized equations.

$$\frac{1}{R_e P_r}\sum_{j=1}^{3}\langle\bar{h}\rangle^i\langle\bar{T}\rangle^i(1 - K_v)\nabla\phi \cdot \boldsymbol{s}_j = -\frac{1}{R_e P_r}\sum_{j=1}^{3}\langle\bar{\varsigma}\rangle^i_{s_j}\langle\bar{T}\rangle^i_{s_j} \tag{7.37}$$

$$\langle\bar{\varsigma}\rangle^i_{s_j} = -(1 - K_v)\nabla\phi \cdot (\langle\bar{h}\rangle^i_{s_j}\boldsymbol{s}_j) = -(1 - K_s)\langle\bar{h}\rangle^i_{s_j}s_j\left(\frac{\partial\phi}{\partial n}\right)_{s_j} \tag{7.38}$$

Thus, the discretization process will be the same as the discretization of a convective term. It should be noted that, a centered discretization of the porosity-induced heat flux may produce negative coefficients in coefficient matrix at weakly convective flows.

7.2.4.5 Near-wall treatment for energy equation

The near-wall REV can best represent the near-wall thin layer of fluid where the heat exchange occurs. Thus, the normal unit heat flux can be given by:

$$\langle \overline{q_w} \rangle^v = -\phi_{bo} \frac{\partial \langle \overline{T_f} \rangle^i}{\partial n} - (1 - \phi_{bo})K_v \frac{\partial \langle \overline{T_v} \rangle^i}{\partial n} \tag{7.39}$$

where, the first term in the right hand side of Equation (7.39) represents the heat flux from wall into fluid and, the second term in the right hand side represents the heat flux from wall into vegetation stems. Under the assumption of local thermal equilibrium hypothesis $\langle \overline{T_f} \rangle^i = \langle \overline{T_v} \rangle^i = \langle \overline{T} \rangle^i$, the normal unit heat flux can be expressed as:

$$\langle \overline{q_w} \rangle^v = -(\phi_{bo} + (1 - \phi_{bo})K_v) \frac{\partial \langle \overline{T} \rangle^i}{\partial n} \tag{7.40}$$

When the wall heat flux is known, Equation (7.40) can be used in order to compute the temperature at ghost cells.

The near-wall porosity reduces the accuracy of the solution if wall function method is not modified. Using the same hypothesis as the ones used in derivation of Equations (7.39) and (7.40), the modified standard wall function can be given by:

$$\langle \overline{q_w} \rangle^v = -\frac{\phi_{bo} C_\mu^{1/4} \langle \overline{k_P} \rangle^{i\,1/2} (\langle \overline{T} \rangle_P^i - T_w)}{T^{\cdot\cdot}} - (1 - \phi_{bo})K_v \frac{(\langle \overline{T} \rangle_P^i - T_w)}{n_P} \tag{7.41}$$

In Equation (7.41) the authors made use of the fact that, the heat flux from wall toward vegetation stems will be finally absorbed by fluid. In Equation (7.41), $T^{\cdot\cdot}$ is the near-wall universal temperature (in the literature it is symbolized with T^+). For the momentum equations vegetation effect if taken into account through a body-force. Thus, near-wall treatment for momentum equations consists of a reduction in the effective wall area. This will be automatically done when the wall area is multiplied by near-wall porosity.

7.2.4.6 Boundary conditions

The employed boundary conditions are the velocity inlet, the constant pressure (or equivalently, the water surface elevation) boundary, and the wall condition. Variables have to be known at the inlet. At the constant pressure boundary, it is assumed that the gradient of variables is zero except for velocity components and pressure. Following Versteeg and Malalasekera [42], in order to derive the velocity components, mass is locally conserved at the cells adjacent to the constant pressure boundary where pressure is fixed. The standard wall function approach [43] is applied to the momentum, turbulence, and energy equations.

7.2.4.7 Residuals

In Section 7.2.5, residuals are calculated in two different ways: the scaled residual, and the normalized residual. The continuity residual is given by:

$$\langle \overline{\vartheta_R} \rangle^i = \frac{\sum_{i=1}^{N_{cell}} |\langle \overline{\vartheta}^{\circ} \rangle^i|}{\langle \overline{\vartheta_{ref}^{\circ}} \rangle^i} \tag{7.42}$$

For a scaled error, $\langle \overline{\vartheta_{ref}^{\circ}} \rangle^i$ is the volumetric inlet discharge. For a normalized error, $\langle \overline{\vartheta_{ref}^{\circ}} \rangle^i$ is the largest absolute magnitude of the continuity residual in the first five iterations. The residual for any variable, $\langle \overline{\varphi} \rangle^i$, is expressed as:

$$\langle \overline{R_\varphi} \rangle^i = \frac{\sum_{i=1}^{N_{cell}} \left| \sum_{j=1}^{3} a_j^\varphi \langle \overline{\varphi} \rangle_j^i + s_{u_\varphi} - a_0^\varphi \langle \overline{\varphi} \rangle_0^i \right|}{\langle \overline{R_{ref}} \rangle^i} \tag{7.43}$$

where, for scaled errors, $\langle \overline{R_{ref}} \rangle^i = \sum_{i=1}^{N_{cell}} |a_0^\varphi \langle \overline{\varphi} \rangle_0^i|$, and for normalized errors, $\langle \overline{R_{ref}} \rangle^i$ is the largest absolute magnitude of the φ residual in the first five iterations.

7.2.5 Numerical results

In Section 7.2.5.1 the code is validated against experimental data of Pasche [44]. The research case (b) is examined in Section 7.2.5.2 where, the numerical results are compared with the experimental data of Tominaga et al. [45]. In Section 7.2.5.3, a channel with semi-circular alternate vegetated zones is simulated. The research cases (c) and (d) are investigated in this section.

7.2.5.1 Pasche (1984) test

For this test case, the authors used the data presented in [3] for the emergent vegetation test case performed by Pasche [44]. Flow Reynolds number is 2.71×10^5 with, $L_{ref} = 1\ m$ and $U_{ref} = 0.272796\ m/s$. The water specific gravity and dynamic viscosity are $998.2\ kg/m^3$ and $0.001003\ N.m/s^2$, respectively. The gravitational acceleration is $9.806\ m/s^2$, bed slope is 0.0005, stem diameter is $0.012\ m$, and stems are uniformly arranged with a spacing equal to $0.09474\ m$. The drag coefficient is assumed equal to 1.0, Manning's number is $0.01\ s/m^{1/3}$, and the total inlet discharge is $0.0345\ m^3/s$. Errors are normalized, and the convergence criterion is set to 10^{-3}. Because of the experimental setups, in this test case the rod-free near-

boundary porosity model is used. The geometrical details together with some hydraulic parameters of the channel are depicted in Figure 7.4-*a* and 7.4-*b*.

In Figure 7.4-*c* the computed velocity profiles are compared with the experimental data of Pasche [44]. As it can be observed in this figure, grid refinement improves the accuracy of the computed results near $x = 0.6$. For $x \leq 0.2$ the computed data slightly over predicts the measured data. This may be due to the difference between the actual and the reported Manning's number. In Figure 7.4-*d*, turbulent kinematic energy, tangential stress, and vorticity profile show a pick at $x = 0.5$ where, the border of vegetated zone exists and the velocity gradient is high. The turbulence kinematic energy is very small near the wall in vegetated zone. This may limit the application of high Reynolds number turbulence models when vegetation density is high.
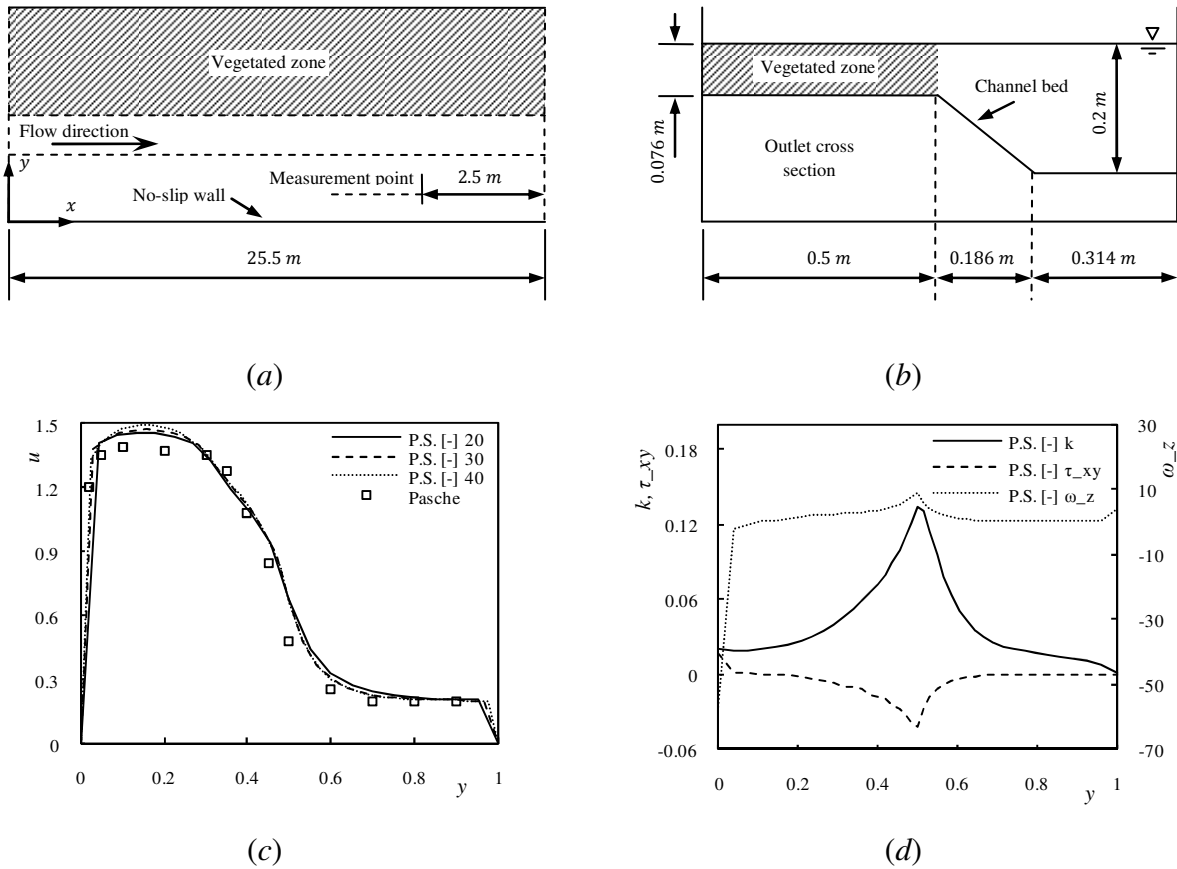

Figure 7.4. Flow in Pasche [44] channel; (*a*) and (*b*) Geometrical detail, (*c*) velocity profile (20, 30, and 40 represent approximate number of grid points in transverse direction), (*d*) turbulence kinematic energy, k, tangential shear stress, τ_{xy}, and the streamwise vorticity, ϖ; P.S., Present Solver.

7.2.5.2 Tominaga et al. (1998) test

In this test case, the flow Reynolds number is 2.65×10^5 with, $L_{ref} = 0.9\,m$ and $U_{ref} = 0.296296\,m/s$. Bed slope is 0, stem diameter is $0.005\,m$, and the emergent stems are uniformly arranged with a spacing equal to $0.05\,m$. Manning's number is $0.015\ s/m^{1/3}$, and the total inlet discharge is $0.04\,m^3/s$. Errors are scaled, and the convergence criterion is set to 10^{-3}. Other details are as in Section 7.2.5.1. The geometrical details together with some hydraulic parameters of the channel are depicted in Figure 7.7. Following [29] the drag coefficient is calculated as:

$$\langle \overline{C_d} \rangle^i \approx \begin{cases} (10^3/R_e)^{0.25} & for\ R_{e_d} \le 10^3 \\ min(0.79 + [(10^{-3}R_e - 2)/20.5]^2, 1.15) & for\ 10^3 \le R_{e_d} \le 4 \times 10^4 \end{cases}$$

In this test, unstructured triangular grids with uniform grid size are used, and a steady solution is performed. The grid resolution effect on numerical results is presented in Figure 7.5 where, the numerical data are also compared with the experimental data of Tominaga et al. [45] and numerical solution from [29]. In this figure, the grid with twenty grid-points in transverse direction is very coarse and, in turn, the predicted velocity profile is not accurate enough. This is especially significant near the outer wall. The most accurate simulation is obtained when a grid with forty grid-points in the transverse direction is used. Unfortunately manning's number is not reported in [45]. Since in [29] the Manning's number of 1.5 has been suggested, the authors made the same choice to make the simulations comparable with those from [29]; see Figure 7.5. The small inconsistency between measured and computed results in Figure 7.5-*e* then is a consequence of the uncertainty in Manning's number. In Figure 7.6, the effect of secondary force on velocity profile is investigated. When the secondary force is included in momentum equations, the computed velocity profile is more accurate in section 1 and 2. In section 3 and 4, the computed secondary force shifts the velocity profile toward the inner bank. The same phenomenon is observed by Moradi Larmaei et. al. [33]. This may limit the application of vorticity equation to the channels with low sinuosity. When vegetation damping source term is included in vorticity equation [see Equation (7.18)], the computed velocity profile does not significantly change (Figure 7.6). In Figure 7.7-*a*, the streamwise vorticity profiles computed with and without inclusion of vegetation damping source term in vorticity equation are compared. The vegetation damping source term reduces the absolute magnitude of the streamwise vorticity in vegetated zone but, in this region both the absolute magnitude of vorticity
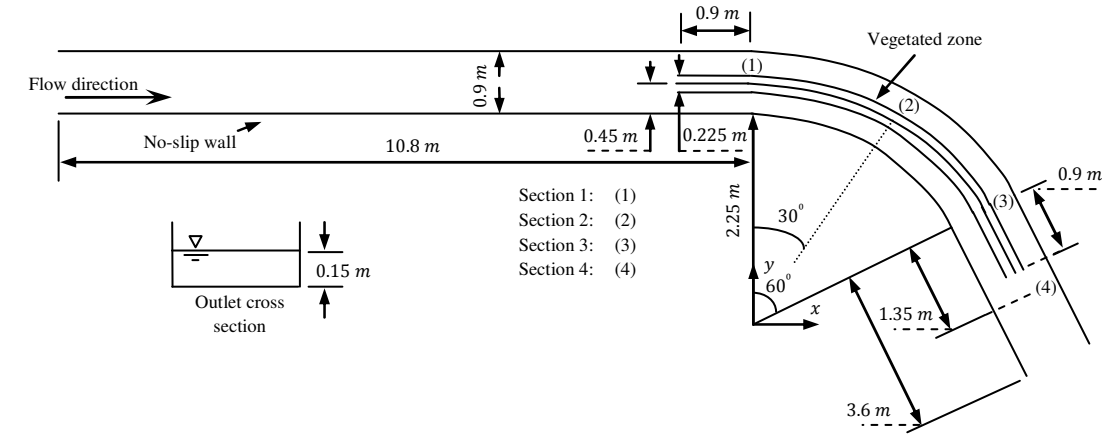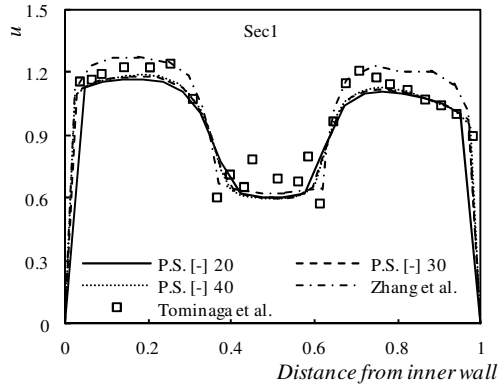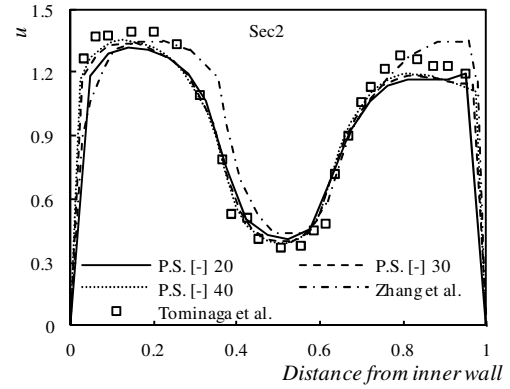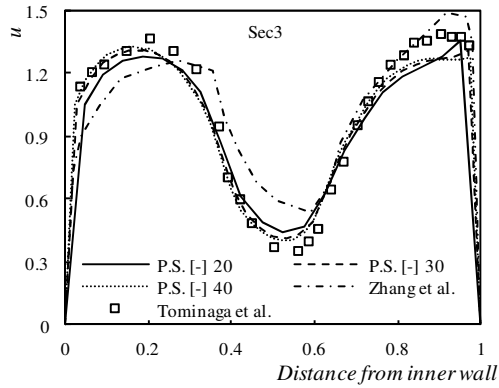
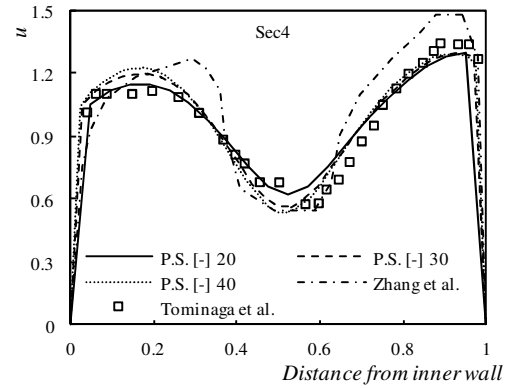Figure 7.5. Geometrical detail, and grid resolution effect on velocity profile in Tominaga et al. [45] test; P.S., Present Solver. Results are also compared with those from Zhang et al. [29].

and velocity are small. When the absolute magnitude of vorticity and velocity is small, the computed secondary shear will be small [see Equation (7.6)]. Thus, the secondary force will not significantly change when vegetation damping source term is included in vorticity equation. If the secondary force does not significantly change, the velocity profile remains the same. Contours of gage water surface elevation near vegetated zone are presented in Fig. 7b. Vegetation drag force increases the gage water surface elevation and the hydrostatic pressure in vegetated zone.
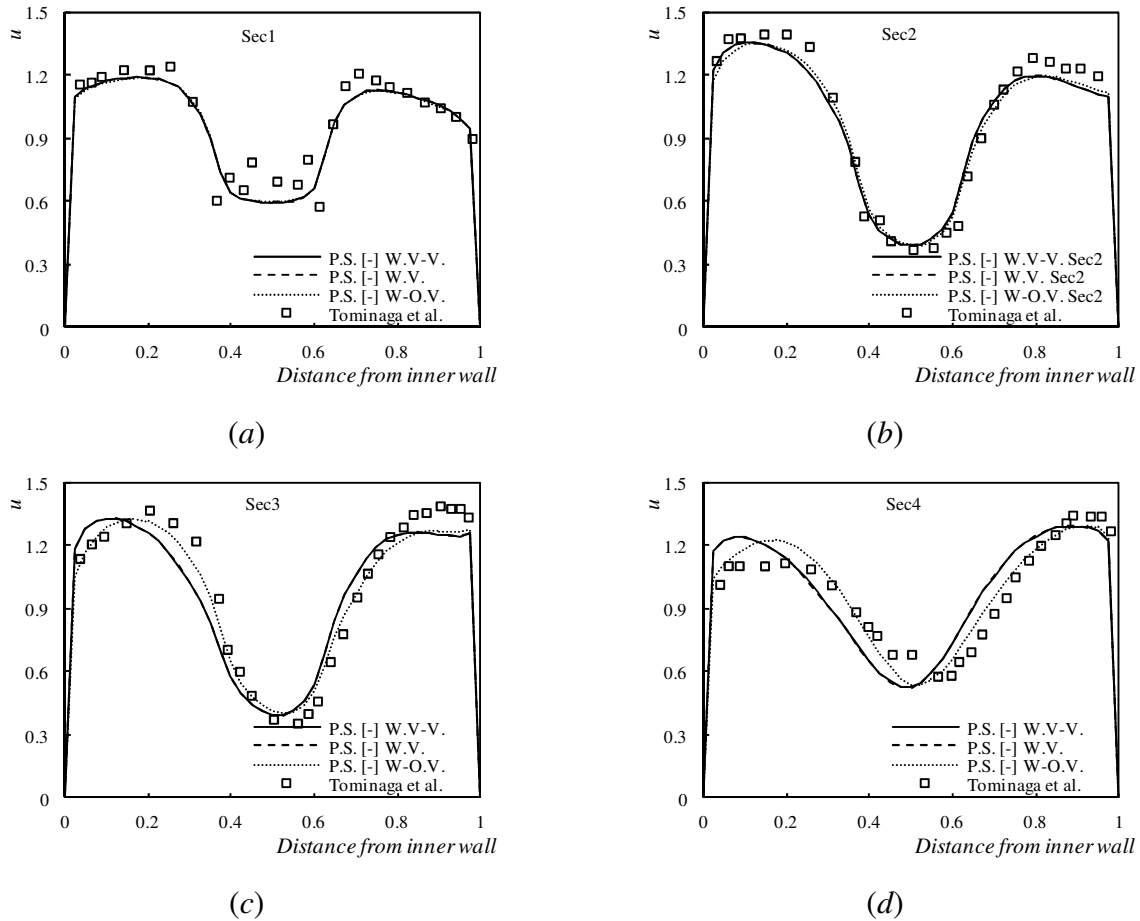

Figure 7.6. Secondary force effect on velocity profile in Tominaga et al. [45] test; W.V-V., With Vorticity – Vegetation damping included, W.V., With Vorticity, W-O.V., Without Vorticity; P.S., Present Solver.
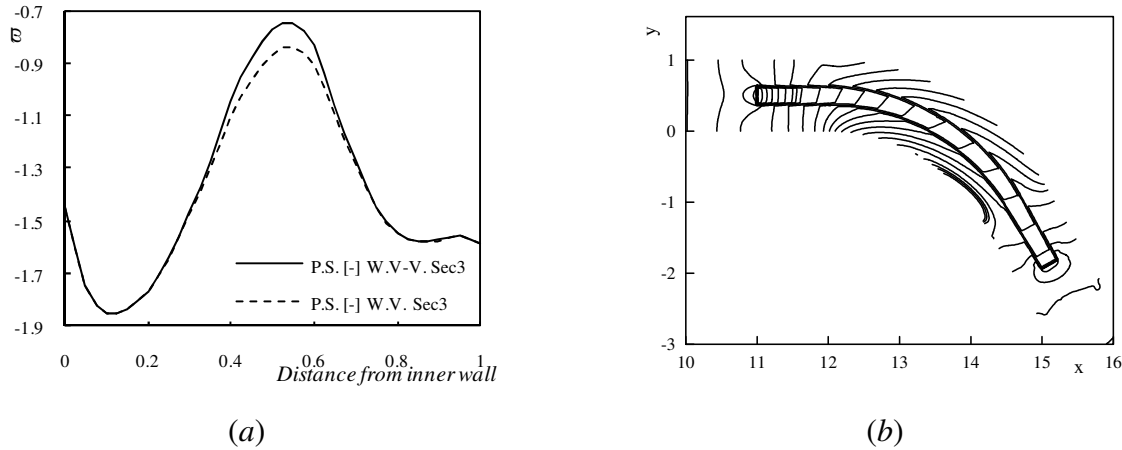
Figure 7.7. (*a*) Vegetation damping effect on vorticity; W.V-V., With Vorticity – Vegetation damping included, W.V., With Vorticity; P.S., Present Solver. (*b*) Contours of gage water surface elevation near vegetated zone.

7.2.5.3 Alternate vegetated zones

This section is divided into four subsections. Section 7.2.5.3.1 is devoted to a simple validation test where, the channel is not vegetated. In Section 7.2.5.3.2, a turbulent flow, $R_{e_D} = 5000$, over two thin alternate vegetation zones is simulated. The test case in Section 7.2.5.3.3 is the same as the test case in section 7.2.5.3.2 but, the vegetation zones are dense. In Section 7.2.5.3.4 the same test as the test in section 7.2.5.3.3 is performed but with $R_{e_D} = 450$. In all these test cases, a steady flow with an unsteady heat transfer is assumed. A steady flow simulation is performed until convergence is attained. Using this converged solution an unsteady heat and fluid flow is then simulated. Water thermal conductivity is assumed $0.6 \ w/(m.°k)$ and its specific heat capacity is assumed $4182 \ j/(kg.°k)$. Vegetation stems are assumed to have the same material property as oak where, stems density is assumed $600 \ kg/m^3$, their thermal conductivity is assumed $0.17 \ w/(m.°k)$, and their specific heat capacity is assumed $2000 \ j/(kg.°k)$. The inlet temperature is $300 \ °k$, walls temperature is constant and equal to $150 \ °k$, and the reference temperature is $300 \ °k$. The time step size is $0.05 \ s$ except in Section 7.2.5.3.4 where the time step size is $0.5557 \ s$. In the first test case the side walls are assumed free-slip but, in the rest of the test cases the side walls are assumed no-slip. In Sections 7.2.5.3.2 to 7.2.5.3.4, stems are emergent and, they are arranged in a staggered manner. In all test cases, the number of grid points in the transverse direction is about 40 and, the heat flux through the channel surface and its bed is

assumed zero. The geometrical details together with some hydraulic parameters of the channel are depicted in Figure 7.8-*a*.

(*a*)

(*b*)

(*c*)

Figure 7.8. (*a*) Geometrical detail in alternate vegetated zones test case, (*b*) and (*c*) Longitudinal and transverse temperature profiles in a frictionless straight channel and a frictionless two dimensional duct; $dt140$, $dt160$, $dt180$, and $dt200$ represent the number of time step where a plot is generated; P.S., Present Solver.

7.2.5.3.1 Straight channel before planting stems

In this test case, the flow Reynolds number is 4.98×10^5 where, $L_{ref} = 1\,m$ and $U_{ref} = 0.5\,m/s$. Bed slope is 0, Manning's number is $0.0\,s/m^{1/3}$, and the total inlet discharge is $0.1\,m^3/s$. Errors are normalized, and the convergence criterion is set to 10^{-3}. Other details which are not mentioned in Section 7.2.5.3, are as in Section 7.2.5.1.

Since there is no resisting force, the water surface will be horizontal and, in turn, a depth-averaged simulation will be equivalent to a two dimensional simulation. In Figures 7.8-*b* and 7.8-*c*, the numerical results obtained with the present solver for sections L and T1 are compared with

the numerical data obtained using Fluent6.3 software for the same sections. The longitudinal and transverse temperature profiles predicted with the present solver and Fluent6.3 are exactly similar. Since the free-slip wall boundary condition is used in this test, the magnitude of the near-wall turbulence is small and, in turn, in many cells the computed magnitude of the dimensionless distance from the wall is smaller than 11.63. Though, it is still possible to compare two numerical tools which exactly use the same scheme, it has to be mentioned that the computed temperature profiles are not accurate.
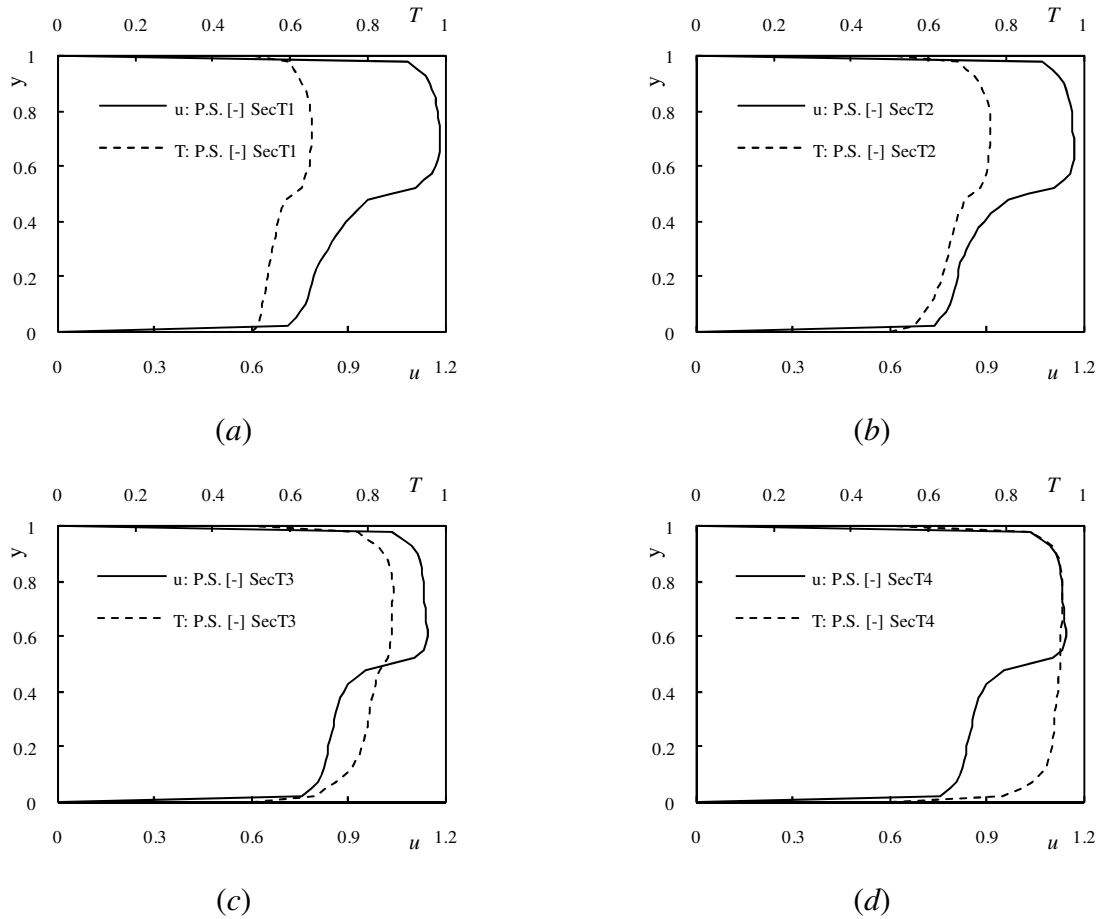

Figure 7.9. Velocity and temperature profiles in the channel with alternate vegetated zones, $R_{e_D} = 5000$, and $H_v = 0.1$; P.S., Present Solver.

7.2.5.3.2 Channel with thin alternate vegetated zones and high R_{e_D}

In this test case, the Bed slope is 0.001, stem diameter is 0.01 m, and the spacing between stems is 0.1 m. Manning's number is 0.01 $s/m^{1/3}$, drag coefficient is assumed 1.0, and the total inlet

discharge is $0.1\,m^3/s$. Errors are scaled, and the convergence criterion is set to 10^{-3}. Other details are as in Section 7.2.5.3.1.
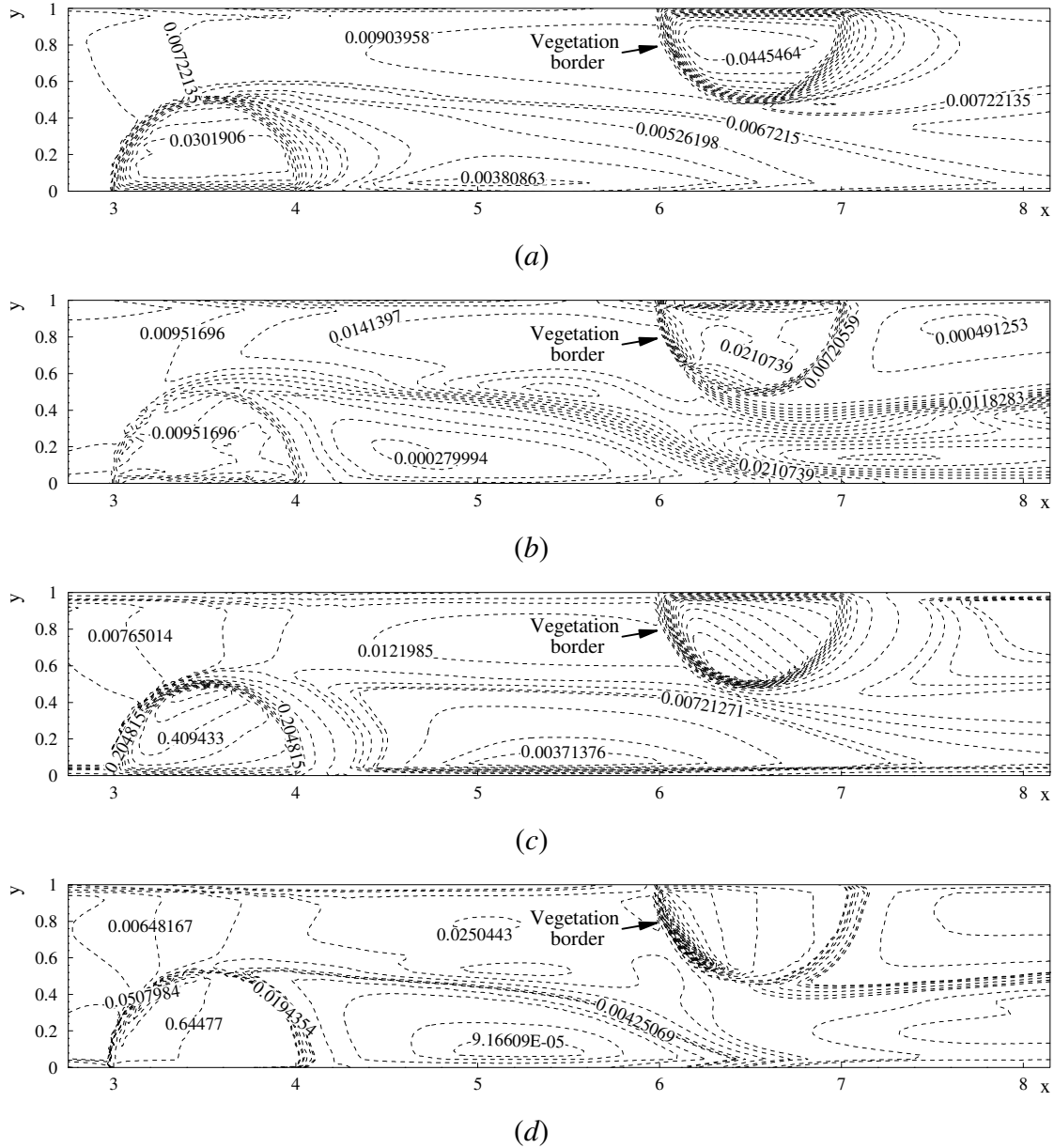

(a)

(b)

(c)

(d)

Figure 7.10. Distribution of turbulence parameters when $R_{e_D} = 5000$; (a) and (b), contours of turbulence kinematic energy, (c) and (d) contours of turbulence dissipation rate; (a) and (c), $H_v = 0.1$, (b) and (d), $H_v = 0.025$.

The simulated velocity and temperature profiles at $t = 160\Delta t$ are presented in Figure 7.9. A thin vegetation zone, $\lambda = 0.2382$ and $\phi = 0.9909$, significantly deflects the flow but, its effect on

temperature filed is less significant. The distribution of turbulence kinematic energy and its dissipation rate is shown in Figures 7.10-a and 7.10-c. Since the R_{e_D} is high, the production of turbulence due to vegetation stems is high and, in turn, the magnitude of the turbulence kinematic energy and its dissipation rate in vegetated zones is higher than the nearby area. There is an area downstream of every vegetated zone where the turbulence kinematic energy and its dissipation rate have the minimum magnitude. This is where a high Reynolds number turbulence model can become inapplicable if the condition gets worse. In this test case, the computed magnitude of the dimensionless distance from the wall in all near-wall cells is bigger than 11.63.

7.2.5.3.3 Channel with alternate dense vegetated zones and high R_{e_D}

Compared with Section 7.2.5.3.2, the spacing between stems is changed from $0.1\ m$ to $0.025\ m$. As a result, vegetation density changes to $\lambda = 5.178$ and, its porosity changes to $\phi = 0.855$. Other details are as in Section 7.2.5.3.2.

The profile of velocity and temperature at several transverse directions at $t = 200\Delta t$ are presented in Figure 7.11. In this figure, the dense vegetated zone highly deflects the flow. The average velocity in vegetated zone is about one third of the inlet velocity and, in turn, the stem Reynolds number calculated with the resultant flow velocity is $R_{e_d} \approx R_{e_D}/3 \approx 1667$, which is still in fully turbulent region. Compared with the thin vegetated zones in Section 7.2.5.3.2, a dense vegetation zone highly alters the temperature profile. In Figure 7.11, the porosity-induced heat flux has no effect on the calculated temperature profile. Porosity-induced heat flux is part of the diffusive heat flux [see Equation (7.21)] and, in turn, its contribution to total heat flux at high Reynolds numbers is significant if porosity gradient is very high. Since a computational cell is either fully vegetated or it is not, the porosity gradient increases with grid refinement. A grid with 40 grid points in transverse direction is a normal choice in civil engineering [3,13,29]. Thus, at high stem Reynolds number the porosity-induced heat flux can be ignored. Contours of turbulence kinematic energy and its dissipation rate are presented in Figure 7.10. Compared with a thin vegetated zone, the low turbulence kinematic energy region downstream of a dense vegetated zone is bigger. This will make a high Reynolds number turbulence model inapplicable since in many near-wall cells the computed magnitude of the dimensionless distance from the wall may fall below 11.63. In order to have an accurate solution, the authors increased the magnitude of the turbulence kinematic energy at the inlet; i.e. compared to the test case in

Section 7.2.5.3.2, the inlet flow is assumed more turbulent. This can be identified in contours of turbulence kinematic energy in Figure 7.10-*b*. It should be noted that, the vegetation porosity of about 0.855, which is assumed in this test, is much higher than the minimum field condition with $\phi = 0.35$.
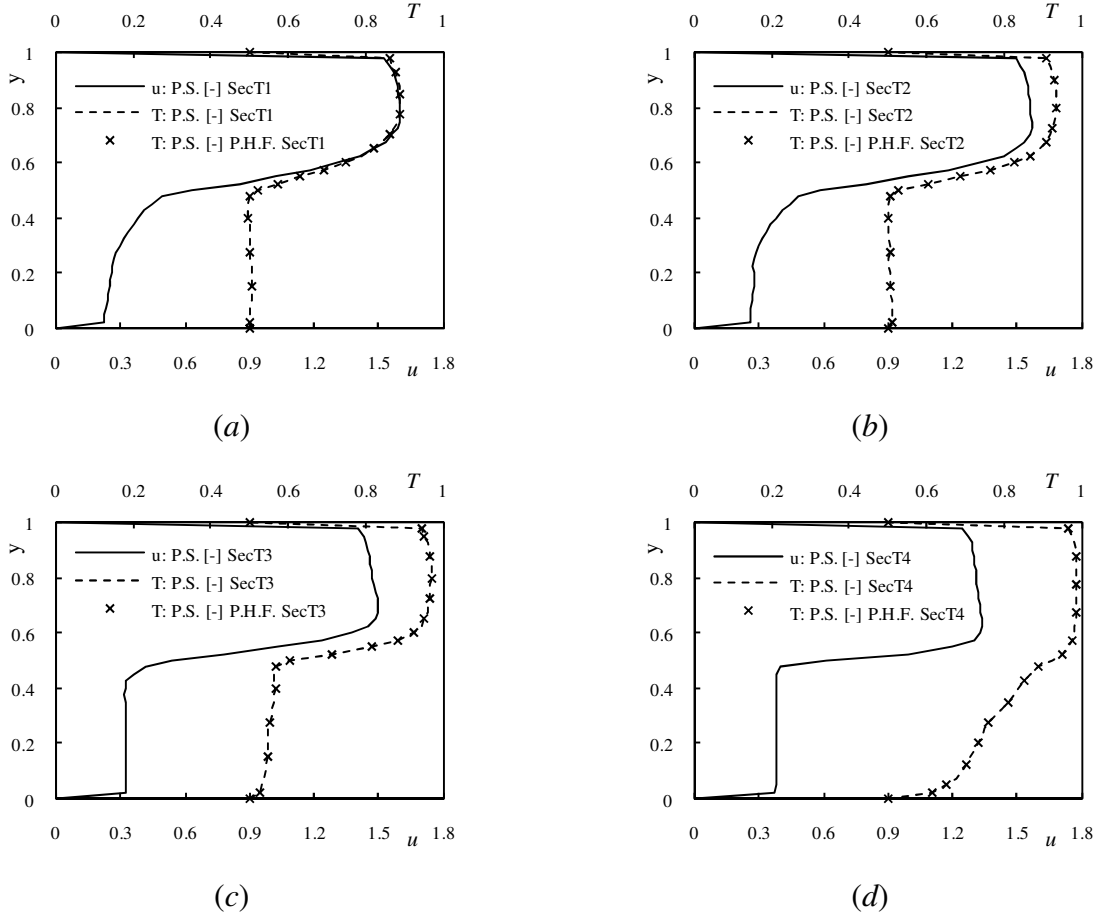

Figure 7.11. Velocity and temperature profiles in the channel with alternate vegetated zones, $R_{e_D} = 5000$, and $H_v = 0.025$; P.H.F., Porosity-induced Heat Flux is included, P.S., Present Solver.

7.2.5.3.4 Channel with alternate dense vegetated zones and low R_{e_D}

Compared with Section 7.2.5.3.3, the total inlet discharge is changed from $0.1\,m^3/s$ to $0.009\,m^3/s$. Thus, the flow Reynolds number is 4.47×10^4 where, $L_{ref} = 1\,m$ and $U_{ref} = 0.045\,m/s$. Other details are as in Section 7.2.5.3.3.
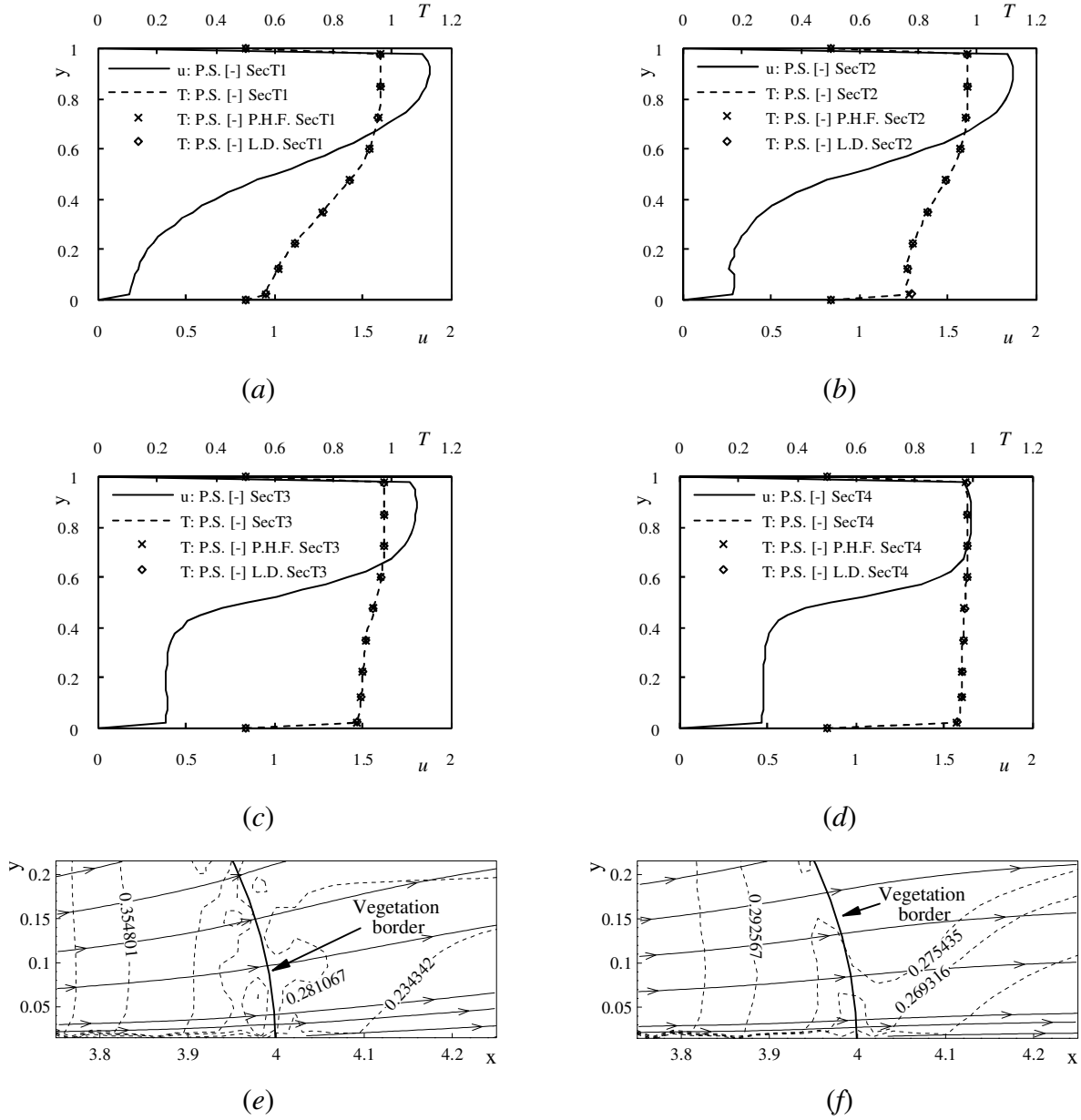
Figure 7.12. (*a*) to (*d*) Velocity and temperature profiles in the channel with alternate vegetated zones; P.H.F., Porosity-induced Heat Flux is included, L.D., Laminar Dispersion is included, P.S., Present Solver; (*e*) and (*f*) Velocity distribution downstream of a vegetated zone; dash-lines are contours of u velocity, solid-lines are streamlines; (*a*) to (*e*) $R_{e_D} = 450$, (*f*) $R_{e_D} = 5000$; $H_v = 0.025$.

The relative difference between the minimum and maximum velocity at $t = 200\Delta t$ in Figures 7.12-*a* to 7.12-*d* is comparable with the relative difference in Figure 7.11; i.e. even in a slow-

moving flow a dense vegetation zone highly deflects the flow. An oscillation in velocity profile can be observed in Figure 7.12-*b* near $y \approx 0.2$. This oscillation is due to a slow moving fluid near the wall where the border of vegetated zone exists; see Figure 7.12-*e*. Such oscillation is not significant for the test case in Section 7.2.5.3.3 where the flow Reynolds number is high (Figure 7.12-*f*). A stagnation point would occur in this area (near the wall where vegetation border exists) if the magnitude of the inlet velocity was further reduced. In vegetated zone in Figures 7.12-*a* and 7.12-*b*, the stem Reynolds number, R_{e_d}, is about 150 and, in Figures. 7.12-*c* and 7.12-*d* the stem Reynolds number is about 225 (which are in Forchheimer flow regime). The relevant stem Peclet numbers, P_{e_d}, for these stem Reynolds numbers are about 0.9 and 1.5, respectively. In these regions, the laminar thermal dispersion is comparable with the molecular diffusion. Since the authors assumed a highly turbulent inlet flow, the laminar thermal dispersion may not be comparable with turbulent diffusion (this is done in order to keep the computed magnitude of the dimensionless distance from the wall above 11.63). Neither the laminar thermal dispersion, nor the porosity-induced heat flux significantly changed the temperature profile.

7.2.6 Conclusion

In this article, the latest developments of porous media science are used in order to simulate heat and fluid flow in non-flexible vegetated porous media. Among all aspects of this work, it is especially unique because of simulating turbulent heat transfer in a partially vegetated channel using the porous media science. At the same time, four research cases are introduced and investigated:

- Research case (a): vegetation porosity and density are defined from a unit-cell. Either the vegetation density or its porosity can be derived from the other one and, in turn, momentum is conserved. Regarding field condition and flumes setup, a strategy is suggested in order to calculate the near-boundary vegetation porosity.

- Research case (b): a dissipation source term is developed for vorticity equation in order to take account of vegetation damping effect on secondary flows. It is shown that, this damping source term significantly reduces the absolute magnitude of the vorticity in vegetated zones but, its contribution to the total secondary force is negligible. According to the simulations performed in this article, in a vegetated zone both the absolute magnitude of the streamwise

vorticity and the velocity magnitude are small and, in turn, the secondary force is not significant. Thus, the vegetation damping effect on the absolute magnitude of the streamwise vorticity can be ignored.

- Research case (c): It is shown that, when a channel is partially vegetated, there will be a zone downstream of the vegetated regions where the turbulence kinematic energy is low. The magnitude of turbulence kinematic energy downstream of a dense vegetated zone can be small enough to make a high Reynolds number turbulence model inapplicable. Thus, at high R_{e_D} the standard $k - \varepsilon$ model is applicable only to the vegetated zones with low vegetation density. The choice of the appropriate turbulence model depends on the turbulence strength in main channel, vegetated zones, and the region downstream of vegetated zones.

- Research case (d): a model is suggested for taking account of vegetation material effect on the heat flux through walls. Some numerical simulations are also performed in order to investigate the effect of porosity-induced heat flux and the laminar thermal dispersion on temperature field near a vegetated zone. It is observed that the porosity-induced heat flux can be ignored when the average grid spacing is more than 0.025, vegetation density is less than 5.178, and the flow Reynolds number is high. As a good estimation, for the same range of vegetation density and grid spacing the porosity-induced heat flux can be still ignored when the flow Reynolds number is low. It is shown that, when the standard $k - \varepsilon$ model is valid for simulating a partially vegetated channel, the laminar thermal dispersion can be ignored. The numerical results also indicate that, compared to the velocity field the temperature field will be less affected by a thin vegetated zone.

7.2.7 Acknowledgments

7.2.8 References

[1] X. Sun, K. Shiono, P. Rameshwaran, J.H. Chandler, Modelling vegetation effects in irregular meandering river, J. Hydraul. Res. 48 (6) (2010) 775-783.

[2] Y. Tanino, H.M. Nepf, Laboratory investigation of mean drag in a random array of rigid, emergent cylinders, J. Hydraul. Eng. 134 (1) (2008) 34-41.

[3] W. Wu, F.D. Shields Jr, S.J. Bennett, S.S.Y. Wang, A depth-averaged two-dimensional model for flow, sediment transport, and bed topography in curved channels with riparian vegetation, Water Resour. Res. 41(3) (2005) W03015.

[4] J.-t. Zhang, X.-h. Su, Numerical Model for Flow Motion with Vegetation, J. Hydrodyn. Ser. B 20 (2) (2008) 172-178.

[5] M.J.S. de Lemos, The double-decomposition concept for turbulent transport in porous media, in: D.B. Ingham, I. Pop, (Eds.), Transport phenomena in porous media III, Elsevier, Oxford, 2005, pp. 1-33.

[6] M.J.S. de Lemos, Turbulence in porous media: modeling and applications, Elsevier, London, UK, 2006.

[7] M.H.J. Pedras, M.J.S. de Lemos, Thermal dispersion in porous media as a function of the solid-fluid conductivity ratio, Int. J. Heat Mass Transfer 51 (21-22) (2008) 5359-5367.

[8] M.B. Saito, M.J.S. de Lemos, Interfacial heat transfer coefficient for non-equilibrium convective transport in porous media, Int. Commun. Heat Mass Transfer 32 (6) (2005) 666-676.

[9] M.B. Saito, M.J.S. de Lemos, A correlation for interfacial heat transfer coefficient for turbulent flow over an array of square rods, J. Heat Transfer 128 (5) (2006) 444-452.

[10] M.B. Saito, M.J.S. de Lemos, Laminar heat transfer in a porous channel simulated with a two-energy equation model, Int. Commun. Heat Mass Transfer 36 (10) (2009) 1002-1007.

[11] M.B. Saito, .J.S. de Lemos, A macroscopic two-energy equation model for turbulent flow and heat transfer in highly porous media, Int. J. Heat Mass Transfer 53 (11-12) (2010) 2424-2433.

[12] W. Wu, S.S.Y. Wang, A depth-averaged two-dimensional numerical model of flow and sediment transport in open channels with vegetation, in: S.J. Bennett, A. Simon, (Eds.), Riparian Vegetation and Fluvial Geomorphology, American Geophysical Union, Washington, DC, 2004, pp. 281.

[13] T. Fischer-Antez, T. Stoesser, P. Bates, 3D numerical modelling of open-channel flow with submerged vegetation, J. Hydraul. Res. 39 (3) (2001) 303-310.

[14] C.-T. Hsu, Dynamic Modeling of Convective Heat Transfer in Porous Media, in: K. Vafai, (Ed.), Handbook of Porous Media, Taylor & Francis, Boca Raton, Fla., 2005, pp. 39-80.

[15] E. Arquis, J.P. Caltagirone, P. Le Breton, Determination of the dispersion properties of a periodic medium from local analysis of heat transfer, Comptes Rendus de l'Academie des Sciences, Serie II (Mecanique, Physique, Chimie Sciences de la Terre et de l'Univers) 313 (10) (1991) 1087-92.

[16] F. Kuwahara, A. Nakayama, Numerical determination of thermal dispersion coefficients using a periodic porous structure, Transactions of the ASME, J. Heat Transfer 121 (1) (1999) 160-3.

[17] F. Kuwahara, A. Nakayama, H. Koyama, A numerical study of thermal dispersion in porous media, Transactions of the ASME, J. Heat Transfer 118 (3) (1996) 756-61.

[18] F.E. Teruel, Rizwan-Uddin, Characterization of a porous medium employing numerical tools: Permeability and pressure-drop from Darcy to turbulence, Int. J. Heat Mass Transfer 52 (25-26) (2009) 5878-5888.

[19] S.-U. Choi, H. Kang, Reynolds stress modeling of vegetated open-channel flows, J. Hydraul. Res. 42 (1) (2004) 3-11.

[20] W.X. Huai, Y.H. Zeng, Z.G. Xu, Z.H. Yang, Three-layer model for vertical velocity distribution in open channel flow with submerged rigid vegetation, Adv. Water Resour. 32 (4) (2009) 487-492.

[21] T.-Y. Hsieh, J.-C. Yang, Numerical examination on the secondary-current effect for contaminant transport in curved channel, J. Hydraul. Res. 43 (6) (2005) 644-659.

[22] W. Wu, S.S.Y. Wang, Depth-averaged 2-D calculation of flow and sediment transport in curved channels, Int. J. Sediment Res. 19 (4) (2004) 241-257.

[23] R.S. Bernard, STREMR: Numerical model for Depth-averaged incompressible Flow, U.S. Army Engineer Waterway Experiment Station, Vicksburg, MS, 1993.

[24] J.F. Rodriguez, F.A. Bombardelli, M.H. Garcia, K.M. Frothingham, B.L. Rhoads, J.D. Abad, High-resolution numerical simulation of flow through a highly sinuous river reach, Water Resour. Manage. 18 (3) (2004) 177-199.

[25] A.A. Alshare, P.J. Strykowski, T.W. Simon, Modeling of unsteady and steady fluid flow, heat transfer and dispersion in porous media using unit cell scale, Int. J. Heat Mass Transfer 53 (9-10) (2010) 2294-2310.

[26] F.E. Teruel, Rizwan-uddin, A new turbulence model for porous media flows. Part I: Constitutive equations and model closure, Int. J. Heat Mass Transfer 52 (19-20) (2009) 4264-4272.

[27] F.E. Teruel, Rizwan-Uddin, Numerical computation of macroscopic turbulence quantities in representative elementary volumes of the porous medium, Int. J. Heat Mass Transfer 53 (23-24) (2010) 5190-5198.

[28] C.L. Jang, Y. Shimizu, Vegetation effects on the morphological behavior of alluvial channels, J. Hydraul. Res. 45 (6) (2007) 763-772.

[29] M.-L. Zhang, C.W. Li, Y.-M. Shen, A 3D non-linear k-epsilon turbulent model for prediction of flow and mass transport in channel with vegetation, Appl. Math. Modell. 34 (4) (2010) 1021-1031.

[30] X. Zhang, H.M. Nepf, Thermally driven exchange flow between open water and an aquatic canopy, J. Fluid Mech. 632 (2009) 227-243.

[31] W. Rodi, Turbulence models and their application in hydraulics, IAHR Monograph, Balkema, Rotterdam, Netherlands, 1993.

[32] F. Lopez, M. Garcia, Open-channel flow through simulated vegetation: turbulence modeling and sediment transport, US Army Corps of Engineers, Waterw. Exp. Stn., Vicksburg, 1997.

[33] M. Moradi Larmaei, J. Behzadi , T.-F. Mahdi, Grid-independent depth-averaged simulations with a collocated unstructured finite volume scheme, Int. J. Numer. Methods Fluids (2011) Article first published online: 22 MAR 2011, DOI: 10.1002/fld.2538.

[34] F.D. Rocamora Jr, M.J.S. De Lemos, Laminar recirculating flow and heat transfer in hybrid porous medium-clear fluid computational domains, in: Proceedings of IMECE2000, ASME, Int. Mech. Eng. Congr., ASME-HTD-366-5, Orlando, FL, 2000, pp. 113–122, ISBN 0-7918-1908-6.

[35] F. Kuwahara, M. Shirota, A. Nakayama, A numerical study of interfacial convective heat transfer coefficient in two-energy equation model for convection in porous media, Int. J. Heat Mass Transfer 44 (6) (2001) 1153-9.

[36] C.M. Rhie, W.L. Chow, Numerical Study of the turbulent flow past an airfoil with trailing edge separation, AIAA J. 21 (11) (1983) 1525-1532.

[37] M. Moradi Larmaei, J. Behzadi, T.-F. Mahdi, Treatment of checkerboard pressure in collocated unstructured finite volume scheme, Numer. Heat Transfer, Part B Fundamentals 58 (5) (2010) 121–144.

[38] S.V. Patankar, Numerical heat transfer and fluid flow, Hemisphere, New York, 1980.

[39] M. Moradi Larmaei, T.-F. Mahdi, A new method for the treatment of wetting-drying fronts, Appl. Math. Modell. Submitted (2010), submitted.

[40] M. Ghisalberti, H. Nepf, Shallow flows over a permeable medium: The hydrodynamics of submerged aquatic canopies, Transp. Porous Media 78 (2) (2009) 309-326.

[41] T.-A. Okamoto, I. Nezu, Turbulence structure and "Monami" phenomena in flexible vegetated open-channel flows, J. Hydraul. Res. 47 (6) (2009) 798-810.

[42] H.K. Versteeg, W. Malalasekera, An introduction to computational fluid dynamics: the finite volume method, Pearson Prentice Hall, Toronto, 1995, ch. 6 and 9.

[43] B.E. Launder, D.B. Spalding, The Numerical Computation of Turbulent Flows, Comput. Meth. Appl. Mech. Eng. 3 (1974) 269-289.

[44] E. Pasche, Turbulence mechanism in natural streams and the possibility of its mechanical representation, Mitteilungen Institut für Wasserbau und Wasserwirtschaft, No. 52, RWTH, Aachen, Germany, 1984.

[45] A. Tominaga, M. Nagao, I. Nezu, Effects of vegetation on flow structures and bed profiles in curved open channels. in: J.H.W. Lee, A.W. Jayawardena, Z.Y. Wang, (Eds.), Second

international symposium on environmental hydraulics, A.A. Balkema, Hong Kong, China, 1998, pp. 329-334.

[46] M. Moradi Larmaei, T.-F. Mahdi, Vorticity equation for the secondary flow effect in depth-averaged simulations, Adv. Water Resour. (2011) Submitted.

CHAPTER 8   GENERAL DISCUSSION

The main objective of this thesis is the development of a depth-averaged solver for simulation of heat and fluid flows in vegetated channels. The development process was started with developing a two-dimensional solver which then was extended to a depth-averaged solver. Many innovations have been made for improving computations in terms of computational efficiency and accuracy of the results. The steps taken for development of the solver allowed for high certainty in its reliability, and minimized the programming mistakes.

8.1   Two-dimensional solver

The two-dimensional solver is able to simulated unsteady heat and fluid flows. The solver is validated with both numerical and experimental data from literature, it supports several boundary conditions, and it can solve both laminar and turbulent flows. In the two-dimensional solver, special attention is paid to the problem of checkerboard pressure field. A relaxation factor independent solution which is free of any spurious oscillation is necessary for having an accurate solution. The Rhie and Chow type technique then is used for having a smoother pressure field, and MBLT technique is developed for improving the performance of the Rhie and Chow type pressure interpolation techniques. A hypothesis is also developed for choosing an appropriate relaxation factor in Rhie and Chow type methods.

8.2   Depth-averaged solver

The depth-averaged solver is able to simulate heat and fluid flows in vegetated channels. Special attention is paid to discretization of equations in order to achieve oscillation-free solutions at regions with very small water depth. TV-LI technique is developed for reducing the computational cost in fine grids. This technique employs a simultaneous depth and distance weighted averaging. A high order wetting-drying treatment is also developed for capturing temporal movement of the interface between water and land. Compared to a first order technique, this technique is highly efficient when water flows down a slope. A mass conserving technique is innovated in order to prevent formation of cells with negative water depth. Such cells may affect the stability of a numerical solver. Vorticity equation is solved in order to compute the stream-wise vorticity which is used for calculating the secondary force. This secondary force will have a

non-zero magnitude where the streamlines are curved. Vegetation is modeled with equivalent matrix of stems, and porous media science is used for simulation of heat and fluid flows in vegetated zones. In order to increase the accuracy near the boundaries, the near-boundary porosity is defined. The effect of this porosity on transfer processes near the boundaries then is taken into account in near-boundary treatments. A source term is developed for the vorticity equation in order to take account of vegetation damping effect on secondary flows. This term reduces the absolute magnitude of the stream-wise vorticity within vegetated zones and, in turn, it reduces the secondary force in these zones. The local thermal equilibrium hypothesis is applied to transport of heat in vegetated zones. The one-energy equation model then is generalized in order to be applicable to partially vegetated channels.

8.3   Geo-data interpolation

The precision of reconstructed bed topography highly affects the accuracy of a solution and, in turn, sufficient accuracy in interpolation of geo-data is necessary. In this thesis, a tool is developed for the interpolation of geo-data into cells' center. This tool employs three different techniques for interpolation of geo-data. Every supported technique in this tool is suitable for certain arrangement of geo-data. With three different techniques which this tool supports, it is possible to interpolate any data with appropriate accuracy.

CONCLUSION AND RECOMMANDATIONS

The main objective of this thesis is the development of a depth-averaged solver. The solver is validated and its performance is verified. The following conclusions result from the specific objectives of this dissertation:

- In order to have a relaxation factor independent solution, the Rhie and Chow type pressure correction term has not to be under-relaxed, and the mass conservation criterion has to be strict enough.

- Since in turbulent flows the sources of momentum are not exactly similar to the ones in laminar flow, a treatment for checkerboard pressure field in laminar flows will not necessarily have the same efficiency in turbulent flows. Moreover, an increase in cell Reynolds number increases the absolute magnitude of the checkerboard oscillations.

- The efficiency of the Rhie and Chow type pressure correction technique will reduce when the checkerboard oscillations are anisotropic. In equilateral triangular grids LTs are perfect and, in turn, the pressure oscillation will be isotropic. Thus, perfect LTs increase the performance of the Rhie and Chow type pressure correction method. Pressure field will be smoother when MBLT technique, which is devised for enforcing the desired property of perfect LTs into the grid, is applied. It is observed numerically that checkerboard oscillations produce reverse flow. Thus, they are less likely when there is a pressure gradient.

- Multiplication of transport equations by appropriate power of water depth together with semi-implicit discretization of bed source terms avoids numerical oscillations at small water depths.

- According to numerical results, TV-LI scheme shows the same degree of accuracy compared to LI scheme. However, the TV-LI scheme efficiently reduces the computational efforts at fine grids.

- Since in depth-averaged simulations with finite volume technique grid usually lies on a horizontal plane, bed source terms have to be integrated over the actual bed area rather than the cell area. This extremely affects the results when bed slope is high.

- When grid allows continues downstream directions, numerical results can be affected by false currents. Grid refinement in unstructured triangular grids can break these downstream directions down, and weaken the false currents.

- When Courant number is less than one, the assumption of zero velocity at the face between wet and dry cells does not reduce the accuracy of numerical results. For instance, the simulated wave front in a dam-break over dry bed was not hindered.

- With appropriate modification of pressure correction, formation of regions with negative water depth can be prevented. Thus, there will be no need for mass redistribution.

- A high order wetting-drying technique efficiently prevents false wetting and, in turn, it prevents spurious extension of thin layers of fluid throughout the computational domain. Since with such high order technique wet region is smaller compared to the case when a low order technique is used, the computational efficiency will eventually increase.

- In dam-break over a shallow wet bed, the solution is independent of the water depth at shallow wet bed when the dimensionless water depth at the shallow side is less than 10^{-3}. When the developed wetting-drying technique is used, the appropriate dimensionless threshold water depth is about 10^{-3} to 10^{-4}.

- A model is developed for taking account of vegetation effect on secondary force. It is observed that, in vegetated zones the absolute magnitude of the stream-wise vorticity and velocity are small and, in turn, the secondary force is negligible. Thus, the vegetation damping effect on the absolute magnitude of the stream-wise vorticity can be ignored.

- In partially vegetated channels there will be a zone downstream of the vegetated regions where the turbulence kinematic energy is small. This may make a high Reynolds number turbulence model inapplicable to such channels when vegetation density is high. The choice of the appropriate turbulence model depends on the turbulence strength in main channel, vegetated zones, and the region downstream of the vegetated zones.

- When vegetation touches the wall, it affects the near-wall heat flux. The diffusive heat flux due to porosity gradient can be ignored when the average grid spacing is more than 0.025, vegetation density is less than 5.178, and the flow Reynolds number is high. As a good estimation, for the same range of vegetation density and grid spacing, the diffusive

heat flux due to porosity gradient can still be ignored when flow Reynolds number is small. When the standard $k - \varepsilon$ modell is valid for simulating a partially vegetated channel, the laminar thermal dispersion can be ignored. The numerical results also indicate that, compared to the velocity field the temperature field will be less affected by a thin vegetated zone.

- When the assumption of shallow flow is strongly held, the computed secondary force improves the accuracy of the velocity field. For high magnitude of the depth to width ratio, the calculated secondary force still improves the accuracy of the computed velocity field if the channel bend is short.

- In a channel with fully vegetated cross section where the extent of the vegetated zone in stream-wise direction is less than the channel length, the gradient of water surface elevation in vegetated zone will be high. Since in such cases the magnitude of the secondary force will not be comparable to the hydrostatic pressure force, the secondary force effect can be ignored.

Recommendations:

- A combination of level one MBLT and quad-split boundary layer grids successfully removed the checkerboard oscillations in a two-dimensional duct. It is also possible to successfully apply the MBLT grid of any level just outside the boundary layer. It then is recommended to develop a grid generator which is able to apply quad-split boundary layer grids together with MBLT to complicated geometries.

- With a high order method, the reconstructed pressure field will have higher resolution. This will affect the underlying assumptions about checkerboard pressure fields. A study of the performance of MBLT grids then is recommended in such solutions.

- The solver can work with variable density and viscosity which are functions of sediment concentration. SF-Field tool which interpolates geo-data into grid also interpolates the data required for sediment transport. An extension of the solver to simulate sediment transport then is recommended.

- Since the two-dimensional code is available, it can be simply extended to three dimensions. Problems such as investigation of MBLT in Tetrahedron grids then can be studied.

REFERENCES

Acharya, S., Baliga, B. R., Karki, K., Murthy, J. Y., Prakash, C., & Vanka, S. P. (2007). Pressure-based finite-volume methods in computational fluid dynamics. *Journal of Heat Transfer, 129*(4), 407-424.

Alshare, A. A., Strykowski, P. J., & Simon, T. W. (2010). Modeling of unsteady and steady fluid flow, heat transfer and dispersion in porous media using unit cell scale. *International Journal of Heat and Mass Transfer, 53*(9-10), 2294-2310.

Arquis, E., Caltagirone, J. P., & Le Breton, P. (1991). Determination of the dispersion properties of a periodic medium from local analysis of heat transfer. *Comptes Rendus de l'Academie des Sciences, Serie II (Mecanique, Physique, Chimie Sciences de la Terre et de l'Univers), 313*(10), 1087-1092.

Bechteler, W., & Farshi, D. (2001). 2-D simulation of channel flows with moveable bed. *International Journal of Sediment Research, 16*(2), 114-120.

Begnudelli, L., & Sanders, B. F. (2007). Conservative wetting and drying methodology for quadrilateral grid finite-volume models. *Journal of Hydraulic Engineering, 133*(3), 312-322.

Begnudelli, L., Valiani, A., & Sanders, B. F. (2010). A balanced treatment of secondary currents, turbulence and dispersion in a depth-integrated hydrodynamic and bed deformation model for channel bends. *Advances in Water Resources, 33*(1), 17-33.

Behzadi, J. (2007). *A numerical simulation of incompressible flow past 3D aximetrical bodies.* M.Sc, Amirkabir University of Technology, Tehran, Iran.

Bennett, S. J., Wu, W., Alonso, C. V., & Wang, S. S. Y. (2008). Modeling fluvial response to in-stream woody vegetation: Implications for stream corridor restoration. *Earth Surface Processes and Landforms, 33*(6), 890-909.

Bernard, R. S. (1993). STREMR: Numerical model for Depth-averaged incompressible Flow. Vicksburg, MS: U.S. Army Engineer Waterway Experiment Station.

Biron, P. M., Ramamurthy, A. S., & Han, S. (2004). Three-dimensional numerical modeling of mixing at River confluences. *Journal of Hydraulic Engineering, 130*(3), 243-253.

Blanckaert, K., Duarte, A., & Schleiss, A. J. (2010). Influence of shallowness, bank inclination and bank roughness on the variability of flow patterns and boundary shear stress due to secondary currents in straight open-channels. *Advances in Water Resources, 33*(9), 1062-1074.

Brufau, P., Garcia-Navarro, P., & Vazquez-Cendon, M. E. (2004). Zero mass error using unsteady wetting-drying conditions in shallow flows over dry irregular topography. *International Journal for Numerical Methods in Fluids, 45*(10), 1047-1082.

Brufau, P., Vazquez-Cendon, M. E., & Garcia-Navarro, P. (2002). A numerical model for the flooding and drying of irregular domains. *International Journal for Numerical Methods in Fluids, 39*(3), 247-275.

Cao, Z., & Pender, G. (2004). Numerical modelling of alluvial rivers subject to interactive sediment mining and feeding. *Advances in Water Resources, 27*(5), 533-546.

Cao, Z., Pender, G., Wallis, S., & Carling, P. (2004). Computational dam-break hydraulics over erodible sediment bed. *Journal of Hydraulic Engineering, 130*(7), 689-703.

Castro Diaz, M. J., Fernandez-Nieto, E. D., & Ferreiro, A. M. (2008). Sediment transport models in Shallow Water equations and numerical approach by high order finite volume methods. *Computers and Fluids, 37*(3), 299-316.

Cheesewright, R., McGrath, G., & Petty, D. G. (1990). LDA measurement of turbulent flow in a duct of square cross section at low Reynolds number (1011). Aeronational Engineering Department, Queen May Westfield College,University of London.

Chen, D., & Duan, J. G. (2008). Case study: Two-dimensional model simulation of channel migration processes in West Jordan River, Utah. *Journal of Hydraulic Engineering, 134*(3), 315-327.

Chenier, E., Eymard, R., & Herbin, R. (2009). A collocated finite volume scheme to solve free convection for general non-conforming grids. *Journal of Computational Physics, 228*(6), 2296-2311.

Choi, S.-U., & Kang, H. (2004). Modelisation des contraintes de Reynolds dans des ecoulements en canal encombres de vegetation Title of translation: Reynolds stress modeling of vegetated open-channel flows. *Journal of Hydraulic Research, 42*(1), 3-11.

Croft, T. N. (1998). *Unstructured mesh -- finite volume algorithms for swirling turbulent reacting flows.* PhD, University of Greenwich, London, UK.   http://staffweb.cms.gre.ac.uk/~ct02/research/thesis/main.html

Cui, J., & Neary, V. S. (2008). LES study of turbulent flows with submerged vegetation. *Journal of Hydraulic Research, 46*(3), 307-316.

Dalal, A., Eswaran, V., & Biswas, G. (2008). A finite-volume method for Navier-Stokes equations on unstructured meshes. *Numerical Heat Transfer, Part B: Fundamentals, 54*(3), 238-259.

Darwish, M., Sraj, I., & Moukalled, F. (2009). A coupled finite volume solver for the solution of incompressible flows on unstructured grids. *Journal of Computational Physics, 228*(1), 180-201.

Date, A. W. (1993). Solution of Navier-Stokes equations on non-staggered grid. *International Journal of Heat and Mass Transfer, 36*(7), 1913-1922.

Date, A. W. (1996). Complete pressure correction algorithm for solution of incompressible Navier-Stokes equations on a nonstaggered grid. *Numerical Heat Transfer, Part B: Fundamentals, 29*(4), 441-458.

Date, A. W. (2003). Fluid dynamical view of pressure checkerboarding problem and smoothing pressure correction on meshes with colocated variables. *International Journal of Heat and Mass Transfer, 46*(25), 4885-4898.

Date, A. W. (2005). Solution of transport equations on unstructured meshes with cell-centered colocated variables. Part I: Discretization. *International Journal of Heat and Mass Transfer, 48*(6), 1117-1127.

Davidson, L. (1996). A pressure correction method for unstructured meshes with arbitrary control volumes. *International Journal for Numerical Methods in Fluids, 22*(4), 265-281.

de Lemos, M. J. S. (2005). The double-decomposition concept for turbulent transport in porous media. In D. B. Ingham & I. Pop (dir.), *Transport phenomena in porous media III*. (1e éd., Vol. 3). Oxford: Elsevier.

de Lemos, M. J. S. (2006). *Turbulence in porous media: modeling and applications* (1e éd.). London, UK: Elsevier.

De Vriend, H. J. (1981). Flow measurments in a curved rectangular channel, Part II: rough bottom (9-79). Delft, Netherlands: Laboratory of Fluid Mechanics, Delft University of Technology.

Delis, A. I., & Katsaounis, T. (2005). Numerical solution of the two-dimensional shallow water equations by the application of relaxation methods. *Applied Mathematical Modelling, 29*(8), 754-783.

Delis, A. I., & Papoglou, I. (2008). Relaxation approximation to bed-load sediment transport. *Journal of Computational and Applied Mathematics, 213*(2), 521-546.

Di Martino, B., Giacomoni, C., Martin Paoli, J., & Simonnet, P. (2011). Simulation of the spread of a viscous fluid using a bidimensional shallow water model. *Applied Mathematical Modelling, 35*(7), 3387-3395.

Duan, J. G., & Julien, P. Y. (2005). Numerical simulation of the inception of channel meandering. *Earth Surface Processes and Landforms, 30*(9), 1093-1110.

Duan, J. G., & Nanda, S. K. (2006). Two-dimensional depth-averaged model simulation of suspended sediment concentration distribution in a groyne field. *Journal of Hydrology, 327*(3-4), 426-437.

Dunn, C. J. (1996). *Experimental determination of drag coefficients in open channel with simulated vegetation.* M. S., University of Illinois at Urbana Champaign, Urbana, IL.

Ferziger, J. H., & Peric, M. (1996). *Computational methods for fluid dynamics*. Berlin, Germany: Springer.

Fischer-Antez, T., Stoesser, T., & Bates, P. (2001). 3D numerical modelling of open-channel flow with submerged vegetation. *Journal of Hydraulic Research, 39*(3), 303-310.

FLUENT 6.3 User's Guide. (2010). Consulté le December 15, tiré de http://hpce.iitm.ac.in/Manuals/Fluent_6.3/Fluent.Inc/fluent6.3/help/html/ug/node1047.htm#print-plot-resid

Fraccarollo, L., Capart, H., & Zech, Y. (2003). A Godunov method for the computation of erosional shallow water transients. *International Journal for Numerical Methods in Fluids, 41*(9), 951-976.

Fue-Sang, L. (2000). A pressure-based unstructured grid method for all-speed flows. *International Journal for Numerical Methods in Fluids, 33*(3), 355-374.

Gao, W., & Liu, R. (2009). A hybrid finite volume/finite element method for incompressible generalized Newtonian fluid flows on unstructured triangular meshes. *Acta Mechanica Sinica/Lixue Xuebao, 25*(6), 747-760.

George, K. J., & Stripling, S. (1995). Improving the simulation of drying and wetting in a two-dimensional tidal numerical model. *Applied Mathematical Modelling, 19*(1), 2.

Ghia, U., Ghia, K. N., & Shin, C. T. (1982). High-Re solutions for incompressible flow using the Navier-Stokes equations and a multigrid method. *Journal of Computational Physics, 48*(3), 387-411.

Ghisalberti, M., & Nepf, H. (2009). Shallow flows over a permeable medium: The hydrodynamics of submerged aquatic canopies. *Transport in Porous Media, 78*(2), 309-326.

Harvie, D. J. E., & Fletcher, D. F. (2001). A new volume of fluid advection algorithm: the defined donating region scheme. *International Journal for Numerical Methods in Fluids, 35*(2), 151-172.

Hernandez-Duenas, G., & Karni, S. (2011). Shallow Water Flows in Channels. *Journal of Scientific Computing, 48*(1-3), 190-208.

Hieu, P. D., Katsutoshi, T., & Ca, V. T. (2004). Numerical simulation of breaking waves using a two-phase flow model. *Applied Mathematical Modelling, 28*(11), 983-1005.

Hirt, C. W., & Nichols, B. D. (1981). Volume of fluid (VOF) method for the dynamics of free boundaries. *Journal of Computational Physics, 39*(1), 201-225.

Hsieh, T.-Y., & Yang, J.-C. (2005). Numerical examination on the secondary-current effect for contaminant transport in curved channel. *Journal of Hydraulic Research, 43*(6), 644-659.

Hsu, C.-T. (2005). Dynamic Modeling of Convective Heat Transfer in Porous Media. In K. Vafai (dir.), *Handbook of Porous Media*. (2e éd., pp. 39-80). Boca Raton, Fla.: Taylor & Francis.

Huai, W. X., Zeng, Y. H., Xu, Z. G., & Yang, Z. H. (2009). Three-layer model for vertical velocity distribution in open channel flow with submerged rigid vegetation. *Advances in Water Resources, 32*(4), 487-492.

Huang, S.-L., Jia, Y. F., & Wang, S. S. Y. (2006). Numerical modeling of suspended sediment transport in channel bends. *Journal of Hydrodynamics, 18*(4), 411-417.

Jang, C. L., & Shimizu, Y. (2007). Vegetation effects on the morphological behavior of alluvial channels. *Journal of Hydraulic Research, 45*(6), 763-772.

Jimenez-Hornero, F. J., Giraldez, J. V., Laguna, A. M., Bennett, S. J., & Alonso, C. V. (2007). Modelling the effects of emergent vegetation on an open-channel flow using a lattice model. *International Journal for Numerical Methods in Fluids, 55*(7), 655-672.

Kang, H., & Choi, S.-U. (2006). Turbulence modeling of compound open-channel flows with and without vegetation on the floodplain using the Reynolds stress model. *Advances in Water Resources, 29*(11), 1650-1664.

Kang, S., & Kim, Y. (2002). Pressure-based unstructured-grid finite-volume method for simulating laminar reacting flows. *Numerical Heat Transfer, Part B: Fundamentals, 41*(1), 53-72.

Ketabdari, M. J., Nobari, M. R. H., & Moradi Larmaei, M. (2008). Simulation of waves group propagation and breaking in coastal zone using a Navier-Stokes solver with an improved VOF free surface treatment. *Applied Ocean Research, 30*(2), 130-143.

Khosronejad, A., Rennie, C. D., Salehi Neyshabouri, S. A. A., & Townsend, R. D. (2007). 3D numerical modeling of flow and sediment transport in laboratory channel bends. *Journal of Hydraulic Engineering, 133*(10), 1123-1134.

Klopstra, D., Barneveld, H. J., Van Noortwijk, J. M., & Van Velzen, E. H. (1997). Analytical model for hydraulic roughness of submerged vegetation. *Proceedings of the 1997 27th Congress of the International Association of Hydraulic Research, IAHR. Part A*, *San Francisco, CA*.(Vol. A, pp. 775-780): ASCE New York NY USA.

Knock, C., & Ryrie, S. C. (1994). Parameterization of dispersion in the depth-averaged transport equation. *Applied Mathematical Modelling, 18*(10), 582-587.

Kuwahara, F., & Nakayama, A. (1999). Numerical determination of thermal dispersion coefficients using a periodic porous structure. *Transactions of the ASME. Journal of Heat Transfer, 121*(1), 160-163.

Kuwahara, F., Nakayama, A., & Koyama, H. (1996). A numerical study of thermal dispersion in porous media. *Transactions of the ASME. Journal of Heat Transfer, 118*(3), 756-761.

Kuwahara, F., Shirota, M., & Nakayama, A. (2001). A numerical study of interfacial convective heat transfer coefficient in two-energy equation model for convection in porous media. *International Journal of Heat and Mass Transfer, 44*(6), 1153-1159.

Lai, Y. G. (2010). Two-dimensional depth-averaged flow modeling with an unstructured hybrid mesh. *Journal of Hydraulic Engineering, 136*(1), 12-23.

Lane, S. N. (1998). Hydraulic modelling in hydrology and geomorphology: A review of high resolution approaches. *Hydrological Processes, 12*(8), 1131-1150.

Lane, S. N., & Ferguson, R. I. (2005). Modelling reach-scale fluvial flows. In P. D. Bates, S. N. Lane & R. I. Ferguson (dir.), *Computational fluid dynamics: application in environmental hydraulics*. (pp. 217-269). Chichester, England: John Wiley & Sons.

Launder, B. E., & Spalding, D. B. (1974). The Numerical Computation of Turbulent Flows. *Computer Methods in Applied Mechanics and Engineering, 3*, 269-289.

Liang, Q., & Borthwick, A. G. L. (2009). Adaptive quadtree simulation of shallow flows with wet-dry fronts over complex topography. *Computers and Fluids, 38*(2), 221-234.

Liu, T., Wang, X., & Cui, P. (2005). Preliminary study on 1D numerical experiment of water debris flow in gully. *Sichuan Daxue Xuebao (Gongcheng Kexue Ban)/Journal of Sichuan University (Engineering Science Edition), 37*(SUPPL.), 143-147.

Lopez, F., & Garcia, M. (1997). Open-channel flow through simulated vegetation: turbulence modeling and sediment transport (WRP-CP-10). Vicksburg: US Army Corps of Engineers, Waterw. Exp. Stn.

Lopez, F., & Garcia, M. H. (2001). Mean flow and turbulence structure of open-channel flow through non-emergent vegetation. *Journal of Hydraulic Engineering, 127*(5), 392-402.

Lu, Y.-J., Wang, Z.-Y., Zuo, L.-Q., & Zhu, L.-J. (2005). 2D numerical simulation of flood and fluvial process in the meandering and island-braided middle Yangtze River. *International Journal of Sediment Research, 20*(4), 333-349.

Lu, Y., Dou, G., Han, L., Shao, X., & Yang, X. (2004). 3D mathematical model for suspended load transport by turbulent flows and its applications. *Science in China, Series E: Technological Sciences, 47*(2), 237-256.

Martin, J. C., & Moyce, W. J. (1952). An experimental study of the collapse of liquid columns on a rigid horizontal plane. *Philosophical Transactions of the Royal Society of London. Series A, Mathematical and Physical Sciences, 244*(882), 325-334.

Minh Duc, B. (1998). *Berechnung der stroemung und des sedimenttransorts in fluessen mit einem tieffengemittelten numerischen verfahren.* Doctoral dissertation, The University of Karlsruhe, Karlsruhe, Germany.

Mohamadian, A., Le Roux, D. Y., Tajrishi, M., & Mazaheri, K. (2005). A mass conservative scheme for simulating shallow flows over variable topographies using unstructured grid. *Advances in Water Resources, 28*(5), 523-539.

Mohammadian, A., Tajrishi, M., & Lotfi Azad, F. (2004). Two dimensional numerical simulation of flow and geo-morphological processes near headlands by using unstructured grid. *International Journal of Sediment Research, 19*(4), 258-277.

Moradi Larmaei, M., Behzadi , J., & Mahdi, T.-F. (2010). Treatment of checkerboard pressure in the collocated unstructured finite-volume scheme. *Numerical Heat Transfer, Part B: Fundamentals, 58*(2), 121–144.

Moradi Larmaei, M., Behzadi , J., & Mahdi, T.-F. (2011). Grid-independent depth-averaged simulations with a collocated unstructured finite volume scheme. *International Journal for Numerical Methods in Fluids*, Article first published online: 22 MAR 2011.

Moradi Larmaei, M., & Mahdi, T.-F. (2010). *Analysis of SIMPLE algorithm for depth averaged simulations*. 6th International Symposium on Environmental Hydraulics, Athens, Greece, June 23-25.

Moradi Larmaei, M., & Mahdi, T.-F. (2011). A new method for the treatment of wetting-drying fronts. *Applied Mathematical Modelling,* Article in Press.

Moradi Larmaei, M., & Mahdi, T.-F. (2012a). Depth-averaged turbulent heat and fluid flow in a vegetated porous media. *International Journal of Heat and Mass Transfer*, Article in Press.

Moradi Larmaei, M., & Mahdi, T.-F. (2012b). Vorticity equation for the secondary flow effect in depth-averaged simulations. *Advances in Water Resources*, Submitted.

Mosselman, E. (2005). Basic equations for sediment transport in CFD for fluvial morphodynamics. In P. D. Bates, S. N. Lane & R. I. Ferguson (dir.), *Computational fluid dynamics: application in environmental hydraulics*. (pp. 71-90). Chichester, England: John Wiley & Sons.

Murillo, J., Garcia-Navarro, P., Brufau, P., & Burguete, J. (2006). Extension of an explicit finite volume method to large time steps (CFL > 1): Application to shallow water flows. *International Journal for Numerical Methods in Fluids, 50*(1), 63-102.

Murillo, J., Garcia-Navarro, P., Brufau, P., & Burguete, J. (2008). 2D modelling of erosion/deposition processes with suspended load using upwind finite volumes. *Journal of Hydraulic Research, 46*(1), 99-112.

Murillo, J., Garcia-Navarro, P., & Burguete, J. (2008). Analysis of a second-order upwind method for the simulation of solute transport in 2D shallow water flow. *International Journal for Numerical Methods in Fluids, 56*(6), 661-686.

Murillo, J., Garcia-Navarro, P., Burguete, J., & Brufau, P. (2006). A conservative 2D model of inundation flow with solute transport over dry bed. *International Journal for Numerical Methods in Fluids, 52*(10), 1059-1092.

Nagata, N., Hosoda, T., & Muramoto, Y. (2000). Numerical analysis of river channel processes with bank erosion. *Journal of Hydraulic Engineering, 126*(4), 243-252.

Nikolos, I. K., & Delis, A. I. (2009). An unstructured node-centered finite volume scheme for shallow water flows with wet/dry fronts over complex topography. *Computer Methods in Applied Mechanics and Engineering, 198*(47-48), 3723-3750.

Nobari, M. R. H., Ketabdari, M. J., & Moradi, M. (2009). A modified volume of fluid advection method for uniform Cartesian grids. *Applied Mathematical Modelling, 33*(5), 2298-2310.

Norris, S. E., Were, C. J., Richards, P. J., & Mallinson, G. D. (2011). A Voronoi-based ALE solver for the calculation of incompressible flow on deforming unstructured meshes. *International Journal for Numerical Methods in Fluids, 65*(10), 1160-1179.

Okamoto, T.-A., & Nezu, I. (2009). Turbulence structure and "Monami" phenomena in flexible vegetated open-channel flows. *Journal of Hydraulic Research, 47*(6), 798-810.

Pasche, E. (1984). Turbulence mechanism in natural streams and the possibility of its mechanical representation (52). Aachen, Germany: Mitteilungen Institut für Wasserbau und Wasserwirtschaft, No. 52, RWTH.

Patankar, S. V. (1980). *Numerical heat transfer and fluid flow*. New York: Hemisphere.

Pedras, M. H. J., & de Lemos, M. J. S. (2008). Thermal dispersion in porous media as a function of the solid-fluid conductivity ratio. *International Journal of Heat and Mass Transfer, 51*(21-22), 5359-5367.

Pimpalnerkar, S., Kulkarni, M., & Date, A. W. (2005). Solution of transport equations on unstructured meshes with cell-centered colocated variables. Part II: Applications. *International Journal of Heat and Mass Transfer, 48*(6), 1128-1136.

Rahman, M. M., Siikonen, T., & Miettinen, A. (1997). Pressure-correction method for solving fluid flow problems on a collocated grid. *Numerical Heat Transfer, Part B: Fundamentals, 32*(1), 63-84.

Rhie, C. M., & Chow, W. L. (1983). Numerical Study of the turbulent flow past an airfoil with trailing edge separation. *AIAA Journal, 21*(11), 1525-1532.

Rocamora Jr, F. D., & De Lemos, M. J. S. (2000). Laminar recirculating flow and heat transfer in hybrid porous medium-clear fluid computational domains. *34th ASME-National heat transfer conference*, *Pittsburgh, PA*. ASME-HTD-I463CD, paper NHTC2000-12317 (on CD-ROM).

Rodi, W. (1993). *Turbulence models and their application in hydraulics* (3e éd.). Balkema, Rotterdam, Netherlands: IAHR Monograph.

Rodriguez, J. F., Bombardelli, F. A., Garcia, M. H., Frothingham, K. M., Rhoads, B. L., & Abad, J. D. (2004). High-resolution numerical simulation of flow through a highly sinuous river reach. *Water Resources Management, 18*(3), 177-199.

Roe, P. L. (1997). Approximate Riemann Solvers, Parameter Vectors, and Difference Schemes. *Journal of Computational Physics, 135*(2), 250.

Rozovskii, I. L. (1957). Flow of water in bends of open channel. Kiev: Academy of Sciences of the Ukrainian SSR.

Saito, M. B., & de Lemos, M. J. S. (2005). Interfacial heat transfer coefficient for non-equilibrium convective transport in porous media. *International Communications in Heat and Mass Transfer, 32*(5), 666-676.

Saito, M. B., & de Lemos, M. J. S. (2006). A correlation for interfacial heat transfer coefficient for turbulent flow over an array of square rods. *Journal of Heat Transfer, 128*(5), 444-452.

Saito, M. B., & de Lemos, M. J. S. (2009). Laminar heat transfer in a porous channel simulated with a two-energy equation model. *International Communications in Heat and Mass Transfer, 36*(10), 1002-1007.

Saito, M. B., & de Lemos, M. J. S. (2010). A macroscopic two-energy equation model for turbulent flow and heat transfer in highly porous media. *International Journal of Heat and Mass Transfer, 53*(11-12), 2424-2433.

Schlichting, H. (1962). *Boundary layer theory[M]* (4e éd.). New York: McGraw-Hill.

Shen, W. Z., Michelsen, J. A., Srensen, N. N., & Srensen, J. N. (2003). An improved SIMPLEC method on collocated grids for steady and unsteady flow computations. *Numerical Heat Transfer, Part B: Fundamentals, 43*(3), 221-239.

Shin, J., Kim, K.-H., Lee, K.-K., & Kim, H.-S. (2010). Assessing temperature of riverbank filtrate water for geothermal energy utilization. *Energy, 35*(6), 2430-2439.

Sleigh, P. A., Gaskell, P. H., Berzins, M., & Wright, N. G. (1998). An unstructured finite-volume algorithm for predicting flow in rivers and estuaries. *Computers and Fluids, 27*(4), 479-508.

Soares-Frazao, S., & Zech, Y. (2011). HLLC scheme with novel wave-speed estimators appropriate for two-dimensional shallow-water flow on erodible bed. *International Journal for Numerical Methods in Fluids, 66*(8), 1019-1036.

Sotiropoulos, F. (2005). Introduction to statistical turbulence modelling for hydraulic engineering flows. In P. D. Bates, S. N. Lane & R. I. Ferguson (dir.), *Computational fluid dynamics: application in environmental hydraulics.* (pp. 91-120). Chichester, England: John Wiley & Sons.

Steffler, P. M. (1984). *Turbulent flow in a curved rectangular channel.* PhD, University of Alberta, Alberta, Canada.

Stoesser, T., Ruether, N., & Olsen, N. R. B. (2010). Calculation of primary and secondary flow and boundary shear stresses in a meandering channel. *Advances in Water Resources, 33*(2), 158-170.

Stone, B. M., & Shen, H. T. (2002). Hydraulic resistance of flow in channels with cylindrical roughness. *Journal of Hydraulic Engineering, 128*(5), 500-506.

Sun, T., Meakin, P., & Jossang, T. (2001). A computer model for meandering rivers with multiple bed load sediment sizes 1. Theory. *Water Resources Research, 37*(8), 2227-2241.

Sun, X., Shiono, K., Rameshwaran, P., & Chandler, J. H. (2010). Modelling vegetation effects in irregular meandering river. *Journal of Hydraulic Research, 48*(6), 775-783.

Tang, X., & Knight, D. W. (2008). A general model of lateral depth-averaged velocity distributions for open channel flows. *Advances in Water Resources, 31*(5), 846-857.

Tanino, Y., & Nepf, H. M. (2008). Laboratory investigation of mean drag in a random array of rigid, emergent cylinders. *Journal of Hydraulic Engineering, 134*(1), 34-41.

Teruel, F. E., & Rizwan-Uddin. (2009a). Characterization of a porous medium employing numerical tools: Permeability and pressure-drop from Darcy to turbulence. *International Journal of Heat and Mass Transfer, 52*(25-26), 5878-5888.

Teruel, F. E., & Rizwan-uddin. (2009b). A new turbulence model for porous media flows. Part I: Constitutive equations and model closure. *International Journal of Heat and Mass Transfer, 52*(19-20), 4264-4272.

Teruel, F. E., & Rizwan-Uddin. (2010). Numerical computation of macroscopic turbulence quantities in representative elementary volumes of the porous medium. *International Journal of Heat and Mass Transfer, 53*(23-24), 5190-5198.

Toda, Y., Ikeda, S., Kumagai, K., & Asano, T. (2005). Effects of flood flow on flood plain soil and riparian vegetation in a gravel river. *Journal of Hydraulic Engineering, 131*(11), 950-960.

Tominaga, A., Nagao, M., & Nezu, I. (1998). Effects of vegetation on flow structures and bed profiles in curved open channels. *Second international symposium on environmental hydraulics*, *Hong Kong, China*.(pp. 329-334). Rotterdam: A.A. Balkema. tiré de

Toro, E. F. (2001). *Shock-capturing methods for free-surface shallow flows*. Chichester, England John Wiley & Sons.

Touazi, O., Chenier, E., & Eymard, R. (2008). Simulation of natural convection with the collocated clustered finite volume scheme. *Computers and Fluids, 37*(9), 1138-1147.

Velasco, D., Bateman, A., & Medina, V. (2008). A new integrated hyro-mechanical model applied to flexible vegetation in riverbeds. *Journal of Hydraulic Research, 46*(5), 579-597.

Versteeg, H. K., & Malalasekera, W. (1995). *An introduction to computational fluid dynamics : the finite volume method*. Toronto: Pearson Prentice Hall.

Voller, V. R. (2010). A model of sedimentary delta growth: A novel application of numerical heat transfer methods. *International Journal of Numerical Methods for Heat and Fluid Flow, 20*(5), 570-586.

Wang, X.-g., Yan, Z.-m., & Guo, W.-d. (2007). Three-dimensional simulation for effects of bed discordance on flow dynamics at Y-shaped open channel confluences. *Journal of Hydrodynamics, 19*(5), 587-593.

Wang, Z.-Q., & Cheng, N.-S. (2005). Secondary flows over artificial bed strips. *Advances in Water Resources, 28*(5), 441-450.

Wang, Z.-Q., & Cheng, N.-S. (2006). Time-mean structure of secondary flows in open channel with longitudinal bedforms. *Advances in Water Resources, 29*(11), 1634-1649.

Wilson, C. A. M. E., Yagci, O., Rauch, H. P., & Olsen, N. R. B. (2006). 3D numerical modelling of a willow vegetated river/floodplain system. *Journal of Hydrology, 327*(1-2), 13-21.

Wu, F.-C., Shen, H. W., & Chou, Y.-J. (1999). Variation of roughness coefficients for unsubmerged and submerged vegetation. *Journal of Hydraulic Engineering, 125*(9), 934-941.

Wu, W. (2004). Depth-averaged two-dimensional numerical modeling of unsteady flow and nonuniform sediment transport in open channels. *Journal of Hydraulic Engineering, 130*(10), 1013-1024.

Wu, W., Shields Jr, F. D., Bennett, S. J., & Wang, S. S. Y. (2005). A depth-averaged two-dimensional model for flow, sediment transport, and bed topography in curved channels with riparian vegetation. *Water Resources Research, 41*(3), W03015.

Wu, W., & Wang, S. S. Y. (2004). Depth-averaged 2-D calculation of flow and sediment transport in curved channels. *International Journal of Sediment Research, 19*(4), 241-257.

Wu, W., & Wang, S. S. Y. (2004). A depth-averaged two-dimensional numerical model of flow and sediment transport in open channels with vegetation. In S. J. Bennett & A. Simon (dir.), *Riparian Vegetation and Fluvial Geomorphology*. (pp. 281). Washington, DC: American Geophysical Union.

Wu, W., & Wang, S. S. Y. (2008). One-dimensional explicit finite-volume model for sediment transport with transient flows over movable beds. *Journal of Hydraulic Research, 46*(1), 87-98.

Wu, W., & Wang, S. Y. (2007). One-dimensional modeling of dam-break flow over movable beds. *Journal of Hydraulic Engineering, 133*(1), 48-58.

Xia, J., Falconer, R. A., Lin, B., & Tan, G. (2010). Modelling flood routing on initially dry beds with the refined treatment of wetting and drying. *International Journal of River Basin Management, 9*(3), 1-19.

Xia, J., Lin, B., Falconer, R. A., & Wang, G. (2010). Modelling dam-break flows over mobile beds using a 2D coupled approach. *Advances in Water Resources, 33*(2), 171-183.

Zhang, J.-t., & Su, X.-h. (2008). Numerical Model for Flow Motion with Vegetation. *Journal of Hydrodynamics, 20*(2), 172-178.

Zhang, K. K. Q., Rovagnati, B., Gao, Z., Minkowycz, W. J., & Mashayek, F. (2007). An introduction to the lattice grid. *Numerical Heat Transfer, Part B Fundamentals, 51*(5-6), 415-431.

Zhang, M.-L., Li, C. W., & Shen, Y.-M. (2010). A 3D non-linear k-epsilon turbulent model for prediction of flow and mass transport in channel with vegetation. *Applied Mathematical Modelling, 34*(4), 1021-1031.

Zhang, N., Zheng, Z. C., & Yadagiri, S. (2011). A hydrodynamic simulation for the circulation and transport in coastal watersheds. *Computers & Fluids, 47*(1), 178-188.

Zhang, X., & Nepf, H. M. (2009). Thermally driven exchange flow between open water and an aquatic canopy. *Journal of Fluid Mechanics, 632*, 227-243.

Zhao, D. H., Shen, H. W., Tabios, G. Q., Lai, J. S., & Tan, W. Y. (1994). Finite-volume two-dimensional unsteady-flow model for river basins. *Journal of Hydraulic Engineering, 120*(7), 863-882.

Zhou, J. G., Causon, D. M., Mingham, C. G., & Ingram, D. M. (2001). The surface gradient method for the treatment of source terms in the shallow-water equations. *Journal of Computational Physics, 168*(1), 1-25.

Zokagoa, J.-M., & Soulaimani, A. (2010). Modeling of wetting-drying transitions in free surface flows over complex topographies. *Computer Methods in Applied Mechanics and Engineering, 199*(33-36), 2281-2304.

Zoppou, C., & Roberts, S. (2000). Numerical solution of the two-dimensional unsteady dam break. *pplied Mathematical Modelling, 24*(7), 457-475.

APPENDIX 1 – Additional validation tests

In this appendix additional validation tests will be presented. These tests support the validity of the solver in different circumstances. In this appendix, W-D.B. denotes the Wetting-Drying Boundary, D.B. denotes the Dry Boundary which is related to a case equivalent to the W-D.B. case but without floodplains, P.S. denotes the Present Solver, and [-] denotes that the actual simulation is performed dimensionless.

Laminar heat transfer in a two-dimensional duct

In this test, density, dynamic viscosity, laminar conductivity, and specific heat capacity are $50\,kg/m^3$, $0.5\,N.m/s^2$, $0.6\,W/(m.°K)$, and $0.84\,J/(kg.°K)$, respectively. Reference length, velocity, and temperature are $1.0m$, $1.0\,m/s$, and $300°K$, respectively. The time step size for unsteady solution is $0.02s$. Grid is 10×50 at the domain boundaries, and flow Reynolds and Prandtl numbers are 100 and 0.7, respectively. Errors are scaled and convergence criterion is set to 10^{-3} and 10^{-6} for flow and energy equations, respectively. This test shows that, the results of steady and unsteady solution are similar, and relaxation factor has no effect on simulations. The dimensionless temperature is defined as $T = \left(T^* - T_{ref}\right)/\left(T_{wall} - T_{ref}\right)$.

<center>(<i>a</i>)   (<i>b</i>)   (<i>c</i>)</center>
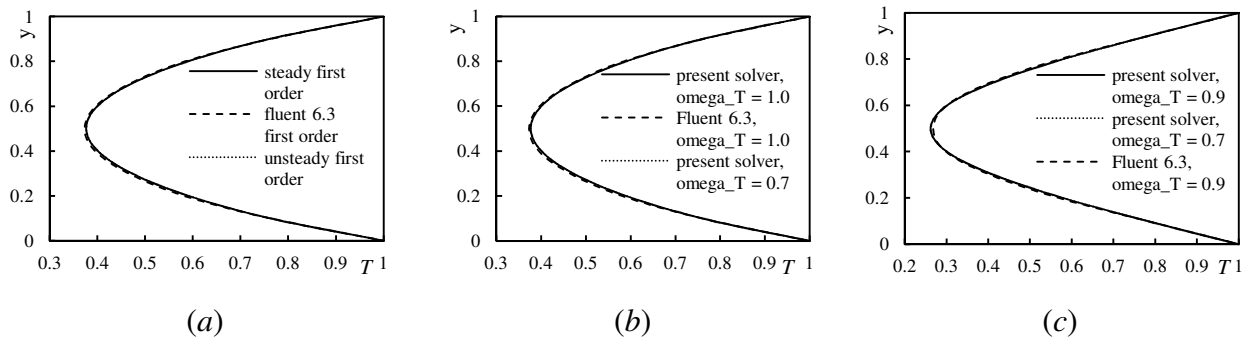
Figure A1.1. Temperature profile in a laminar duct; (*a*) comparison of steady and unsteady solutions, (*b*) effect of relaxation factor in a first order solution, and (*c*) effect of relaxation factor in a second order solution.

Lid-driven pool

This test is similar to the lid-driven cavity test in Chapter 3, but the problem includes a pool not a cavity. In this test, the depth of fluid at initial condition and the point of reference water surface is $0.3m$, and the height of pool's walls is $1.0m$. Thus, there will be no flooding when lid start moving. This test proves the performance of the wall boundary condition applied to wetting-drying front. As it can be seen in Figure A1.3, grid significantly affects the checkerboard system in water surface. This figure also shows that dimensionless and dimensional solutions are equivalently accurate.
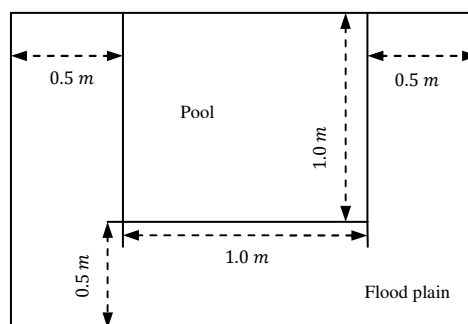
Figure A1.2. Geometrical detail of the lid-driven pool.
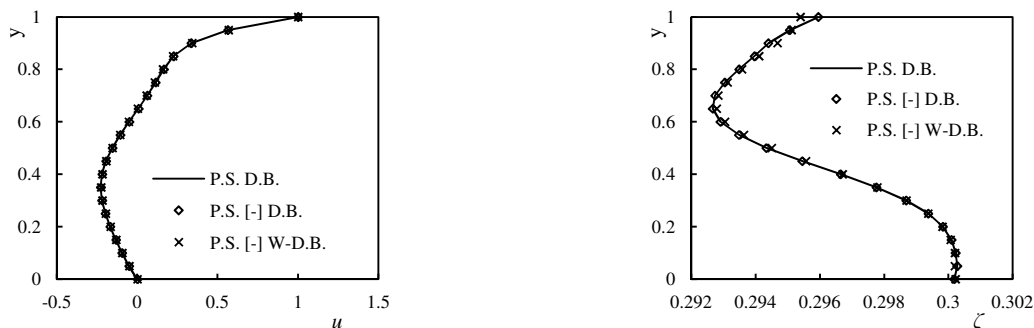
Figure A1.3. Profile of velocity and pressure at a cross section in horizontal center of channel.

Turbulent duct

This test is similar to the duct test case in Chapter 3 with $R_e = 4410$. In this test, the solver is used to solve a turbulent flow both dimensional and dimensionless. The solutions then are compared.
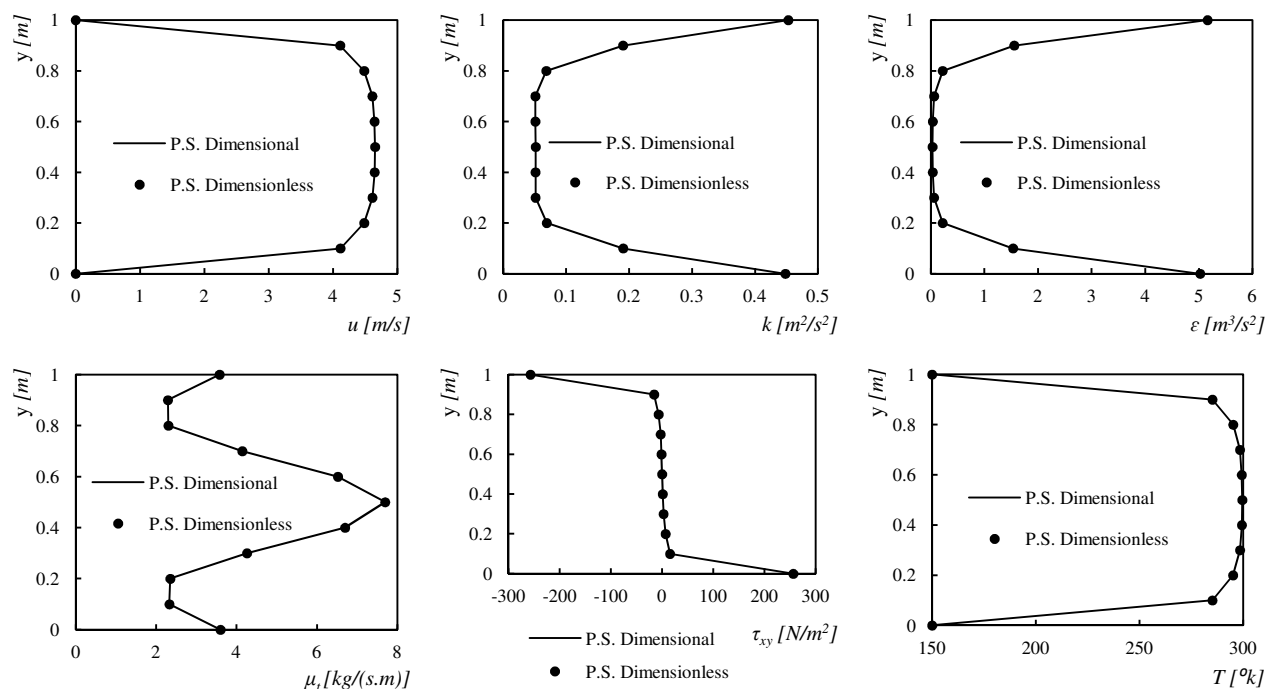
Figure A1.4. Comparison of flow variables in a turbulent duct; with Dimensional and Dimensionless, it is meant that the actual simulation is dimensional or dimensionless, but presentations are dimensional.
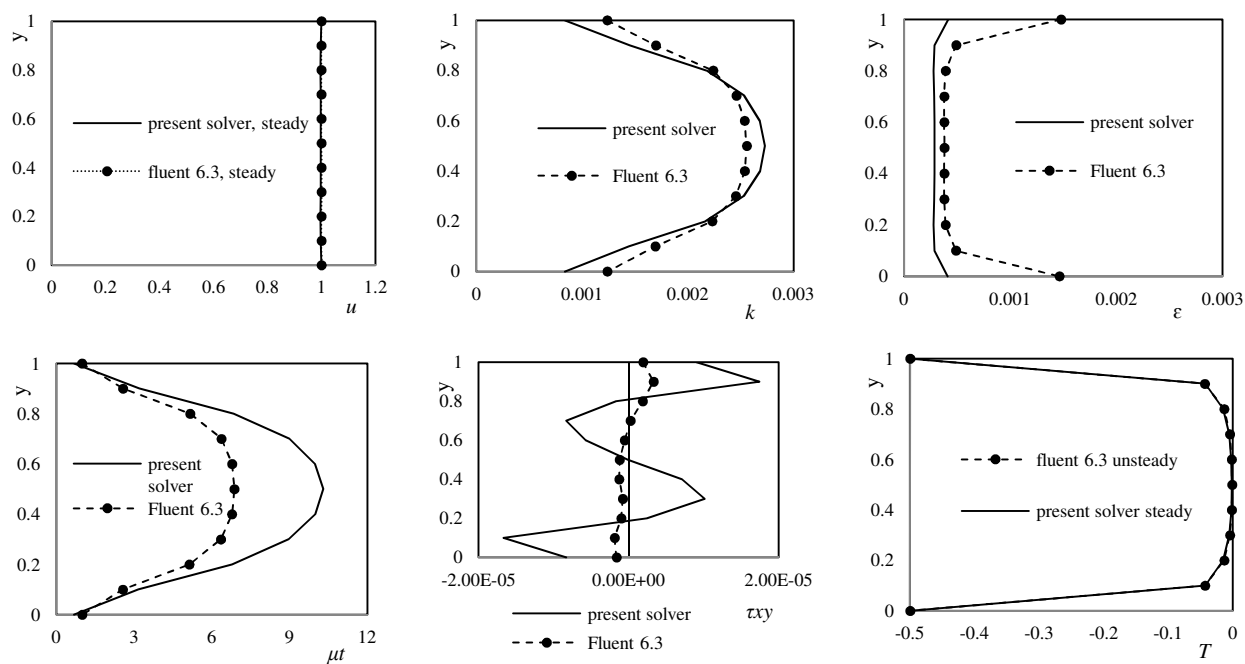
Figure A1.5. Comparison of flow variables in a turbulent duct with free-slip walls.

The wall boundary condition then is changed in Figures A1.5 and A1.6 to free-slip and rough no-slip conditions, and solutions are compared with those of Fluent6.3. In this test, the dimensionless temperature is defined as $T = \left(T^* - T_{ref}\right)/T_{ref}$.
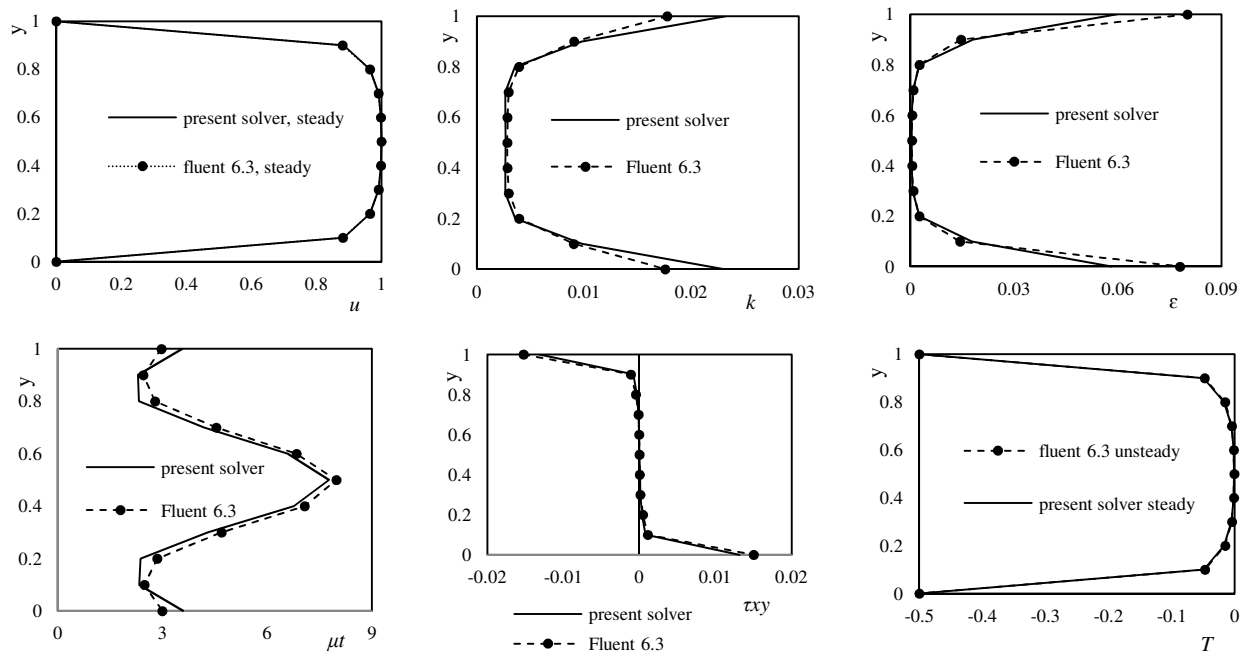
Figure A1.6. Comparison of flow variables in a turbulent duct with rough no-slip walls.

Shear free channel

This test is similar to the shear free channel test in Chapter 4, but there are floodplains beside side walls. The height of the floodplain is $1.0m$ from reference level and, in turn, they will not be flooded. A comparison is made between the computed results for the problems with and without floodplain. The small differences are because the solutions are not grid independent, and the grids used for the problems with and without floodplain are not the same.
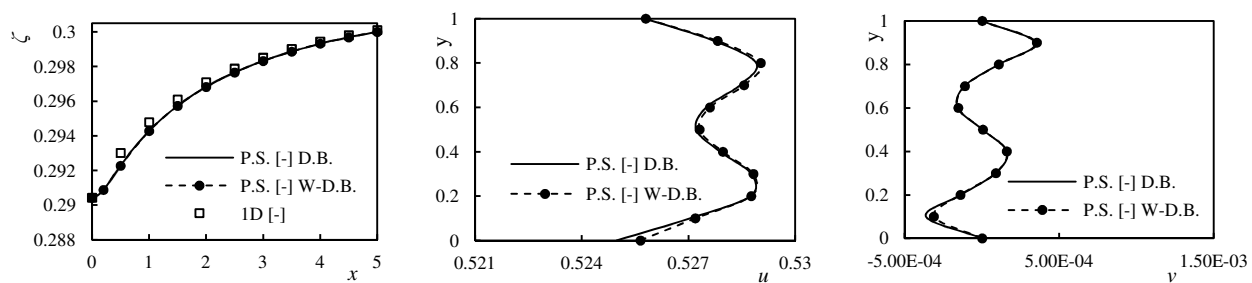
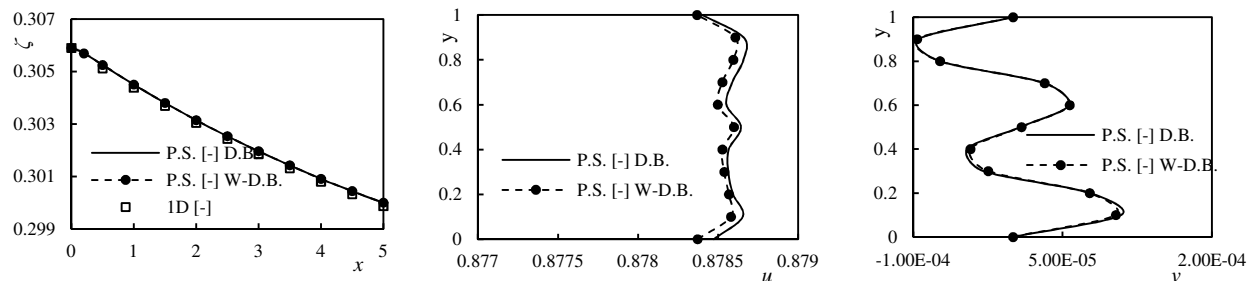Figure A1.7. Comparison of flow variables in a turbulent channel with free-slip walls and bed.

Pressurised channel

This test is similar to the test case in Chapter 4, but there are floodplains in sides of channel. The height of the floodplain is $1.0m$ from reference level and, in turn, they will not be flooded. A comparison is made between the computed results for the problems with and without floodplain. The small differences in Figure A1.8 are because the solutions are not grid independent, and the grids used for the problems with and without floodplain are not the same.

Figure A1.8. Comparison of flow variables in a turbulent channel with free-slip walls and rough bed.

In Figure A1.9 grids used for the channels with and without floodplains are exactly similar in wet region. As it can be observed, results are the same.
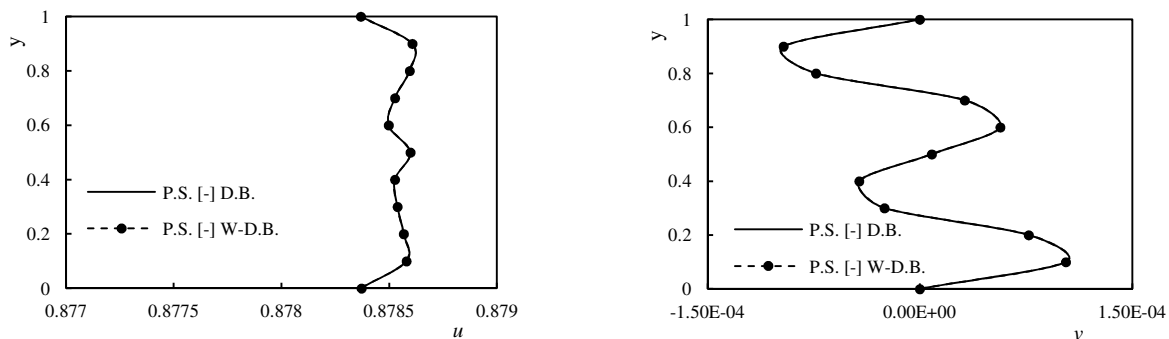
Figure A1.9. Comparison of flow variables in a turbulent channel with free-slip walls and rough bed; grids are exactly similar for the cases with and without flood plain.

In Figure A1.10 first order and second order simulations are compared. Since stream-wise velocity is uniform and the transverse velocity almost zero, the difference between first and second order velocities is not significant. When the second order technique is used, the

oscillations slightly increase. Since there is no slope limiter in Shallow Fluent, such increase in oscillations is not surprising.
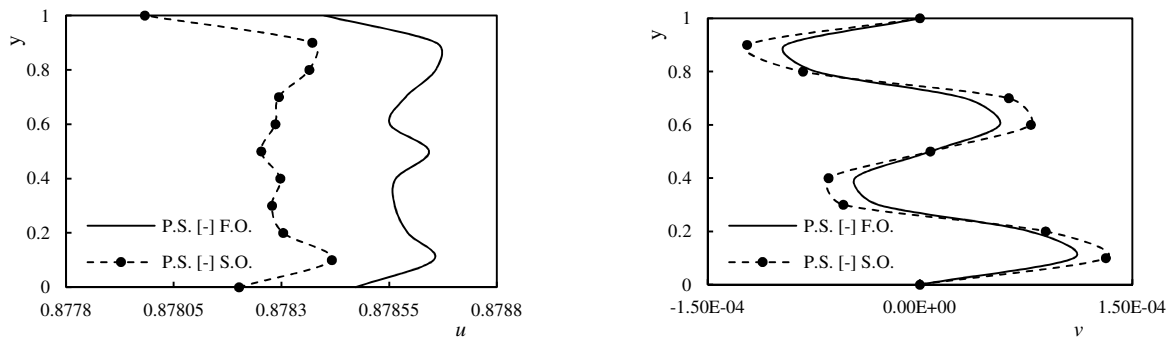

Figure A1.10. Comparison of profiles of stream-wise and transverse velocities in a turbulent channel with free-slip walls and rough bed.

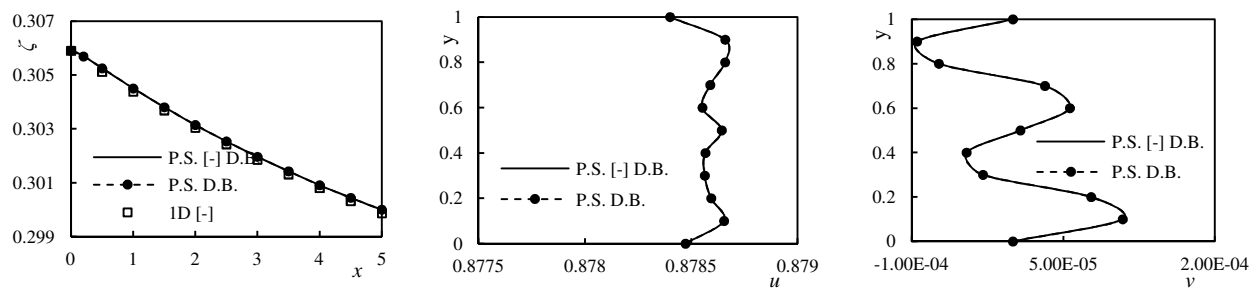As it can be observed in Figure A1.11, results computed with dimensional and dimensionless manner are similar.

Figure A1.11. Comparison of dimensional and dimensionless variables in a turbulent channel with free-slip walls and rough bed.
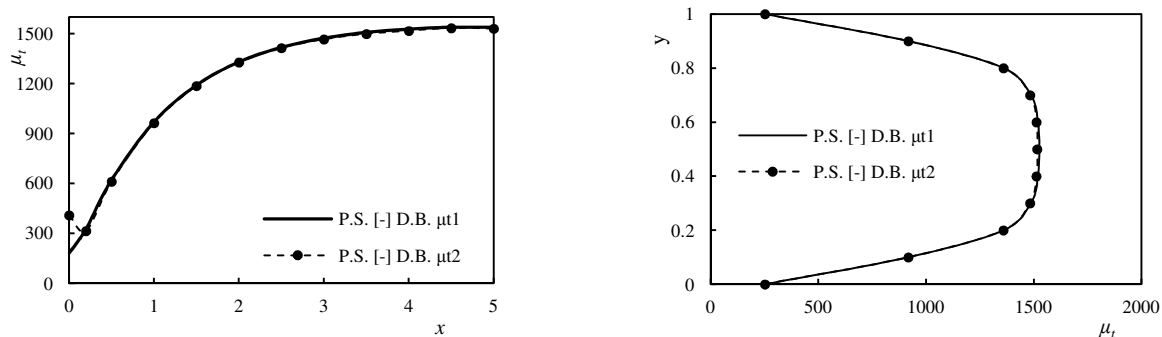
Figure A1.12. Longitudinal and transverse profiles of eddy viscosity.

While the effect of the inlet turbulence on eddy viscosity is only significant at the inlet, it significantly affects the other flow variables. This can be observed in Figure A1.12 for eddy viscosity and in Figure A1.13 for other flow variables. In these tests $k_1 = 4.88392 \times 10^{-4}$, $\varepsilon_1 = 8.44532 \times 10^{-5}$; $k_2 = 3.614510 \times 10^{-4}$, $\varepsilon_2 = 1.6130884 \times 10^{-5}$ at the inlet. Since pressure at the beginning of channel is higher, false currents significantly increase. The case 2 does not represent a good prediction of inlet turbulence since the longitudinal profile of eddy viscosity shows a minimum point after the inlet.
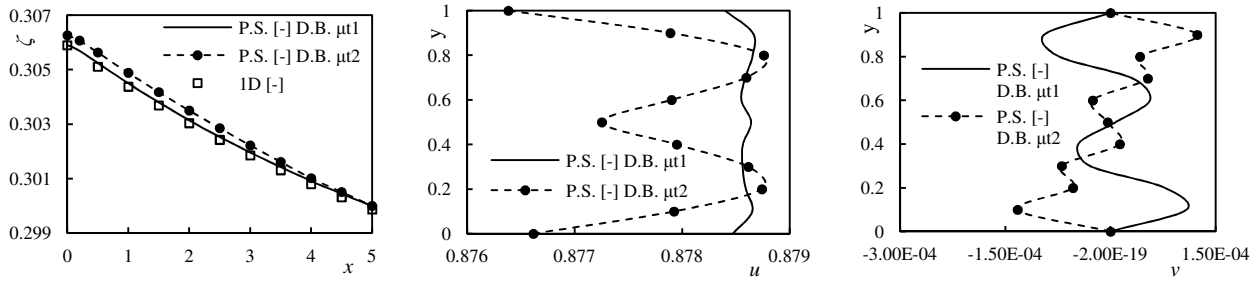

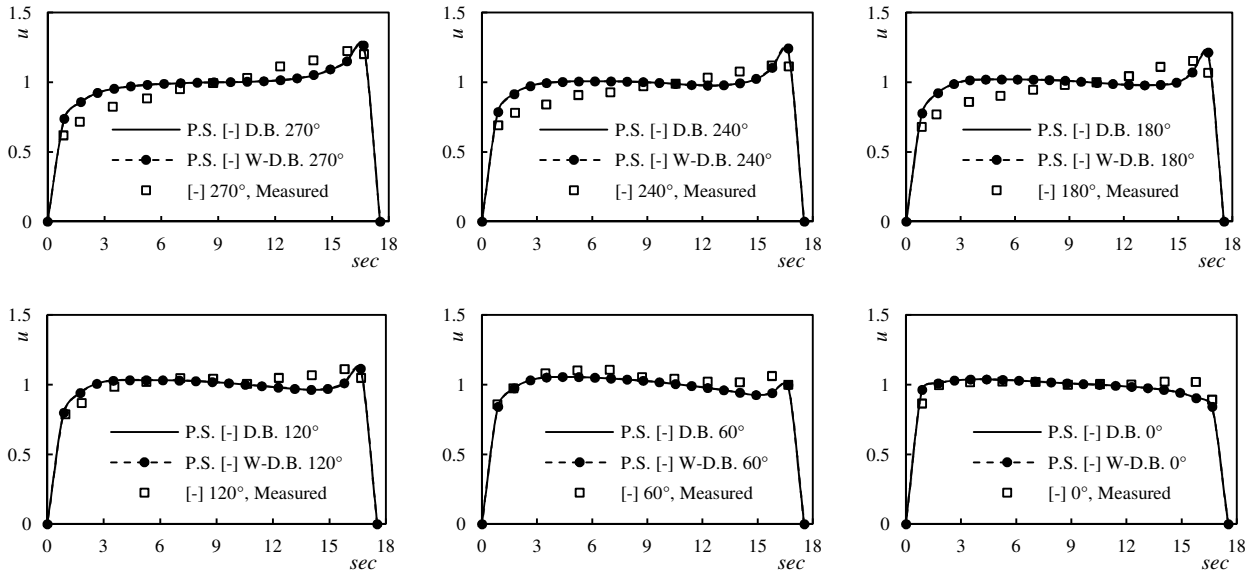Figure A1.13. Profiles of flow variables for different inlet turbulence.

Figure A1.14. Comparison of the dimensional and dimensionless profiles of stream-wise velocity for Steffler's (1981) bend.

Steffler's (1981) bend

This test is similar to the test case in Chapter 4, but there are floodplains beside side walls with the height equal to $1.0m$. As it can be seen in Figures A1.14 and A1.15, dimensional and dimensionless solutions are similar and the computed results with and without floodplains are the same. In Figure A1.14, the secondary force is taken into account.
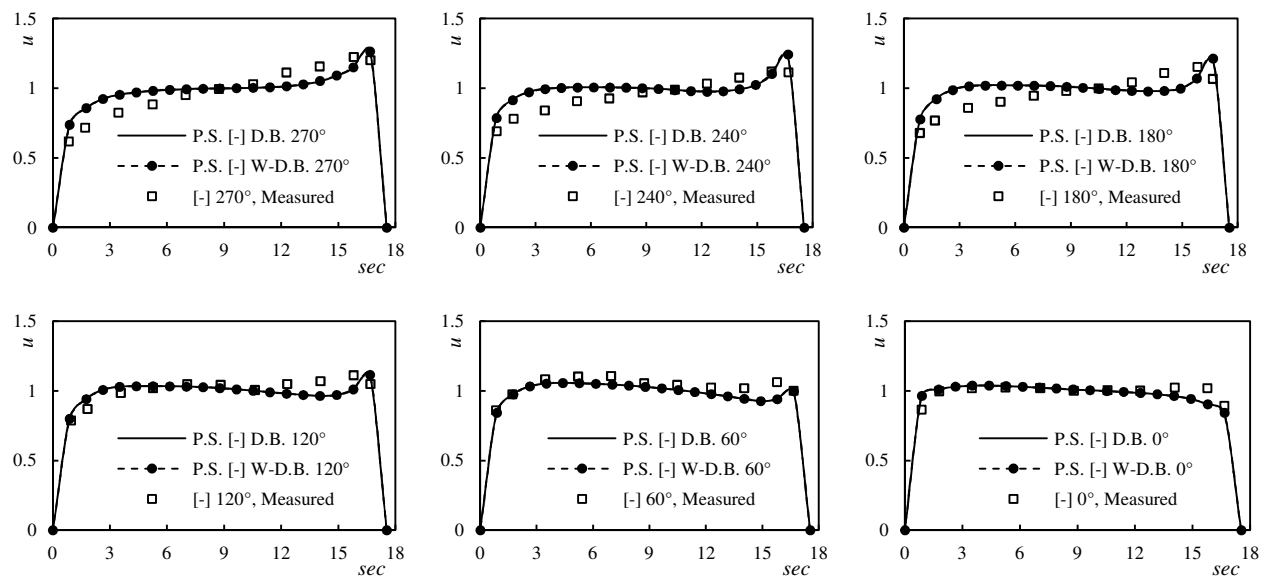

Figure A1.15. Comparison of velocity profiles for the Steffler's (1981) bend with and without floodplain.